# ABSTRACT

Title of Dissertation: PETROLOGIC, GEOCHEMICAL, AND SPECTRAL CHARACTERISTICS OF OXIDIZED PLANETARY DIFFERENTIATION

Samuel Dean Crossley (Doctor of Philosophy), 2021

Dissertation directed by: Professor Jessica M. Sunshine, University of Maryland Department of Astronomy

Meteorites provide evidence that planetary formation occurred across a wide range of oxidation environments in the early Solar System. While the process of differentiation for many reduced, oxygen-poor assemblages has been thoroughly explored, significantly less is known about how differentiation occurred in more oxidized regions of the Solar System. Results from petrologic and geochemical investigations of oxidized chondrites (Rumurutiites) and primitive achondrites (brachinites) reveal that significant mineralogic differences occur with increasing degrees of oxidation. As a consequence, the differentiation pathways of oxidized and reduced assemblages diverge during the earliest stages of partial melting. While reduced materials differentiate to form a basaltic crust, magnesian peridotite mantle, and metallic core, oxidized materials may instead form felsic crusts, ferroan peridotite mantles, and sulfide-dominated cores. These pathways are evident in distinct siderophile trace element systematics for oxidized and reduced endmembers of the brachinite meteorite family. The compositions of olivine between oxidation endmembers are resolvable using remote sensing techniques that are applicable to

asteroids. Most olivine-dominated asteroids examined in this work are consistent with having formed in oxidized environments, similar to R chondrites and brachinites, or in even more oxidizing environments not recorded among the meteoritic record. This provides strong evidence that environments capable of supporting oxidized, sulfide-dominated core formation are widespread among asteroidal materials. Several of these asteroids are likely mantle restites, based on their olivine composition and the estimated abundances of pyroxene. The predominance of oxidized over reduced environments among olivine-dominated asteroids is likely related to their respective petrogenetic histories: reduced assemblages must reach and sustain much higher temperatures to fully melt and segregate their pyroxene contents from olivine, which requires larger and earlier-accreted parent bodies. Consequently, sampling reduced mantle restites without significant pyroxene contamination would require catastrophic parent body destruction without mixing crustal and mantle materials. Oxidized materials, in contrast, have much higher initial olivine/pyroxene ratios, and thus are much more prone to producing asteroids dominated by olivine.

# PETROLOGIC, GEOCHEMICAL, AND SPECTRAL CHARACTERISTICS OF OXIDIZED PLANETARY DIFFERENTIATION

by

Samuel Dean Crossley

Dissertation submitted to the Faculty of the Graduate School of the
University of Maryland, College Park, in partial fulfillment
of the requirements for the degree of
Doctor of Philosophy
2021

Advisory Committee:

Professor Jessica M. Sunshine, Chair
Dr. Richard D. Ash
Dr. Timothy J. McCoy
Dr. Catherine Corrigan
Professor Richard J. Walker
Professor Megan E. Newcombe
Professor Christine Hartzell

# Preface

In this dissertation, Chapter 2 ("Sulfide-dominated partial melting pathways in brachinites") is a verbatim transcript of work previously published in *Meteoritics and Planetary Science* for which I was the lead author. I collected all of the compositional data for meteorites apart from bulk trace element measurements, which were collected by co-author Dr. Igor Puchtel. Manuscript revisions were contributed by co-authors, Drs. Jessica Sunshine, Richard Ash, Timothy McCoy, Catherine Corrigan, David Mittlefehldt, and Igor Puchtel. Reviews from Drs. James Day and Richard Greenwood also contributed significantly to improving the quality of the final publication.

Chapter 3 ("Parent body conditions prior to the onset of melting") is work that has been submitted to *Geochimica et Cosmochimia Acta* for publication. I collected all of the compositional data for meteorites. I was the lead author, and manuscript revisions were contributed by co-authors, Drs. Richard Ash, Jessica Sunshine, Catherine Corrigan, and Timothy McCoy.

Chapter 4 ("Petrologic interpretations of olivine-dominated asteroids") has been written with the expectation that it will be submitted to a peer-reviewed journal. Spectral data for meteorite powders was collected by Takahiro Hiroi at Brown University's RELAB facility, and all modeling of meteorite and asteroid spectra were conducted by me. Revisions for this chapter were provided by Drs. Jessica Sunshine and Richard Ash.

# Dedication

I'd like to dedicate this work to my family and dearest friends. To my parents, I am thankful every day for your unfailing love and support. Dad, your inquisitive spirit has always inspired me to look at the world with the same sense of wonder and a yearning to understand it more deeply. Mom, you have nurtured my creative spirit in its every manifestation. I cherish you both more with each day, and I am forever grateful for the privilege of being born the son of Lyle and Nancy Crossley.

To my dear old friends, thank you for sticking by me throughout my time abroad and during graduate school. For Matt, CeeAnn, and Kaitlyn, thanks for keeping a chair at the table for me. For all of my amazing Peace Corps padi dem, tenki boku-- you helped me believe in myself. To my good friend, Amadu, I dedicate this work to us both so that we never forget what we are capable of. To my dog, Erebos, thanks for being the best office mate ever and for volunteering as the unofficial department therapy dog for so many years.

To my wife, Kanu, I dedicate this work to you because every day you remind me that life can be so beautiful. Wherever the road takes us, I know that it will be good because we have each other. I can't think of anything better than that.

With love,

Sam

# Acknowledgements

There are many people I'd like to acknowledge, without whom, this work could not have been accomplished. First and foremost, I'd like to thank my advisors, Jess Sunshine and Richard Ash for our many, many hours of discussion. I consider myself fortunate to have been able to learn from you both over the past 5 years, and all of the effort you've put into helping me start a career is something that I will carry with me for years to come.

To my PhD mentors elsewhere, Cari Corrigan, Tim McCoy, Nicole Lunning, and Duck Mittlefehldt, thank you all for your guidance and contributions. It has been a privilege to learn from you thus far, and I hope there will be plenty of opportunities to continue to do so in the future.

To academic advisors of days past, Rhiannon Mayne, Steve Rosscoe, and Mark Ouimette, thank you for all your support and the roles you each played in getting me to where I am today. Rhiannon, I wouldn't have gotten into Planetary Science without you, nor met the good folks at the Smithsonian or UMD — I will always be grateful for everything you've done for me. Steve, I first became interested in research and graduate school because of you, so in a way, this is your fault. Thanks for taking the time to work with me on coccoliths and always taking the extra effort to get your students involved. Mark, your classes were what first got me interested in Geology. I still remember coming to you after class and telling you that I wanted to major in Geology – you hugged me, welcomed me in, and I've had the best time ever since.

There are many other collaborators and participating scientists who I'd like to thank for their help with analyses and data processing. Many thanks to Loan Le for helping assemble EDS maps and just being a great friend while I was working at ARES. I'm grateful for the time spent with the late Kent Ross, who helped me collect countless EMP data points over many weeks with some of the most colorful language I've ever heard – you're missed dearly, Kent. Thanks to Anne Peslier for help collecting yet more EMP data. To Tim Gooding and Tim Rose at SI, thanks for all your help getting the probe and SEM to work for me. To Igor Puchtel, thanks for all the time you spent teaching me about isotope dilution and the late-night lab work. Finally, thanks to Ashley King for conducting XRD analyses for us when we no longer had lab access due to the pandemic.

Of course, I'd also like to acknowledge the many sources of funding that contributed to this work. Since 2017, my PhD program was fully funded through the NASA Fellowship Activity program (NNH17ZHA001N), which enabled me to work for 8 weeks each year at NASA Johnson Space Center. For the Spring 2021 semester, I was funded by UMD's Wylie Dissertation Fellowship. I was also fortunate enough to receive the CMNS Dean's Fellowship for the 2018-2019 academic year. Funding for travel to conferences, where I presented my work to the broader community, was provided by LPI, USRA, Planetary Science Foundation, and UMD's Goldhaber and ESSC travel awards.

# Table of Contents

# List of Tables

# List of Figures

# Chapter 1: Introduction and Background

## *1.1 Early Solar System History*

The Solar System began as a slowly rotating molecular cloud of gas and dust. Due to disturbance from some external source, perhaps galactic shock waves, a nearby supernovae, or a collision with another molecular cloud, this cloud began to contract and collapse under its own gravity (Fig 1.1). Ongoing contraction increased its rotational velocity, flattening the nebular envelope into a disk. As the early Sun reached critical mass from consumption of infalling gases, it began nuclear fusion of deuterium and, as the temperature and pressure rose, hydrogen fusion began. Once fusion began, charged particles streamed from the solar surface referred to as solar wind. The force and energy exerted by the solar wind and solar radiation led to the evaporation and ejection of infalling material, stopping further accretion onto the nascent Sun. The consequent thermal structure of the disk, with a hot center cooling toward its edge, resulted in a chemical gradient of volatile-poor environments near the Sun to increasingly volatile-rich environments in the outer Solar System. Among the most important distinctions between the volatile-poor and volatile-rich regions is the “snow-line”, the evolving boundary beyond which water ice is stable. The condensation of volatile species in the cooler outer disk allowed the growth of the ice and gas giants. The presence of water ice also led to a more oxidized nebular region beyond the snow line. (e.g., Pontopiddan et al., 2014).

As the disk continued to cool, elements condensed into solid phases in sequence according to their volatilities (e.g., Lodders et al., 2003; Wood et al., 2019),

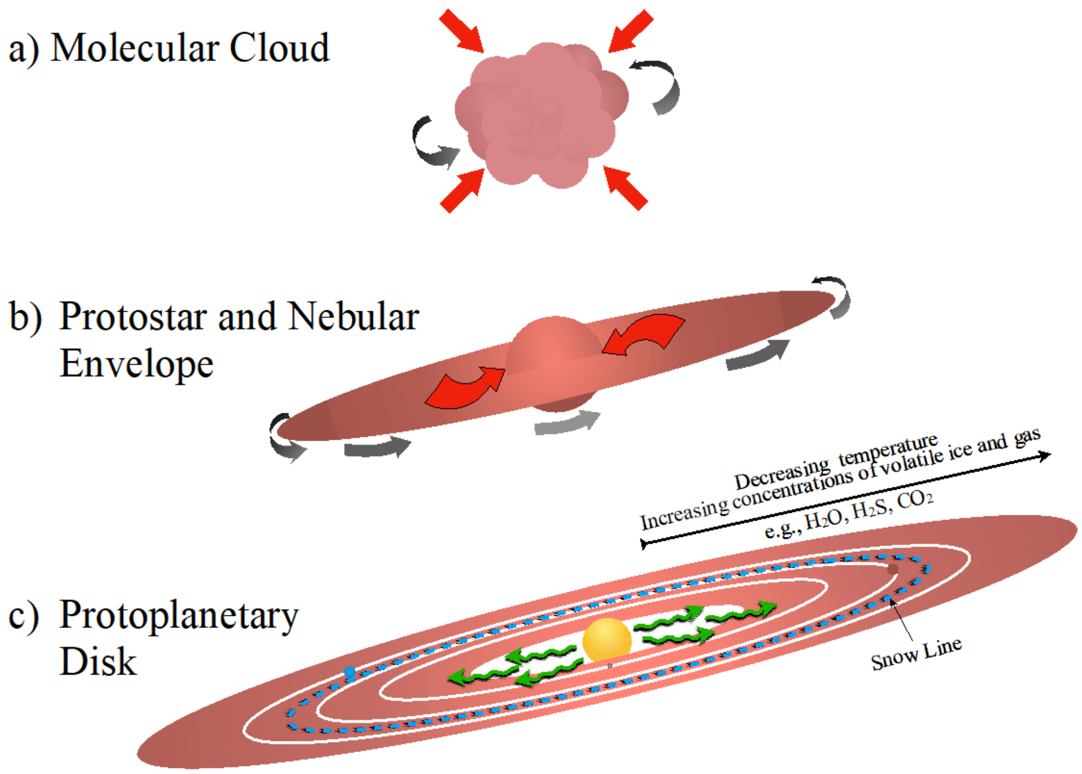

**Fig. 1.1. Formation of the Protoplanetary Disk.**

The Solar System began as a molecular cloud of gases (a) that began to contract and rotate under its own gravitation influence. As this process progressed, a thick nebular envelope surrounded a protostar (b) that had yet to begin runway nuclear reaction. Infalling gas and dust onto the surface of the protostar eventually resulted in the birth of the Sun through nuclear fusion, and the rotation of the nebular envelope flattened it into a protoplanetary disk (c) in which the first solid materials began to coalesce and form primitive planetary bodies. The heat and energy in the inner regions of the disk (green arrows) prevented volatile ices from condensing, resulting in a compositional gradient with those phases increasing with heliocentric distance beyond a proposed “snow line” (e.g., Grossman et al., 2008; Pontoppidan et al., 2014).

and the compositional gradient imposed by the Sun resulted in distinct mineralogic chemistries for solid grains that condensed in different regions of the disk. The rock forming elements largely entered the Solar System as small (sub-micron) solid particles, having condensed in the outflows of a previous generation of stars, or in the interstellar medium. These small grains were processed in the early Solar System, largely through melting, evaporation and recondensation via grain-grain collision, gas-solid interactions and irradiation. These grains eventually coalesced and accreted to form primitive planetary bodies known as planetesimals. The planetesimals underwent geological processing while continuing to collide and accrete to form larger planetary embryos, clearing out much of the remaining nebular dust and gas, and eventually growing into the terrestrial planets of the contemporary Solar System.

Within the larger planetary bodies, heat produced from the decay of short-lived radioactive elements was intense enough to produce extensive melting. This resulted in differentiation according to the density of its melted components, i.e., sequestration of a dense metallic core toward the center with an overlying rocky mantle and crust (Fig. 1.2). The precise melting temperatures and phase relations of minerals are determined in part by their composition at the onset of melting. Thus, the initial mineralogy and bulk chemistry of a planetary body, established by the nebular environment in which it formed, ultimately contribute to directing its subsequent evolutionary path. Consequently, some of the compositional diversity of planets in the contemporary Solar System can be attributed to the initial compositions that were inherited from the solar nebula and protoplanetary disk.

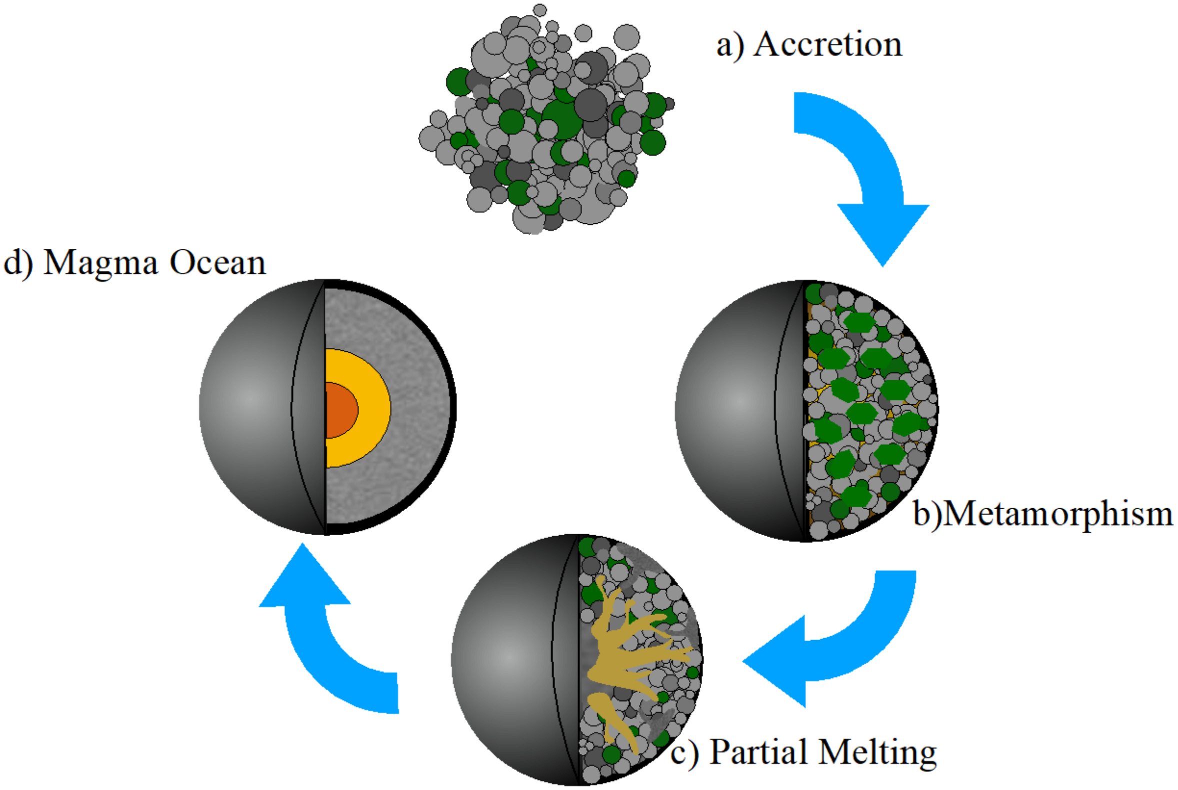

**Fig. 1.2. Planetary Differentiation Diagram.**
Planetary formation begins with the accretion of solid materials through mutual gravitation attraction (a). Heat from the radioactive decay of elements raises the planetesimal to metamorphic temperatures, causing solid-state changes to mineralogy and reducing heterogeneity of mineral chemistries (b). As temperatures increase further, melting begins in Fe-Ni-S phases (metals and sulfides) followed by melting of peridotitic materials to form basaltic melts, which will segregate from solid residues due to density contrast if melting is extensive enough to permit migration. In larger bodies capable of retaining enough heat from radioactive decay, complete melting may occur, resulting in a global magma ocean (c) (e.g., Righter and Drake, 1996).

### *1.2 Introduction to Meteoritics*

Meteorites are fragments of extraterrestrial materials from asteroids and planetary surfaces. The most ancient components of these materials are Calcium Aluminium-rich Inclusions (CAI), which are refractory solids found in chondrites and have an age of 4.567 Ga, an age cited widely in cosmochemistry and geology as the beginning of the Solar System. Over the next few million years gas and dust was processed in the nebula, planetesimals accreted, metamorphosed, melted and segregated. The study of meteorites provides opportunities to investigate the sequence of events early in the formation of the Solar System through the interpretation of the chemistries, mineralogies, and textures of meteorites. These attributes can be used to categorize meteorites within a taxonomy that describes nebular compositional environments (i.e., its cosmochemistry), parent body processes (e.g., metamorphism and differentiation), and genetic relationships within each group (e.g., Krot, 2014).

Meteorites are divided into stony, stony-iron, and iron meteorite groups. The stony meteorites are dominated by silicate rock-forming minerals such as olivine, pyroxene $(Ca,Fe,Mg)SiO_3$, and plagioclase $(CaAl_2Si_2O_8)$, and can be further divided according to their subsequent petrogenetic histories. Chondrites are chemically primitive, with refractory element ratios like that of the Sun, which shows that they have undergone limited geological processing since their accretion, usually confined to isochemical metamorphism or hydrous alteration. Other stony meteorites have undergone varying degrees of geological processing, ranging from the loss of low degrees of partial melts to complete melting and planetary differentiation. Iron meteorites are composed primarily of Fe and Ni and most are believed to sample the metallic cores of differentiated asteroids (e.g., Haack and McCoy, 2007). Stony-iron meteorites are intimate mixtures of silicates and Fe,Ni metal, thought to sample core-mantle boundaries or mechanical mixtures resulting from chaotic disruption during impact (e.g., Haack and McCoy, 2007). Meteorites can be further divided into groups and subgroups based on bulk chemistries, mineral chemistries, mineral textures, stable isotopic compositions (i.e., oxygen isotopes), and other characteristics to gain insight into the genetic relationships of materials sourced from common parent bodies (e.g., Krot, 2014; Fig. 1.3). Some estimates for the number of distinct parent bodies represented by meteorites may exceed 150 (Burbine et al., 2002).

More recently it has been recognized that there is a fundamental dichotomy of meteoritic and planetary materials based upon their isotopic compositions (Warren, 2011). This classification schema for meteorites divides samples into "non-carbonaceous" and "carbonaceous" types (e.g., Warren, 2011). The names of the two groups are based on nomenclature that describes the mineralogic characteristics of some of its members. However, it should be noted that such descriptions are not representative of all members (i.e., not all "non-carbonaceous" isotopic group members are C-poor and vice versa). This schema is based on the observation that meteorites fall into one of two groups when plotting bulk measurements of nucleosynthetic isotopic ratios. A popular hypothesis for the formation of the two isotopic reservoirs is that non-carbonaceous meteorites are sourced from the relatively volatile poor inner solar system, carbonaceous meteorites are from the more volatile-rich outer solar system, with the two reservoirs separated by the gravitational barrier of the nascent Jupiter (e.g., Kruijer et al., 2020). However, it should be noted that the cause of the isotopic dichotomy is still uncertain and may be the product of multiple factors in early Solar System history (e.g. Scott et al., 2018). If the isotopic dichotomy is truly representative of inner and outer solar system reservoirs, the variety of oxidation states among meteorites each isotopic group paints a complex picture of the distribution of volatiles in the early solar system (e.g., Righter et al., 2016; Fig. 1.3).

## *1.3 Insights into Nebular Environments from Primitive Meteorites*

Chondrites are widely recognized to sample primitive planetary bodies, as their textures provide clear evidence for having formed as aggregates of fragmented mineral grains and chondrules initially bound together by fine-grained matrices that accreted from nebular dust and gas (e.g., Shu et al., 1997). The compositional variety among chondrite groups implies a significant diversity of cosmochemical environments in the protoplanetary disk (e.g., Krot et al., 2014; Fig. 1.3). Chondrites record a range of oxygen fugacities (i.e., the effective concentration of oxygen in a system) that span well over nine orders of magnitude (e.g., Righter et al., 2016). Over such a large $fO_2$ range, the mean valency of Fe cations in a system shift from $Fe^0$, to $Fe^{2+}$, to $Fe^{3+}$ with increasing $fO_2$. The different charges of cations determine their mineralogic affinities at specific temperatures, wherein $Fe^0$ exists primarily as native metal, $Fe^{2+}$ partitions primarily into silicates, and $Fe^{3+}$ into oxides. Consequently, the stabilities of certain mineral assemblages change with varying $fO_2$ at a given temperature. For this reason, $fO_2$ is typically reported in log unit deviations relative to a mineral oxidation buffer that represents T-$fO_2$ conditions at which two or more

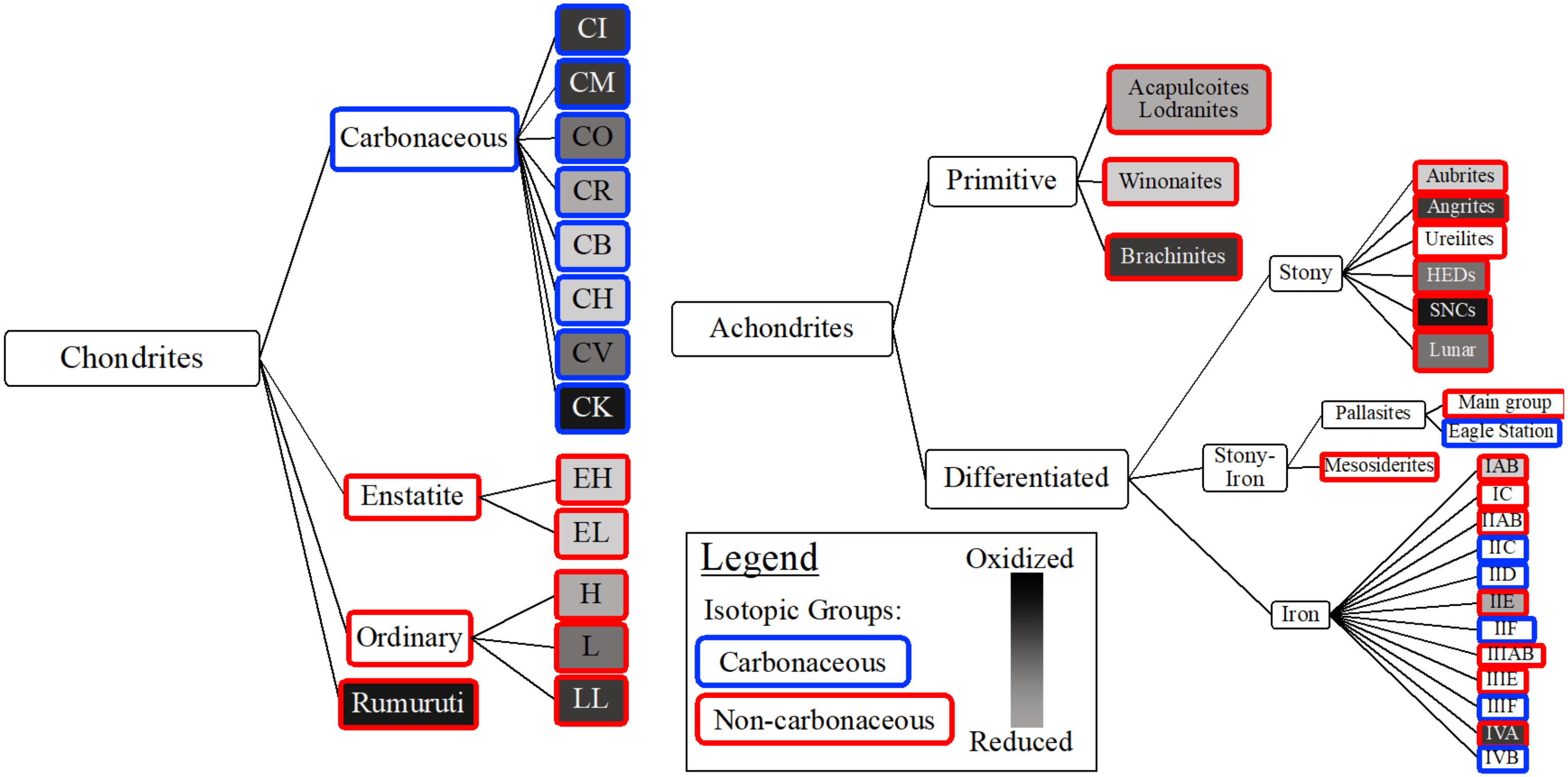

**Fig. 1.3. Diagram of Meteorite Taxonomy**
After Krot (2014). Meteorites include a wide variety of materials, from primitive, unmelted chondrites to differentiated components that sample crusts, mantles, and cores of asteroids. The wide range of oxidation conditions among both sets of the isotopic dichotomy paint a complicated picture for the distribution of volatiles if it is truly reflective of segregated inner and outer Solar System reservoirs. Carbonaceous and non-carbonaceous isotopic classifications are summarized in Kleine et al. (2020). Relative oxidation state is extrapolated from Righter et al. (2016), and white fields indicate a lack of oxidation data for that group.

oxidation states of an ion can coexist in thermodynamic equilibrium (i.e., the lowest Gibbs free energy state). For example, most meteorite oxygen fugacities are reported relative to the iron-wüstite (IW) buffer, which includes temperatures and $fO_2$ conditions at which native metallic Fe and the mineral wüstite (FeO) can coexist in equilibrium (e.g., Frost, 1991). At more oxidizing conditions (e.g., log $fO_2$ = IW+1), $Fe^{2+}$ is the dominant valency, while more reducing conditions (e.g., IW-1) favor native metallic $Fe^0$.

Mineralogies correspondingly vary with $fO_2$ in chondrites. The most reduced enstatite (E) chondrites (~IW-6) are dominated by Fe-poor low-Ca pyroxene, enstatite ($MgSiO_3$) and Fe-Ni metal, while the most oxidized Rumuruti (R) and Karoonda (CK) chondrites (IW to IW+3) are dominated by fayalitic (FeO-rich) olivine, e-sulfides, and magnetite. Mineralogic and geochemical differences brought on by nebular oxidation shape the subsequent evolutionary pathways of planetary materials by altering their melting temperatures and phase relations (e.g., McCoy et al., 2006).

### *1.4 Meteoritic Insights into Parent Body Processes*

Inferring the nebular conditions from which a parent body formed can be complicated by subsequent alteration, but evidence for initial environmental conditions can still be derived from mineral chemistry in most cases. In the most primitive chondrites, the matrix and chondrule minerals are in chemical and isotopic disequilibrium. Varying degrees of subsequent alteration (metamorphism and hydrous alteration) on the parent body are present in nearly all chondrites (e.g., Huss et al., 2006), which are categorized according to the intensity of thermal or aqueous alteration interpreted from mineral textures and chemistries. The least metamorphosed or hydrously altered chondrites are classified as petrologic type 3 with higher numbers scaling up to type 6 that indicate progressive thermal alteration (i.e., metamorphism) prior to silicate melting while lower numbers indicate increasing degrees of low-temperature aqueous alteration scaling down to 1 (e.g., Huss et al., 2006). Broadly, increasing degrees of metamorphism homogenize the chemistries of mineral grains as they approach equilibrium at high temperatures, while aqueous alteration hydrates silicates forming phyllosilicates and clays (e.g., Brearley et al., 2006). These processes are not mutually exclusive, as some highly oxidized chondrites are believed to have first been aqueous altered, then dehydrated through subsequent thermal alteration induced by metamorphism or impactors (e.g., Righter and Neff, 2007). In rare cases, evidence for high temperature hydrothermal alteration has also been found in primitive meteorites (e.g., McCanta et al., 2008).

As temperatures increase above the mineral solidus (i.e., conditions at which minerals begin to melt), the first phases to melt are within the Fe-Ni-S system at the Fe-FeS eutectic (988°C; Kullerud, 1963; Mittlefehldt et al., 1996). For most chondritic compositions, these are predominantly opaque mineral phases such as Fe,Ni metals and Fe,Ni-sulfides. The density of Fe-Ni-S liquid (5-10 g/cm$^3$) is greater than that of silicates (~3 g/cm$^3$) and will sink toward the center of the body if enough melting occurs to provide viable pathways for melt migration (e.g., McCoy et al., 2006).

As temperatures further increase, low-temperature silicate phases (feldspars and pyroxene) begin melting at ~1,100 °C, producing low density liquids that buoyantly ascend to form a basaltic crust (e.g., Stolper and Walker, 1980). The melting of silicates marks a transition in meteorite classification from chondrites to achondrites (Tomkins et al., 2020). Achondritic meteorites include a wide variety of materials that share common textural, mineralogic and geochemical evidence for silicate melting, ranging from basaltic crusts and peridotitic restites to metallic core fragments (e.g., Mittlefehldt, 2007).

The achondrites examined in this dissertation are all olivine-dominated restites (solid residues after partial melting), including the highly oxidized brachinites and a mineralogically similar set of ungrouped “brachinite-like” achondrites. Brachinite mineralogies and trace element chemistries are consistent with formation as restites after loss of both metal and silicate melts of up to 30% from their oxidized chondritic precursor (Day et al., 2012; Gardner-Vandy et al., 2013). Given the limited melt fractions segregated from brachinites, they are classified as primitive achondrites, consistent with their roughly chondritic bulk chemistries and igneous mineral textures (e.g., Keil, 2014). Previous work has examined the oxidation state of some brachinites, but the relationship between these samples and ungrouped brachinite-like achondrites is still unclear (Day et al., 2012), particularly with regard to the relative oxidation states of their precursors. Additional background context for these groups is discussed in further detail in subsequent chapters (Section 2.1) that investigate the redox relationship between the two sets of meteorites.

### *1.5. Trace Element Geochemistry in Meteorites*

While subsequent parent body alteration obscures the initial textures and mineralogies of nebular materials, their petrogenetic and nebular histories can be unraveled through investigation of their trace element systematics. Due to their very low abundances, trace elements partition predictably among mineral phases as functions of bulk composition, pressure, and temperature (e.g., Walker, 2016). Thus, they can be used to model key formational processes of meteorites by providing constraints on parameters like oxidation state, parent body size, and the extent of melting. The affinities of elements in geologic systems fall into three broad categories: lithophile, chalcophile, and siderophile (Goldschmidt, 1937). While siderophile trace elements as a whole preferentially partition into Fe metal, individual partitioning behaviors vary as functions of their volatilities and their compatibilities within mineral crystal lattices. The volatility of an element refers to the temperature at which it condenses into a solid phase during cooling of the nebular gas, and, from a geological point of view (which differs from an astronomical classification), includes refractory (≥1,400 K), moderately volatile (~800-1400 K), and highly volatile (<800 K) elements (e.g., McDonough and Sun, 1990; Lodders et al., 2003; Wood et al., 2019). The mineralogical compatibility of an element is largely controlled by the size of the ion, its charge, and availability of cation sites in a crystal lattice that can accommodate those characteristics. These parameters can change significantly depending the bulk composition of a body, temperature, and the ambient pressure (e.g., Chabot and Jones, 2003; Walker et al. 2016). Consequently, both the volatilities and mineralogic compatibilities of siderophile trace elements must be considered when interpreting nebular and petrogenetic histories of meteorites. For example, the highly siderophile elements (HSEs) typically partition into metals over silicates by a factor of $\geq 10^4$ (Walter et al., 2000), and this predictable behavior has been used to model metallic formation with geochemical analyses of iron meteorites (e.g., Walker, 2016). However, HSEs will also partition into Fe-sulfides in the absence of metal, as observed in terrestrial massive sulfide deposits (e.g., Barnes et al., 2006). Furthermore, the partitioning behaviors of moderately siderophile elements (MSEs), such as Mo and W, can be redox-sensitive during metamorphism and igneous processes, partitioning into silicates and oxides at higher oxygen fugacities due to changes in average valence state (e.g., O'Neill and Pownceby, 1993; Jennings et al., 2021). Thus, insight into the oxidation state and petrogenesis of a meteorite and its parent asteroid can be gained from investigating the partitioning of trace elements as recorded among meteorite mineral assemblages.

### *1.6. Linking Meteorites and Asteroids*

Correlating meteorites with their asteroid parent bodies would provide much needed spatial context to meteorite origins and lend insight into the true population of asteroidal materials in the Solar System. However, such an endeavor requires a toolset that is applicable to both meteorites and asteroids. Sample return missions like OSIRIS-ReX and Hayabusa are ideal because they provide an opportunity to directly measure the mineralogy and mineral chemistries of asteroid surfaces for comparison with meteorites, but these sample return missions are technically challenging, prohibitively expensive, and only sample objects that in near-Earth orbits . Rather than directly sample an asteroid's surface, remote sensing via telescopic observations can provide important constraints on the composition of asteroids if it is well correlated with laboratory measurements of meteorites.

The optical reflectance characteristics of minerals are resolvable with remote measurements, both in telescopic observations of asteroids and laboratory measurements of meteorites. These characteristics can be used to directly interpret mineralogy using principals of Crystal Field Theory, which describes how the composition and physical characteristics of a mineral at the atomic level determine its interactions with light and which components of the electromagnetic sprectrum are consequently reflected or absorbed (Burns, 1970). In particular, minerals with transition metal cations occupying sites with octahedral symmetries, such as $Fe^{2+}$ in olivine (Fig. 1.4), distort the partially filled 3d electron shell of the Fe cation, splitting it into a low and a high energy level. Energy from incident light can be absorbed by the valence shell of the cation, causing an electronic transition in which electrons temporarily jump to the higher energy state. The energy of the absorbed component is inversely proportional to the distance between the cation and surrounding ligand group (anion complexes surrounding the cation) (Burns, 1970; Sunshine et al., 1990). Thus, minerals with different crystal structures and/or compositions can produce distinct reflectance spectra that are useful for constraining the potential mineralogy of planetary materials even without direct compositional analysis.

### *Asteroid Taxonomy Based on Reflectance Spectroscopy*

As a first order approach to classification, asteroids are categorized by the shape of their reflectance spectra in the visible to near-infrared regions from 0.45 to 2.45 µm (e.g., Bus and Binzel, 2002; DeMeo et al., 2009). Based on the geometry of reflectance spectra, the widely used Bus-DeMeo asteroid taxonomy divides 371 asteroids into 24 spectral groups (Fig. 1.5). The shapes of these spectra can provide some insight into their mineralogies. For example, the V-type asteroids possess reflectance spectra dominated by absorption features produced by pyroxene and

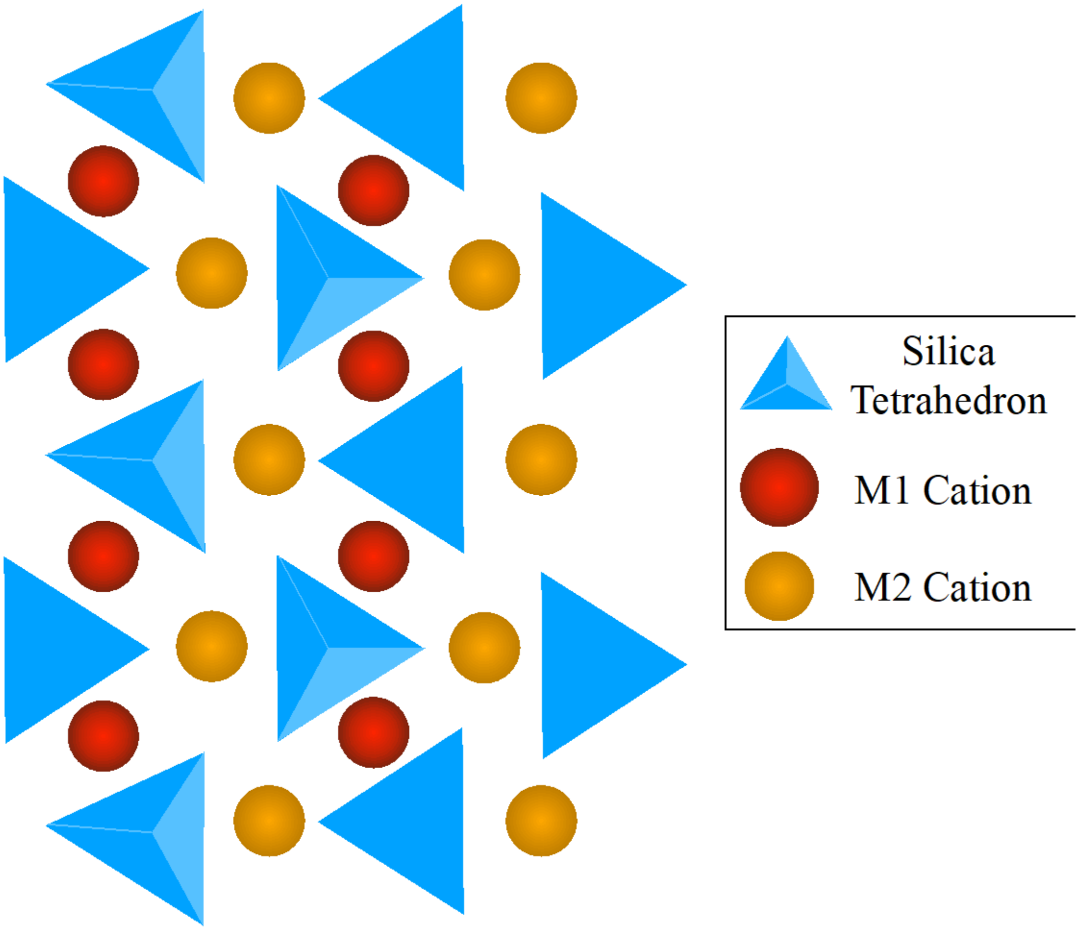

**Fig. 1.4. Diagram of Olivine Crystallography.**
The M1 and M2 cation sites of olivine are occupied primarily by $Fe^{2+}$ and $Mg^{2+}$. These cation sites have octahedral coordinations, which distort the *3d* electron orbitals of $Fe^{2+}$, splitting them into low and high energy levels. Absorptions in the near-infrared region of reflectance spectra are produced by $Fe^{2+}$ occupying these sites.

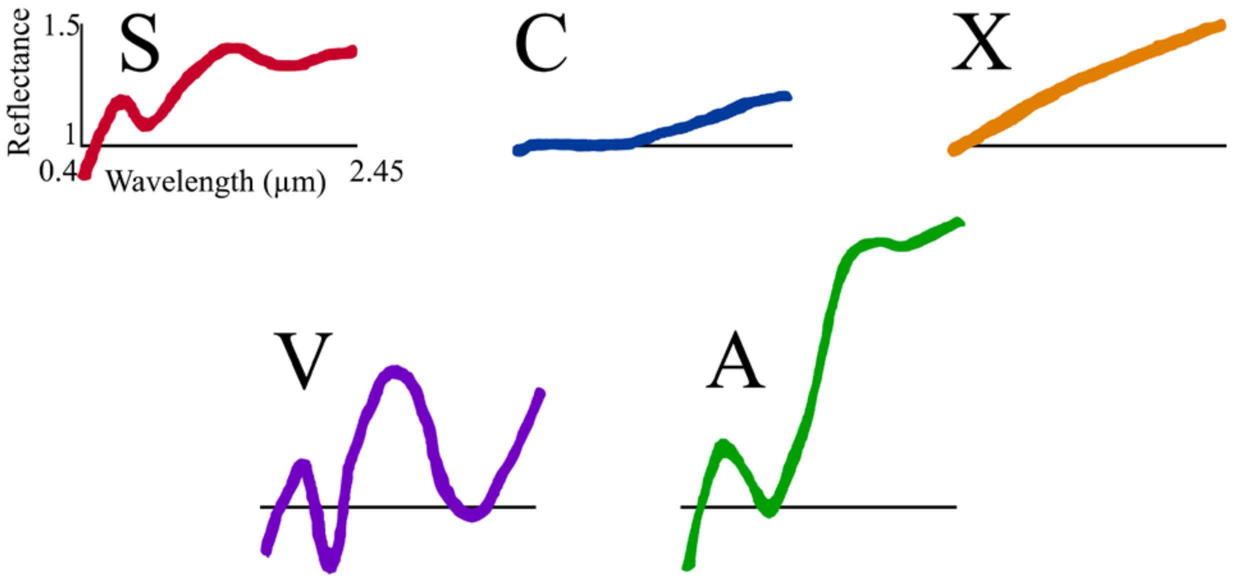

**Fig. 1.5. Examples of Bus-DeMeo Asteroid Spectral Classes.**
The spectral shapes of different asteroid classes are reflective of their mineralogies. S-type complex asteroids have spectral shapes that may include mixtures of olivine and pyroxene, often associated with ordinary chondrite-like mineralogies, although any genetic relationship is hotly debated (e.g., Lucas et al., 2017). C-type complex asteroids are generally described as “opaque-rich” due to their low albedos and broad, shallow absorptions at 1 µm. These may include materials similar to some carbonaceous chondrites (e.g., DeMeo et al., 2009). X-type asteroids have nearly featureless spectra with steep reddened slopes, possibly due to metallic surfaces or virtually FeO-free silicates (e.g., Cloutis et al., 1990). V-type asteroid spectra are dominated by pyroxene absorption features and are broadly agreed to be basaltic (e.g., Adams, 1974). A-type asteroids are the focus of this work and are dominated by an olivine absorption complex at ~1 µm ± a small absorption feature near 2 µm indicative of minor pyroxene.

consequently, bear spectra similar to basaltic meteorites (e.g., Adams, 1974). This association is the driving force behind the general assumption that basaltic eucrite meteorites and genetically-related howardites and diogenites (HEDs, collectively) sample the largest V-type asteroid, 4 Vesta (e.g., McSween et al., 2013). However, caution should be applied to such interpretations, as the spectral similarities between 4 Vesta and eucrites merely implies similar mineralogies; many of the smaller V-type “vestoid” asteroids could also serve as potential parent bodies for HED meteorites (e.g., Burbine et al., 2009). More detailed spectroscopic investigations are required to provide insight required for linking meteorites with potential parent bodies that possess comparable mineralogies, mineral chemistries, and interpreted petrogenetics.

### *1.7. Quantitative Spectroscopic Investigations of Meteorites and Asteroids*

Commonly, the remotely collected spectra are compared with laboratory measurements of mineral separates or mixtures, and the common geometric characteristics of the spectra are used to make remote interpretations (e.g., Clark, 1987). One popular method by which asteroids are related to meteorite lithologies involves comparing the centers and areas of absorption complexes and correlating these characteristics with modal mineralogies and mineral chemistries of meteorite powders (e.g., Gaffey et al., 1993). While such methods are computationally convenient, they are not based on the physical properties of mineral-light interactions, and thus are subject to misinterpretation from a number of factors: spectral features can be nonunique, overlapping, and reproducible through a variety of mineral combinations and observational conditions (e.g., Sunshine et al., 2007). It is critical that spectra be quantitatively modeled with parameters based on real physical constraints imposed by Crystal Field Theory, petrology, and astronomical context. One such approach is that of the radiative transfer model (Hapke, 1981), which under ideal circumstances can reproduce spectral mixtures within 5% of their actual modal mineralogies. However, this method requires *a priori* knowledge of the light-scattering properties of surface materials, such as roughness, average grain size, and geometry (Hapke, 1981). These factors are poorly constrained for asteroids. An inverse approach to spectral interpretation that is based on fundamental principles of Crystal Field Theory provides the best opportunity to interpret the mineralogy of asteroids where surface properties are unknown.

The approach used in this work to quantitatively determine meteorite and asteroid mineralogy from reflectance spectra is based on the Modified Gaussian Model (MGM) developed by Sunshine et al., (1990). Absorptions resulting from electronic transitions are modeled as modified gaussian features (Fig. 1.6) whose parameters correspond to the physical properties of minerals and mineral-light interactions as predicted by Crystal Field Theory. The diagnostic spectral characteristics of minerals can thus be used to remotely interpret their approximate compositions and abundances based on spectra alone (i.e., with no *a priori* knowledge of the sample). A detailed description of the mathematics and operational procedures for MGM fitting is provided in Chapter 4 (Section 4.2).

### *1.8 Overview of the Findings from this Research*

This dissertation investigates the effects of oxygen concentrations on mineral assemblages during early stages of planetary differentiation to understand how initial oxygen content affected the mineralogies and evolution of planetary objects in the

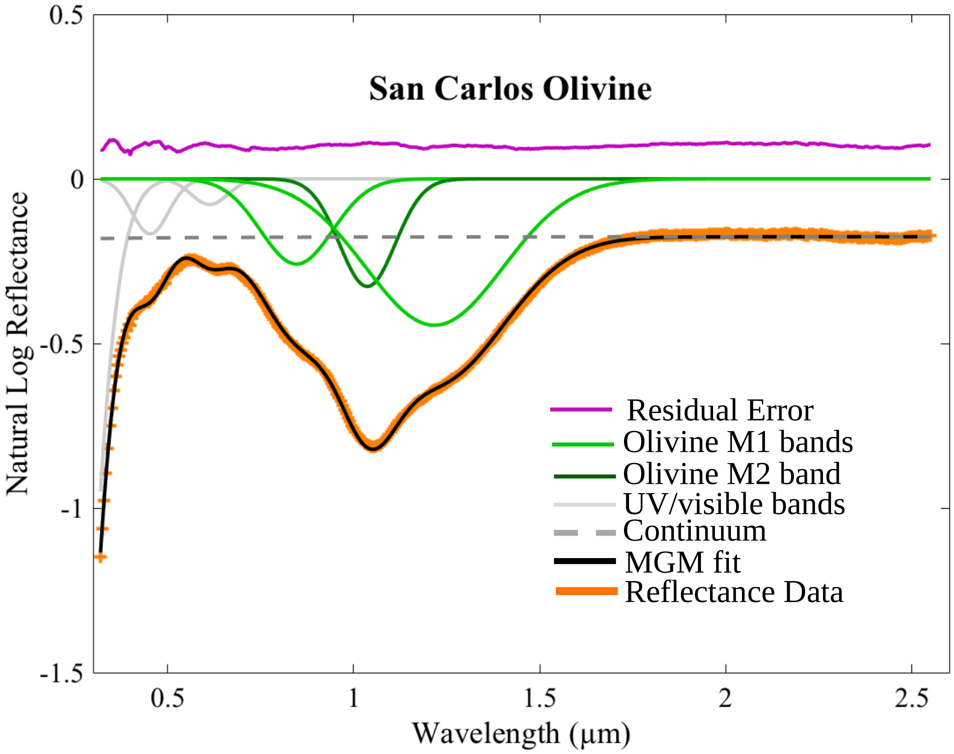

**Fig. 1.6. Example Modified Gaussian Model Fit to San Carlos Olivine Spectrum.** MGM has repeatedly demonstrated its ability to accurately replicate the shape of olivine spectra while adhering to the physical constraints imposed on band parameters from principals of Crystal Field Theory. The relative strengths of the three olivine bands and their band centers vary predictably with FeO content (Sunshine and Pieters, 1998) and can be used to ensure self-consistent estimates of composition from model solutions. Estimates for laboratory-based samples are generally within 10% of their measured values (Sunshine and Pieters, 1998; Sunshine et al., 2007).

early Solar System. A multidisciplinary approach was employed to understand the effects of oxygen content in a mineralogic context for meteorites and subsequently apply the findings to asteroids that represent potential analogs for the sources of these meteorites. This coordinated approach provides a robust method of investigating the current compositional populations asteroids and their distribution in the Solar System..

Calculations of oxygen fugacity ($fO_2$), i.e., the chemical activity or effective concentration of oxygen, for selected meteorites within the brachinite family were positively correlated with the ferrous iron ($Fe^{2+}$) content in the mineral olivine, $(Fe,Mg)_2SiO_4$ (Chapter 2). High $fO_2$ in these samples was also correlated with unique trace element chemistries that imply distinct evolutionary pathways during the differentiation of highly oxidized planetary bodies. In particular, trace elements with high affinities for metal indicate that the primitive precursors of oxidized brachinites lacked metal above trace quantities.

To further investigate the trace element systematics of highly oxidized precursors prior to melting, the mineralogy and geochemistry of Rumuruti (R) chondrites, proposed analogs for brachinite precursors, were investigated (Chapter 3). Results of this investigation mirror the distinct geochemistry of brachinites and support the hypothesis that, in lieu of metal, highly oxidized planetary differentiation likely deviates from typical models of differentiation via the formation of planetary cores dominated by Fe,Ni-sulfides.

The positive correlation between $fO_2$ and olivine $Fe^{2+}$ content among brachinite meteorites was resolved using remote analytical techniques applicable to both meteorites and asteroids (Chapter 4). By modeling absorption features in the reflected light spectra of both brachinites and potentially analogous A-type (olivine-dominated) asteroids, the approximate oxidation states of asteroids in the main belt were interpreted using estimated olivine composition as a proxy for $fO_2$. The majority of olivine-dominated asteroids are consistent with oxidizing conditions, and include both primitive (i.e., chondritic) mineralogies as well as probable mantle restites. These results provide new insight into the populations of different oxidized materials in the Solar System.

Chapter 5 explores outstanding questions raised by the findings of this dissertation, and subsequent future directions for investigating hypotheses for oxidized differentiation and core formation. Applications to upcoming NASA missions and relevance to the broader field of planetary science in general are also discussed.

# Chapter 2: Sulfide-dominated partial melting pathways in brachinites.

This chapter has been previously published in Meteoritics and Planetary Science.

**Crossley S. D.**, Ash R. D., Sunshine J. M., Corrigan C. M., McCoy T. J., Mittlefehldt D. W. and Puchtel I. S. (2020) Sulfide-dominated partial melting pathways in brachinites. *Meteoritics and Planetary Science* **55**, 2021–2043.

## *Abstract*

Petrogenetic relationships among members of the brachinite family were established by analyzing major and trace element concentrations of minerals for ten representative specimens: Al Huwaysah 010, Eagles Nest, Northwest Africa (NWA) 4882, NWA 5363, NWA 7297, NWA 7299, NWA 11756, Ramlat as Sahmah (RaS) 309, and Reid 013. The brachinite family, which includes brachinites and ungrouped achondrites with compositional and isotopic similarities to brachinites, are FeO-rich, olivine-dominated achondrites whose compositional and mineralogic variability is correlated with oxidation state. Most classical brachinites are derived from precursors that were more oxidized and sulfur-rich than those of ungrouped "brachinite-like" achondrites. This is manifest in the distinct Fe-Ni-S systems among brachinite family precursors, which were sulfide-dominated for the most oxidized brachinites and metal-dominated for the least oxidized brachinite-like achondrites. Consequently, highly siderophile element behavior was controlled through melting and removal of their dominant host phase in the precursor, which was likely pentlandite for the most oxidized brachinites and kamacite/taenite for less oxidized brachinites and most brachinite-like achondrites. Anomalous Ir/Os and Pt/Os ratios of oxidized brachinites

may be attributed to selective complexing during melting of As-rich pentlandite, although further experimental work is needed to model this process. The apparent redox trend among the brachinite family is consistent with silicate FeO content and Fe/Mn ratios, which may be used as a proxy for determining the relative oxidation state of brachinite family members. Based on our analyses, we make several recommendations for reclassification of samples into a continuum of oxidized to reduced endmembers for the brachinite family.

Along with a common range of $\Delta^{17}O$, this evidence is consistent with either formation on a common heterogeneous parent body or at least from the same nebular reservoir with variable O and S fugacities, resulting in mineralogically distinct igneous products for oxidized and reduced endmembers. Sulfur-bearing, oxidized differentiation may extend to other bodies that formed at or beyond the snow line in the early solar system, and should be considered when interpreting observational data for asteroids in upcoming missions.

## *2.1 Introduction*

Stages of planetary formation are recorded in meteorites at various states of arrested differentiation (*e.g.*, Righter and Drake, 1996; Greenwood *et al.* 2017). Primitive achondrites provide insight into the earliest stages of differentiation prior to extensive silicate melting, during which metal-silicate segregation and core formation began. Among primitive achondrites, brachinites are the most oxidized group (Righter *et al.*, 2016). As such, they provide an opportunity to investigate evolutionary pathways during early stages of igneous differentiation for oxidized parent bodies. Several studies have investigated geochemical and isotopic links between brachinites and oligoclase-rich cumulates Graves Nunatuk (GRA) 06128/9 (*e.g.*, Day *et al.*, 2012; Wang *et al.*, 2014), finding the latter to be representative of a melt fraction corresponding to a brachinite residue. Additionally, a number of individual FeO-rich achondrites illustrate the diversity of igneous products generated from partial melting on oxidized parent bodies (Day *et al.*, 2019). In this study, we investigate the brachinite group and potentially related ungrouped achondrites by examining their range of oxidation states with corresponding changes in mineralogy and geochemistry in order to better understand how their evolutionary pathways are affected by oxidation state.

Approaches to brachinite classification differ (*e.g.*, Day *et al.*, 2012; Keil, 2014; Goodrich *et al.*, 2017). Generally, brachinites are olivine-dominated (>75 vol%) primitive achondrites with minor high-Ca pyroxene and Fe-sulfides, but they can also include trace to minor amounts of low-Ca pyroxene, plagioclase, FeNi metal, and phosphates (Keil, 2014 and references therein). Olivine in brachinites is ferroan (~$Fo_{65-70}$) relative to other primitive achondrites, such as acapulcoite-lodranites ($Fo_{86-97}$; Mittlefehldt, 2007), which is indicative of their formation in a comparatively oxidizing environment (IW-1 to ~IW, Gardner-Vandy *et al.*, 2013; Righter *et al.*, 2016) relative to the acapulcoite-lodranite clan. Evidence for limited igneous processing of brachinites is supported by their large range of oxygen isotopic compositions ($\Delta^{17}O$ = ~0 to -0.3, Supplementary Fig. A1) due to incomplete melting of their parent body that prevented isotopic homogenization (Greenwood *et al.*, 2012, 2017). Igneous textures and near-chondritic trace element and modal mineral abundances also support a primitive achondrite classification for brachinites as restites after limited partial melting (*e.g*, Day *et al.*, 2012; Gardner-Vandy *et al.*, 2013; Keil, 2014; Goodrich *et al.*, 2017). In contrast, grain alignment and minor element concentrations in some brachinites (*e.g.*, Allan Hills 84025) are consistent with a cumulate origin (Mittlefehldt *et al.*, 2003; Goodrich *et al.*, 2017). Therefore, melting on the brachinite parent body may have been localized and heterogeneous, which is consistent with conclusions for other FeO-rich primitive achondrites (Day *et al.*, 2019).

A growing number of newly discovered meteorites have been classified as "ungrouped brachinite-like achondrites" (*e.g.*, Day *et al.*, 2012, 2019; Goodrich *et al.*, 2017). These ungrouped achondrites have one or more characteristics that are similar to brachinites with regard to modal olivine abundance, O-isotopic composition (Supplemental Fig. A1), and relatively high FeO content of olivine. Olivine is typically less ferroan (*e.g.*, $\geq Fo_{70}$) than in most brachinites (Day *et al.*, 2012; Goodrich *et al.*, 2012; Goodrich *et al.*, 2017) and Fe/Mn ratios are usually lower (<60), which may indicate that some ungrouped brachinite-like achondrites formed in less oxidizing environments than the brachinites (Goodrich and Delaney, 2000; Goodrich *et al.*, 2017). For clarity, we use the term "brachinite family" to collectively refer to all primitive achondrites that fit within the compositional, isotopic, and textural characteristics of the majority of brachinites and some brachinite-like achondrites as described above. This excludes, for example, brachinite-like achondrites Lewis Cliffs (LEW) 88763 and Tafassasset, which bear similar mineralogies to brachinites, but differ in oxygen isotope space (Gardner-Vandy *et al.*, 2012; Day *et al.*, 2015).

Oxygen fugacity ($fO_2$), *i.e.*, the activity of oxygen, has been calculated for a few brachinites and ungrouped achondrites, but methods for calculating $fO_2$ differ among studies, resulting in a range in reported oxygen fugacities for brachinites (generally ~IW-1, but up to IW+3) that precludes a direct comparison of oxidation conditions among the brachinite family (Gardner-Vandy *et al.*, 2013; Righter *et al.*, 2016; Goodrich *et al.*, 2017). Inconsistencies among various oxybarometers and Fe-Mg-Mn systematics merits further assessment of $fO_2$ and its effects on the residual lithologies of brachinite family achondrites.

Brachinites and ungrouped brachinite-like achondrites are also resolvable from one another in terms of their highly siderophile element (HSE) contents (Day *et al.*, 2012). Brachinite HSE abundances are typically subchondritic with additional depletions in Ir and Pt relative to Os and Ru, while ungrouped brachinite-like achondrites contain both roughly chondritic abundances and relative proportions of HSEs. Sulfides are the dominant carriers of the HSEs in most brachinites and typically reflect the characteristic depletions in Ir and Pt seen in bulk samples. The HSE content in brachinites was modeled in Day *et al.* (2012) through the complete removal of liquid FeNi metal according to parameterization in Chabot and Jones (2003), which measured solid/liquid metal distribution coefficients with variable concentrations of sulfur. Their measured brachinite HSE ratios were inconsistent with model calculations, and the authors suggested this may be the result of multiple HSE-bearing phases in the residue, two-stage melt fractionation, fractional fusion, or a non-chondritic starting composition, but they also highlight complications associated with each of these scenarios. As an alternative, we propose that relative Ir and Pt depletions in brachinites were inherited from atypical distribution of HSEs among precursor sulfides, which then melted in the absence of FeNi metal.

If brachinites are residues after limited melt loss, their precursors must have contained at least as much FeO in olivine as the brachinites, as partial melting cannot produce a residue that is more ferroan than its precursor (Sunshine *et al.*, 2007). Given that brachinites are isotopically non-carbonaceous (Warren, 2011), the Rumuruti (R) chondrite group is the only suitable analogue for the brachinite precursor among known chondritic meteorites. Partial melting experiments support a brachinite precursor composition similar to R chondrites (Gardner-Vandy *et al.*, 2013), although a direct relationship between brachinites and R chondrites is precluded by distinct O-isotopic compositions (*e.g.*, Greenwood *et al.*, 2017). More recent experimental work (Collinet and Grove, 2020), found that the relatively low bulk Mg/Si of both R chondrites (0.96) and ordinary chondrites (0.95) are inconsistent with pyroxene/olivine ratios in brachinites (Collinet and Grove, 2020), suggesting that neither group could produce brachinite mineralogies through partial melting and that the precursor instead resembled something intermediate between carbonaceous and non-carbonaceous mineralogies. Additionally, R chondrite $fO_2$ (>IW+1) is more oxidizing than of most brachinites (Righter *et al.*, 2016). It is therefore important to recognize that R chondrites are not perfect analogues for the brachinite precursor, but the similar range in mineralogies and mineral chemistries provide reasonable bases for comparison. The R chondrites also lack metals above trace abundances, but typically contain several weight percent pentlandite and pyrrhotite (*e.g.*, Bischoff *et al.*, 2011), providing an opportunity to examine the distribution of HSEs among a sulfide-dominated Fe-Ni-S system that may help explain the anomalous distribution and interelement HSE ratios seen in brachinites (Day *et al.,* 2012).

No in situ HSE measurements for R chondrite sulfides have been published to-date. In this study, we assess the distribution of siderophile and chalcophile elements among sulfides and metals for a suite of brachinites, ungrouped brachinite-like achondrites, and one R chondrite in order to assess whether brachinite HSE contents could be inherited from an R chondrite-like precursor. We then assess the evolutionary pathways of such oxidized materials at the onset of planetary differentiation in comparison to more reduced counterparts.

## *2.2 Methods*

### *2.2.1 Sample Selection and Preparation*

Brachinite samples used in this study are Eagles Nest, Northwest Africa (NWA) 4882, NWA 7297, NWA 7299, NWA 11756, Ramlat as Sahmah (RaS) 309, and Reid 013 (Supplementary Table S2.1). Ungrouped “brachinite-like” achondrites used in this study are Al Huwaysah 010 and NWA 5363. The R chondrite analyzed is NWA 11304. Meteorite classifications were taken from the latest update of the Meteoritical Bulletin Database (Gattacceca *et al.*, 2018). Probe mounts and/or thin sections were used for petrographic characterization and *in situ* compositional analyses. Chips adjacent to thick sections were acquired for bulk analyses of the HSE and Re-Os isotope system in samples NWA 4882 and NWA 11756 (48 and 8.1 mg, respectively). Masses for each sample were limited due to the sample availability and are significantly less than those typically used for bulk analyses (≥100 mg). Due to sample heterogeneity, the bulk measurements reported here are biased toward their local mineralogies and may not be representative of larger samples. We compared bulk measurements to calculated bulk HSE concentrations from modal recombination of in situ measurements. For NWA 11756, we selected a chip that included grains of altered metal, which contain the highest concentrations of HSEs by several orders of magnitude based on our in situ measurements. In NWA 4882, the primary host of HSEs are sulfides, which are uniformly distributed throughout our polished section. We use the official classifications described in the Meteoritical Bulletin to refer to samples throughout this study, but then suggest several reclassifications

### *2.2.2 Modal Mineralogy*

Modal mineralogy was determined through construction of lithologic distribution maps following methods outlined in Beck *et al.* (2012). Element maps were collected via energy-dispersive X-ray spectroscopy (EDS) at the Department of Mineral Sciences, Smithsonian Institution (SI) using the ThermoFisher energy dispersive x-ray detector attached to the FEI Nova NanoSEM 600 and at NASA Johnson Space Center (JSC) using a JEOL 7600F field emission scanning electron microscope (SEM). Individual element maps were stacked into a single data cube using Environment for Visualizing Images (ENVI 4.4) image processing software. Mineral phases were identified by using grains previously analyzed via electron microprobe (EMP) to define regions of interest (ROIs). A representative grain for each mineral phase was outlined as an ROI, and the average pixel values in each layer of the ROI were summed and used to define classification parameters for olivine, high- and low-Ca pyroxene, plagioclase, chromite, Fe-sulfide, metal, Ca-phosphates, Fe-rich terrestrial alteration, and epoxy/cracks. A classification map was generated from these parameters, and mineral modes were calculated according to the number of pixels for each mineral class. The average sum pixel value in an ROI is used to define each class within 2-10% relative uncertainty in order to limit misclassification while allowing for some mineral heterogeneity and noise in EDS data. Unclassified pixels are typically <10% of total pixels and are usually associated with noise in the original EDS data files.

### *2.2.3 Compositional Analyses*

*In situ* major element data were collected via EMP at the following facilities: University of Maryland, Geology Department, using a JEOL 8900; Smithsonian Institution, using a JEOL 8350F; and NASA Johnson Space Center using a JEOL 8350F and Cameca SX-100. Operating conditions were set at 1 µm spot size, 20kV, and 40 nA for all phases, apart from plagioclase, which was set at 10 µm spot size, 10 kV and 20 nA to minimize Na loss. Natural and synthetic standards were used for calibration and measured in duplicate before and after each analytical session. Detection limits for MnO and ZnO were <0.04 wt%, and all other listed elements were <0.03 wt%.

To ensure that *in situ* measurements of metals and sulfides were representative of bulk composition, bulk HSE concentrations and Os isotope compositions for two brachinite family members were analyzed via isotope dilution at the Isotope Geochemistry Laboratory (IGL) of the University of Maryland (College Park, MD, USA). To obtain the Re-Os isotopic and HSE abundance data (Supplementary Table

S2.10), 48 mg of NWA 4882 and 8.1 mg of NWA 11756, 6 mL of Os-purged, triple-distilled concentrated $HNO_3$, 3 mL of triple-distilled concentrated HCl, and appropriate amounts of mixed $^{185}$Re-$^{190}$Os and HSE ($^{99}$Ru,$^{105}$Pd,$^{191}$Ir,$^{194}$Pt) spikes were sealed in double internally-cleaned, chilled 25 mL Pyrex™ borosilicate Carius Tubes (CTs) and heated to 270°C for 96 hours. Osmium was extracted from the acid solution by $CCl_4$ solvent extraction (Cohen and Waters, 1996), back-extracted into HBr, and purified via microdistillation (Birck *et al.*, 1997). Ruthenium, Pd, Re, Ir, and Pt were separated and purified using anion-exchange chromatography following a protocol modified from Rehkämper and Halliday (1997).

Osmium isotopic measurements were carried out via negative thermal ionization mass spectrometry (N-TIMS: Creaser et al., 1991). All samples were analyzed using a secondary electron multiplier detector of a *ThermoFisher Triton* mass spectrometer at IGL. The measured isotopic ratios were corrected for mass fractionation using $^{192}$Os/$^{188}$Os = 3.083. The internal precision of measured $^{187}$Os/$^{188}$Os for all samples was between 0.03% and 0.05% relative. The $^{187}$Os/$^{188}$Os ratio of 300-500 pg loads of the in-house *Johnson-Matthey* Os standard measured during the two-year period leading up to the current analytical sessions averaged 0.11377±10 (2SD, $N = 64$). This value characterizes the external precision of the isotopic analyses (0.10%), which was used to estimate the true uncertainty on the measured $^{187}$Os/$^{188}$Os ratio for each individual sample (0.10%). This value is also within the uncertainty of the average $^{187}$Os/$^{188}$Os = 0.11379 measured for the Johnson-Matthey Os standard on the Faraday cups of the *IGL Triton* (Puchtel *et al.*, 2018). As such, no further corrections have been done.

The measurements of Ru, Pd, Re, Ir, and Pt were performed at the Plasma Laboratory, University of Maryland College Park, on Faraday cups of a *ThermoFisher Neptune Plus* ICP-MS in static mode using $10^{13}$ Ohm resistors. Isotopic mass fractionation was monitored and corrected for by interspersing samples and standards. The external precision of the analyses was estimated on the basis of standard measurements performed during the period of the analytical campaign to be $^{185}$Re/$^{187}$Re = 0.25%, $^{99}$Ru/$^{101}$Ru = 0.26%, $^{191}$Ir/$^{193}$Ir = 0.15%, $^{194}$Pt/$^{196}$Pt = 0.10%, and $^{105}$Pd/$^{106}$Pd = 0.08% relative (2SD). The accuracy of the data were assessed by comparing the results obtained at IGL with the reference values for the reference materials IAG MUH-1 (Austrian harzburgite), IAG OKUM (ultramafic komatiite), and NRC TDB-1 (Diabase PGE Rock Material) (Puchtel *et al.*, 2018).

The average total analytical blank measured was (in pg): Ru 6.0, Pd 17, Re 0.53, Os 0.42, Ir 1.2, and Pt 174 ($N$ = 9). For the whole-rock brachinite family samples, the average total analytical blank constituted less than 0.1% for Os, Re, Ir, Ru, and Pd, and less than 1% for Pt of the total element analyzed. We cite ±0.1% as the uncertainty on the concentrations of Os, Re, and Pd, ±0.2% as the uncertainty on the concentrations of Ir, 0.3 on the concentrations of Ru, and 1.0% on the concentrations of Pt, of the total element analyzed. The calculated uncertainty on the Re/Os ratio was propagated for each sample by multiplying the estimated uncertainties on the Re and Os abundances for the sample in question. These uncertainties were 0.2% relative.

*In situ* trace element data were collected via laser ablation inductively-coupled mass spectrometry (LA-ICP-MS) at UMD’s Plasma Laboratory using a New Wave Research UP-213-nanometer laser ablation unit attached to a ThermoFinnigan

Element2 single collector ICP-MS. Samples were ablated into a stream of helium (approximately 0.6 L $\text{min}^{-1}$), which was then mixed with Ar (approximately 0.9 L $\text{min}^{-1}$) before introduction into the mass spectrometer. Laser ablation was by spot analyses using a spot size varying from 15 to 80 μm, depending on the size of the grain to be ablated. The output of the laser was modified to ensure the fluence remained between 2 and 4 $\text{Jcm}^{-2}$, typically an output of approximately 60% of the total available power. The repetition rate of the laser was 7 Hz. Samples were standardized using iron meteorites Hoba, Coahuila, Filomena, and NIST 610 glass standard. Replicate analyses of standards typically yielded an external precision better than ±6 % (2σ) for the HSEs. Specific precisions are reported in Supplementary Table S2.2. Standards were analyzed in identical fashion to their respective samples. All samples were cleaned with a brief, low power pulse of the laser prior to the data gathering ablation. Gas background measurements were taken for 20 s prior to sample analysis. LAMTRACE was used for data reduction. Upper limits for concentration were calculated by setting the detection limit for any given isotope measured as three times the mean measured gas background.

Average trace element contents for metal and sulfide phases were multiplied by their respective modal abundances for comparison with bulk measurements. Discrepancies between bulk measurements and modal recombination are likely due to sample heterogeneity, and may not be representative of larger sections. However, we provide evidence in the following discussion that our bulk measurements accurately illustrate the main carrier phases of HSEs in these samples.

### *2.2.4. Calculation of oxygen fugacities*

Oxygen fugacity ($fO_2$) was calculated following methods in Gardner-Vandy *et al.* (2013). These methods utilize the quartz-iron-fayalite (QIFa) system to quantify the relationship between $fO_2$ and FeO content in olivine, given:

$$2Fe + SiO_2 + O_2(g) = Fe_2SiO_4 \qquad \text{QIFa} \tag{2.1}$$

Equation (1) can be related to temperatures (T) between 773 and 1673 K when expressed in terms of equilibrium constants (K):

$$logK = \log\frac{a_{Fa}}{a_{Fe}^2 \cdot a_{SiO_2} \cdot fO_2} = \frac{29592}{T} - 7.61 \tag{2.2}$$

Where $_{Fa}$ is the activity of fayalite, $_{Fe}$ is the activity of Fe metal, and $_{SiO2}$ is the activity of silica. Activities were calculated with the MELTS online supplemental calculator (Sack and Ghiorso 1991 a,b) using electron microprobe measurements of olivine. Oxygen fugacity was also calculated using the quartz-iron-ferrosilite (QIFs) system, which similarly quantifies the relationship between $fO_2$ and FeO content in low-Ca pyroxene, given:

$$Fe + SiO_2 + \tfrac{1}{2} O_2(g) = FeSiO_3 \qquad \text{QIFs} \tag{2.3}$$

Equation (3) can be related to temperatures between 737 and 1073 K when expressed in terms of K:

$$logK = \log\frac{a_{Fs}}{a_{Fe} \cdot a_{SiO_2} \cdot 0.5 fO_2} = \frac{29482}{T} - 7.43 \tag{2.4}$$

Where $a_{Fs}$ is the activity of ferrosilite. We approximated Gibbs free energy minimization by solving the last third of Equation (2) with olivine-chromite closure temperatures, then solved for $fO_2$ using the calculated activities. Similarly, the last third of Equation (4) was solved using two-pyroxene closure temperatures calculated from methods in Kretz (1982). The activity of Fe in FeNi metal was set equal to the average mole fraction of Fe. In samples that did not contain metal or were too weathered for reliable measurements, we used Ni concentrations in Fe-rich alteration products to estimate $a_{Fe}$. The $fO_2$ calculated from $a_{Fe}$ estimated from terrestrial alteration products should be regarded as the lower limit of $fO_2$ for that sample, given the possibility that terrestrial contamination may have diluted Ni concentrations. Following the approach of previous studies (Benedix *et al.*, 2005; Gardner-Vandy *et al.*, 2013), $a_{SiO2}$ was assumed to be 0.9, which Benedix *et al.* (2005) found to be consistent with the experimental results in Larimer (1968) for olivine-metal-low-Ca pyroxene systems within an $fO_2$ range of IW-1 to IW-3. While there was no free silica observed in any of our samples, Equations (1) and (3) can be combined and rewritten as:

$$Fe + FeSiO_3 + \frac{1}{2}O_2(g) = Fe_2SiO_4 \qquad (2.5)$$

so that free silica is no longer a factor in the reaction. Thus, by assuming a constant silica activity for Equations (2) and (4), oxygen fugacity may be calculated using the two systems together. Results for both QIFa and QIFs calculations in this work fall within the oxygen fugacity range of experiments in Larimer (1968) and are comparable with $fO_2$ calculations for brachinites in Gardner-Vandy *et al*. (2013). While not all samples contained low-Ca pyroxene in this study, we otherwise find that the consistency between the two thermodynamic calculators lends credibility to QIFa (Equation 2) as a standalone proxy for relative oxidation state if used for comparative purposes only.

## *2.3 Results*

### *2.3.1 Petrography and major element chemistry of brachinite family achondrites*

Mineral endmembers are presented in Table 2.1, and major element mineral chemistries from electron microprobe measurements are presented in Supplementary Tables S2.2-S2.8. Modal mineralogies calculated from lithologic distribution maps (Fig. 2.1, Supplemental Figs. S2.2-S2.8) are presented in Table 2.7. Both are discussed below along with petrographic descriptions for each sample. All brachinite family achondrites in this study exhibit equilibrated textures, such as olivine 120° triple joints and homogeneous major mineral chemistries. All the samples in this study are hot desert finds and are affected by terrestrial alteration to varying degrees. Since Fe metal is the first phase to be altered resulting from weathering, followed by sulfides (Wlotzka, 1993), it is possible that some of these samples once contained metals and/or sulfides that are no longer observable or have altered to iron oxides.

#### *Al Huwaysah 010*

Al Huwaysah 010 is composed of ~80 vol% olivine ($Fo_{82.4}$), 12 vol% Ca-rich pyroxene ($Wo_{43.3}En_{45.1}Fs_{11.6}$), 4 vol% plagioclase, and ~1 vol% of chromite and sulfides. Olivine, pyroxene, and chromite typically fall within the range of 200-300 µm, although a few olivine and pyroxene grains reach a diameter of ~400 µm. Weathering in Al Huwaysah 010 is extensive with pervasive Fe-rich alteration (2 vol%) and iddingsite rims on olivine. In thin section, weathering veins (up to 100 µm

**Table 2.1.** Average silicate endmember compositions for brachinites, ungrouped achondrites, and R chondrite NWA 11304.

| | | *Brachinites* | | | | | | | *Ungrouped Achondrites* | | *R chondrite* |
|---|---|---|---|---|---|---|---|---|---|---|---|
| | | Eagles Nest | RaS 309 | Reid 013 | NWA 4882 | NWA 7297 | NWA 7299 | NWA 11756 | Al Huwaysah 010 | NWA 5363 | NWA 11304 |
| *Olivine* | *n=* | *12* | *37* | *16* | *24* | *44* | *72* | *10* | *8* | *10* | *17* |
| | Fo% | 68.53 | 64.74 | 65.27 | 65.69 | 69.09 | 69.51 | 73.25 | 82.35 | 69.95 | 61.83 |
| | σ | 0.21 | 0.56 | 0.53 | 0.62 | 1.01 | 0.57 | 0.24 | 0.08 | 0.43 | 0.5 |
| | Fe/Mn | 63.44 | 74.76 | 69.75 | 73.01 | 62.68 | 59.41 | 51.63 | 31.98 | 59.4 | 79.14 |
| | σ | 1.19 | 2.15 | 8.02 | 7.65 | 3.25 | 1.00 | 1.13 | 0.46 | 1.80 | 1.43 |
| *High-Ca Pyroxene* | *n=* | *3* | *12* | *4* | *11* | *20* | *31* | *8* | *10* | *5* | *3* |
| | Fs% | 10.65 | 10.11 | 9.80 | 9.84 | 9.97 | 10.09 | 9.25 | 11.55 | 9.94 | 12.77 |
| | σ | 0.16 | 0.63 | 0.14 | 0.52 | 0.31 | 0.39 | 0.20 | 0.23 | 0.14 | 6.37 |
| | En% | 45.83 | 43.38 | 43.24 | 43.23 | 46.28 | 46.8 | 46.54 | 45.10 | 45.79 | 41.72 |
| | σ | 0.14 | 0.29 | 0.32 | 0.32 | 0.20 | 0.76 | 0.28 | 0.20 | 0.21 | 4.01 |
| | Wo% | 43.52 | 46.51 | 46.97 | 46.93 | 43.75 | 43.11 | 44.21 | 43.34 | 44.27 | 45.51 |
| | σ | 0.29 | 0.45 | 0.20 | 0.47 | 0.46 | 0.97 | 0.31 | 0.31 | 0.31 | 2.37 |
| *Low-Ca Pyroxene* | n= | *n.d.* | *n.d.* | *5* | *5* | *10* | *30* | *10* | *n.d.* | *n.d.* | *15* |
| | Fs% | | | 27.57 | 26.78 | 25.14 | 24.15 | 22.38 | | | 20.51 |
| | σ | | | 0.58 | 0.28 | 0.57 | 0.15 | 0.11 | | | 11.53 |
| | En% | | | 70.6 | 70.86 | 72.78 | 73.34 | 75.56 | | | 78.21 |
| | σ | | | 0.82 | 0.51 | 0.58 | 0.18 | 0.28 | | | 12.02 |
| | Wo% | | | 1.84 | 2.36 | 2.09 | 2.15 | 2.06 | | | 1.28 |
| | σ | | | 0.41 | 0.26 | 0.04 | 0.05 | 0.04 | | | 1.14 |

**Table 2.2.** Average major element compositions of metal and Fe-rich terrestrial alteration in brachinites (wt%).

| *FeNi Metal* | NWA 7299 | σ | *Altered Metal* | NWA 7297 | σ | NWA 11756 | σ |
|---|---|---|---|---|---|---|---|
| n= | 25 | | n= | 3 | | 9 | |
| Fe | 81.09 | 0.19 | $Fe_2O_3$ | 82.62 | 7.49 | 89.03 | 4.10 |
| Co | 1.35 | 0.02 | CoO | 0.55 | 0.53 | 0.55 | 0.29 |
| Ni | 18.14 | 0.15 | NiO | 4.97 | 2.11 | 6.05 | 3.70 |
| S | 0.01 | 0.01 | $SO_3$ | 0.68 | 0.20 | 0.75 | 0.22 |
| Cr | n.d. | 0.01 | $Cr_2O_3$ | 0.02 | 0.02 | 0.01 | 0.01 |
| P | 0.02 | 0.01 | $P_2O_5$ | 0.10 | 0.07 | 0.08 | 0.06 |
| Sum | 100.60 | | $SiO_2$ | 4.89 | 7.42 | 1.36 | 1.28 |
| | | | Sum | 93.83 | | 97.83 | |

**Table 2.3.** Average major element compositions of sulfides in brachinites (wt%).

| | Eagles Nest | σ | RaS 309* | σ | Reid 013 | σ | NWA 4882 | σ | NWA 7297 | σ | NWA 7299 | σ | NWA 11756 | σ |
|---|---|---|---|---|---|---|---|---|---|---|---|---|---|---|
| n= | 5 | | 7 | | 5 | | 56 | | 11 | | 16 | | 7 | |
| Fe | 63.03 | 0.88 | 58.30 | 6.73 | 63.42 | 0.88 | 45.30 | 1.46 | 40.31 | 3.60 | 63.31 | 0.52 | 58.52 | 1.67 |
| Co | 0.08 | 0.04 | 0.31 | 0.11 | 0.07 | 0.05 | 0.13 | 0.05 | 0.26 | 0.18 | 0.07 | 0.01 | 0.18 | 0.12 |
| Ni | 0.35 | 0.55 | 0.79 | 0.31 | 0.20 | 0.12 | 0.96 | 0.28 | 2.59 | 1.20 | 0.01 | 0.01 | 1.10 | 1.21 |
| S | 37.12 | 0.40 | 0.18 | 0.11 | 36.81 | 0.45 | 46.81 | 2.36 | 38.59 | 7.31 | 36.32 | 0.35 | 38.82 | 0.39 |
| Cr | 0.08 | 0.05 | 0.002 | b.d.l. | 1.44 | 1.62 | 0.02 | 0.01 | 0.06 | 0.04 | 0.06 | 0.01 | 0.06 | 0.01 |
| P | 0.01 | 0.01 | 0.01 | 0.01 | 0.01 | 0.01 | 0.03 | 0.02 | 0.01 | 0.01 | n.d. | | n.d. | |
| Si | n.d. | b.d.l. | 0.60 | 0.69 | 0.01 | 0.01 | 0.94 | 0.78 | 1.16 | 0.75 | n.d. | | 0.04 | 0.03 |
| Zn | 0.01 | 0.01 | n.d. | | 0.04 | 0.04 | n.d. | | n.d. | | n.d. | | n.d. | |
| Mg | n.d. | | 0.25 | 0.14 | n.d. | | 0.33 | 0.22 | 0.09 | 0.09 | n.d. | | n.d. | |
| Cu | 0.15 | 0.09 | n.d. | | 0.06 | 0.07 | 0.01 | 0.01 | 0.04 | 0.06 | 0.01 | 0.01 | n.d. | |
| Sum | 100.67 | | 60.45 | | 101.96 | | 94.18 | | 82.96 | | 99.78 | | 98.73 | |

n.d. = not detected.

b.d.l. = below detection limit

*Large sulfide grains in RaS 309 are highly altered, which likely accounts for low S.

**Table 2.4.** Major element concentrations of Fe-Ni-S inclusions in brachinites.

| | Eagles Nest | | NWA 4882 | | RaS 309 | | | | | | | | Reid 013 | | |
|---|---|---|---|---|---|---|---|---|---|---|---|---|---|---|---|
| | *Taenite* | σ | *Taenite* | σ | *MSS* | σ | *Kamacite* | σ | *Taenite* | σ | *Tetrataenite* | σ | *Kamacite* | *Taenite* | σ |
| n= | 5 | | 4 | | 10 | | 9 | | 5 | | 2 | | 1 | 4 | |
| Fe | 73.72 | 1.41 | 69.25 | 16.29 | 62.9 | 2.42 | 93.73 | 2.52 | 63.20 | 2.10 | 31.53 | 7.60 | 97.52 | 68.40 | 8.58 |
| Co | 1.33 | 0.19 | 1.85 | 0.44 | 0.10 | 0.41 | 1.33 | 0.27 | 1.50 | 0.24 | 2.60 | 0.37 | 1.24 | 1.53 | 0.40 |
| Ni | 25.13 | 2.21 | 28.54 | 15.35 | 0.43 | 2.55 | 5.02 | 1.73 | 32.32 | 1.87 | 51.32 | 8.90 | 2.39 | 29.91 | 7.93 |
| S | 0.02 | 0.01 | 0.04 | 0.01 | 36.01 | 1.93 | 0.16 | 0.39 | 0.05 | 0.04 | 0.06 | 0.01 | 0.01 | 0.03 | 0.02 |
| Cr | 0.02 | 0.02 | 0.02 | 0.02 | 0.17 | 0.37 | 0.48 | 0.57 | n.d. | | 0.03 | 0.02 | n.d. | n.d. | 0.01 |
| P | 0.01 | 0.01 | 0.01 | 0.01 | 0.001 | 0.01 | 0.005 | 0.005 | 0.001 | b.d.l. | n.d. | | 0.017 | 0.005 | b.d.l. |
| Si | 0.02 | 0.01 | 0.04 | b.d.l. | 0.03 | 0.04 | 0.07 | 0.11 | 0.57 | 0.70 | 2.92 | 4.07 | 0.03 | 0.02 | 0.01 |
| Zn | n.d. | | n.d. | | 0.01 | b.d.l. | n.d. | | n.d. | | n.d. | | n.d. | n.d. | |
| Mg | 0.01 | 0.01 | 0.12 | 0.12 | 0.01 | 0.01 | 0.14 | 0.25 | 0.99 | 1.37 | 2.14 | 3.00 | 0.02 | 0.02 | 0.01 |
| Cu | 0.23 | 0.24 | 0.12 | 0.12 | 0.03 | 0.07 | 0.02 | 0.03 | 0.16 | 0.04 | 0.16 | 0.06 | 0.05 | 0.13 | 0.02 |
| Sum | 100.49 | | 100.49 | | 99.71 | | 100.96 | | 98.80 | | 90.76 | | 101.26 | 100.04 | |

n.d. = not detected.

b.d.l. = below detection limit

**Table 2.5.** Major element concentrations of sulfides and altered metal in ungrouped achondrite NWA 5363.

| | Sulfide | σ | Altered Metal | σ |
|---|---|---|---|---|
| n= | 9 | | 4 | |
| Fe | 43.58 | 2.85 | 84.60 | 0.48 |
| Co | 0.52 | 0.36 | 0.56 | 0.11 |
| Ni | 5.24 | 3.93 | 5.81 | 0.86 |
| S | 34.01 | 9.40 | 0.69 | 0.02 |
| Cr | 0.07 | 0.10 | 0.02 | 0.03 |
| P | 0.03 | 0.03 | 0.14 | 0.01 |
| Si | 1.48 | 0.37 | 4.80 | 1.15 |
| Zn | n.d. | | 96.62 | |
| Sum | 84.94 | | | |

n.d. = not detected

**Table 2.6.** Sulfide compositions in R chondrite NWA 11304.

| | *Pentlandite* | σ | *Pyrrhotite* | σ |
|---|---|---|---|---|
| n= | 7 | | 10 | |
| Fe | 35.15 | 0.38 | 61.63 | 0.52 |
| Co | 1.21 | 0.20 | 0.088 | 0.04 |
| Ni | 30.96 | 0.23 | 0.233 | 0.06 |
| S | 33.25 | 0.23 | 38.056 | 0.32 |
| Cr | 0.02 | 0.04 | 0.028 | 0.04 |
| P | 0.02 | 0.04 | 0.008 | 0.04 |
| Si | n.d. | | 0.01 | 0.01 |
| Zn | n.d. | | n.d. | |
| Sum | 100.62 | | 100.05 | |

n.d. = not detected.

**Table 2.7.** Modal mineralogies of brachinites and ungrouped achondrites.

| | Al Huwaysah 010 | Eagles Nest | NWA 4882 | NWA 5363 | NWA 7297 | NWA 7299 | NWA 11756 | RaS 309 | Reid 013 |
|---|---|---|---|---|---|---|---|---|---|
| Olivine | 79.7 | 81.9 | 97.1 | 67.8 | 77.5 | 74.6 | 75.5 | 80.6 | 92.3 |
| High-Ca pyroxene | 4 | 7.6 | 0.7 | 21.5 | 4.7 | 5.3 | 5.3 | 11.6 | 3.0 |
| Low-Ca pyroxene | trace | n.d. | trace | n.d. | 1.1 | 9.1 | 12.1 | trace | trace |
| Sulfide* | 0.7 | 1.3 | 1.3 | 8.5 | 3.0 | 2.2 | 0.6 | trace | trace |
| Metal* | n.d. | trace | trace | n.d. | n.d. | 0.7 | n.d. | trace | trace |
| Chromite | 0.9 | 1.1 | 0.7 | 0.3 | 1.0 | 1.2 | 1.0 | 3.8 | 0.9 |
| Phosphate | n.d. | n.d. | n.d. | n.d. | n.d. | 0.2 | trace | n.d. | n.d. |
| Plagioclase | 12.5 | n.d. | trace | n.d. | n.d. | 4.2 | 0.1 | n.d. | n.d. |
| Fe alt. | 2.3 | 8.2 | 0.1 | 2.0 | 12.7 | 1.6 | 5.4 | 4.0 | 3.8 |
| Ca alt. | n.d. | n.d. | n.d. | n.d. | n.d. | 0.9 | n.d. | n.d. | n.d. |

n.d.= not detected

alt. = alteration

*Fe-rich terrestrial alteration products likely account for the apparent lack of sulfides and/or metals in some desert finds

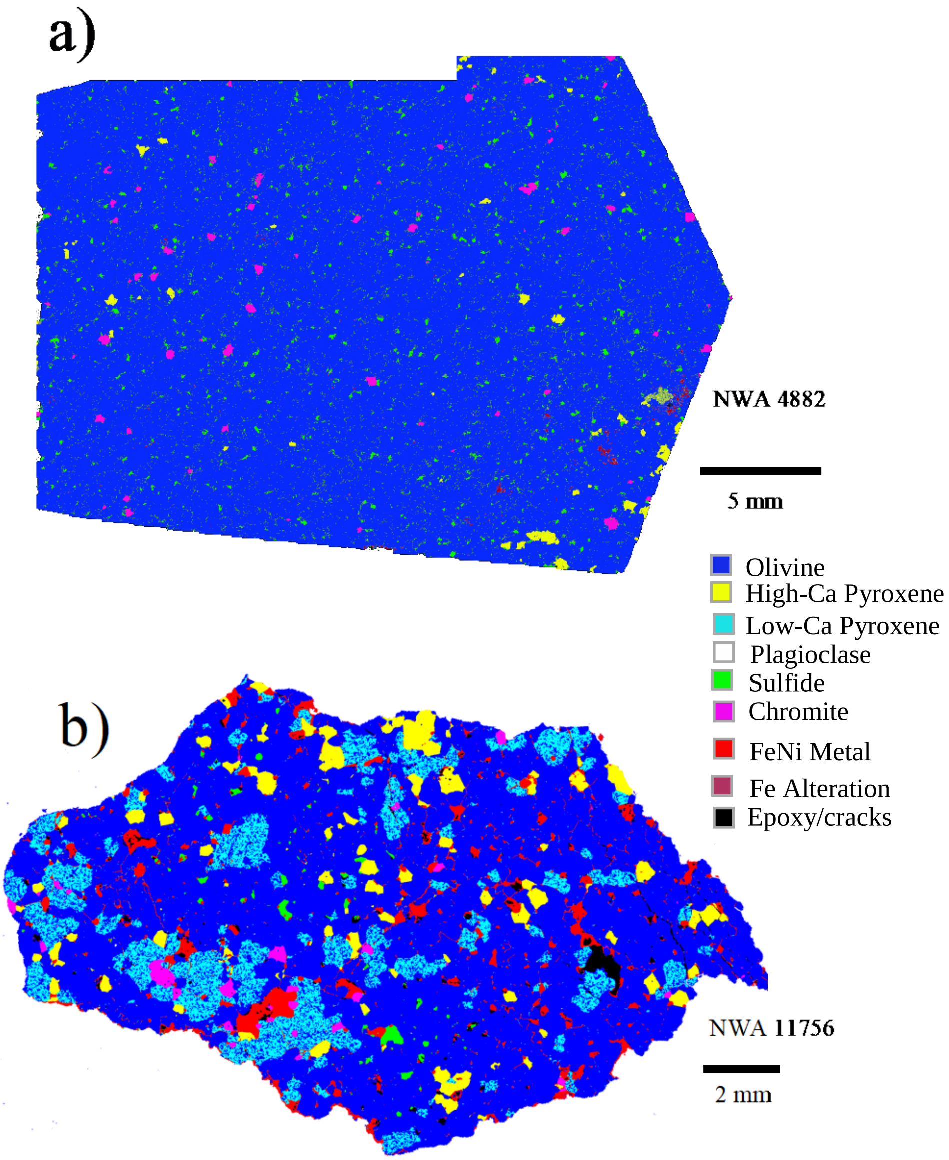

**Fig. 2.1. Mineral maps of brachinites.**
a) NWA 4882 is typical of most brachinites in that it is dominated by olivine with minor abundances of high-Ca pyroxene, chromite, and sulfides. b) As discussed in the text, the modal mineralogy of NWA 11756 is more typical of ungrouped brachinite-like achondrites, despite its classification as a brachinite. Irregularities in the low-Ca pyroxene phases of NWA 11756 are due to noise in the original EDS maps, which can result in misclassification as olivine. Consequently, low-Ca pyroxene abundance is likely underestimated. Additional mineral maps for the remaining specimens are available in supplemental materials.

diameter) are composed largely of opaque secondary Fe-oxides, and silicate minerals are obscured by dark red-brown rusting, indicating the mobilization of Fe in these phases. The cores of olivine grains were analyzed to minimize the effects of terrestrial alteration on the measurements, and yielded the most magnesian olivine compositions in this study. Plagioclase was detected via EDS, but due to the extensive weathering, we could not identify analyzable grains for EMP analyses.

### *Eagles Nest*

Eagles Nest is 82 vol% olivine ($Fo_{68.5}$), 8 vol% high-Ca pyroxene ($Wo_{43.5}En_{45.8}Fs_{10.6}$), 1 vol% troilite, and 1 vol% chromite. Iron-rich alteration (8 vol%) coexists alongside troilite and as veinlets along grain boundaries. Olivine grain size is typically ~500 µm, while high-Ca pyroxene is typically ~300 µm and subhedral. Troilite (up to ~200 µm) is both subhedral and anhedral between grains of olivine. Small (<10 µm), round inclusions of troilite are also present within silicate phases. In reflected light, some of the intergranular Fe-rich veins show an irregular yellow luster, similar to alteration around troilite. Trace amounts of unaltered taenite (~25 wt% Ni) are present among intergranular veins of Fe-rich alteration and as <10 µm inclusions within silicates and sulfides. Our observations are consistent with modal mineralogy and mineral chemistries of Eagles Nest reported in Swindle *et al.*, (1998).

### *Northwest Africa (NWA) 4882*

NWA 4882 (Fig. 12.) is ~97 vol% olivine ($Fo_{65.7}$), 1 vol% pyrite, 1 vol% high-Ca pyroxene ($Wo_{46.9}En_{43.2}Fs_{9.8}$), 1 vol% chromite, and accessory low-Ca pyroxene and plagioclase. While alteration is significant in NWA 4882, it is largely limited to margins of our section and to Fe-rich alteration veins between olivine grain boundaries. Typical olivine grain size is 200-500 µm and high-Ca pyroxene is ~350 µm. Chromite grains are anhedral and approximately 350 µm in diameter. Pyrite (50-150 µm) is uniformly distributed throughout this sample as subhedral grains intergranular to silicate phases. Alteration of pyrite is evident in most grains, and likely accounts for much of the intergranular Fe-rich veins. NWA 4882 is unique among brachinites in that its dominant sulfide phase is pyrite, rather than troilite or pyrrhotite. Trace amounts of taenite (28.5 wt% Ni) and low-Ca pyroxene ($Wo_{2.4}En_{70.9}Fs_{26.8}$) coexist in reaction textures along some olivine rims.

### *Northwest Africa 5363*

The modal mineralogy for NWA 5363 is ~68 vol% olivine ($Fo_{70}$), 22 vol% high-Ca pyroxene ($Wo_{44.3}En_{45.8}Fs_{9.9}$), 9 vol% troilite, and accessory chromite. Iron-rich alteration products (~1 vol%) line grain boundaries and often coexist with sulfides. Olivine and pyroxene grains are typically 200-400 µm. Troilite is subhedral and found between silicate grains, typically 150-200 µm and subhedral, although one grain is over 400 µm along its longest axis. Alteration is prevalent in some troilite grains, although many are free from obvious alteration. Discrete grains of Fe-rich alteration (up to 200 µm) are also present, sometimes coexisting with minimally altered troilite. It is unclear whether some of this alteration is derived from FeNi metal because none was identified in the section. While NWA 5363 is classified as an ungrouped brachinite-like achondrite, our sample does not contain the low-Ca pyroxene, plagioclase, or unaltered FeNi metal that are characteristic of other ungrouped specimen. However, the lack of low-Ca pyroxene may also be a result of sample heterogeneity.

*Northwest Africa 7297*

NWA 7297 contains ~77 vol% olivine ($Fo_{69.1}$), 5 vol% high-Ca pyroxene ($Wo_{43.8}En_{46.3}Fs_{10}$), 3 vol% troilite, 1 vol% low-Ca pyroxene ($Wo_{2.1}En_{72.8}Fs_{25.1}$), and 1 vol% chromite. Iron-rich alteration (13 vol%) is prevalent along grain boundaries and with sulfides. Olivine and pyroxene grain sizes are ~600 µm, chromite grains are 150-200 µm, and troilite is typically 200-300 µm. Sulfides in this sample are visibly altered as evidenced by red-brown rust in reflected light. Sulfides yield low microprobe totals, although these phases still contain 30-45 wt% S. Large (>500 µm) blebs of Fe-rich alteration show some yellow luster and may indicate the Fe-rich alteration is derived from sulfides, although these phases do not contain appreciable S. It should be noted that there are no published O-isotope measurements for NWA 7297, so it is possible that this sample may be unrelated to brachinites.

*Northwest Africa 7299*

NWA 7299 contains 74 vol% olivine ($Fo_{69.5}$), 9 vol% low-Ca pyroxene ($Wo_{2.1}En_{73.3}Fs_{24.5}$), 5 vol% high-Ca pyroxene ($Wo_{43.1}En_{46.8}Fs_{10.1}$), 4 vol% plagioclase, 2 vol% troilite, 1 vol% chromite, and accessory taenite and Ca-phosphate. Poikiloblasts of low-Ca pyroxene enclose blebby chromite and subhedral olivine. Iron-rich alteration is present along grain boundaries, but several large blebs of taenite (up to 1 mm) are free of significant terrestrial alteration apart from the outermost ~20 µm, making NWA 7299 the least altered metal-bearing sample in this study. Olivine and pyroxene are typically 200-500 µm in diameter, and Fe/Mn ratios are 59.4 and 36.7, for olivine and high-Ca pyroxene respectively. Troilite is ~200 µm and exists as subhedral to anhedral grains between silicate phases, although several coexist with blebs of taenite and as <10 µm inclusions in silicates. Plagioclase ($Ab_{74}An_{24.6}Or_1$) occurs as ~100-300 µm grains. Most chromite grains are 100-200 µm, although one large chromite chadacryst, 1.5 mm in its longest axis, is enclosed by low-Ca pyroxene. Ca-phosphates (~100 µm) occur as several anhedral grains throughout the section. There are no published O-isotope measurements for NWA 7299, so this sample may also be unrelated to brachinites.

### *Northwest Africa 11756*

The modal mineralogy for NWA 11756 (Fig. 2.1) is 76 vol% olivine ($Fo_{73.3}$), 12 vol% low-Ca pyroxene ($Wo_{2.1}En_{75.6}Fs_{22.4}$), 5 vol% high-Ca pyroxene ($Wo_{44.2}En_{46.5}Fs_{9.3}$), ~1 vol% chromite, and accessory troilite, plagioclase, and Ca-phosphate. A significant amount of Fe-rich, Ni-bearing alteration material is present (10 vol%). These alteration products yielded low wt% totals, but recalculating Fe as $Fe_2O_3$ yielded totals >90 wt%. These phases typically coexist with sulfides, and were probably originally kamacite (NiO ~6 wt%). Olivine and pyroxenes are typically ~250-600 µm. Troilite often occurs as subhedral to anhedral grains of 50-150 µm. Chromite are typically 250 µm in diameter and often coexist with sulfides and Fe-rich alteration. This section also contains one 300 µm grain of plagioclase ($Ab_{64}An_{35}Or_{0.4}$).

### *Ramlat as Sahmah (RaS) 309*

RaS 309 contains 81 vol% olivine ($Fo_{64.7}$), 12 vol% high-Ca pyroxene ($Wo_{46.5}En_{43.4}Fs_{10.1}$), 4 vol% chromite, and trace amounts of sulfides and FeNi metal.

Weathering in RaS 309 occurs as Fe-rich alteration (~4 vol%) along grain boundaries and as alteration products of troilite (~100 µm), which has lost sulfur, resulting in low totals (<<36 wt% S) with ≤1 wt% Ni. In thin section, red-brown alteration is also pervasive among silicates. Olivine and pyroxene are typically ~150-400 µm in diameter. Chromite is most commonly 150-350 µm. Unaltered sulfides exist primarily as ~10 µm rounded inclusions in silicates and oxides. These inclusions typically consist of pyrrhotite, pentlandite, taenite, and/or awaruite exsolution.

### *Reid 013*

Reid 013 is composed of 92 vol% olivine ($Fo_{65.3}$), 3 vol% high-Ca pyroxene ($Wo_{46.9}En_{43.3}Fs_{9.8}$), 1 vol% chromite, and trace troilite, low-Ca pyroxene, and FeNi metal. Olivine and pyroxene grain sizes are 300-400 µm. Chromite ranges from a typical grains size of ~100 µm up to 450 µm. Troilite occurs as small, rounded inclusions (<10 µm) within silicates phases and chromite. Reid 013 is significantly weathered, as indicated by Fe-rich alteration (3.8 vol%) along grain boundaries and alteration of some olivine to iddingsite along the exterior of the sample. Trace amounts of low-Ca pyroxene ($Wo_{1.8}En_{70.6}Fs_{27.6}$), unaltered taenite (29.9 wt% Ni), and one grain of kamacite (2.4 wt% Ni) are included in silicates and chromite.

### *Northwest Africa 11304*

NWA 11304 is the one R chondrite in this study. It is classified as R4, but appears to contain clasts of multiple petrologic types, as evidenced by FeO variability among olivine grains ($Fo_{50-82}$). Representative compositions for olivine and pyroxenes in the dominant lithology, which is consistent with an R4 classification, are presented in Table 2.1, and sulfides are presented in Table 2.6. The dominant opaque phases are pentlandite and pyrrhotite, which occur both as discrete phases in the matrix and as exsolutions in large (>100 µm) sulfide blebs. Magnetite (~10 µm) is present in trace amounts, and typically is found within or adjacent to sulfides. Several clasts show quench textures from impact melting and segregation of sulfides and silicates. Discrete platinum group element phases, such as Pt metal, $PtAs_2$ and IrAsS were identified with EDS, typically in or near sulfides, and are generally <10 µm on the longest axis.

### *2.3.2 Calculated oxygen fugacities*

Equations (2 and 4) were used to calculate $fO_2$ from activities from electron microprobe measurements of olivine and low-Ca pyroxene (Supplemental Tables S2.3-S2.7). Olivine-chromite and two-pyroxene closure temperatures and calculated oxygen fugacities are listed in Table 2.8, and oxygen fugacities versus Fe/Mn for olivine are shown in Fig. 2.2.

Oxygen fugacities are reported as log deviations from the iron-wüstite (IW) buffer and are correlated with olivine Fe/Mn ratios. Olivine-chromite temperatures range from 970°C to 1050°C for brachinites and ungrouped achondrites. All calculated temperatures exceed the 950°C FeNi-FeS eutectic (Kullerud, 1963). Calculated log $fO_2$ values for the QIFa system are between IW-1.16 and IW-2.14, which is broadly consistent with $fO_2$ calculations for other brachinites (Nehru *et al.*, 1996; Goodrich *et al.*, 2006; Gardner-Vandy *et al.*, 2013), although our method of calculation yields less oxidized values for data from other studies. For example, log $fO_2$ for NWA 5400 using our method is IW-1.6, while Gardner-Vandy *et al.* (2013) calculated an $fO_2$ of IW-1.1 using the same data measurements. The difference in

**Table 2.8.** Calculated mineral closure temperatures and oxygen fugacities

| Meteorite Name | Classification | Ol-Cr T (°C) | Two Pyroxene T (°C) | Fa $fO_2$ (Δ IW) | Fs $fO_2$ (Δ IW) |
|---|---|---|---|---|---|
| RaS 309[a] | Brachinite | 1049 ± 14 | | -1.35 ± 0.03 | |
| NWA 4882[a] | Brachinite | 1049 ± 44 | 844 ± 53 | -1.21 ± 0.04 | -1.82 ± 0.01 |
| Reid 013[a] | Brachinite | 1041 ± 26 | 836 ± 28 | -1.16 ± 0.02 | -1.04 ± 0.01 |
| Hughes 026[b] | Brachinite | 1038 ± 21 | 893 ± 84 | -1.19 ± 0.03 | -1.4 |
| ALH 84025[c] | Brachinite | 970 ± 46 | | -1.28 ± 0.07 | |
| NWA 5400[b] | Ungrouped | 1028 ± 22 | 901 ± 26 | -1.58 ± 0.03 | -1.98 ± 0.01 |
| NWA 5363* | Ungrouped | 1021 ± 57 | 903 ± 18 | -1.99 ± 0.02 | -2.14 ± 0.02 |
| Eagles Nest | Brachinite | 1047 ± 9 | | -1.45 ± 0.02 | |
| NWA 7299 | Brachinite | 1056 ± 22 | 925 ± 37 | -1.66 ± 0.03 | -1.99 ± 0.04 |
| NWA 7297* | Brachinite | 1022 ± 27 | 883 ± 10 | -1.95 ± 0.07 | -2.17 ± 0.04 |
| MIL 090405/6[d] | Ungrouped | 1019 ± 23 | 952 ± 21 | -2.11 ± 0.04 | -2.04 ± 0.03 |
| NWA 11756 | Brachinite | 1026 ± 31 | 977 ± 28 | -2.14 ± 0.02 | -2.24 ± 0.06 |

*no metal in our sample, used Ni content in Fe-rich alteration to estimate mol% Fe

[a] calculated with average mol% Fe of all exsolved metal phases

[b] calculated from data in Gardner-Vandy *et al.* (2013) and references therein. No uncertainties reported for opx in Hughes 026.

[c] calculated from data in Mittlefehldt *et al.* (2003)

[d] calculated from data in Day *et al.* (2019)

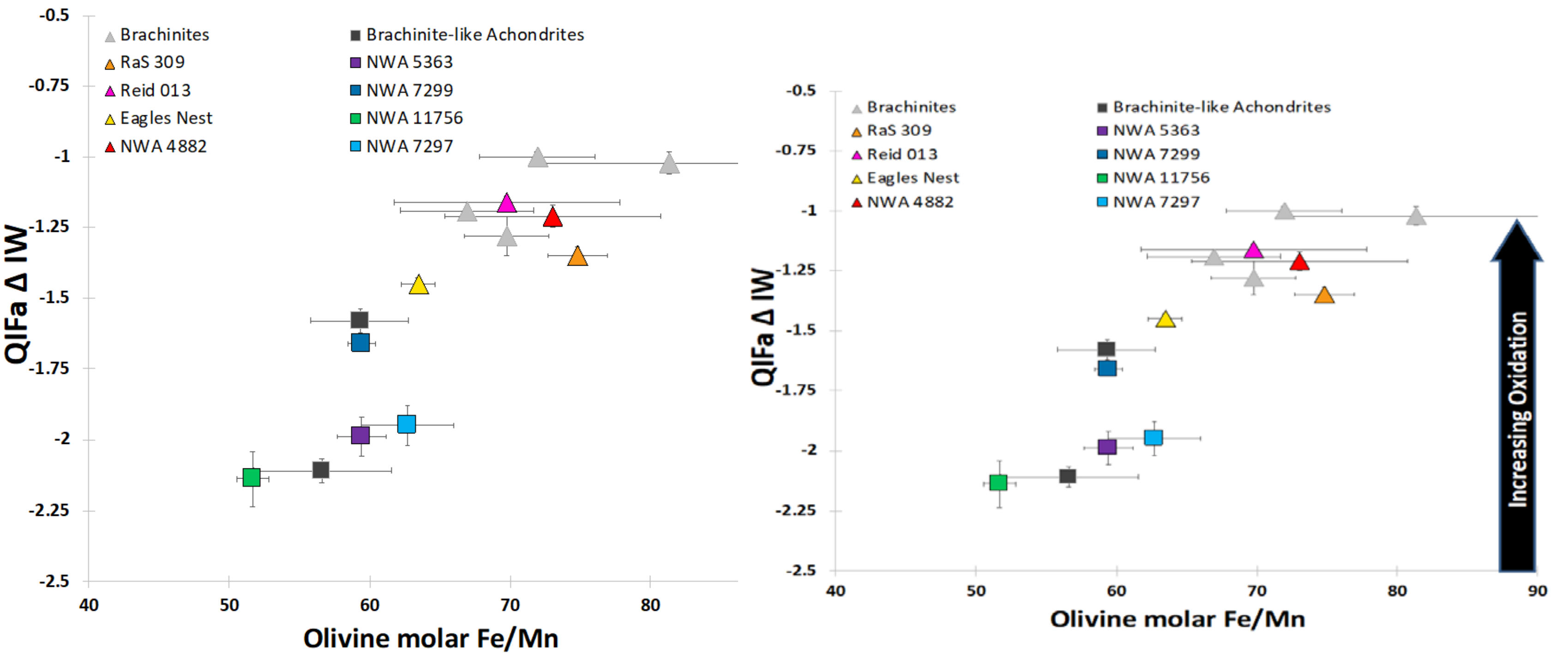

**Fig. 2.2. Calculated brachinite $fO_2$ vs. Fe/Mn**

(a) Calculated QIFa log $fO_2$ vs. Fe/Mn in olivine are correlated, consistent with a redox trend within the brachinite family. This demonstrates that average molar Fe/Mn in olivine is a useful proxy for determination of relative oxidation state. Terrestrial weathering is the most likely cause for the large Fe/Mn uncertainties in these samples. (b) QIFs log $fO_2$ vs. Fe/Mn in low-Ca pyroxene falls along a similar trend, although MIL 090405/6 (Day *et al.*, 2019) retains an anomalously high Fe/Mn ratio and (cont'd) the overall range of Fe/Mn is much smaller. Oxygen fugacity ($fO_2$) of brachinites (triangles) and brachinite-like achondrites (squares) are presented in Table 2.8. For samples that did not contain measurable FeNi metal, the activity of Fe in metal () was estimated based on the Ni content of Fe-rich alteration products. Greyscale symbols are from data in Gardner-Vandy *et al.* (2013) and Day *et al.* (2019). Calculated QIFas $fO_2$ are plotted in Supplementary Fig. S2.8.

calculated $fO_2$ likely occurs during Gibbs free energy minimization calculations, which are approximated using our methodology, while calculations in Gardner-Vandy *et al.* (2013) utilized proprietary thermodynamic software and datasets to supplement iterative $fO_2$ calculations until Gibbs free energy was minimized. This highlights the limitations involved when comparing $fO_2$ values calculated across different methodologies, and it should be noted that the $fO_2$ values reported in this study are intended to be internally consistent and used for comparative purposes. Uncertainties for our calculations were propagated through equations from variance in EMP measurements.

Two-pyroxene closure temperatures range from 844 to 947°C and are systematically lower than their corresponding olivine-chromite temperatures. Calculated log $fO_2$ values using the QIFs system are between IW-1.04 to IW-2.24. Oxygen fugacities calculated in this system are typically lower than their corresponding QIFa calculations, apart from Reid 013. While the two methods of calculation yield slightly different $fO_2$ values, their results are within 0.6 log units and well within the oxidation conditions described in previous work (*e.g.,* Gardner-Vandy *et al.*, 2013), which also calculated less oxidizing conditions with the QIFs system. Our sections of Eagles Nest and RaS 309 did not contain low-Ca pyroxene, so $fO_2$ could only be calculated for their QIFa system. While the lack of low-Ca pyroxene in some samples prevents us from applying the QIFs equation, the correlation between the two systems in other samples allows us to assume that the $fO_2$ values calculated only from QIFa are reasonable estimates for samples lacking low-Ca pyroxene. Uncertainties for $fO_2$ calculations are based on variance of EMP measurements, which were propagated through Equations 2 and 4.

Oxygen fugacities for NWA 4882, RaS 309, and Reid 013 were calculated using Fe activities from metal inclusions within silicates (Table 2.4). These inclusions likely exsolved well below temperatures recorded by olivine-spinel and two-pyroxene thermometers, given the range of Fe content among kamacite, taenite, and tetrataenite (Kitakaze *et al.*, 2016). As Equations 2 and 4 rely on Fe activity of metals at closure temperatures recorded by the olivine-spinel and two pyroxene thermometers, we used the mean Fe activity of all metal phases in each sample to represent pre-exsolution metal composition in oxygen fugacity calculations. Consequently, the uncertainties reported for $fO_2$ calculations in these samples are based on variance of fayalite and and ferrosilite activities only. Due to pervasive weathering, no metal or distinguishable altered metal grains could be identified in Al Huwaysah 010. Without a reasonable estimate for Fe activity in metal, we could not calculate oxygen fugacity for this sample.

### 2.3.3 Highly siderophile element content

Average trace element concentrations for sulfides and metals in brachinites, ungrouped achondrites, and R chondrite NWA 11304 are presented in Table 2.9. Individual sulfide HSE contents are highly variable in each sample (Fig. 2.3), but

**Table 2.9.** Representative in situ trace element concentrations (in ppm, unless stated otherwise) in sulfides and metals of brachinites, ungrouped achondrites, and R chondrite NWA 11304.

| | | *Sulfides* | | | | | | |
|---|---|---|---|---|---|---|---|---|
| | | RaS 309 | NWA 4882 | Eagles Nest | NWA 7299 | NWA 7297* | NWA 11756 | NWA 5363 |
| | n= | 11 | 10 | 4 | 12 | 11 | 6 | 8 |
| Fe | (wt%) | 63 | 50 | 63 | 63 | 45 | 55 | 63 |
| Co | | 4020 | 3330 | 1200 | 380 | 3660 | 2370 | 4510 |
| Ni | | 10900 | 56200 | 16000 | 3100 | 13200 | 22000 | 40900 |
| Cu | | 13.8 | 3.53 | 279 | 65.3 | 236 | 87.4 | 389 |
| Zn | | n.d. | 10.69 | 5.71 | 7.37 | n.d. | 0.35 | 0.79 |
| Ga | | 6.49 | n.d. | 1.36 | 0.14 | 0.07 | n.d. | 0.36 |
| Ge | | 1452 | 0.01 | 0.35 | 8.57 | 13.8 | 1.45 | 27.6 |
| As | | 4.82 | 0.14 | 3.64 | 3.35 | 2.38 | 0.29 | 3.72 |
| Mo | | 11.5 | 44.4 | 7.88 | 4.99 | 6.86 | 3.64 | 8.24 |
| Ru | | 4.11 | 5.37 | 0.76 | 0.22 | 0.18 | 0.08 | 0.42 |
| Rh | | 0.12 | 0.40 | 0.17 | 0.01 | 0.06 | 0.01 | 0.10 |
| Pd | | 0.09 | 1.52 | 2.50 | 0.02 | 0.03 | 0.01 | 0.02 |
| Sb | | n.d. | 0.29 | 1.24 | n.d. | n.d. | n.d. | n.d. |
| W | | 0.19 | 0.03 | 1.29 | 0.04 | 0.13 | 0.00 | 0.20 |
| Re | | 0.03 | 0.81 | 0.01 | 0.00 | 0.52 | 0.16 | 0.55 |
| Os | | 2.58 | 4.17 | 0.15 | 0.09 | 0.11 | 0.004 | 0.13 |
| Ir | | 0.26 | 0.78 | 0.17 | 0.03 | 0.12 | 0.01 | 0.24 |
| Pt | | 0.16 | 0.24 | 0.27 | 0.12 | 0.15 | 0.001 | 0.06 |
| Au | | n.d. | 0.03 | 0.42 | 0.04 | 0.07 | 0.03 | 0.09 |

**Table 2.9 cont’d**

| | *Metals* | | | *NWA 11304 (R chondrite)* | | |
|---|---|---|---|---|---|---|
| | Eagles Nest* | NWA 7299 | NWA 11756* | | pentlandite | pyrrhotite |
| n= | 4 | 8 | 5 | | 5 | 7 |
| Fe | 63 | 81 | 60 | Fe | 35 | 63 |
| Co | 1290 | 13450 | 3340 | Co | 11753 | 637 |
| Ni | 19000 | 153000 | 34700 | Ni | 309200 | 8980 |
| Cu | 306 | 468 | 150 | Cu | 1830 | 560 |
| Zn | 10.1 | 1.35 | 1.93 | Zn | 29.2 | n.d. |
| Ga | 134 | 9.48 | 13.2 | Ga | 10.0 | 1.05 |
| Ge | 8.55 | 1900 | 227 | Ge | 8.6 | 1.36 |
| As | 25.7 | 29.9 | 14.0 | As | 30.3 | n.d. |
| Mo | 17.7 | 13.1 | 4.40 | Mo | 0.86 | 4.00 |
| Ru | 8.69 | 54.1 | 3.42 | Ru | 15.6 | 0.82 |
| Rh | 2.12 | 4.49 | 0.75 | Rh | 2.31 | 0.03 |
| Pd | 11.7 | 5.23 | 1.68 | Pd | 11.9 | 0.02 |
| Sb | 9.0 | n.d. | n.d. | Sb | n.d. | n.d. |
| W | 20.7 | 9.94 | 0.47 | W | 0.29 | 0.01 |
| Re | 0.05 | 4.80 | 0.23 | Re | 0.13 | 0.18 |
| Os | 2.34 | 39.4 | 12.5 | Os | 3.64 | 1.90 |
| Ir | 2.25 | 47.15 | 4.89 | Ir | 6.18 | 0.40 |
| Pt | 4.54 | 83.81 | 4.25 | Pt | 1.04 | 0.06 |
| Au | 1.68 | 3.24 | 0.34 | Au | n.d. | n.d. |

*Measured in Fe-rich alteration products.
n.d. = not detected

**Table 2.10.** Bulk HSEs in NWA 4882 and NWA 11756 (ppb).

| | Mass (g) | Re | Os | Ir | Ru | Pt | Pd |
|---|---|---|---|---|---|---|---|
| NWA 4882 | 0.048 | 31.346 | 127.36 | 53.66 | 190.8 | 61.98 | 26.48 |
| NWA 11756 | 0.0081 | 28.502 | 2899.7 | 2518 | 2395 | 3602 | 964.0 |

Isotopic ratios are reported in Supplementary Table S2.1.

average sulfide HSE contents in each sample distinguish sulfide-dominated mineral assemblages (Fig. 2.4a) from metal-bearing ones (Fig. 2.4b,c). In the absence of metal, sulfides are the dominant carriers of HSEs in brachinites, and average Ir/Os and Pt/Os ratios are distinctly subchondritic, which is consistent with measurements for other brachinites (Day *et al.*, 2012). Overall HSE concentrations in these sulfides range from chondritic to 10x bulk CI chondrite. In contrast, HSEs strongly partition into metal ($K_d^{metal/sulfide}$ ~10 to $10^3$) when present in the mineral assemblages and retain roughly chondritic HSE ratios, apart from Pd, which is the least compatible HSE in FeNi metal (Palme, 2008). In RaS 309 and Reid 013, both FeNi metal and sulfides are present, but exist as <10µm inclusions that are too small for analysis via laser ablation. In R chondrite NWA 11304, HSEs are hosted primarily in pentlandite, but pyrrhotite can also contain near-chondritic concentrations. Both phases are variable in abundance and proportion of HSEs, but pentlandite is consistently depleted in Pt relative to other HSEs, and average pyrrhotite concentrations are depleted in both Pt and Ir, similar to sulfides in brachinites.

Bulk HSE abundances (Table 2.10, Fig. 2.3a) were measured in NWA 4882 and NWA 11756 to assess how well modal recombination of *in situ* measurements could reproduce bulk rock HSE contents. The two samples were chosen because they represent mineralogic extremes in oxidation state of the study with enough mass available for destructive analysis. The opaque assemblage of NWA 4882 is

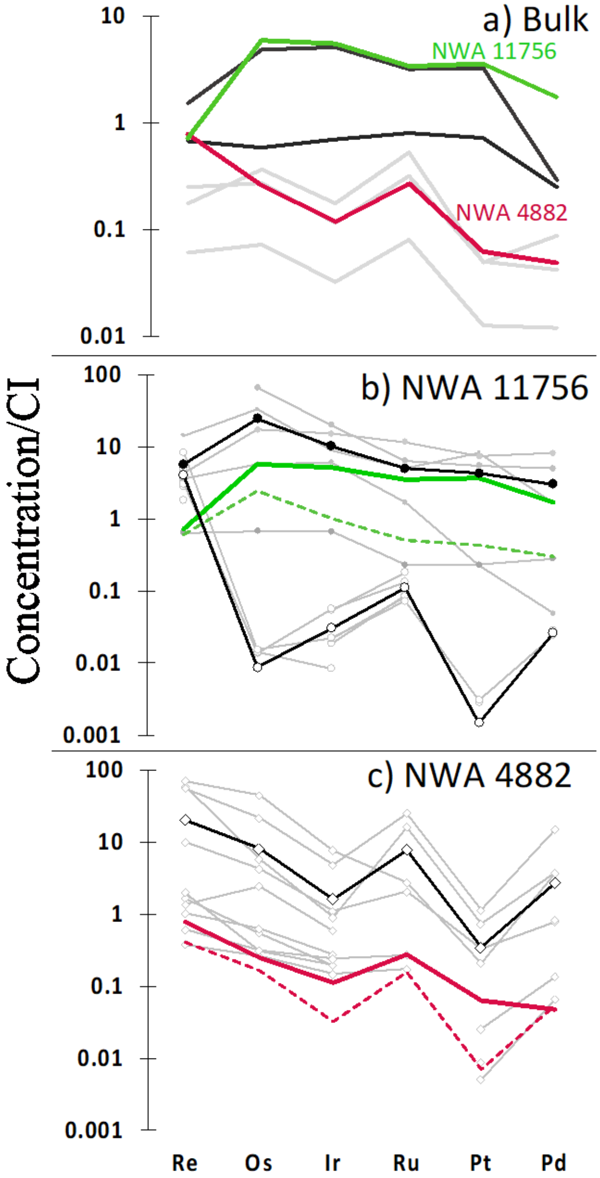

**Fig. 2.3. Highly siderophile element (HSE) concentrations**
a) Bulk data for brachinites (grey) and brachinite-like achondrites (black) from Day et al. (2012). Colored lines are bulk measurements from this study. (b) NWA 11756 HSEs are primarily concentrated in metal (solid symbols) with minimal contribution from sulfides (open symbols). (c) In NWA 4882, HSEs are held in sulfides with no metal present in this sample. In (b) and (c), dashed lines are modal recombinations of bulk HSEs from averaged in situ analyses of metals and sulfides (black lines with symbols). Individual in situ analyses are colored grey with symbols. Deviations between bulk measurements and modal recombination are likely due to sample heterogeneity, but illustrate the main HSE carrier phase in each endmember sample, regardless.  CI normalization is from McDonough and Sun (1995).

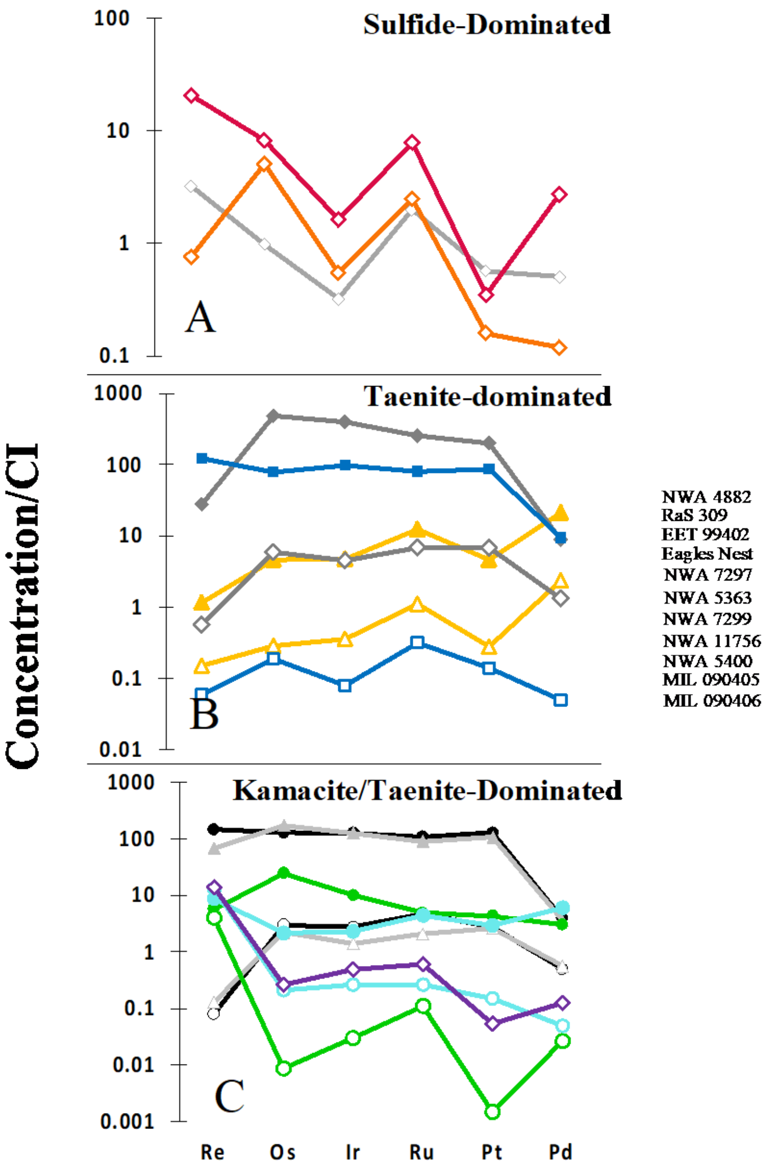

**Fig. 2.4. CI-normalized HSE concentrations in sulfides**
a) The most oxidized brachinites (IW-1.16 to -1.35) have sub-chondritic Ir/Os and Pt/Os controlled by sulfides. Metals and sulfides in intermediate brachinites (b), with $fO_2$= IW-1.45 to -1.66, retain roughly chondritic relative HSE abundances and the majority of HSE are held in taenite. Eagles Nest falls into the intermediate, taenite-dominated category, but its HSEs are anomalous. It is likely that some of the ablated material was a combination of weathered sulfide and metal. Metals in least oxidized brachinite-like achondrites (c) dominate HSE concentrations with roughly chondritic HSE ratios. Sulfide HSE ratios in (c) are variable but are typically 2-3 orders of magnitude lower in abundance than in coexisting kamacite and taenite. NWA 7297 Fe alteration products and sulfides differ by only 1-2 orders of magnitude, likely due mixing of weathered metals and sulfides in the ablated materials. Data for ALH 84025, EET 99402, MIL 090405/6, and NWA 5400 are from Day *et al.* (2012, 2019CI normalization data from McDonough and Sun (1995).

dominated by pyrite, which controls bulk HSE content and is characterized by marked depletions in Ir and Pt relative to Os and Ru. Modal recombination of HSEs in NWA 4882 sulfides (~1 vol%) can approximate interelement HSE ratios (Fig. 2.3c), although the absolute concentrations differ between bulk measurements and those calculated from modal recombination. In NWA 11756, altered FeNi metal is the primary carrier of HSEs, (Figs. 2.3b and 2.4c) and sulfides play a negligible role. Modal recombination of NWA 11756 metal (10 vol%) and sulfide (1 vol%) roughly approximates HSE ratios in bulk measurement. Individual grain analyses are highly variable in both NWA 4882 and NWA 11756, and together with sample heterogeneity can easily explain the differences between modal recombination calculations and bulk measurements. While our bulk measurements may not be representative of larger sections, they adequately illustrate the main carriers of HSE phases in their respective mineral assemblages when considered with in situ measurements.

All of the samples analyzed in this study are hot desert finds and have experienced varying degrees of terrestrial alteration. Apart from those in NWA 7299, all larger metal grains (>10 µm) have altered to iron oxides, as evidenced by visible rusting and low totals in EMP measurements. However, measured HSE abundances and interelement ratios of weathered sulfides and metals can still be considered representative of parent body processes (Hyde *et al.*, 2014). In Al Huwaysah 010, continuous Fe-rich weathering veins throughout the sample prevented analysis of any individual altered metal or sulfide grains.

## 2.4 Discussion

### 2.4.1 Effects of oxidation state on residual mineralogies

Calculated $fO_2$ of brachinites and ungrouped brachinite-like achondrites reveals an oxidation trend consistent with the observed trend seen in Fe/Mn ratios of olivine (Fig. 2.2, Supplementary Fig. S2.9). While oxidation state appears correlated with mineral composition, it may also be correlated with modal mineral abundances. Some caution should be applied, however, given the heterogeneous nature of the samples and uncertainty in modal analyses. Nonetheless, brachinites and brachinite-like achondrites with the lowest calculated $fO_2$ in this study (*e.g.*, NWA 5363 and NWA 11756) exhibit the highest pyroxene/olivine ratios (~0.3). In contrast, the most oxidized samples (*e.g.*, NWA 4882 and Reid 013) exhibit significantly lower pyroxene/olivine ratios (0.007-0.03). The most likely explanation for the differences in pyroxene/olivine ratios is $fO_2$ during melting, as recent melting experiments have shown the ratio to increase with more reducing initial conditions in chondrites (Collinet and Grove, 2020). The more oxidized lithologies with higher silicate FeO concentrations would also have begun melting at lower peak temperatures and presumably experienced higher degrees of partial melting, given that additional FeO depresses the melting point of silicates relative to more magnesian compositions. Extraction of a felsic melt component, potentially analogous to oligoclase-dominated GRA 06128/9 (Day *et al.*, 2012; Lunning *et al.*, 2017), is consistent with experimental work in which brachinites form as residues after 14-31% partial melting of an R chondrite-like precursor (Gardner-Vandy *et al.*, 2013; Lunning *et al.*, 2017). If the differences in modal mineralogy can be explained through variable degrees of partial melting, this should also be evident in bulk rare-earth element (REE) concentrations for brachinites and ungrouped brachinite-like achondrites. This seems plausible from existing REE data (Day *et al*., 2012), which show that more highly oxidized, FeO-rich samples (*e.g.*, NWA 3151, 4872, and 4882) are more highly fractionated with regard to MREE and HREE abundances when compared to metal-bearing assemblages (NWA 5400 and 6077). LREEs are less clear, most likely due to desert alteration (Day *et al.*, 2012). Further bulk REE measurements, particularly for brachinite-like achondrites, would help to clarify the relationship among $fO_2$, pyroxene/olivine ratios, and partial melting.

The abundance of FeNi metal relative to sulfides in primitive achondrites is most likely inherited as a result of the O and S abundances of precursors. Oxidation of Fe metal in precursors results in the partitioning of $Fe^{2+}$ into silicates, leaving more Ni-rich metal, which is modally less abundant after oxidation due to loss of Fe. In R chondrites, S concentrations are roughly twice that of ordinary chondrites (Bischoff *et al.*, 2011), resulting in sulfidation of FeNi metal to form pentlandite and pyrrhotite. If R chondrites serve as appropriate analogues for oxidized brachinite precursors, the dominance of sulfides over metals can explain the trace amounts of FeNi metal in most brachinites without invoking a complex melting history or nonchondritic starting composition to account for HSE content. Potentially, given the weathered nature of these samples, FeNi metal may have been altered more extensively than sulfides (Wlotzka, 1993), resulting in calculated modal mineralogies that underrepresent metals in favor of sulfides. However, we show this to be unlikely, given the high concentrations and unique interelement ratios of HSEs in oxidized brachinite sulfides, which contrasts with samples bearing both metal and sulfide.

### *2.4.2 Partial melting and HSE behavior in the Fe-Ni-S system of brachinite family endmembers*

If brachinites formed from precursors similar to R chondrites (Gardner-Vandy *et al.*, 2013), melting in the Fe-Ni-S system would be dominated by pyrrhotite and pentlandite. While brachinites can contain up to several per cent pyrrhotite by volume, pentlandite has only been observed in trace amounts in exsolution with pyrrhotite (*e.g.*, Mittlefehldt *et al.*, 2003). If brachinite precursors were similar to R chondrites, partial melting in the Fe-Ni-S system must have preferentially consumed pentlandite over pyrrhotite. R chondrite pentlandite would begin melting at ~865°C until it was completely consumed, followed by melting of pyrrhotite at higher temperatures (*i.e.*, 1190°C for pure FeS) (Fig. 2.5) (Kitakaze *et al.*, 2016). Brachinites record olivine-chromite closure temperatures of 900-1050°C, so it is likely that any pentlandite would have been completely melted, leaving only residual, Ni-poor pyrrhotite. Liquid pentlandite would be immiscible in felsic or basaltic melt, and may have entirely segregated from silicates during melting due to density contrast (pentlandite $\rho = 4.6\text{-}5\ g/cm^3$). This was first hypothesized by Nehru *et al*. (1983), who suggested segregation of an Fe-Ni-S melt component from Brachina to account for subchondritic bulk Pt concentrations and relatively high concentrations of W. Further evidence of sulfide-dominated melt loss was also found in the enrichment of light Fe isotopes in GRA 06128/9, which is consistent with preferential melting and removal of sulfides from a chondritic precursor (Wang *et al*., 2014). In this scenario, small

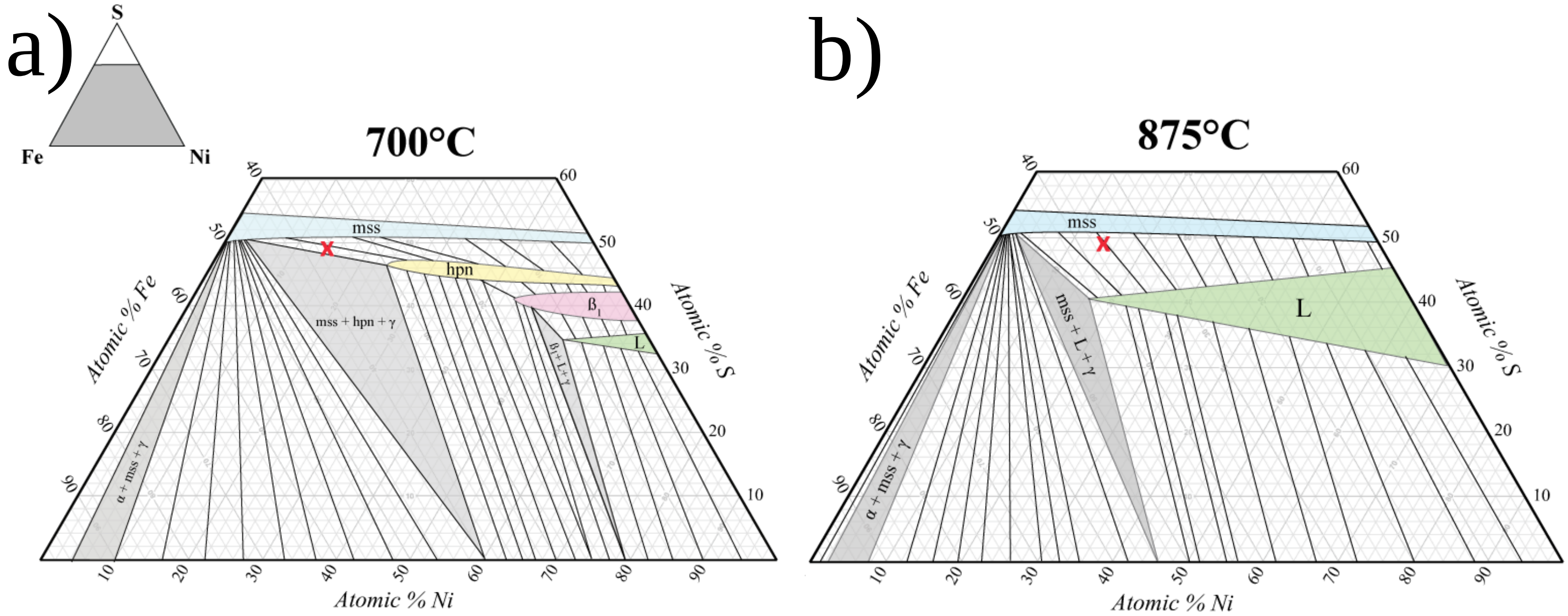

**Fig. 2.5. Fe-Ni-S ternary phase diagrams**
After Kitakaze *et al.* (2016); the red X is the bulk sulfide composition of the R chondrite type specimen, Rumuruti (Bischoff *et al.*, 2011). The blue field is monosulfide solid solution (mss), yellow is high-form pentlandite (hpn), pink is $Ni_3S_2$ ($\beta_1$), green is liquid (L), α is kamacite, and γ is taenite. Black tie lines define coexisting compositions at equilibrium. Grey areas have three coexisting phases. NWA 11304 sulfides appear to have equilibrated near (a) ~700°C. At (b) 875°C pentlandite is completely melted. Olivine-chromite closure temperatures in brachinites exceed those in experimental work, but it is reasonable to assume that the liquidus expands to consume the most Ni-rich MSS and propagates toward pure FeS (melting point ~1190°C). This evolutionary pathway is distinct from Fe-Ni-S systems in ordinary chondrites, which populate the α+mss+γ fields.

melt droplets of sulfides were entrained in a buoyant felsic melt component, which is consistent with pentlandite observed in GRA 06128/9 (Day *et al.*, 2012). No analogues for pentlandite-dominated core material have been observed, although it is unclear how a pentlandite melt would have evolved during sulfide-silicate segregation and core formation. In phase diagram space, liquid Fe-Ni-S compositions from the melting of pentlandite and pyrrhotite at 875°C would crystallize as a mixture of pyrrhotite, pentlandite, and Ni-rich metal (Fig. 2.5; Kitakaze *et al.*, 2011; 2016). This can be seen in inclusions of sulfides and FeNi metal within olivine grains of brachinite RaS 309. These inclusions retain bulk compositions that fall within the range of a pentlandite-dominated melt. Further experimental work in this compositional space could provide insights into the unique differentiation pathways of sulfur-bearing, oxygen-rich parent bodies and core formation.

The similarities between HSE ratios for R chondrite and brachinite pyrrhotites provides further evidence that the precursor of the most oxidized brachinites was similar to R chondrites (Table 2.9, Fig. 2.6). Depletions in Ir and Pt in some brachinites may be explained by the removal of discrete platinum-group element (PGE) arsenides and sulfarsenides, as seen in many R chondrites (Bischoff *et al.*, 2011 and references therein). While pentlandite-dominated HSE systematics are currently unexplored in the meteoritic literature, terrestrial hydrothermal ore experiments suggest that Ir and Pt may form selective complexes with As and S during melting (Helmy and Bragagni, 2017). In As-rich sulfide melting experiments,

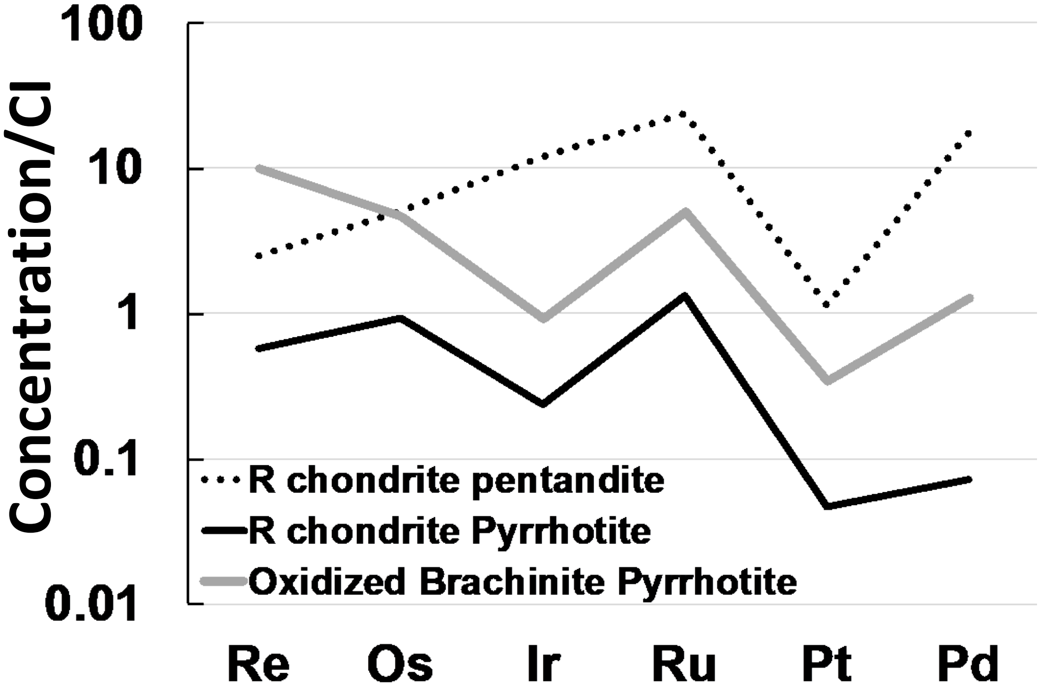

**Fig. 2.6. HSE concentrations of sulfides in R chondrites and brachinites.** Averaged, CI-normalized concentrations reflect similar Ir and Pt depletions in pyrrhotites of both groups. The unique HSE patterns of brachinites may be reproduced if pentlandite was melted and removed from an R chondrite-like precursor, further experimental work is needed to assess the behavior of HSEs in a sulfide-dominated Fe-Ni-S system.

Pt and Ir form nanoclusters with As in sulfide melts even when undersaturated in HSEs (Helmy *et al.*, 2013), which could provide a transport mechanism for the preferential extraction of Ir and Pt relative to Os and Ru. This mechanism may also facilitate the nucleation of discrete PGE phases in impact-melted R chondrite sulfides that cooled *in situ*. Currently, it is unclear how these phases would behave during subsequent metamorphism and/or hydrothermal alteration; these factors must be assessed in future work, as some R chondrites appear to have experienced hydrothermal alteration (*e.g.*, McCanta *et al.*, 2008). However, the presence of PGE phases in R chondrites, their effects on sulfide trace element abundances, and the lack of appreciable FeNi metal make it clear that HSE behavior in oxidized materials is distinct from reduced counterparts. Instead of HSE contents being controlled by the melting and extraction of FeNi metal, HSE distribution in oxidized, S-bearing systems is controlled by melting of sulfides. Removal of pentlandite from the system, potentially with nm-scale PGE arsenides and sulfarsenides, leaves Ir and Pt-depleted pyrrhotite in the residue, similar to what is seen in brachinite sulfides. The removal of FeNiS melt is also consistent low Ir/Os and Pt/Os for pentlandite in GRA 06128/9, the potential silicate melt analogue for brachinites (Day *et al.*, 2009, 2012; Shearer *et al.*, 2010). It is likely that this process also accounts for the variability in HSE content among individual brachinite sulfides due to the formation of PGE phases during melting. Consequently, solid metal-liquid metal distribution coefficients are not suitable for modeling partial melting in these systems. Potentially, this mechanism may yet be consistent with fractional fusion suggested by Day *et al.* (2012), but no distribution coefficients have been reported to-date for HSEs among pyrrhotite-pentlandite assemblages in relevant $fO_2$, $fS_2$, and temperature space. Experimental work is needed to assess inter-sulfide HSE behavior and the formation of PGE phases during partial melting of S-bearing, oxidized chondritic bodies like the R chondrites.

### *2.4.3 Brachinite family endmember characteristics*

Typically, brachinite classification has relied on three parameters: O-isotopes, olivine modal abundance, and olivine FeO content (*e.g.*, Nehru *et al.*, 1996; Goodrich *et al.*, 2017; Day *et al*., 2012, 2019; Keil, 2014). However, parameterization and distinctions between brachinites and brachinite-like achondrites have been vaguely defined and are generally not associated with specific formational conditions or processes. This has been problematic for understanding petrogenetic processes involved in the formation of brachinite family members, as members with contrasting characteristics are grouped with brachinites or ungrouped brachinite-like achondrites, obscuring potential trends in mineral chemistry or modal mineralogy. However, oxygen fugacity calculations across a suite of brachinite family achondrites reveal an oxidation gradient from ~IW-1 to IW-2.1 using the QIFa calculator (Fig. 2.2a) that can explain differences in modal mineralogy, mineral chemistry, and trace element distribution among FeO-rich, olivine-dominated achondrites due to distinct endmember formational conditions and subsequent igneous processing. Due to the apparent redox relationship between most brachinites and brachinite-like achondrites, we suggest that "brachinite family" be used as an umbrella term for all isotopically noncarbonaceous olivine-dominated assemblages within $Fo_{\sim 65\text{-}75}$ and $\Delta^{17}O$ = ~0 to -0.3. Sub-categories therein should be referred to by relative oxidation state interpreted

**Table 2.11. Characteristcs of brachinite family endmembers.**

| | Oxidized Endmembers | Reduced Endmembers |
|---|---|---|
| Metal Content | trace | >1 vol% |
| Forsterite Content | $Fo_{<70}$ | $Fo_{>70}$ |
| Average Fe/Mn (olivine) | >65 | <60 |
| Primary HSE Host(s) | sulfides | taenite/kamacite |
| Bulk (and sulfide) Ir/Os, Pt/Os | subchondritic | chondritic |
| QIFa $fO_2$ | >IW-1.35 | ≤ IW-1.45 |
| Endmember Examples: | Hughes 026<br>NWA 4882<br>Reid 013<br>RaS 309 | Eagles Nest*<br>MIL 090405/6<br>NWA 5363*<br>NWA 5400<br>NWA 7297<br>NWA 7299<br>NWA 11756 |

*Unclear HSE systematics, but likely contained >trace metal (see text)

$\Delta^{17}O$ = 0 to -0.03; olivine-dominated; $Fo_{60-80}$.

from olivine FeO content, average silicate Fe/Mn ratios, modal mineralogy, Ni content of metal, and relative HSE abundances when available (Table 2.11).

The most oxidized brachinites (QIFa log $fO_2$ = IW-1. to -1.3) are correlated with minor/trace abundances of orthopyroxene and plagioclase, sulfides as dominant HSE carriers, and depletions in Ir and Pt relative to Os and Ru. The abundance of HSEs in sulfides and the relative depletions in Ir and Pt are consistent with the distribution of HSEs among R chondrite sulfides and discrete PGE phases. It is therefore likely that these samples formed as residues after partial melting of a precursor most similar to R chondrites, as suggested by experimental work in Gardner-Vandy *et al.* (2013). Silicates in the oxidized endmembers of the brachinite family are the most FeO-rich (typically $Fo_{\leq 65}$) and have the highest average Fe/Mn ratios for olivine (>65). This subgroup includes NWA 4882, RaS 309, and Reid 013 from this study, as well as ALH 84025, Hughes 026, NWA 3151, and NWA 4969 based on measurements reported in Gardner-Vandy *et al.* (2013).

Reduced brachinite family achondrites (QIFa log $fO_2$ = IW-1.45 to IW-2.1) typically contain greater abundances of minor phases orthopyroxene, plagioclase, and FeNi metals. Although metals typically contain superchondritic HSE concentrations that dominate bulk concentration by several orders of magnitude, sulfide HSEs in some samples may be non-negligible and can approach chondritic concentrations. Ir/Os and Pt/Os ratios are roughly chondritic. The most reduced among these endmembers (<IW-1.5) appear to have experienced the least extensive melting, as suggested by near-chondritic minor phase abundances and bulk trace element chemistries measured in Day *et al.* (2012). Co concentration in NWA 7299 FeNi metal (~1.3 wt%) and FeO content of olivine ($Fa_{69.5}$) fall within the range of LL chondrites (Rubin, 1990). It is likely that NWA 7299 and other reduced endmembers are residues after limited partial melting of a precursor with O and S abundances more similar to some ordinary chondrites than to R chondrites. The most reduced endmembers include NWA 5363, NWA 7297, and NWA 11756 from this study, and also MIL 090405/6 based on data from Day *et al.* (2019). Eagles Nest and NWA 7299 from this study are also grouped with the reduced brachinite endmembers along with NWA 5400 and NWA 6077 (Day *et al.*, 2012; Gardner-Vandy *et al.*, 2013), although their metal phases appear to be predominantly taenite, while the the most reduced endmembers likely included more kamacite, based on Ni content of Fe-rich alteration. Given their metal content, mineral chemistries, HSE concentrations, and/or

modal mineralogies, they represent the upper $fO_2$ limits of the reduced brachinite family endmembers.

### *2.4.4 Terrestrial weathering effects in the brachinite family*

All of these samples are desert finds. As such, extensive terrestrial alteration in many samples can make it difficult to conclude whether HSEs in alteration products were once hosted by Fe metal or sulfides. In Eagles Nest, for example, some Fe-rich alteration contains ~10x the concentration of HSEs in extant sulfides, but HSE ratios are identical. Hyde *et al.* (2014) found that the interelement ratios and abundances of HSEs, apart from Re, are not affected by terrestrial alteration, so the identical HSE ratios of sulfides and Fe-alteration in Eagles Nest may suggest that the Fe-alteration phases formed from sulfides with variable HSE abundances or that analyzed sulfides were contaminated by metal inclusions. The identification of multiple taenite grains (~10 μm) in Eagles Nest in both alteration veins and sulfides supports the latter interpretation. It is possible that a more significant amount of metals once present in oxidized brachinite family endmembers were lost to weathering, but this is unlikely, as the superchondritic concentrations of HSEs in NWA 4882 and RaS 309 sulfides suggest that metals were present in no more than trace quantities.

The extensive terrestrial alteration in Al Huwaysah 010 prevented in situ analysis of any sulfides and metals. The Meteoritical Bulletin 101 (Ruzicka *et al.*, 2012) states that Al Huwaysah 010 is “related to brachinites and ungrouped achondrites NWA 1500 and NWA 4042”, although that potential relationship is not clearly defined. Olivine in Al Huwaysah 010 is significantly more magnesian than in

NWA 1500 (average = $Fo_{65-73}$; Goodrich *et al.*, 2011). Olivine in NWA 4042 ($Fo_{79.3}$) is the closest match to Al Huwaysah 010 ($Fo_{82.4}$), but its pyroxene is Ca-poor ($Wo_{1.0}Fs_{16.2}$), in contrast to Al Huwaysah 010, which contains exclusively high-Ca pyroxene in our sample. Minor amounts of low-Ca pyroxene ($Wo_{0.07}Fs_{13.9}$) have been reported in other sections of Al Huwaysah 010 (Ruzicka *et al.*, 2012), which are most similar to NWA 4042. The anomalous compositional and mineralogic characteristics of Al Huwaysah 010 distinguish it from other samples in this study, despite sharing similar oxygen isotopes (Greenwood *et al.*, 2017). It appears to be most similar to NWA 4042, but shares few characteristics described for NWA 1500. If Al Huwaysah 010 can be considered a member of the brachinite family, it would be the most magnesian endmember, but we cannot comment on its oxidation state based on our observations.

### *2.4.5 Brachinite family parent body(ies)*

While it is difficult to definitively conclude whether brachinite family members all come from a common parent body, their redox trend and shared oxygen isotopic range (Greenwood *et al.*, 2017) are consistent with such an origin. At the very least, they formed in similar nebular reservoirs. Given the range of redox conditions and potential precursors within the brachinite family, their parent body(ies) likely incorporated a mixture of materials with heterogeneous oxygen and sulfur fugacities. Due to the limited degree of melting inferred for brachinite family members, the heterogeneity of precursor components was preserved.

The relationship among brachinite family members is not only informative for understanding the effects of oxidation and sulfidation during parent body evolution, but also for remote observations of potential parent bodies. FeO content in olivine is discernable in visual-to-near-infrared spectroscopy, and the potential for heterogeneous parent bodies could result in misinterpretation of heterogeneous FeO content as an intermediate composition between endmembers. Future investigations into the distribution of olivine-dominated (A-type) asteroids (*e.g.*, Sunshine *et al.*, 2007) and their silicate FeO contents may clarify the relationships among the brachinite family as well as their parent bodies.

## *2.5 Conclusions*

- The brachinite family exhibits a range of oxidation states (QIFa $fO_2$~IW-1 to IW-2.1), wherein most classical brachinites are derived from a precursor that was more oxidized and sulfur-rich than that of ungrouped brachinite-like achondrites. This is manifest in the distinct Fe-Ni-S systems of endmember precursors, which were sulfide-dominated for brachinites and metal-dominated for brachinite-like achondrites.
- The similarities between HSE ratios for R chondrite and brachinite pyrrhotites provides further evidence that the precursor of the most oxidized brachinites was more similar to R chondrites than to ordinary chondrites, at least in terms of their Fe-Ni-S systematics.
- Unlike less oxidized bodies, where HSE contents are controlled by the melting and extraction of FeNi metal, HSE distributions in S-bearing, oxidized systems are controlled by melting of sulfides.

- Pentlandite in the oxidized brachinite precursor began melting at ~865°C producing As-rich melt that preferentially extracted Ir and Pt, resulting in the anomalous HSE patterns observed in oxidized brachinites.
- HSE behavior in S-rich, oxidized systems is distinct from reduced, metal-dominated systems and requires further constraints from experimental studies to support modeling of partial melting and potential core formation.
- Whereas reduced materials differentiate to produce an FeNi metal core, a magnesian peridotitic mantle, and a mafic basaltic crust, oxidized materials may produce a Fe-Ni-sulfide-dominated core, a ferroan peridotitic mantle, and a more felsic crust.

These findings merit further examination into the formation of oxidized parent bodies, particularly in the interest of understanding bodies that formed beyond the snow line in the early solar system, which presumably possessed a much greater availability of volatile materials than most regions in the inner solar system. The incorporation of greater amounts of volatiles directly influences the characteristics of mineral constituents in planetary precursors, which in turn direct the evolutionary path of the parent body during melting and differentiation. Potential products of S-bearing, oxidized differentiation, such as felsic crustal materials and core components derived from sulfide-dominated melts, should be considered both in future meteoritical research and in observational studies of asteroids. This area of research could greatly expand our knowledge of the range of planetary materials in the solar system.

# Chapter 3: Oxidized Parent Body Conditions Prior to the Onset of Melting

S. D. Crossley*[1], R. D. Ash[1], J. M. Sunshine[1,2], C. M. Corrigan,[3] and T. J. McCoy[3]
[1] Department of Geology, University of Maryland, College Park
[2] Department of Astronomy, University of Maryland, College Park
[3] Department of Mineral Sciences, Smithsonian Institution NMNH, Washington DC

## *Abstract*

Models of planetary core formation beginning with melting of Fe,Ni metal and lesser amounts of troilite (FeS) are not readily applicable to oxidized and sulfur-rich chondrites containing only trace quantities of metal. Cores formed in these bodies must be dominated by sulfides. Siderophile trace elements used to model metallic core formation could be used to similarly model oxidized, sulfide-dominated core formation and identify related meteorites if their trace element systematics can be quantified. Additionally, insufficient information exists regarding the behavior of core forming elements in sulfides during metamorphism.

Analyses of major, minor, and trace element concentrations of sulfides are reported for the oxidized, brecciated (clasts of petrologic types 3-5) R chondrite Northwest Africa 11304. Sulfide-dominated core forming components in oxidized chondrites ($fO_2 \geq$ IW) follow metamorphic pathways that are distinct from reduced, metal-bearing counterparts. Most siderophile trace elements partition into pentlandite at approximately 10x bulk chondritic abundances, but Pt, W, Mo, Ga, and Ge are depleted by 1-2 orders of magnitude relative to siderophile elements with similar volatilities. Similar measurements for hydrothermally altered R chondrite La Paz Icefield 04840 are also reported, and the siderophile trace element systematics are further modified by oxidation of sulfides to magnetite. Incongruent melting of

pentlandite at 865 °C, would fractionate siderophile elements in distinct proportions and segregate into a Ni,S-rich core at an earlier than metal segregation. However, Hf-W ages of core formation may be obscured due to the large fraction of oxidized W retained by silicates ($D_W^{\text{sulfide-silicate}}$ ~0.1), preventing accumulation of excess $^{182}W$.

Oxidized, sulfide-dominated core formation differs from metallic core formation models both physically and geochemically. If oxygen and sulfur abundances varied radially with heliocentric distance, then inner and outer solar system bodies may have followed distinct evolutionary pathways of differentiation and core formation controlled by their initial oxygen and sulfur content.

### *3.1 Introduction*

The compositions and proportions of core-forming phases are controlled by the cosmochemistry of the nebular environments in which they formed (e.g., Lodders et al., 2003; Wood et al., 2019). Thus, a parent body that accreted in the presence of abundant oxygen and sulfur would ultimately produce a core that is compositionally distinct from one that is dominated by FeNi metal. In the protoplanetary disk, the effective concentrations of oxygen and sulfur (i.e., oxygen and sulfur fugacities, $fO_2$ and $fS_2$, respectively) are predicted to have increased with heliocentric distance due to evaporation of volatile phases in the high temperature regions of the inner disk (Grossman et al., 2008). As a result, much of the iron in many outer solar system bodies presumably partitioned into silicates, oxides, and sulfides after oxidation and sulfidation of nebular metals (e.g., Kerridge, 1976; Frost, 1991; Lauretta et al., 1998). Since these reactions occur prior to the onset of partial melting and parent body differentiation, they have significant effects on the melting temperatures of minerals and the igneous evolution of the parent body (e.g., Tomkins et al., 2020).

For the most oxidized and sulfur-rich chondrites, which include Rumuruti (R) chondrites and many carbonaceous chondrites (e.g., Righter and Neff, 2007; Righter et al., 2016), FeNi metal is present in only trace quantities, and the core-forming minerals are instead dominated by sulfides: pentlandite ($Fe_{4.5}Ni_{4.5}S_8$) and pyrrhotite ($Fe_{1-x}Ni_xS$), with variable abundances of magnetite (total opaque minerals 3-18 vol%; Righter and Neff, 2007; Bischoff et al., 2011). Consequently, cores that formed from comparatively oxidized and S-rich bodies would have bulk compositions comprised of FeNi sulfides rather than FeNi metal.

A variety of geochemical methods have been used to investigate core formation. Notably, highly siderophile trace elements (HSEs) Re, Os, Ir, Ru, Rh, Pt, and Pd can be used to model metal-silicate segregation and core formation (e.g., Chabot and Jones, 2003), as these elements partition strongly into FeNi metals ($D^{metal/silicate} \geq 10^4$; Walker, 2016) but will partition into pentlandite in the absence of metal (e.g., Crossley et al., 2020). Numerous studies have used the fractionation of HSEs, according to their compatibilities in Fe metal, to model the melting (e.g., Day et al., 2012) and crystallization histories of planetary cores (e.g., Walker 2016). In principle, this tool should be applicable to sulfides as well. Consequently, siderophile elements may be used to model core formation on highly oxidized, sulfur-rich bodies, but only if their partitioning behaviors are known at the onset of melting.

Rumuruti-type (R) chondrites provide the ideal samples to study the distribution of siderophile trace elements in oxidized, sulfur-rich systems because they formed in high $fO_2$ (IW-1 to IW+4; Righter and Neff, 2007; McCanta et al., 2008) and high $fS_2$ environments (2 order of magnitude greater than the iron-troilite buffer, IT+2; Miller et al. 2017). Despite a dearth of Fe,Ni metal, R chondrites still contain chondritic abundances of siderophile trace elements (Isa et al., 2014) with the majority of HSEs held in pentlandite (Crossley et al., 2020). Many of the more than 250 R chondrites that have been identified are breccias composed of clasts that are variably metamorphosed, including petrologic types 3-6 and some hydrothermally altered samples (e.g., Bischoff et al., 2006, 2011; Gattacceca et al., 2020). These breccias provide an opportunity to observe the effects of thermal alteration on opaque mineral assemblages and trace element systematics throughout metamorphism on the R chondrite parent body. The lack of exogenous materials among R chondrite breccias (Bischoff et al., 2006) further reduces the risk of comparing metamorphic effects among genetically unrelated materials that is inherent when comparing separate samples. R chondrites also share bulk chemical, mineralogic, and isotopic similarities with more thoroughly studied, reduced, and metal-bearing ordinary chondrites (Greenwood et al., 2000; Bischoff et al., 2011; Miller et al., 2017), providing an opportunity to isolate the effects of high $fO_2$ and $fS_2$ on core forming mineral phases and compare sulfide-dominated to metal-dominated siderophile element partitioning behaviors during parent body metamorphism.

Published datasets are lacking for siderophile trace element systematics during the metamorphism of highly oxidized, sulfur-rich R chondrites. To investigate the equilibrium distribution of siderophile elements during metamorphism, major and trace element concentrations in sulfides and oxides are reported for two R chondrites, Northwest Africa 11304 and La Paz Icefield 04840. These samples include clasts of petrologic types 3-5, as well as hydrothermally altered materials (e.g., Satterwhite and Righter, 2006; Gattacceca et al., 2020). While siderophile element systematics among R chondrite sulfides share many similarities with those of ordinary chondrite metals during metamorphism, several distinct mechanisms relating to the high $fO_2$ and $fS_2$ of R chondrites result in the fractionation of Pt, W, Mo, Ga, Ge, and other siderophiles relative to elements with similar volatilities.

## *3.2 Methods*

### *3.2.1 Sample selection and preparation*

Two R chondrites are analyzed in this study: Northwest Africa (NWA) 11304 and La Paz Icefield (LAP) 04840,11. A probe mount of NWA 11304 was used for *in situ* compositional analyses, and a thin section was subsequently made for petrographic investigation from the same section after destructive analyses were completed. *In situ* sulfide and oxide mineral chemistries were measured from a 50 µm-thick section of LAP 04840 (R6; Satterwhite and Righter, 2006). The probe mount and thin section of NWA 11304 are from the personal collection of Dr. Richard Ash, and the polished thin section of LAP 04840 is from the Antarctic Meteorite Collection at NASA’s Johnson Space Center.

NWA 11304’s weathering grade is classified as W2 (moderate weathering; Gattacceca et al., 2020). Some reddening is present around the edges of the sample thin section and along cracks but textural evidence of extensive alteration is not present throughout the interior of NWA 11304 thin section, in BSE maps, or in elemental maps. Most sulfides in this section of NWA 11304 lack Fe-rich alteration greater than 20% of their surface area, which is more consistent with a W1 classification (Wlotzka, 1993). Similarly, LAP 04840 is classified with an Antarctic weathering grade A/B (Gattacceca et al., 2020), which is comparable to W1 (Wlotzka, 1993). The minimal weathering of sulfides in both samples provides suitable materials for analyses of siderophile element systematics during metamorphism and hydrothermal alteration.

### *3.2.2 Petrologic type classification*

Petrologic types are determined following methods for ordinary chondrites in Huss et al. (2006) based on textural characteristics and the percent mean deviation (PMD) of FeO content in chondrule and matrix olivine (Table 3.1, supplementary materials provided in Table S3.1). Given that parameters from Huss et al. (2006) were originally established for ordinary chondrites, samples are also compared to descriptions for R chondrites of various petrologic types summarized in Bischoff et al. (2011).

### *3.2.3 Modal mineralogy*

Modal mineralogy for NWA 11304 is calculated by creating mineral classification maps (e.g., Beck *et al.*, 2012; Crossley *et al.*, 2020). Element maps are created from energy-dispersive X-ray spectroscopy (EDS) analyses at the Smithsonian Institution National Museum of Natural History Department of Mineral Sciences (SI) using a ThermoFisher energy dispersive X-ray detector attached to a FEI Nova NanoSEM 600. Seventeen individual element maps are stacked into layers of a data cube using Environment for Visualizing Images (ENVI 4.4) image processing software. The final mineral classification map of NWA 11304 is provided in supplementary materials (Fig. S3.1). Mineral modes are calculated by counting pixels for each class (Table S3.2). To estimate uncertainty for mineral modes, homogeneous grains of each mineral phase are identified by SEM and EMPA, then are examined for misclassified pixels in the mineral classification maps. Less than 10% of pixels in each of these grains are misclassified and can be attributed to noise in the original EDS data. Therefore, mineral mode uncertainties are estimated to be ±7 vol% for olivine, ±2 vol% for plagioclase, and less than ±1 vol% for other phases. Step-by-step instructions for this methodology are provided in supplementary materials.

EDS and EMPA data necessary for constructing modal mineral maps of LAP 04840 could not be collected due to limited facility accessibility imposed by public health policies during the COVID-19 pandemic. For this sample, opaque minerals are identified via reflected light optical microscopy using an OMAX petrographic polarizing microscope, and digital images are assembled into a mosaic to calculate the volume percent of opaque phases by pixel counting. Within opaque assemblages, phases are distinguished in digital images at higher magnification by their relative brightness in greyscale (pentlandite > pyrrhotite >> magnetite). Each phase is identified, masked in separate layers using Adobe Photoshop, and the proportion of pixels for phases in each layer is used to calculate the modal mineralogy of opaque assemblages in volume percent (Table S3.2).

### *3.2.4 Compositional Analyses*

Major and minor element concentrations for mineral phases are collected via electron microprobe (EMP) at SI using a JEOL 8530 F+. Operating conditions are set at 1 µm spot size, 10 kV, and 20 nA for all mineral phases. Natural and synthetic standards are used for calibration and are measured in duplicate before and after each analytical run. For LAP 04840, our measurements yield systematically low values for Fe and S in sulfides and oxides due to spectrometer failure for those elements that occurred between calibration and the first analytical run while operating the instrument with limited facilities access due to public health policies. The troilite and chromite standards are therefore renormalized by their official compositions (Jarosewich, 2002 and references therein) and are used to correct the EMPA measurements. Our corrected measurements for Fe and S are within ~2 at% of the values reported for sulfides in McCanta et al. (2008). Detection limits and renormalizing calculations for EMP measurements are provided in supplementary materials (Tables S3.3-S3.4).

Trace elements are measured *in situ* via laser ablation inductively-coupled mass spectrometry (LA-ICP-MS) at University of Maryland Plasma Laboratory using a New Wave Research UP-213 laser ablation unit attached to a ThermoFinnigan Element2 single collector ICP-MS. Samples are ablated into a stream of helium (approximately 0.6 L min$^{-1}$), which is then mixed with Ar (approximately 0.9 L min$^{-1}$) before introduction into the mass spectrometer. Laser ablation is done via spot analyses using a spot size varying from 15 to 80 µm, depending on the size of the grain ablated. The output of the laser is modified to ensure the fluence remained between 2 and 4 $Jcm^{-2}$, typically an output of approximately 60% of the total available power. The repetition rate of the laser is 7 Hz for NWA 11304 and 10 Hz for LAP 04840. For siderophile and chalcophile element measurements, samples are standardized using iron meteorites Coahuila, Filomena, and NIST 610 alumino-silicate glass standard (described by Walker et al., 2008). All samples are cleaned with a brief, low power pulse of the laser prior to the data gathering ablation. Gas background measurements are taken for 20 s prior to each sample analysis. LAMTRACE is used for data reduction (Achterbergh et al., 2001). Upper limits for concentration are calculated by setting the detection limit for any given isotope measured as three times the mean measured gas background. Replicate analyses of standards yielded external precisions less than ± 5% (2σ) for all elements analyzed. Specific precisions and detection limits are reported in supplementary materials (Table S3.5). Standards are analyzed in identical fashion to their respective samples.

Trace element analyses are biased toward sulfide and oxides grains larger than ~20 µm due to the minimum useful diameter of the laser. As such, these measurements do not account for the trace element compositions of smaller matrix sulfides common in petrologic types 3 and 4.

## 3.3 Results

### 3.3.1 Northwest Africa 11304: Petrography and petrologic type classifications

The textures in NWA 11304 are consistent with other breccias and the sample is composed primarily of R chondrite petrologic type 4 materials with several type 3 and 5 clasts, as well as two clasts that experienced extensive impact-induced melting of sulfides and silicates (Tables 3.1-3.2, Fig. 3.1, and Table S3.2 in supplementary materials). Clast boundaries are distinguishable in BSE images, modal mineral maps, and by plane and cross-polarized light (Figs. S3.1-S3.2 in supplementary materials).

*Petrologic type 3*

Petrologic type 3 materials (Fig. 3.1a) together comprise approximately 12 vol% of the sample. They are composed of 60 vol% olivine, 15 vol% feldspar, 13

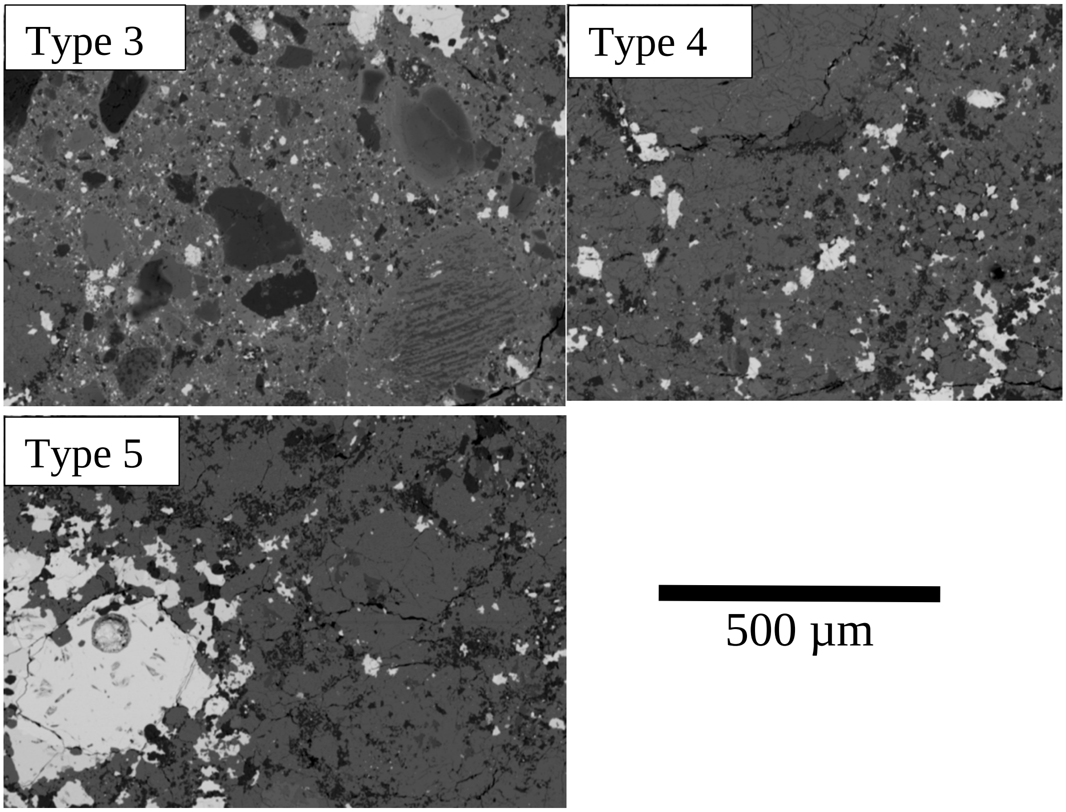

**Fig. 3.1. BSE images of petrologic types among NWA 11304 clasts**.
This sample is a genomict breccia containing clasts of (a) petrologic type 3, (b) type 4, and (c) type 5. Sulfides (white) coalesce and coarsen, silicates (greys) homogenize, and chondrules and matrix grains recrystallize from type 3 to 5. The circular feature in the type 5 sulfide (c) is a laser ablation pit. Detailed petrographic descriptions for each petrologic type are presented in the text.

**Table 3.1.** Modal mineralogies and parameters for petrologic type classifications of clasts in NWA 11304.

| NWA 11304 Clasts: | Type 3 | | Type 4 | | Type 5 | | Impact Melts | |
|---|---|---|---|---|---|---|---|---|
| | Volume% | | Volume% | | Volume% | | Volume% | |
| Whole Sample | 12 | | 54 | | 28 | | 5 | |
| Olivine | 66 | | 63 | | 62 | | 64 | |
| Plagioclase | 16 | | 16 | | 17 | | 14 | |
| Low-Ca Pyroxene | 14 | | 9 | | 7 | | 10 | |
| High-Ca Pyroxene | 3 | | 6 | | 4 | | 5 | |
| Pyrrhotite | 4 | | 3 | | 4 | | 3 | |
| Pentlandite | 3 | | 3 | | 4 | | 4 | |
| Oxides | 3 | | 2 | | 2 | | 2 | |
| Phosphates | 0.7 | | 0.7 | | 0.8 | | 0.1 | |
| **Chondrule/Matrix** | **0.7** | | **1.2** | | **n/a** | | **0.4** | |
| | Avg Fa% | PMD[a] | Avg Fa% | PMD[a] | Avg Fa% | PMD[a] | Avg Fa% | PMD[a] |
| Olivine | 43.4 | 22.7 | 38.7 | 15.8 | 38.2 | 1.0 | 35.1 | 25.0 |
| *Matrix* | 53.3 | 11.6 | 41.9 | 10.1 | | | | |
| *Chondrule* | 33.2 | 12.3 | 34.2 | 11.1 | | | | |
| | Avg Fs% | PMD[a] | Avg Fs% | PMD[a] | Avg Fs% | PMD[a] | Avg Fs% | PMD[a] |
| Low-Ca Pyroxene | 20.5 | 53.9 | 25.4 | 21.8 | 30.8 | 3.3 | 48.4 | 21.0 |

[a] PMD = Percent mean deviation of FeO.

Classification parameters are from Huss et al. (2006) and are comparable to R chondrites with similar petrologic type classifications in Bischoff et al. (2011).

Oxide wt% data for silicates provided in supplementary materials.

**Table 3.2.** Average major element chemistries of sulfides in NWA 11304 (wt%).

| | Type 3 | | | | Type 4 | | | |
|---|---|---|---|---|---|---|---|---|
| | Pentlandite | σ | Pyrrhotite | σ | Pentlandite | σ | Pyrrhotite | σ |
| n= | 12 | | 8 | | 13 | | 15 | |
| Fe | 35.3 | 1.8 | 60.8 | 1.4 | 35.2 | 0.3 | 61.8 | 0.42 |
| Co | 1.2 | 0.3 | 0.07 | 0.01 | 1.17 | 0.07 | 0.07 | 0.02 |
| Ni | 25.4 | 2.8 | 0.18 | 0.1 | 30.0 | 0.4 | 0.24 | 0.06 |
| S | 31.5 | 1.7 | 37.0 | 1.4 | 33.2 | 0.2 | 37.9 | 0.5 |
| Cr | 0.07 | 0.09 | 0.05 | 0.06 | 0.01 | 0.021 | 0.02 | 0.05 |
| P | 0.02 | 0.03 | 0.00 | 0.01 | 0.003 | 0.004 | 0.001 | 0.002 |
| Si | 0.2 | 0.3 | 0.02 | 0.04 | 0.001 | 0.003 | 0.001 | 0.002 |
| Zn | | | 0.01 | 0.022 | | | 0.01 | 0.02 |
| Mg | 0.06 | 0.15 | 0.003 | 0.01 | | | 0.001 | 0.002 |
| Cu | 0.10 | 0.07 | 0.07 | 0.04 | 0.121 | 0.05 | 0.06 | 0.04 |
| Sum | 93.8 | | 98.2 | | 99.7 | | 100.2 | |
| Anion/ Cation* | 0.9 | | 1.1 | | 0.9 | | 1.1 | |

*Atomic fraction of S/(Fe+Co+Ni+Zn+Cu)

**Table 3.2 (cont'd).** Average major element chemistries of sulfides in NWA 11304 (wt%).

| | Type 5 | | | | Impact Melted | | | |
|---|---|---|---|---|---|---|---|---|
| | Pentlandite | σ | Pyrrhotite | σ | Pentlandite | σ | Pyrrhotite | σ |
| n= | 12 | | 11 | | 8 | | 7 | |
| Fe | 35.5 | 0.3 | 61.6 | 0.61 | 33.7 | 2.0 | 56.4 | 4.089 |
| Co | 1.092 | 0.192 | 0.06 | 0.01 | 0.96 | 0.127 | 0.07 | 0.02 |
| Ni | 29.8 | 0.4 | 0.267 | 0.08 | 28.1 | 2.0 | 0.234 | 0.08 |
| S | 33.1 | 0.3 | 38.1 | 0.4 | 32.1 | 1.2 | 35.9 | 1.81 |
| Cr | 0.01 | 0.012 | 0.03 | 0.05 | 0.19 | 0.471 | 0.23 | 0.6 |
| P | 0.01 | 0.04 | 0.01 | 0.015 | 0.01 | 0.02 | 0.01 | 0.01 |
| Si | 0.01 | 0.01 | 0.01 | 0.03 | 0.05 | 0.04 | 0.07 | 0.05 |
| Zn | b.d.l. | | 0.01 | 0.02 | b.d.l. | | b.d.l. | |
| Mg | 0.002 | 0.006 | 0.006 | 0.011 | 0.006 | 0.009 | 0.012 | 0.02 |
| Cu | 0.097 | 0.03 | 0.06 | 0.02 | 0.063 | 0.03 | 0.02 | 0.028 |
| Sum | 99.6 | | 100.1 | | 95.2 | | 92.9 | |
| Anion/ Cation* | 0.9 | | 1.1 | | 0.9 | | 1.1 | |

vol% low-Ca pyroxene, 6 vol% sulfide, 3 vol% oxides, <1 vol% Ca-phosphate, and accessory high-Ca pyroxene. These clasts contain the greatest variability in olivine FeO content ($PMD_{FeO}$ = 22.7, Table 3.1), the lowest chondrule/matrix ratios (0.7), and the smallest matrix silicate and sulfide grain sizes (<<1 µm). These parameters are consistent with petrologic subtypes 3.6-3.8 for ordinary chondrites (Huss et al., 2006), although a direct comparison between the two groups is complicated by the differences in mineralogy and mineral chemistries. Both type I and type II chondrules are present in these clasts and include porphyritic olivine, porphyritic pyroxene, and porphyritic olivine-pyroxene textures ranging in size from 250-600 µm in diameter. The matrix is opaque in thin section and dominated by FeO-rich olivine (average Mg# = 46.7), pentlandite, pyrrhotite and albitic plagioclase. Matrix sulfides are randomly dispersed, and larger sulfide nodules (typically 50-150 µm) are often associated with chondrules. Minor and accessory matrix phases include pyroxene (both low and high-Ca), Ca-phosphates, and magnetite. The type 3 clasts include the greatest abundance of low-Ca pyroxene contained in chondrules and chondrule fragments. High-Ca pyroxene is an accessory phase and is most commonly found in chondrule mesostases. Small subhedral magnetite grains (<10 µm) are present in type 3 clasts and are usually associated with sulfide nodules.

The largest sulfide nodule (500 µm) in type 3 clasts appears to have been incorporated as a free-floating sulfide melt droplet, evidenced by its relatively circular shape, embayed boundaries, and quenched margin (Fig. 3.2). In thin section, this nodule contains the largest concentration of magnetite in NWA 11304, constituting roughly half of the nodule’s cross section. Subhedral magnetite grains (~10 µm)

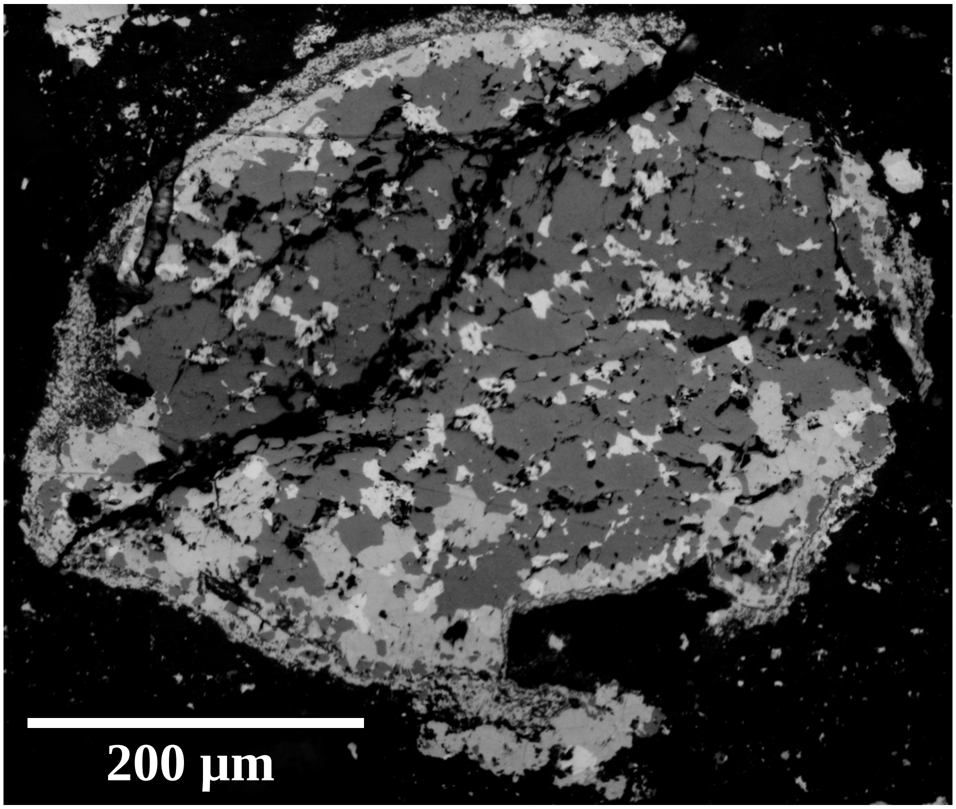

**Fig. 3.2. Magnetite-rich sulfide chondrule in NWA 11304 type 3 clast (RFL).** The largest sulfide chondrule in NWA 11304 contains subhedral magnetite crystals with interstitial pyrrhotite and accessory pentlandite. Smaller magnetite grains line the margin of the sulfide chondrule, which may have formed after oxidation of sulfide reacting with matrix materials. This is the largest concentration of magnetite among clasts of all petrologic types.

cluster in the center of the sulfide nodule with intergranular pentlandite and pyrrhotite. Smaller magnetite grains (≤ 1 μm) populate the margins of this nodule. These textures are consistent with magnetite growth through oxidation of the sulfide nodule either with highly oxidized nebular gasses (i.e., $fO_2$ ~FMQ) or through reaction with the surrounding matrix materials. However, the matrix grains directly in contact with the sulfide nodule display no obvious reaction textures and are consistent with matrix materials throughout the rest of the clast.

Major element compositions for type 3 sulfides are most consistent with equilibration at 500°C (Table 3.2; Fig. 3.3), falling along tie lines between pentlandite and MSS in the 500°C isothermal plane of Fe-Ni-S phase diagrams drawn from experiments (after Kitakaze et al. 2016).

*Petrologic type 4*

Petrologic type 4 materials (Fig. 3.1b) dominate the majority of this section of NWA 11304 (54 vol%). Type 4 materials contain chondrule/matrix ratios (1.2) higher than type 3, but with fewer FeO-poor type I chondrules. Chondrules are typically 0.5-1 mm in diameter, but can range up to 2 mm, and include porphyritic olivine, porphyritic olivine-pyroxene, porphyritic pyroxene, and cryptocrystalline pyroxene chondrule types. Olivine FeO variability in type 4 material ($PMD_{FeO}$ = 15.8) is less than in type 3, indicating an approach to equilibrium compositions, although chondrule olivine has not fully equilibrated with matrix olivine (Table 3.1). Type 4 matrix materials are microcrystalline, with variable grain sizes for plagioclase (typically 10-30 μm). High-Ca pyroxene is twice as abundant as seen in type 3 material, although it is still mostly confined to chondrules with low-Ca pyroxene

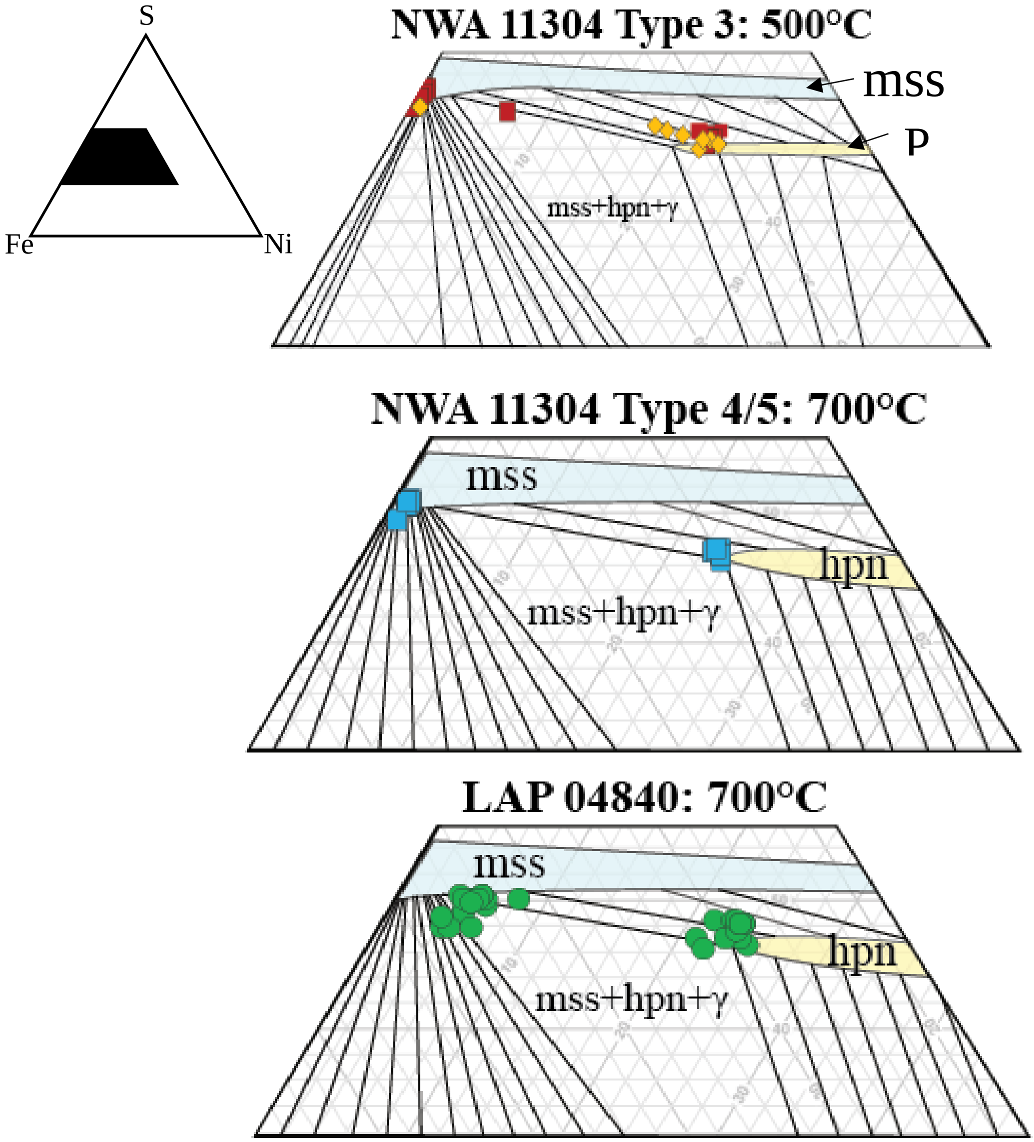

**Fig. 3.3. Isothermal planes for Fe-Ni-S Ternary Phase Diagrams**
After Kitakaze et al. (2016) for sulfides in NWA 11304 petrologic endmembers and LAP 04840. For NWA 11304, type 3 sulfides fall along tie lines at 500°C, and sulfides in petrologic type 4 and 5 clasts are consistent with equilibration at 700°C. In LAP 04840, pentlandite and pyrrhotite compositions vary over several atom percent, probably due to oxidation of sulfides during hydrothermal alteration. Fe/Ni ratios are most consistent with 700°C phase diagrams in Kitakaze et al. (2016). The inferred closure temperature for the sulfide system in LAP 04840 is within the range of temperatures calculated using Fe-Mg silicate-spinel thermometers (McCanta et al. ,2008) and is reasonable for petrologic type 5 materials (Huss et al., 2006).

and/or chondrule olivine. Low-Ca pyroxene abundance decreases by approximately one third from type 3 to type 4. Sulfides larger than 10 µm are more common than in type 3 materials but span a similar range of compositions. However, matrix sulfides (< 10 µm) are still present in type 4 materials. Major element compositions from EMPA for sulfides in type 4 materials are consistent with a higher equilibration temperature (up to 700°C; Table 3.2; Fig. 3.3), but this temperature should be considered as an upper limit because analyses for type 4 sulfides are biased toward the largest grains. These petrographic and compositional characteristics are consistent with 3.8-4.0 petrologic types in ordinary chondrites and are consistent with descriptions of type 4 classifications for other R chondrites (Bischoff et al., 2011). Given the petrographic differences and less variable olivine FeO content in these materials compared to type 3 clasts, the R4 classification assigned to the majority of materials in NWA 11304 is likely accurate (Gattacceca et al., 2020).

*Petrologic type 5*

In petrologic type 5 materials (28 vol%), chondrule and matrix olivine grains are homogenized (Mg# = 62, $PMD_{FeO}$ = 1) and most chondrules are texturally well-integrated with recrystallized matrix materials (Fig. 3.1c). However, several relict chondrules are discernable in thin section. Plagioclase grains are typically 20-50 µm and form networks with high-Ca pyroxene (~50 µm) between large olivine grains (commonly 300-400 µm). Sulfides are most commonly ~100 µm but reach up to 650 µm in diameter, and small matrix sulfide grains are rare. Sulfides are typically composed of homogeneous subhedral pyrrhotite and pentlandite, with pentlandite dominating the largest grains. The boundaries between exsolved pentlandite and pyrrhotite are typically much smoother and more regular in type 5 materials than in more primitive clasts (Fig. 3.4a), indicative of equilibration between the two phases near 700°C (Fig. 3.3). Sulfide sizes and grain boundaries are consistent with coalescing and coarsening during metamorphism, similar to what has been observed for metals in ordinary chondrites (e.g., Kimura et al., 2008). Small HSE-rich grains of arsensides and sulfarsenides (generally ~1µm diameter) are found within all petrologic types, but the largest grains are found in type 5 (up to 10 µm diameter) and are most often in contact with sulfides. Ca-phosphate grain sizes are variable, typically 50-100 µm, but are larger on average than their type 3 and 4 counterparts and are commonly associated with sulfide assemblages. The compositional and textural characteristics of this clast are consistent with petrologic type 5 classifications for both R chondrites (Bischoff et al., 2011) and ordinary chondrites (Huss et al., 2006).

### *Impact-shocked and melted clasts*

Two clasts in this section of NWA 11304 are strongly shocked and comprise approximately 5 vol% of the observable sample (Figs. S3.1-S3.2 in supplementary materials). The less shocked clast contains some chondrules and mafic fragments of olivine and low-Ca pyroxene (up to $Fo_{91}$ and $En_{95}$, respectively), but the majority of olivine is homogeneous (Mg# = 65). The low-Ca pyroxene fragments display embayed disequilibrium textures that indicate destruction via oxidation by the surrounding matrix. Quenched melts of K-rich feldspar and high-Ca pyroxene coexist with submicron FeO-rich olivine and sulfides interstitial to large olivine grains

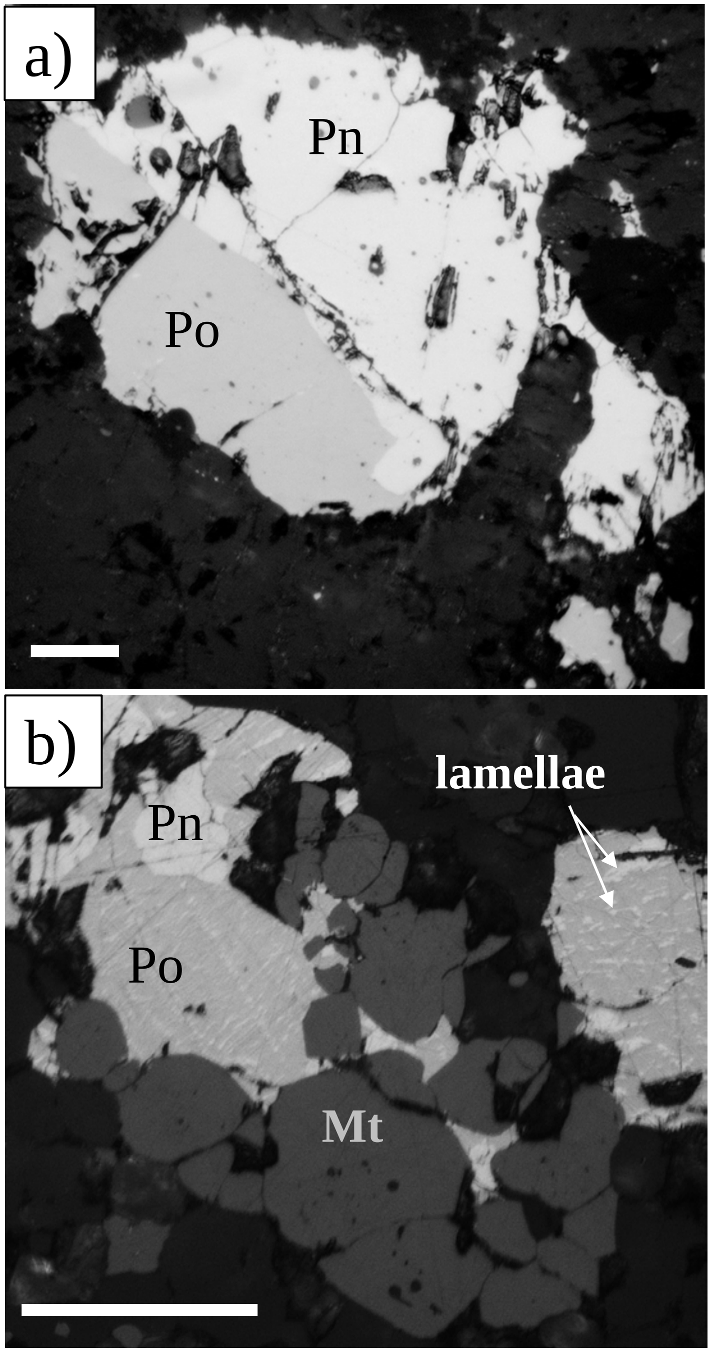

**Fig. 3.4. Reflected light images of R chondrite sulfide assemblages.** Assemblages in type 5 NWA 11304 clasts (a) include homogeneous pentlandite (Pn) and pyrrhotite (Po) with smooth contact surfaces, characteristic of equilibrium between the two phases. In contrast, LAP 04840 sulfide assemblages (b) contain irregular pentlandite-pyrrhotite boundaries and fine-scale exsolution lamellae, and are embayed with magnetite (Mt), indicating disequilibrium brought on by late-stage oxidation of sulfides during hydrothermal alteration. Scale bars are 50 µm.

(Fig. S3.2). K-rich feldspar is only observed in impact-melted clasts and in the mesostasis of porphyritic chondrules in type 3 and 4 materials. Another clast appears to have completely melted and rapidly cooled. This is evident in zoned olivine crystals (Mg# = 91-51, core to rim) with interstitial microcrystalline K-rich feldspar and high-Ca pyroxene, as well as the chaotic distribution of silicate microcrystals throughout a large, highly embayed sulfide assemblage (850 x 1700 µm) that is characteristic of impact melts seen in other R chondrites (Bischoff et al., 2011; Lunning et al., 2017).

### *3.3.2 LaPaz Icefield 04840 petrography and petrologic type classification*

LAP 04840 is classified as an R6 chondrite (Satterwhite and Righter, 2006), and of interest because it is one of three hydrothermally altered R chondrites and is among the most oxidized endmembers of the group (log $fO_2$ = IW+4; McCanta et al., 2008). In tandem with NWA 11304, it provides insight into the siderophile systematics across a range of R chondrite $fO_2$ conditions as well as an opportunity to investigate the effects of hydrothermal alteration on siderophile element distribution among sulfides and oxides. Previous work provides a thorough description of nonopaque mineral phases in this sample (e.g., McCanta et al., 2008). Given that the relationship between oxides and sulfides is of particular interest for this study, this work focuses on measurements of opaque mineral assemblage of LAP 04840 (Table 3.3). Nickel-rich (5 wt%) monosulfide solid solution (MSS) is the most common sulfide phase in LAP 04840. Most MSS grains have exsolution lamellae of pentlandite throughout (1-5 µm diameter). Discrete grains of pentlandite mantle MSS or are included within them. Most large magnetite grains (50-100 µm) are subhedral

**Table 3.3. Modal mineralogy and major element chemistries of opaque mineral assemblages in LAP 04840.**

| | Pentlandite | σ | Pyrrhotite/MSS | σ | | Magnetite | σ |
|---|---|---|---|---|---|---|---|
| vol%[a]= | 0.7 | | 4.1 | | | 0.8 | |
| n= | 173 | | 205 | | | 82 | |
| Fe | 30.0 | 3.0 | 53.5 | 3.0 | FeO | 67.5 | 0.8 |
| Co | 0.94 | 0.13 | 0.26 | 0.15 | CoO | 0.10 | 0.02 |
| Ni | 32.5 | 3.5 | 5.0 | 3.4 | NiO | 0.35 | 0.09 |
| S | 30.3 | 0.8 | 33.6 | 0.6 | SO3 | 0.10 | 0.42 |
| Cr | 0.05 | 0.07 | 0.07 | 0.10 | Cr2O3 | 18.0 | 0.6 |
| P | 0.004 | 0.008 | 0.006 | 0.030 | P2O5 | 0.15 | 0.36 |
| Si | 0.004 | 0.013 | b.d.l. | | SiO2 | 0.10 | 0.09 |
| Zn | n.d. | | n.d. | | ZnO | 0.06 | 0.04 |
| Mg | b.d.l. | | b.d.l. | | MgO | 1.66 | 0.07 |
| Cu | 0.09 | 0.13 | 0.04 | 0.07 | Cu2O | 0.01 | 0.01 |
| | | | | | TiO2 | 1.64 | 0.08 |
| | | | | | Al2O3 | 2.30 | 0.05 |
| | | | | | MnO | 0.24 | 0.03 |
| Sum | 93.9 | | 92.5 | | | 92.21 | |

[a] Volume percent of each phase in the total section. Within opaque assemblages, pentlandite, MSS, and magnetite account for 13, 75, and 12 vol%, respectively.

and associated with anhedral pentlandite and pyrrhotite. Smaller subhedral magnetite grains cluster along the margins of sulfide assemblages (Fig. 3.4b). However, magnetite does not occur exclusively in contact with sulfides. Isolated grains of magnetite are usually smaller (~5-20 µm), although one large magnetite grain (150 µm) does not visibly contact any sulfides in this section.

### *3.3.3 Siderophile trace element concentrations of sulfides*

Across all petrologic types in NWA 11304, most HSE are concentrated in pentlandite (Table 3.4, Fig. 3.5, and Fig. S3.3 in supplementary materials). In clasts of petrologic types 3 and 4, sulfide siderophile element abundances span a continuous range of values from subchondritic concentrations (<< 0.1x CI) in Ni-poor pyrrhotite to super chondritic concentrations (>10x CI) in the most Ni-rich pentlandite endmembers. The continuous range of HSE/Ni ratios between sulfide endmembers likely reflects intermediate monosulfide solid solution in type 3 and 4 clasts and/or fine-scale exsolution lamellae of pentlandite that cannot be resolved during laser ablation measurements. In contrast, EMPA measurements of Ni in type 4 sulfides are not in agreement with Ni concentrations measured by laser ablation, but instead tightly cluster into pentlandite and pyrrhotite endmember compositions. The discrepancy between EMPA and laser ablation measurements is likely due to the difference in spot size between analyses. In contrast to the 1 µm spot size of EMPA, laser ablation analyses in type 4 materials had a minimum diameter of 20 µm and a sampling depth of ~10 µm. Consequently, trace element measurements likely sample fine-scale mixtures of pyrrhotite and pentlandite that are not sampled simultaneously by EMPA. Regardless, endmember trace element concentrations clearly reflect the exsolution of pentlandite and pyrrhotite by petrologic type 5 with the majority of siderophile elements concentrated in pentlandite ($K_d^{pn/po}$ 2-500) as the two phases coarsen and approach equilibrium (Fig. 3.5). However, W, Mo, Pt, Ga, Au and Ge in pentlandite are depleted by orders of magnitude relative to concentrations in OC metals (Fig. 3.6). Concentrations of these elements vary significantly among individual pentlandite grains, typically chondritic to subchondritic, but three grains in NWA 11304 contain superchondritic W concentrations that approach that of OC taenite (~5x CI; Kong & Ebihara, 1996). Olivine, pyroxene, and plagioclase in NWA 11304 also hold chondritic to superchondritic concentrations of W on average (supplementary materials, Table S3.6).

Siderophile element concentrations for both pentlandite and MSS in LAP 04840 (Table 3.5, Figs. 3.7-3.8, and Fig. S3.4 in supplementary materials) are similar to those of pentlandite in NWA 11304. The superchondritic abundances of most siderophile elements in MSS of LAP 04840 is probably due to the ubiquitous exsolution lamellae of pentlandite throughout pyrrhotite grains, which could not be avoided during laser ablation, given the minimum diameter of the laser (20 µm). Most HSE concentrations are ~10x CI, apart from Pt, which is depleted by an order of magnitude relative to CI-normalized Os in pentlandite and two orders of magnitude in MSS. Tungsten is also depleted by an order of magnitude relative to Os. In contrast to NWA 11304, LAP 04840 sulfides hold superchondritic concentrations of Mo (5-9x CI) and Au (up to 7.8x CI) on average.

**Table 3.4.** Average trace element concentrations in NWA 11304 sulfides.

| | | Type 3 | | | | Type 4 | | | |
|---|---|---|---|---|---|---|---|---|---|
| | | Pentlandite | MSS | Pyrrhotite | $K_d$ $^{(Pn/Po)}$ | Pentlandite | MSS | Pyrrhotite | $K_d$ $^{(Pn/Po)}$ |
| | n= | 4 | 6 | 7 | | 10 | 3 | 12 | |
| Fe | (wt%) | 35 | 40 | 62 | 0.57 | 35 | 45 | 58 | 0.60 |
| Co | | 9306 | 4912 | 509 | 18 | 9784 | 5706 | 801 | 12 |
| Ni | (wt%) | 22.6 | 9.7 | 0.69 | 33 | 28 | 14 | 1.25 | 23 |
| Cu | | 1363 | 547 | 308 | 4.4 | 921 | 1125 | 237 | 3.9 |
| Zn | | 47 | 62 | 13 | 3.6 | 5.6 | 19 | 46 | 0.1 |
| Ga | | 14 | 12 | 3.2 | 4.3 | 1.2 | 1.7 | 2.9 | 0.4 |
| Ge | | 4.4 | 4.8 | b.d.l. | | 0.87 | b.d.l. | 3.4 | 0.3 |
| As | | 32 | 6.4 | 0.42 | 76 | 20 | 13 | 1.4 | 14 |
| Se | | 36 | 25 | 18 | 2.0 | 45 | 40 | 22 | 2.0 |
| Mo | | 0.37 | 1.4 | 2.8 | 0.13 | 2.4 | 4.9 | 4.5 | 0.52 |
| Ru | | 25 | 5.8 | 0.23 | 110 | 14 | 3.8 | 1.7 | 8 |
| Rh | | 3.0 | 0.89 | 0.04 | 75 | 2.6 | 1.07 | 0.15 | 18 |
| Pd | | 8.0 | 2.1 | b.d.l. | | 15 | 4.9 | 0.13 | 111 |
| Sn | | b.d.l. | 0.12 | b.d.l. | | b.d.l. | b.d.l. | 0.05 | |
| Sb | | 0.11 | b.d.l. | 0.11 | 0.99 | 0.02 | 0.14 | 0.01 | 2.84 |
| Te | | b.d.l. | b.d.l. | b.d.l. | | b.d.l. | b.d.l. | b.d.l. | |
| W | | 0.07 | 0.05 | 0.02 | 3.7 | 0.01 | 0.05 | 0.02 | 0.6 |
| Re | | 0.35 | 0.05 | 0.19 | 1.8 | 0.48 | 0.14 | 0.09 | 5.1 |
| Os | | 6.5 | 1.2 | 1.8 | 3.7 | 7.7 | 3.3 | 1.4 | 5.6 |
| Ir | | 2.9 | 0.61 | 0.48 | 6.2 | 2.1 | 2.8 | 0.91 | 2.3 |
| Pt | | 0.84 | 1.5 | 0.21 | 4.1 | 3.1 | 3.2 | 1.1 | 2.9 |
| Au | | b.d.l. | 0.14 | 0.01 | | 0.05 | b.d.l. | 0.04 | |

In ppm unless otherwise noted.
Kd values are for pentlandite (Pn) vs. pyrrhotite (Po).
Individual measurements are provided in supplementary materials.

**Table 3.4 (cont'd).** Average trace element concentrations in NWA 11304 sulfides.

| | | Type 5 | | | Impact Melt | | | |
|---|---|---|---|---|---|---|---|---|
| | | Pentlandite | Pyrrhotite | $K_d^{(Pn/Po)}$ | Pentlandite | MSS | Pyrrhotite | $K_d^{(Pn/Po)}$ |
| | n= | 6 | 8 | | 5 | 3 | 2 | |
| Fe | (wt%) | 39 | 60 | 0.65 | 35 | 45 | 60 | 0.58 |
| Co | | 12606 | 647 | 19 | 9786 | 3759 | 1704 | 5.74 |
| Ni | (wt%) | 32.7 | 0.95 | 35 | 31.1 | 11.8 | 4.02 | 7.74 |
| Cu | | 1430 | 414 | 3.5 | 1044 | 755 | 341 | 3.06 |
| Zn | | 0.91 | 0.18 | 5.05 | b.d.l. | 38 | b.d.l. | |
| Ga | | 2.3 | 0.23 | 10 | 0.25 | 2.8 | 0.25 | 1.02 |
| Ge | | 3.5 | 0.93 | 3.8 | 0.69 | b.d.l. | 2.5 | 0.28 |
| As | | 57 | b.d.l. | | 47 | 11 | b.d.l. | |
| Se | | 33 | 15 | 2.1 | 60 | 28 | 15 | 4.08 |
| Mo | | 0.47 | 0.12 | 4.1 | 0.16 | 1.2 | 2.0 | 0.08 |
| Ru | | 20 | 0.04 | 509 | 8.7 | 3.3 | 0.33 | 26.46 |
| Rh | | 3.5 | 0.01 | 458 | 1.8 | 0.57 | 0.01 | 263.99 |
| Pd | | 15 | 0.03 | 433 | 8.3 | 3.0 | 0.65 | 12.79 |
| Sn | | b.d.l. | b.d.l. | | b.d.l. | b.d.l. | b.d.l. | |
| Sb | | 0.36 | 0.01 | 37 | 0.13 | b.d.l. | b.d.l. | |
| Te | | b.d.l. | b.d.l. | | b.d.l. | b.d.l. | b.d.l. | |
| W | | 0.15 | 0.01 | 14 | 0.31 | 0.06 | b.d.l. | |
| Re | | 0.24 | 0.01 | 29 | 0.07 | 0.03 | b.d.l. | |
| Os | | 5.3 | 0.04 | 126 | 3.0 | 1.2 | 0.02 | 126.63 |
| Ir | | 7.3 | 0.11 | 70 | 3.5 | 0.97 | 0.12 | 27.85 |
| Pt | | 1.4 | 0.02 | 62 | 1.2 | 0.31 | 0.05 | 21.48 |
| Au | | b.d.l. | b.d.l. | | b.d.l. | b.d.l. | b.d.l. | |

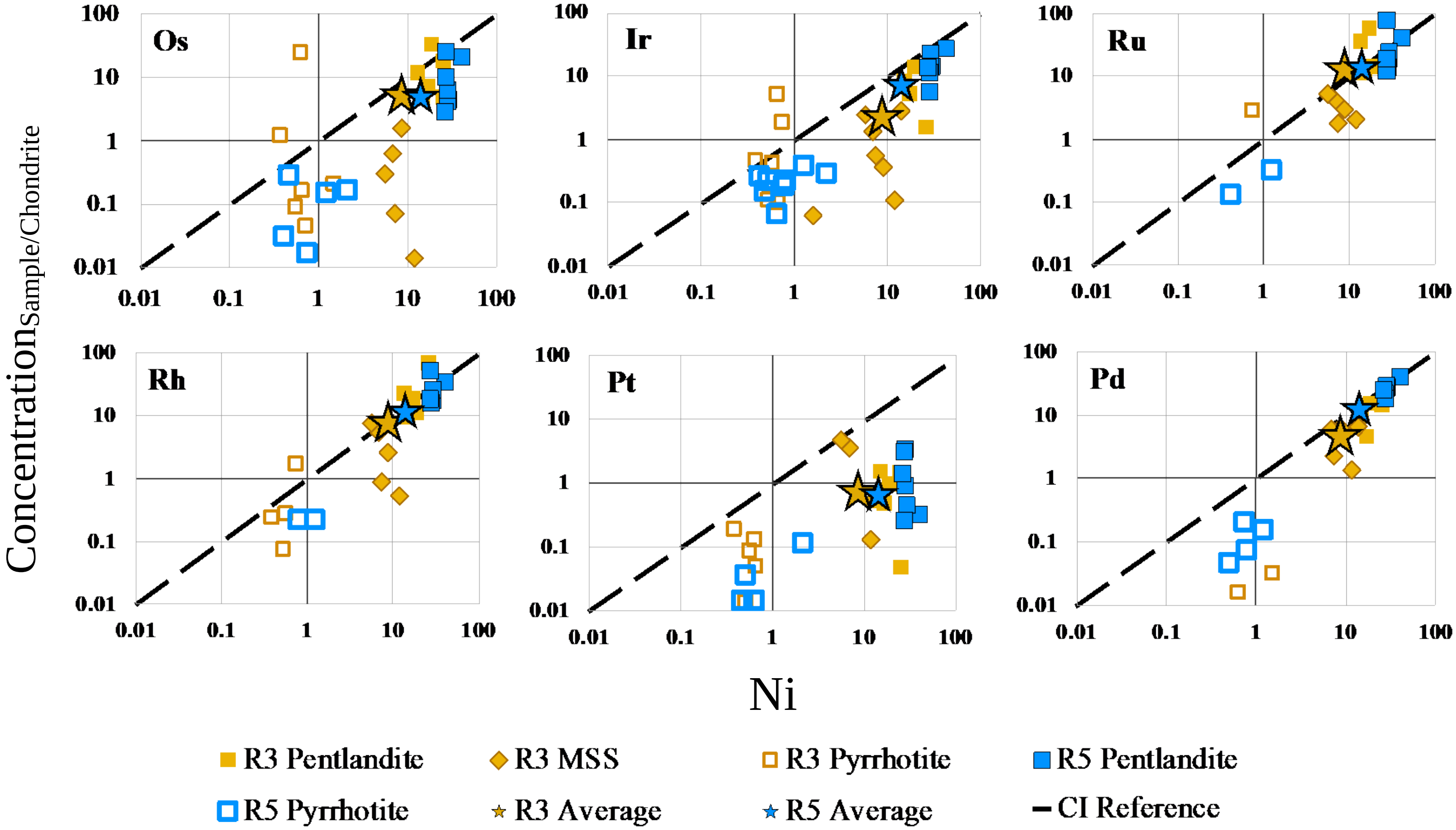

**Fig. 3.5. CI-normalized Ni vs. HSE concentration scatter plots for NWA 11304 sulfides.** Pentlandite inherits the majority of siderophile trace elements during metamorphism from etrologic type 3 to 5. Intermediate MSS and pyrrhotite hold variable concentrations of trace elements in type 3 sulfides, but partition into pentlandite by type 5. Pentlandite-pyrrhotite averages usually fall close to CI ratios, indicating that most siderophile elements are contained primarily within sulfides. However, Ir/Ni ratios are slightly subchondritic and Pt/Ni are strongly subchondritic. These depletions in Ir and Pt may be accounted for with discrete platinum-group alloys that are often associated with sulfides. Additional siderophile element scatter plots are presented in Fig. S3.3 in supporting information.

**Table 3.5.** Average trace element concentrations in LAP 04840 sulfides and oxides.

| | | Pentlandite | Pyrrhotite/MSS | Magnetite |
|---|---|---|---|---|
| | n= | 6 | 24 | 14 |
| Fe | (wt%) | 34 | 60 | 55 |
| Co | | 6584 | 3321 | 204 |
| Ni | (wt%) | 19.4 | 7.95 | 0.34 |
| Cu | | 1224 | 1296 | 20 |
| Zn | | 20 | 4.7 | 1659 |
| Ga | | 1.2 | 0.15 | 125 |
| Ge | | b.d.l. | b.d.l. | 8.8 |
| As | | 12 | 16 | 1.1 |
| Se | | 26 | 50 | 21 |
| Mo | | 4.9 | 8.6 | 1.7 |
| Ru | | 3.2 | 5.6 | 0.64 |
| Rh | | 0.52 | 1.1 | 0.09 |
| Pd | | 24 | 0.14 | 0.02 |
| Sn | | 5.5 | 1.0 | 7.8 |
| Sb | | 0.04 | 0.02 | 0.08 |
| Te | | 7.0 | 20 | 0.59 |
| W | | 0.02 | 0.04 | 0.57 |
| Re | | 0.16 | 0.50 | 0.01 |
| Os | | 2.8 | 4.0 | 1.3 |
| Ir | | 2.0 | 3.8 | 0.83 |
| Pt | | 1.1 | 0.02 | 1.1 |
| Au | | 0.10 | 1.2 | 0.16 |

In ppm unless otherwise noted.

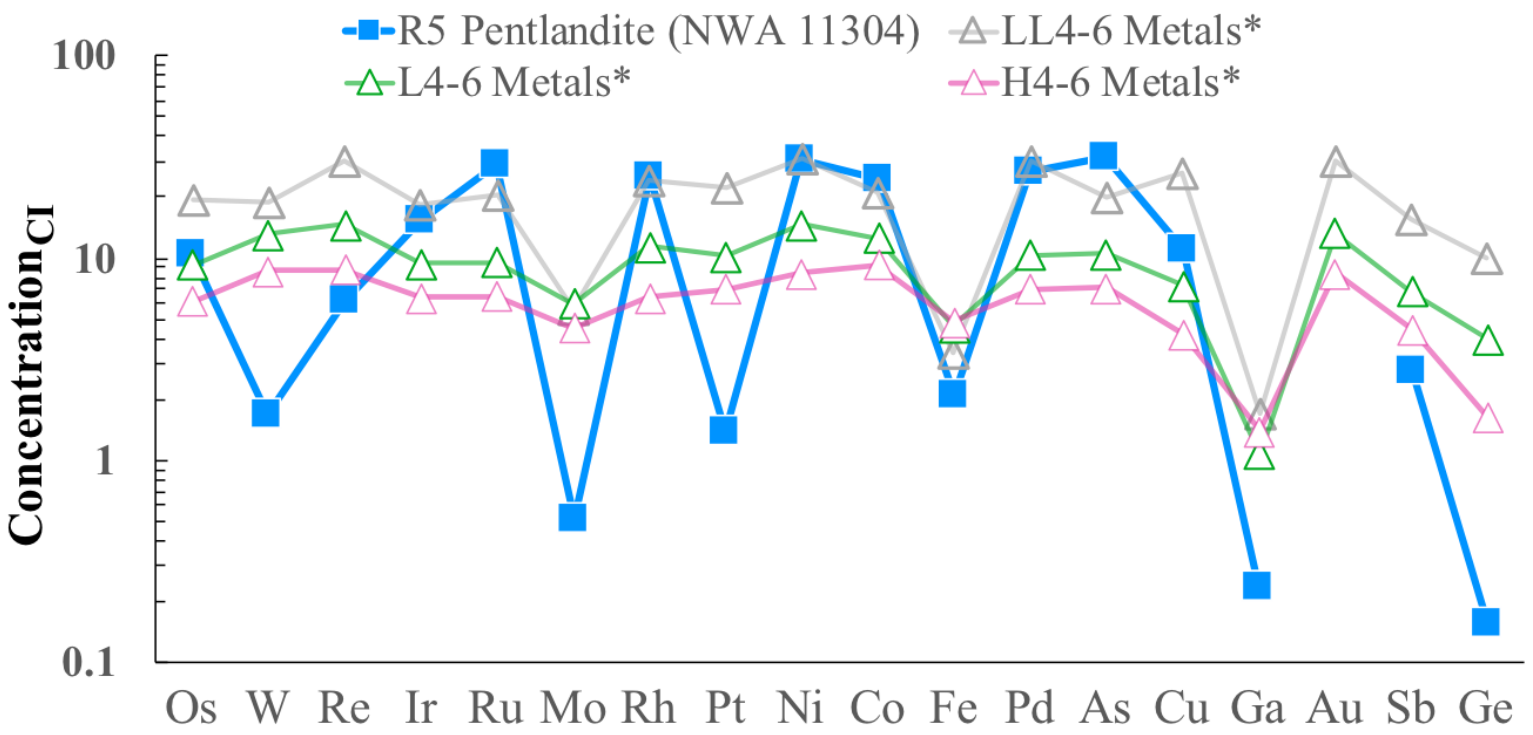

**Fig. 3.6.** Average CI-normalized siderophile element concentrations in equilibrated R chondrite pentlandite and OC metals. Equilibrated pentlandite in NWA 11304 holds superchondritic abundances of most siderophile elements but with interelement ratios that are distinct from OC metals. Pentlandite is comparatively depleted by at least an order of magnitude with regard to W, Mo, and Pt. Lesser relative depletions include Ga, Sb, and Ge. Re and Au depletions may be related to terrestrial weathering (Isa et al., 2014), although NWA 11304 is only moderately weathered (W2; Gattacceca et al., 2020). Uncertainties for metal averages are <5% based on counting statistics (data marked with * are from Kong & Ebihara, 1996), and uncertainties for individual R chondrite measurements are smaller than their symbols. CI normalization from McDonough & Sun (1995).

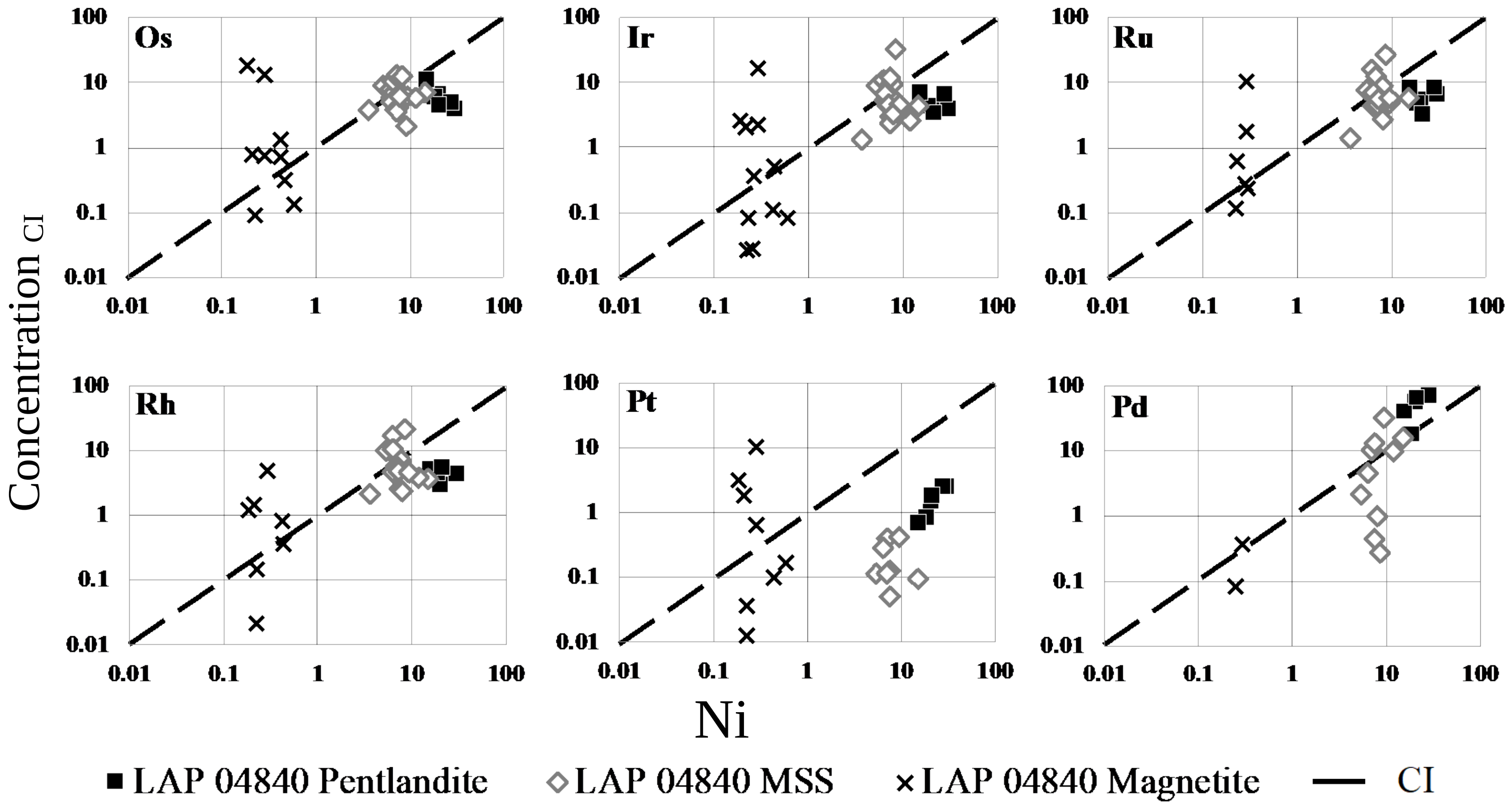

**Fig. 3.7.** Diagrams of Ni vs HSEs in hydrothermally altered LAP 04840 sulfides and oxides**.**
Trace elements partition distinctly during hydrothermal alteration when compared to anhydrous NWA 11304. The variable and high concentrations of HSEs in magnetite are most likely due to oxidation of sulfides during hydrothermal alteration, which fueled the rapid growth of magnetite and distrupted equilibrium between pentlandite and pyrrhotite. As a consequence, siderophile trace elements are distributed between the pentlandite and MSS in roughly equal proportions.

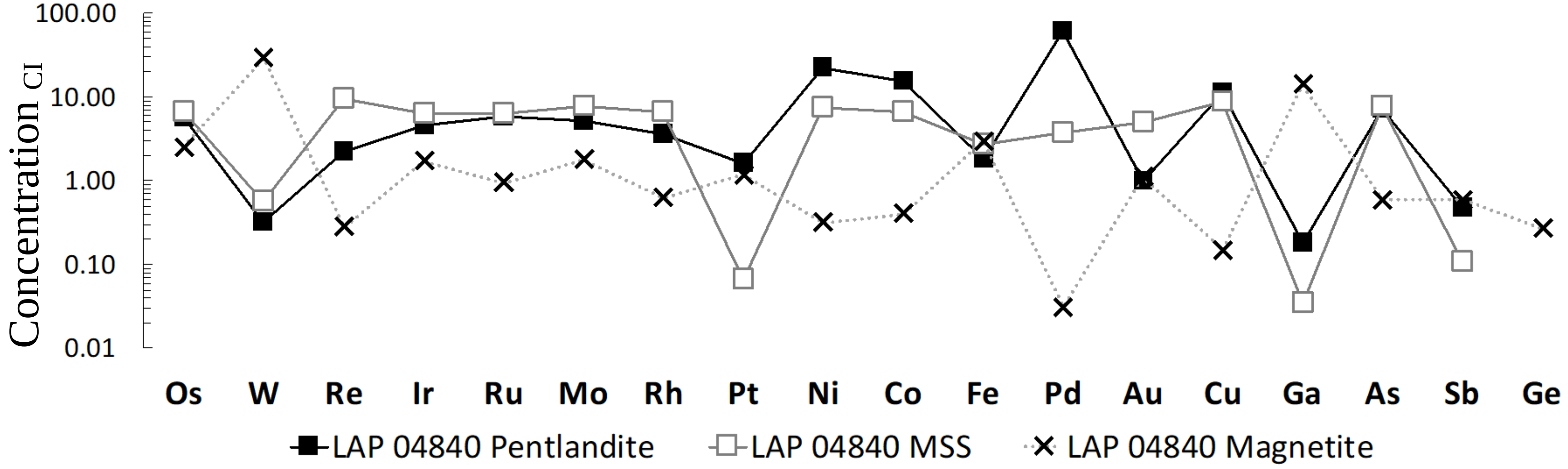

**Fig. 3.8.** Average CI-normalized siderophile element concentrations in LAP 04840 sulfides and magnetite.
In contrast to NWA 11304, siderophile elements are generally even distributed between pentlandite and pyrrhotite with the exception of Pt and Pd. Magnetite holds roughly chondritic abundances of most siderophile elements on average, but contains superchondritic average W concentrations, likely due the highly oxidized nature of LAP 04840.

### *3.3.4 Siderophile trace element concentrations in LAP 04840 magnetite*

Average siderophile trace element concentrations in LAP 04840 magnetite range from subchondritic (0.03x CI) to >20x CI (Table 3.5, Fig. 3.8) but are highly variable among individual measurements (Fig. 3.7). On average, most siderophile elements are present in roughly chondritic concentrations with several notable exceptions. Highly siderophile elements Re, Os, Ir, Ru, Pt, Rh, and Au are roughly chondritic (0.3-2.5x CI), while Pd is subchondritic (0.03x CI). Average concentrations of moderately siderophile elements range from subchondritic Cu (0.15x CI) to strongly superchondritic Ga and W (14 and 29x CI, respectively). Concentrations of W in magnetite span over 4 orders of magnitude, resulting in average W concentrations that are ~100x greater than coexisting sulfides (Fig. S3.4).

## *3.4 Discussion*

### *3.4.1 Metamorphism*

Most siderophile elements follow a weak trend from subchondritic concentrations in pyrrhotite to superchondritic concentrations in pentlandite with intermediate trace element concentrations in MSS (Fig. 3.5). As pentlandite and pyrrhotite exsolve from MSS, coarsen, and approach equilibrium from petrologic types 3 and 4 to type 5, trace element concentrations homogenize in each sulfide phase, preferentially partitioning into pentlandite over pyrrhotite.

While the majority of siderophile elements in R chondrites partition into pentlandite in proportions similar to OC metals (e.g., Kong and Ebihara, 1996; Campbell and Humayun, 2003), some trace elements defy their typical mineralogic affinities and/or volatilities based on nebular condensation temperatures (e.g., Lodders et al., 2003; Wood et al., 2019), indicating that siderophile trace element systematics in oxidized, sulfide-dominated Fe-Ni-S systems involve distinct geochemical mechanisms that deviate from metal-dominated counterparts.

### *Anomalous highly siderophile element behaviors*

Within sulfides, CI-normalized Pt concentrations are depleted by an order of magnitude relative to Os, Ir, Ru, Rh, and Pd (Fig. 3.6). Fractionation of Pt relative to other HSEs cannot be explained through nebular fractionation via evaporation or condensation (Lodders et al., 2003) nor through typical igneous fractionation on the parent body (e.g., Chabot and Jones, 2003; Day et al., 2012, 2016; Walker, 2016). Bulk measurements for other R chondrites, in contrast, have found chondritic concentrations of Pt (Isa et al., 2014). In NWA 11304, discrete Pt-rich arsenides, sulfarsenides, and other alloys (1-10 µm) are often found in association with sulfides in clasts of all petrologic types, and Pt metals are found in sulfides, chondrules, and among matrix assemblages. These phases can explain the Pt depletions among sulfides and account for chondritic bulk compositions. Based on their mineralogic associations in NWA 11304, platinum-group metals are consistent with products of nebular condensation (e.g., Wood et al., 2019) that were incorporated into the R chondrite parent body during accretion. Sperrylite, platarsite, irarsite (IrAsS) and other noble metal alloys found in NWA 11304 are not phases predicted to condense from the solar nebula, but instead probably crystallized directly from sulfides melted during chondrule formation (Helmy et al., 2013; Helmy and Bragagni, 2017; Miller et al., 2017). Throughout subsequent metamorphism, these phases may continue to grow as Pt and other siderophile elements diffuse from the surrounding sulfides, resulting in growth of platinum group element (PGE)-rich phases up to the largest (~10 µm) grain of niggliite (PtSn) observed in the type 5 clast of NWA 11304.

Gold is virtually absent from most sulfides in NWA 11304. Previous work has identified a correlation between gold and weathering grade (Isa et al., 2014), which may imply that trace element concentrations within sulfides in NWA 11304 have been subjected to terrestrial alteration. However, this stands in contrast to the observed low weathering grade of NWA 11304 sulfides. Small (~1 µm) noble metal grains that are rich in Au, Ag, and Fe are identifiable via EDS in the petrologic type 5 clast. These grains probably formed due to incompatibility with pyrrhotite and pentlandite during exsolution from liquid MSS, similar to the petrogenesis of noble metal grains in terrestrial massive sulfide ores (e.g., Barnes et al., 2006).

### *Redox-controlled moderately siderophile element distribution*

The high $fO_2$ of R chondrites is reflected by the redox-sensitive moderately siderophile trace element (i.e., W and Mo) concentrations in sulfides and oxides. Average concentrations of W in NWA 11304 pentlandite are depleted relative to other refractory siderophile elements and compared to concentrations in ordinary chondrite metals (Fig. 3.6). W/Os ratios decrease inversely with redox state from metals in H, L, and LL to R chondrite sulfides (W/Os= 1.4, 1.4, 0.96, and 0.17, respectively). The equal distribution of W among R chondrite sulfides and silicates are consistent equilibration near W-$WO_2$ oxidation buffer, which coincides with the IW buffer up to ~1400°C at 1 bar (O’Neill & Pownceby, 1993) and is at the less oxidized end of the R chondrite $fO_2$ range (Righter and Neff, 2007). Similarly, the subchondritic average concentration of Mo in type 5 pentlandite follows an oxidation trend from OC metals to R chondrite sulfides where Mo/Ru decreases in sequence from H, L, LL (0.70, 0.63, and 0.27, respectively; Kong & Ebihara, 1996), to R $_{\text{Mo/Ru}}$ = 0.02 in NWA 11304. Mo exists primarily in both the $Mo^{4+}$ and $Mo^{6+}$ valence states with minimal contribution of $Mo^0$ near the IW oxidation buffer (Hillgren, 1991; Holzeid et al., 1994).

*Comparison to ordinary chondrites*

Siderophile element systematics among sulfides during R chondrite metamorphism share some similarities with observations for ordinary chondrite metals. Some variability in trace element concentrations remains among individual grains even at high petrologic type (Figs. 3.5 and 3.7; Gilmour and Herd, 2020), indicating that equilibration of siderophile elements is localized within individual grains. However, the two processes deviate regarding the primary carrier phases of siderophile elements: pentlandite in R chondrite NWA 11304 ($K_d^{pn/po}$ ~2-500) versus both kamacite and taenite in ordinary chondrites ($K_d^{T\text{-}K}$ ~1-7; Gilmour and Herd, 2020). The high concentrations of siderophile elements in R chondrite pentlandite are consistent with formation of chondritic sulfides through the sulfidation of nebular Fe,Ni metal (Kerridge, 1976; Lauretta et al., 1998).

### 3.4.2 Hydrothermal alteration

The high $Cr_2O_3$ content in LAP 04840 magnetite could indicate that it formed after hydrothermal alteration of chromite, similar to what has been observed in some terrestrial hydrothermal systems (e.g., Holwell et al., 2017). Magnetite growth would have been further fueled through oxidation of Fe-sulfides during hydrothermal alteration. The magnetite-sulfide assemblages in LAP 04840 bear fine-scale exsolution lamellae of pentlandite in MSS (Fig. 3.4b) that are the consistent with late-stage oxidation seen in terrestrial Fe-sulfides during hydrothermal alteration (e.g., Terranova et al., 2018). This scenario is viable for LAP 04840 if the oxidizing hydrothermal fluid was introduced while the precursor was still hot (McCanta et al., 2008) and had already formed some amount of chromite through metamorphism (Isa et al., 2014). Higher oxidation state also accounts for the higher Ni concentrations of LAP 04840 sulfides and silicates (McCanta et al., 2008) relative to those in NWA 11304 (e.g., Kerridge, 1976). As Fe in sulfides oxidized to $Fe^{2+}$ and $Fe^{3+}$, the residual sulfide assemblage became more Ni-rich, exsolving pentlandite lamellae from Ni-rich MSS during retrograde metamorphism as temperatures decreased.

In contrast to NWA 11304, LAP 04840 siderophile elements are present in roughly equal concentrations between pyrrhotite/MSS and pentlandite. Magnetite also contains variable concentrations of siderophile trace elements that can span several orders of magnitude (Fig. 3.7). The variably high concentrations of siderophile elements in magnetite grains and equal distributions of trace elements between pentlandite and pyrrhotite, are consistent with magnetite growth from the oxidation of sulfides. Given the positive correlation between Ni and siderophile trace element concentrations in sulfides, Ni-rich MSS and pentlandite are both capable of hosting superchondritic concentrations of siderophile elements.

### *3.4.3 Implications for core formation*

The anion/cation ratios (S:Fe,Co,Ni,Zn,Cu) of R chondrite pentlandite (0.90) and pentlandite/pyrrhotite mixtures (0.99) from this study approach the experimental parameters that result in grain boundary wetting during melting of sulfides (Gaetani and Grove, 1999; Brenan and Rose, 2001). For bodies that are similarly oxidized (IW to FMQ) and sulfidized (i.e., $fS_2$ > iron-troilite), sulfide melt migration is further facilitated by decreased surface tension and viscosity of sulfide melts (Mungall and Su, 2005; Iida and Guthrie, 2015). Liquid sulfide can segregate from silicate residues via capillary action at temperatures as low as the pentlandite-pyrrhotite eutectic (865°C; Kitakaze et al., 2016), prior to the silicate eutectic for R chondrites (1020-1050°C; Tomkins et al., 2020). This stands in contrast to models of metal-silicate segregation, which is inhibited by the physical properties of metal-rich melts in solid silicate residues until extensive silicate melting has occurred at temperatures greater than 1100°C (Fig. 3.9; Kushiro and Mysen, 1979; Takashi, 1983; McCoy et al., 2006). If the composition of the segregated sulfide liquid is dominated by pentlandite, an oxidized and sulfur-rich body can still crystallize a small, Ni-rich (50-60 wt %, i.e., awaruite) metal fraction (10-20 vol%; Kitakaze et al., 2016) in equilibrium with sulfide liquid.

### *Consequences for core formation ages*

Due to its high oxygen fugacity, approximately 90% of W resides in the silicates of NWA 11304 by petrologic type 5 (Table S3.6). For similarly oxidized materials, this has potential implications for ages calculated from the Hf-W isotopic system, which rely upon the siderophile affinity of W in $fO_2$ environments below

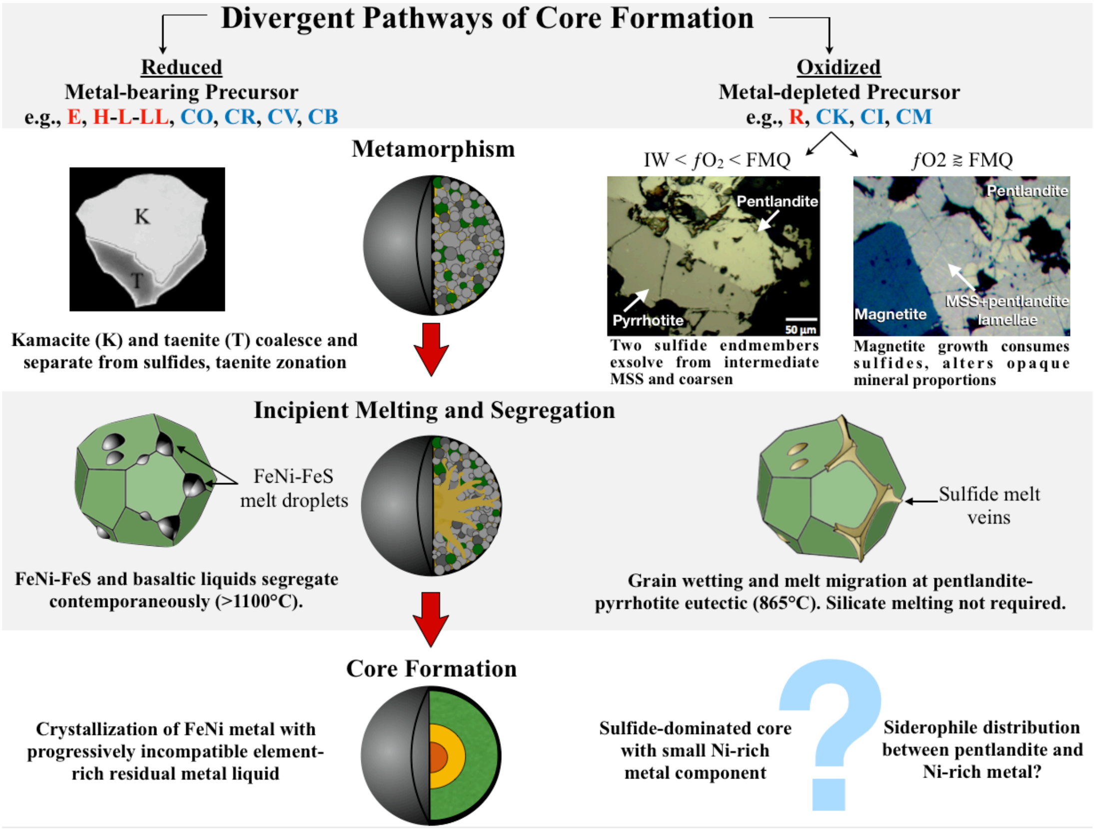

**Fig. 3.9. Schematic of redox-based differentiation pathways.**
Prior to melting, sulfide-dominated opaque assemblages coarsen and exsolve into pentlandite and pyrrhotite endmembers, although equilibria between the two sulfides may be disrupted by magnetite growth during hydrothermal alteration. In contast to metallic liquids in reduced systemas, the anion/cation ratios of sulfide assemblages at high $fO_2$ permit the propagation of sulfide liquids via grain wetting prior to silicate melting. The observed distribution of siderophile elements between sulfide phases can be used to establish starting compositions for melting experiments to investigate the potential for sulfide-dominated core formation on oxidized parent bodies and search for potentially related iron meteorites via characteristic trace element abundances. Chondritic precursor examples are colored according to their isotopic grouping (blue = carbonaceous, red = noncarbonaceous), and demonstrate that oxidation state is not universally correlated with isotopic grouping. BSE image of a metal grain in the Guarana (H6) ordinary chondrite adapted from Reisener and Goldstein (2003). FeNi-FeS melting temperature and diagram for incipient melting of metal adapted from McCoy et al. (2006).

IW-1 ($D_W^{metal\text{-}silicate}$ = 2-600; Schmitt et al., 1989). Even for the comparatively reduced H chondrites (~IW-2; Kessel et al., 2004), Hf-W isotopic measurements yield disparate ages for metal and nonmetal fractions, interpreted as the result of a small fraction of W in silicates due perhaps to closure temperature effects or disequilibrium between metal and matrix phases (Archer et al., 2019). In highly oxidized, sulfur-rich chondrites that formed at or above the iron-wüstite oxidation buffer, such complications with age calculations would be further exacerbated by the high concentration of W in silicates. A large excess $^{182}$W may not develop in the silicate fraction due to high concentrations of W, resulting in age estimates for core-mantle segregation that are too old for the differentiated silicate fractions. Similarly, the retention of radiogenic $^{182}$W in silicates could result in erroneously young age calculations for metals that crystallized from FeNiS melts. Some of these complexities may be mitigated with Hf-W isotopic measurements for R chondrites that demonstrate the initial distribution of W isotopes between sulfides and other phases prior to melting, similar to recent measurements reported for H chondrites (e.g., Archer et al., 2019).

### *Melting of sulfide-magnetite assemblages*

If LAP 04840 was hydrothermally altered as a result of impact mixing (McCanta et al., 2008), then the effects of hydrothermal alteration on its opaque mineral assemblage would not be directly applicable to core formation because the parent body was disrupted prior to differentiation. However, evidence for hydrothermal alteration of R chondrites is limited to petrologic type R6 samples (Gattacceca et al., 2020). In the impact mixing scenario, evidence of hydrothermal alteration should be independent of petrologic type. Thus, the possibility remains that hydrothermal alteration is a thermally-regulated process that only affected highly metamorphosed regions of the R chondrite parent body. Regardless of the source of hydrothermal fluid, the oxidation of Fe,Ni sulfides to magnetite further disturbs the distribution of siderophile elements early in the process of differentiation by increasing the Ni concentration in MSS. Given the range of reported $fO_2$ for R chondrites from IW-1 to IW+3.5 (~FMQ; Righter and Neff, 2007; McCanta et al., 2008; Righter et al., 2016), a coordinated analysis of oxygen fugacities and sulfide/oxide ratios across the R chondrite group would help to quantify the range of initial $fO_2$ conditions and the effects on opaque mineral proportions and their siderophile trace element systematics.

### *Meteoritic evidence for oxidized, sulfide-dominated core formation*

Trace element concentrations within the sulfides of the most oxidized primitive achondrites, i.e., brachinites, are consistent with loss of a FeNiS liquid (Nehru et al., 1983; Crossley et al., 2020). Currently, there are no sulfide-dominated meteorites reported in the Meteoritical Bulletin (Gattacceca et al., 2020) akin to a proposed FeNiS core. However, anomalous Ni-rich iron meteorites like Oktibbeha County may be derived from the minor metal fraction that can crystallize from S-rich FeNiS liquids (Wasson et al., 1980), whereas the corresponding solidified sulfides did not survive, perhaps due to mechanical weakness (Kracher and Wasson, 1982).

The products of oxidized, sulfur-rich core formation may be identified among the meteoritic record, akin to how magmatic iron meteorites sample the cores of planetary embryos (e.g., Haack and McCoy, 2004). If Ni-rich irons like Oktibbeha

County are products of highly oxidized, sulfide-dominated core formation, their trace element chemistries must be reflective of the parent sulfide liquids. In contrast to typical HSE partitioning between liquid and solid Fe,Ni metal (e.g., Malvin et al., 1986; Chabot and Jones, 2003; Walker, 2016), if HSEs fractionate into melting pentlandite, an R chondrite-like precursor would lose effectively all of its HSE content to the first melts produced at 865°C. After segregation of a pentlandite melt, siderophile trace elements would continue to follow Ni during the crystallization of awaruite (~$Fe_{0.4}Ni_{0.6}$) from sulfide liquids. Consequently, Ni-rich metals formed via this process would contain superchondritic concentrations of HSEs. Given the incompatibilities of Au and Pt with exsolving pentlandite and pyrrhotite (e.g., Barnes et al., 2006), awaruite would be correspondingly enriched in these elements relative to other HSEs. Depletions in redox-sensitive W and Mo relative to other MSEs would also be characteristic of awaruite crystallization from a highly oxidized, sulfide-dominated liquid, as these elements would be sequestered in silicate phases during liquid sulfide segregation.

### *3.4.4 Application to upcoming NASA missions*

NASA's Psyche mission is planned to launch in 2022 and will orbit the M-type asteroid 16 Psyche in 2026. Once believed to be an exposed metallic planetary core, recent density estimates (3.4-4.1 g/cm$^3$) fall below the densities of FeNi metals (~8 g/cm$^3$; Smyth and McCormick, 1995), requiring alternative explanations for its formation (Elkins-Tanton et al., 2020). Fe,Ni sulfides have densities (4-5 g/cm$^3$) that are much closer to estimates for 16 Psyche. The possibility that 16 Psyche is a core that is composed primarily of sulfides rather than metals should be included among potential explanations for its comparatively low estimated density (Elkins-Tanton et al., 2020) and high radar albedo measurements (e.g., Shepard et al., 2017).

Generally, oxidized bodies are assumed to produce smaller cores than reduced counterparts, as the oxidation of Fe metal to FeO leads to enhanced Fe incorporation into silicates, which decreases the volume of iron available to participate in core formation (e.g, Rubie et al., 2015). However, the highly oxidized, sulfur-rich R chondrites contain 5-8 vol% sulfides (Bischoff et al., 2011), similar to the proportions of metals in L and LL chondrites (e.g., Jarosewich, 1990). Thus, Psyche could be a sulfide-dominated core if it formed through efficient segregation of 8 vol% sulfides from an R chondrite-like precursor with a minimum diameter of ~560 km (Table S3.7). The addition of 10 vol% silicates and < 15 vol% void space would fully account for Psyche's low bulk density.

The Psyche mission will evaluate whether 16 Psyche's surface is consistent with an oxidized, sulfide-dominated core via the onboard gamma ray and neutron spectrometer, which will be capable of measuring average Fe, Ni, and S concentrations. Equilibrium Fe-Ni-S phase diagrams (Fig. 3.10) show that the phases crystallizing from a FeNiS liquid at temperatures below 865°C will be a mixture of pentlandite and awaruite ($Fe_{0.4}Ni_{0.6}$) ± MSS (Kitakaze et al., 2016). Fe/Ni ratios for the segregated sulfide liquid and its major components (awaruite and pentlandite) are $\leq 1$, whereas Fe/Ni ratios of metal/troilite assemblages and potential immiscible sulfide liquids are $>1$ in more reduced magmatic irons (e.g., Goldstein et al., 2009).

## *3.5 Conclusions*

Sulfide-dominated core forming components in oxidized chondrites ($f\mathrm{O}_2 \geq$ IW) follow metamorphic pathways that are distinct from reduced, metal-bearing counterparts. While metamorphic alterations of R chondrite sulfides share some textural and geochemical affinities with ordinary chondrite metals, the melts generated from oxidized sulfides can migrate more readily. In addition, the behaviors of several key siderophile trace elements among oxidized sulfides deviate from reduced metallic systems, which lead to compositionally distinct products of oxidized, sulfide-dominated core formation that can be identified in meteorites and asteroids.

In summary, specific conclusions from this work include:

- R chondrite sulfide assemblages coarsen and exsolve into pentlandite and pyrrhotite endmembers by petrologic type 5 in a process analogous to the metamorphism of metal and sulfide assemblages in ordinary chondrites.
- The low melting temperature of pentlandite and the wetting properties of sulfide liquids result in core formation in oxidized, S-rich parent bodies at lower temperatures (865-1150°C) before the onset of silicate melting.
- Siderophile trace element concentrations in R chondrite pentlandite are typically superchondritic (~10x CI), but W, Mo, Pt, Ga, and Ge are depleted by factors of 2-25 relative to elements with similar volatilities. Platinum forms discrete arsenide and sulfarsenide phases, while the remaining W, Mo, Ga, and Ge partition into silicates and oxides. The complexity of HSE systematics among oxidized sulfides stands in contrast to their typical partitioning behaviors among metals.

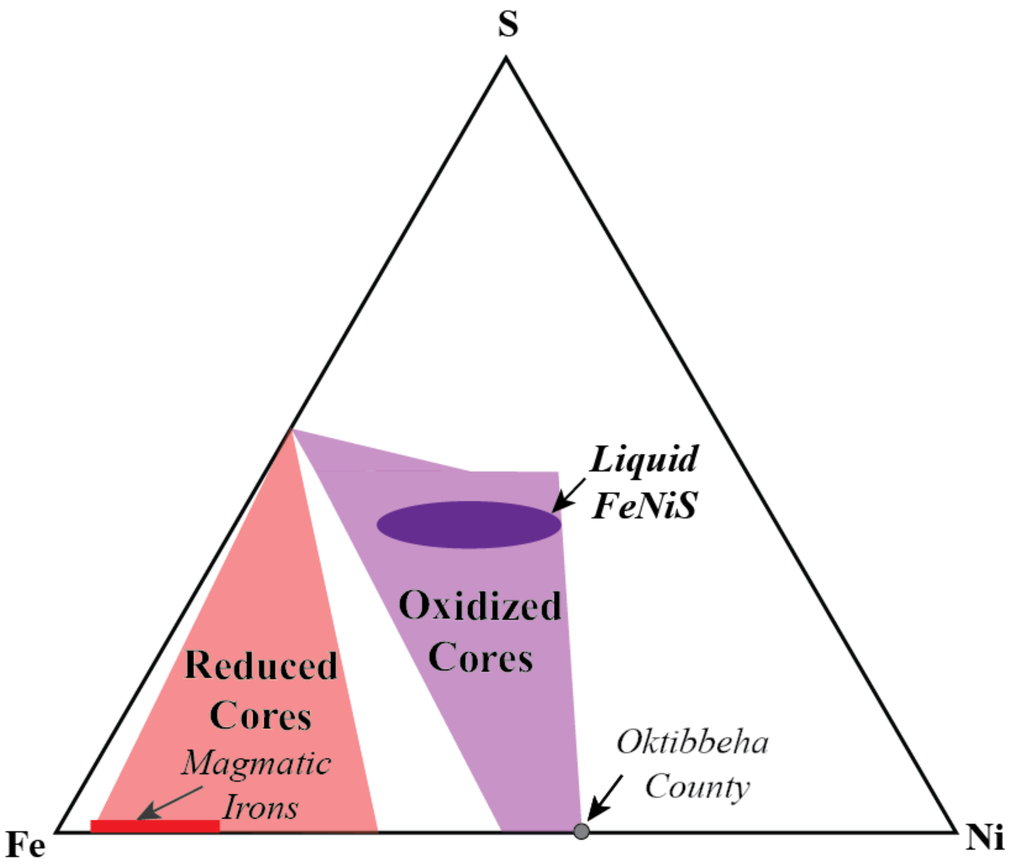

**Fig. 3.10. Fe-Ni-S ternary for oxidized and reduced cores.**
The red field is the compositional range for components of reduced cores and the purple field represents compositions that can crystallize from FeNiS liquid. The liquid FeNiS produced at 875°C in oxidized assemblages crystallizes pentlandite, MSS, Ni-rich metals (Ni wt% 55-60), whereas reduced bodies can only crystallize Ni-poor MSS and metals with Ni concentrations up to 36 wt%. The gamma ray and neutron spectrometer on NASA's Psyche spacecraft will analyze Fe, Ni, and S. If asteroid 16-Psyche has a Fe/Ni ratio of < 1, that would provide strong evidence that it is the core of a highly oxidized and sulfur-rich parent body. Magmatic iron compositions are bulk values for grouped irons in Goldstein et al. (2009). Oktibbeha County is from Wasson et al. (1980).

- The sulfide cores of oxidized, sulfur-rich parent bodies would reflect Mo, W, Ga, and Ge depletions of their precursor sulfides, and Ni-rich metals that crystallize within them. These metal fractions may be represented by anomalous iron meteorites like Oktibbeha County.
- The sequestering of W into silicate fractions can result in erroneously young isotopic age calculations for silicate assemblages and overestimates of ages for the core forming fraction on the order of millions of years in highly oxidized parent bodies.
- Calculated densities for asteroid 16 Psyche are much closer to the densities of sulfides than to densities of Fe,Ni metals. The Psyche mission's gamma ray and neutron spectrometer will be able to measure a suite of elements that includes Fe, Ni, and S. Fe/Ni ratios $\leq 1$ would provide strong evidence that Psyche is an oxidized, sulfide-dominated core.

# Chapter 4: Petrologic Interpretations of Olivine-dominated Asteroids

Samuel D. Crossley*[1], Jessica M. Sunshine[1], Richard D. Ash[1], Timothy J. McCoy[2], and Catherine M. Corrigan[2]

*Corresponding author: sdcross@umd.edu
[1]Department of Geology, University of Maryland, College Park, MD, 20742
[2]Department of Mineral Sciences, Smithsonian Institution NMNH, Washington DC

We would like to thank Ashley King for conducting XRD analyses and providing results for this chapter. We also gratefully acknowledge Takahiro Hiroi for collecting high resolution spectral measurements of meteorite powders used in this chapter.

*Abstract*

Meteorites record a wide range of nebular oxidation conditions that strongly influence mineralogies, mineral chemistries, and petrologic evolution. The populations of these materials are inherently biased toward those that intercept Earth's orbit, survive atmospheric entry, and are subsequently recovered. Asteroids provide an opportunity to investigate the sources of these materials, as well as a larger population of planetary materials that may not be sampled among known meteorites.

This work utilizes diagnostic spectral properties of olivine and pyroxene in visual to near-infrared reflectance spectra to remotely interpret the relative oxidation states of olivine-dominated asteroids and infer their petrogenetic histories based on findings for brachinite family meteorites using the same toolset. In doing so, this work is the first to successfully apply modified gaussian models (MGM) to fit discontinuous spectral data and olivine-dominated spectra with minor pyroxene, which effectively doubles the number of interpretable olivine-dominated asteroids.

Olivine-dominated asteroids have interpreted oxidation states from $fO_2$ ~IW-2 up to and possibly exceeding FMQ. They include both primitive (i.e., chondritic) and

differentiated parent bodies. Most of the olivine-dominated asteroids in the main belt have spectral characteristics consistent with relatively oxidized meteorites (>IW-1). Among these are several asteroids whose inferred compositions and mineralogies are consistent with thermodynamic predictions for oxidized restites. The largest of these asteroids, 354 Eleonora, could represent the mantle of a body that underwent oxidized, sulfide-dominated core formation. The dominance of oxidized olivine over reduced olivine among asteroids at first appears at odds with the meteoritic record, which is dominated by comparatively reduced materials. However, the dearth of reduced restitic asteroids is probably due to petrologic limitations for the types of parent bodies that can form large, isolated olivine domains: reduced assemblages require larger bodies to reach and sustain the high temperatures required for melting and segregating pyroxene and metal from olivine, but oxidized parent bodies have much initial higher olivine/pyroxene ratios, and thus can form ferroan olivine-dominated mineralogies at much lower degrees of melting on smaller parent bodies. Consequently, A-type asteroid taxonomy is biased toward oxidized endmembers. Regardless, the findings of this work demonstrate that oxidized differentiation likely occurred on multiple bodies throughout asteroid belt, and may have been a common event in early Solar System history.

## *4.1 Introduction*

As discussed in Chapter 1, the formation of the protoplanetary disk is predicted to have established a compositional gradient wherein the abundance of volatile phases (e.g., water ice) increased with heliocentric distance (e.g., Grossman et al., 2008; Pontopiddian et al., 2014). Meteorites record evidence that much of the water ice accreted into asteroids was consumed during subsequent parent body alteration (e.g., Brearley et al., 2006), hydrating and/or oxidizing mineralogy and altering subsequent petrologic evolution. Chapters 2 and 3 provide evidence that chondrites and primitive achondrites record a range of redox ($fO_2$) conditions that are correlated with silicate and opaque mineral chemistries and modal abundances. The observed trends of increasing silicate FeO content and olivine/pyroxene ratios coincides with $fO_2$ calculations for other equilibrated meteorite groups from ~IW-6 to IW+3 (FMQ) (Righter et al., 2016) until FeO oxidizes to $Fe_2O_3$ and begins to form magnetite at the expense of FeO in silicates (e.g., Righter and Neff, 2007). If these mineralogic changes can be observed among asteroids, they can be used as proxies for determining the relative oxidation state of asteroids, their petrogenetic histories, and the populations of these materials. Such information can provide much needed context for meteorite origins and lend insight into the representativeness of the meteoritic record by comparison with asteroid populations.

### *Remote Interpretation of Olivine Composition*

Interpreting the redox state of asteroids requires an approach that can remotely infer mineralogy and olivine FeO content as a proxy for $fO_2$. Olivine is remotely resolvable using visual to near-infrared (VNIR) reflectance spectroscopy as a complex absorption feature centered at ~1 µm that is composed of three overlapping absorption bands caused by $Fe^{2+}$ in the M1 and M2 cation sites (e.g., Burns, 1970). The individual absorption band characteristics can be used to determine composition using Modified Gaussian Models (MGM) to deconvolve the olivine spectral complex (Sunshine et al., 1990, 1993, 2007).

Increasing amounts of $Fe^{2+}$ in the M1 and M2 cation sites of olivine distort its crystal lattice, systematically driving the three absorption band centers toward longer wavelengths (Burns, 1970). The relative intensities, or band strength ratios, of olivine also change predictably with $Fe^{2+}$ content, as $Fe^{2+}$ partitions preferentially into the M1 site with increasing concentrations, causing the strengths of the two M1 bands at ~0.85 and 1.20 µm to deepen relative to the M2 band at 1.05 µm (e.g., Sunshine et al., 1993). Olivine strength ratios therefore place additional constraints on the interpretation FeO content from olivine spectra. Utilizing olivine band centers and strength ratios together can provide a powerful, self-consistent tool for remotely interpreting olivine composition.

The M1/M2 band strength ratios can be further altered by temperature (Burns, 1970). Sunshine et al. (2007) demonstrated how temperature differences between laboratory (300 K) and main belt (170 K) environments can mimic different Fa contents by increasing band strength ratios with higher temperatures. As a consequence, care must be taken when comparing laboratory spectra with asteroids in the main belt (Sunshine et al., 2007). Once surface temperature has been accounted for, olivine Fa content can be remotely interpreted from its band centers and band strength ratios (Sunshine et al., 1993; 2007) and used to infer relative oxidation state.

Olivine-dominated asteroids are particularly well suited to such an investigation because there are limited pathways through which an olivine-dominated assemblage can form at asteroidal scale, i.e., as oxidized chondrites or as mantle restites after partial melting. These pathways are further constrained by the Fa content of olivine, as demonstrated with thermodynamic models simulating partial melting of chondrites, wherein Fa content and pyroxene abundances decrease with progressive melting (e.g., Sunshine et al., 2007; Tomkins et al., 2020). MGM solutions for 9 olivine-dominated, A-type, asteroid spectra found that the majority of these materials to be magnesian (< $Fa_{20}$), and therefore are likely residues after partial melting of an ordinary chondrite-like precursor (Sunshine et al., 2007), corresponding to $fO_2$ of approximately IW-2 or lower (e.g., Righter et al., 2016). The remaining asteroids possess spectral characteristics indicative of more fayalitic olivine ($Fa_{60-80}$), consistent with brachinite and R chondrite meteorites that range from $fO_2$ ~IW-1 to IW. Subsequently, Sanchez et al. (2014) used continuum-normalized absorption maxima wavelengths of the 1 µm olivine complex (after Reddy et al., 2011) for A-type asteroid spectra to interpret their olivine FeO content based on comparison with laboratory-based spectra of chondrites and primitive achondrites. In contrast to MGM-derived results, they found all monomineralic A-type asteroid spectra to be consistent with high FeO content ($Fo_{40-75}$) and concluded that these bodies most closely resembled brachinites and/or R chondrites. Since then, the number of observed A-type asteroids has more than doubled (DeMeo et al., 2019), providing an opportunity to better understand the population of oxidation environments in the main belt using olivine Fa content as a proxy for $fO_2$.

### *Olivine-dominated Asteroids with Minor Pyroxene*

One of the principal obstacles to estimating the Fa content of olivine-dominated asteroids is that many contain additional absorption features at ~2 µm, indicative of the presence of pyroxene. The corresponding 1 µm absorption of pyroxene overlaps the olivine complex at ~1 µm and complicates the interpretation of olivine Fa content from MGM fits of olivine (Sunshine et al., 1993, 2007). These features are similarly problematic for the absorption maxima approach, as the 1 µm band of pyroxene distorts the overall olivine complex and can shift its center to shorter or longer wavelengths depending on the proportions and composition of pyroxene (Sanchez et al., 2014). If pyroxene and olivine can be simultaneously deconvolved, they can provide further insights into olivine Fa content, pyroxene Fs content, and the relative proportion of pyroxene. This information is critical for interpreting oxidation states and petrogenetic histories amongst a greater population of olivine-dominated asteroids.

While the overlapping spectral features of olivine and pyroxene can complicate spectral interpretations, previous work with synthetic pyroxenes (Klima et al., 2007, 2011) and pyroxene mixtures (Sunshine and Pieters, 1998) can be used to place reasonable limits on parameters for pyroxene bands to facilitate MGM fitting. The two principal absorption features of pyroxene are centered at ~1 and 2 µm, but like olivine, they vary systematically with composition (e.g., Adams, 1974). The 1 µm absorption (band I) of pyroxene is caused by $Fe^{2+}$ in both M1 and M2 cation sites, while the 2 µm feature (band II) is produced by $Fe^{2+}$ in the M2 site (Burns, 1970). The centers of both bands I and II shift predictably to longer wavelengths with increasing $Fe^{2+}$ content (i.e., ferrosilite, Fs) and $Ca^{2+}$ content (i.e., wollastonite, Wo), and retain relatively consistent band strength ratios (1.62 ± 0.47) and band width ratios (0.43 ± 0.17) from $Fs_{5-90}$ and $Wo_{1-50}$ (Klima et al., 2007; 2011). These attributes can be factored into spectral model solutions to mitigate the complications associated with olivine-pyroxene assemblages.

This work expands on the MGM approach of Sunshine et al. (1993; 2007) to interpret the approximate Fa content of olivine-dominated asteroid spectra, as well as the relative abundance of pyroxene, thus placing constraints on their redox states and petrogenetic histories. Laboratory-based spectra of meteorites with known mineral compositions and modal mineralogies were collected and their Fa contents were calculated to demonstrate the efficacy of this method of interpreting olivine-dominated asteroids. The method is useful for interpreting the redox state and petrogeneses of olivine-dominated asteroids with minor pyroxene content, thus doubling the number of petrologically interpretable olivine-dominated asteroids from previous work.

### *Olivine-dominated Asteroids with Minor Pyroxene*

One of the principal obstacles to estimating the Fa content of olivine-dominated asteroids is that many contain additional absorption features at ~2 µm, indicative of the presence of pyroxene. The corresponding 1 µm absorption of pyroxene overlaps the olivine complex at ~1 µm and complicates the interpretation of olivine Fa content from MGM fits of olivine (Sunshine et al., 1993, 2007). These features are similarly problematic for the absorption maxima approach, as the 1 µm band of pyroxene distorts the overall olivine complex and can shift its center to shorter or longer wavelengths depending on the proportions and composition of pyroxene (Sanchez et al., 2014). If pyroxene and olivine can be simultaneously deconvolved, they can provide further insights into olivine Fa content, pyroxene Fs content, and the relative proportion of pyroxene. This information is critical for interpreting oxidation states and petrogenetic histories amongst a greater population of olivine-dominated asteroids.

While the overlapping spectral features of olivine and pyroxene can complicate spectral interpretations, previous work with synthetic pyroxenes (Klima et al., 2007, 2011) and pyroxene mixtures (Sunshine and Pieters, 1998) can be used to place limits on parameters for pyroxene bands to facilitate MGM fitting. The two principal absorption features of pyroxene are centered at ~1 and 2 µm, but like olivine, they vary systematically with composition (e.g., Adams, 1974). The 1 µm absorption (band I) of pyroxene is caused by $Fe^{2+}$ in both M1 and M2 cation sites, while the 2 µm feature (band II) is produced by $Fe^{2+}$ in the M2 site (Burns, 1970). The centers of both bands I and II shift predictably to longer wavelengths with increasing $Fe^{2+}$ content (i.e., ferrosilite, Fs) and $Ca^{2+}$ content (i.e., wollastonite, Wo), and retain relatively consistent band strength ratios (1.62 ± 0.47) and band width ratios (0.43 ± 0.17) from $Fs_{5-90}$ and $Wo_{1-50}$ (Klima et al., 2007; 2011). These attributes can be factored into spectral model solutions to mitigate the complications associated with olivine-pyroxene assemblages.

This work expands on the MGM approach of Sunshine et al. (1993; 2007) to interpret the approximate Fa content of olivine-dominated asteroid spectra, as well as the relative abundance of pyroxene, thus placing constraints on their redox states and petrogenetic histories. Laboratory-based spectra of meteorites with known mineral compositions and modal mineralogies were collected and their Fa contents were calculated to demonstrate the efficacy of this method of interpreting olivine-dominated asteroids. The method is useful for interpreting the redox state and petrogeneses of olivine-dominated asteroids with minor pyroxene content, thus doubling the number of petrologically interpretable olivine-dominated asteroids from previous work.

## *4.2 Methods*

### *4.2.1 Meteorite analogues*

To test the MGM parameters for olivine FeO content from Sunshine et al. (1993, 2007) and to extend this method to pyroxene-bearing samples, we collected samples and spectra of five members of the brachinite family achondrite meteorites. These samples are discussed in detail from petrographic analyses of thin sections described in Chapter 2 (Section 2.3.1). Two of these samples are considered reduced brachinites (~IW-2), and three are oxidized brachinites (IW-1). Table 4.1 summarizes the relevant mineral compositions, mineralogies, and sources for these materials.

The samples were ground in a mortar and pestle to < 45 µm grain size powders, and their reflectance spectra were collected with the bi-directional spectrometer at Brown University's Keck/NASA Reflectance Experiment Laboratory (RELAB; Pieters and Hiroi, 2004) at an incidence angle of 30°, an emergence angle of 0°, and with a spectral resolution of 5 nm from 0.45-2.60 µm. Mineral compositions were measured by electron microprobe analyses (EMPA) of corresponding thin sections, which are provided in Chapter 2 (Section 2.3.1).

Sample heterogeneity is an inherent risk when comparing thin sections of meteorites to bulk sections, as demonstrated by trace element inconsistencies between

**Table 4.1. Compositional and spectral data for brachinite family achondrites.**

| Sample Name<br>RELAB ID# | Reid 013 [4]<br>MT-JMS-344 | RaS 309 [5]<br>MT-JMS-345 | NWA 4882 [4]<br>MT-JMS-347 | NWA 7297 [6]<br>MT-JMS-346 | NWA 11756 [6]<br>MT-JMS-356 |
|---|---|---|---|---|---|
| Olivine (wt%)[1] | 93 | 91 | 95 | 95 | 81 |
| Fa (mol %)[2] | 35 | 35 | 34 | 31 | 27 |
| MGM Fa (mol %)[3] | **42** | **27** | **39** | **34** | **31** |
| LCP (wt%)[1] | 1 | 1 | 1 | 3 | 10 |
| Fs (mol %)[2] | 28 | n.d. | 27 | 25 | 22 |
| MGM Fs (mol %) | n/a | n/a | n/a | 25 | 25 |
| HCP (wt%)[1] | 6 | 5 | 1 | 1 | 6 |

All meteorite spectra measured at a resolution of 10 nm, incidence angle = 30°, and emergence angle = 0°. Particle sizes for samples are all < 45 µm.

[1] wt% from XRD analyses (this work)

[2] Crossley et al. (2020)

[3] Best fit MGM olivine solution after fitting pyroxene bands

Meteorite Sources: [4] Monnig Meteorite Collection, [5] Swiss Nat. Hist. Mus. Bern, [6] Ash Meteorite Collection brachinite thin sections and chips in Section 2.3.3 (Fig. 2.3). To ensure that interpretations brachinite spectra of were representative of bulk mineralogy and not biased toward thin sections, the modal mineralogies of meteorite powders were calculated via X-ray diffraction (XRD) at London Museum of Natural History. XRD patterns were collected with an INEL X-ray diffractometer with a curved 190 position-sensitive director (PSD) in a static geometry relative to the X-ray beam and sample powder at an incident angle of 4.2° relative to a rotating sample surface, following analytical procedures outlined in King et al. (2015). The duration of analyses was 16 h for each sample to ensure good signal-to-noise ratios. Peaks identified in XRD patterns were used to quantify modal abundance of minerals above 1 vol% with uncertainties from 1-4% for silicates. A more detailed outline of analytical procedures is provided in King et al. (2015).

### *4.2.2 Telescopic spectra of asteroids*

This work examines the telescopic spectra of 16 A-type, olivine-dominated asteroids, including the eight main belt A-type asteroids from Sunshine et al. (2007). Asteroid observational conditions are detailed in Sunshine et al. (2007), DeMeo et al. (2019), and references therein. Data sources for each asteroid and key observational conditions are summarized in Table 4.2. Near-infrared (NIR) data from 0.8-2.5 μm were collected at the 3-meter NASA Infrared Telescope Facility (IRTF) at the Mauna Kea Observatory using the SpeX infrared spectrograph and imager (Rayner et al., 2003). The data were reduced to relative reflectance following methods outlined in Sunshine et al. (2004) and DeMeo et al. (2019). Continuous visible data (0.4-0.9 μm)

**Table 4.2. Data Sources and Calculated Surface Temperatures for Asteroid Spectra.**

| Asteroid Name | Diameter (km)[c] | AU | Surface Temperature (K)[d] | Date(s) of Observation |
|---|---|---|---|---|
| 246 Asporina[a] | 60 | 2.43 | 186 | multiple dates[a] |
| 289 Nenetta[a] | 34 | 2.38 | 188 | multiple dates[a] |
| 354 Eleonora[a] | 155 | 2.91 | 170 | 15-Apr-02 |
| 446 Aeternitas[a] | 45 | 2.71 | 177 | multiple dates[a] |
| 863 Benkoela[a] | 27 | 3.24 | 161 | multiple dates[a] |
| 984 Gretia[a] | 32 | 2.26 | 193 | multiple dates[a] |
| 2501 Lohja[a] | 10 | 2.39 | 188 | 12-Jan-02 |
| 3819 Robinson[a] | 11 | 2.63 | 179 | 26-Jul-04 |
| (8838) 8189 UW2[b] | 13 | 3.14 | 164 | 1-Dec-11 |
| (16520) 1990 WO3[b] | 3 | 2.28 | 192 | 23-Jan-12 |
| (17818) 1996 FE118 [b] | 8 | 2.77 | 174 | 20-Mar-12 |
| (21809) 1999 TG19[b] | 5 | 2.69 | 177 | 19-Sep-12 |
| (31393) 1998 YG8[b] | 2 | 2.20 | 196 | 23-Jan-12 |
| (35925) 1999 JP104[b] | 4 | 2.44 | 186 | 8-Aug-12 |
| (36256) 1999 XT17[b] | 10 | 2.94 | 169 | 20-Mar-12 |
| (92516) 2000 ND25[b] | 4 | 2.19 | 196 | 20-Mar-12 |

[a] Additional observational data in Sunshine et al. (2007); Spectral range = 0.44-2.49 µm

[b] DeMeo et al. (2019); Spectral range = 0.82-2.49 µm + spectral filters at 0.36, 0.47, 0.62, & 0.75

[c] NEOWISE diameters (Mainzer et al., 2016).

[d] Surface temperatures calculated by standard thermal model (Lebofsky and Spencer, 1989)

were collected from SMASS and SMASSII asteroid surveys, which utilized the 2.4-meter Hiltner telescope at the Michigan Dartmouth MIT Observatory in Kitt Peak, Arizona (e.g., Xu et al., 1995; Bus and Binzel, 2002). Near infrared spectra from SpeX were combined with available visible data from SMASS and SMASSII by applying a scaling factor across their shared spectral range (0.8-0.9 µm) after methods Sunshine et al. (2007). For more recently observed A-type asteroids (DeMeo et al., 2019), no continuous visible spectra are available. SpeX near-infrared data are instead combined and scaled with five UV-visible spectral filters from Sloan Digital Sky Survey (SDSS) following methods in DeMeo et al. (2019). Each of these filters sample the UV-visible portion of spectra with photometric sensitivities defined by gaussian profiles centered at 355, 469, 617, and 748, and 893 nm with filter widths of 130, 130, 120, 55, and 100 nm, respectively. Relative reflectance values for SDSS filters are calculated by integrating color data across the range of wavelengths sampled by each filter (York et al., 2000).

### *4.2.3 Modified Gaussian Modeling (MGM)*

The approach used in this work to quantitatively determine meteorite and asteroid mineralogy from reflectance spectra is based on the modified gaussian model (MGM) developed by Sunshine et al., (1990). Absorptions resulting from electronic transitions are modeled as modified gaussian features as defined by the function

$$m(x) = s \cdot exp\left\{\frac{-\left(x^{-1} - \mu^{-1}\right)^2}{2\sigma^2}\right\} \qquad [4.1]$$

where *s* is the strength (amplitude) of an absorption, µ is its center (mean), and $\sigma$ is the full width at half of the maximum amplitude (FWHM). The modification of *x* and μ from the standard gaussian formula alters the slopes on either side of the absorption feature and corresponds to the power law relationship between the energy of an absorption ($e$) and the average bond length between the cation and surrounding ligand groups, or

$$e \propto r^{-1} \tag{4.2}$$

The component absorption bands for a mineral can be deconvolved from reflectance spectra using the inverse stochastic approach of Sunshine et al. (1990) (Fig. 1.6). This approach has been used to successfully interpret olivine composition from diagnostic spectral parameters in meteorite powders and some A-type asteroids (Sunshine et al., 1993; 2007).

MGM is well-suited to the task of interpreting olivine spectra based on individual olivine absorption band parameters (Sunshine et al. 1990) that vary systematically with mineral composition consistent with principles of Crystal Field Theory (Burns, 1970; 1993). MGM fits reproduce measured spectra through a nonlinear least squares analysis by generating a model spectra composed of overlapping absorption features superimposed on a continuum (i.e., background slope). A starting model must be provided to begin the process, and iterative, stochastic adjustments are made to individual absorption band parameters and the continuum. At each iteration, the root mean square (RMS) between the model solution and measured spectrum is calculated, and improvement to RMS results in an accepted model iteration. An accepted iteration replaces the starting model, and the process is repeated until improvement to RMS is negligible (i.e., RMS improvement < resolution of measured spectrum). This method has proven successful for characterizing compositions of olivine and pyroxene based on their calculated absorption band parameters (e.g., Sunshine et al., 1990; 1993; 2007; Sunshine and Pieters, 1998).

### *4.2.4 Fa content of Olivine in the Near-Infrared*

A schematic of the approach used to calculate olivine Fa content is provided in Fig. 4.1. All asteroid and meteorite spectra in this study are dominated by an olivine absorption complex at ~1 µm. Olivine composition is calculated by utilizing the correlation between the three olivine band centers and Fa content, as described by the following equations from Sunshine et al. (1993, 2007):

$$\mathrm{Fa} = 1 - (\mathrm{BIC} \cdot (-0.012187) + 11.1293) \qquad [4.3],$$

$$\mathrm{Fa} = 1 - (\mathrm{BIIC} \cdot (-0.022025) + 23.755) \qquad [4.4],$$

$$\mathrm{Fa} = 1 - (\mathrm{BIIIC} \cdot (-0.010310) + 13.3606) \qquad [4.5],$$

where Fa is the mole fraction of fayalite ($FeSiO_4$) in olivine and BIC, BIIC, and BIIIC are the band centers for olivine absorption bands I, II, and III in nm. Estimated Fa content is then taken as the average of Equations 4.4-4.5. Band I is excluded from calculations of Fa content due to the nonlinear variability between Fa content and the band I center (Sunshine and Pieters, 1998). In this work, the reliability of Fa content calculated from band I (Equation 4.3) is further compromised by the band I center of pyroxene, which can directly overlap the first olivine absorption band.

Three starting models (Table 4.3) are used to interpret olivine Fa content from MGM fits, each corresponding to spectral parameters for olivine at $Fa_{10}$, $Fa_{50}$, and $Fa_{90}$ based on laboratory measurements of olivine that were used to calibrated Equations 4.3-4.5 (Sunshine et al., 1993). Band strength ratios are used to constrain

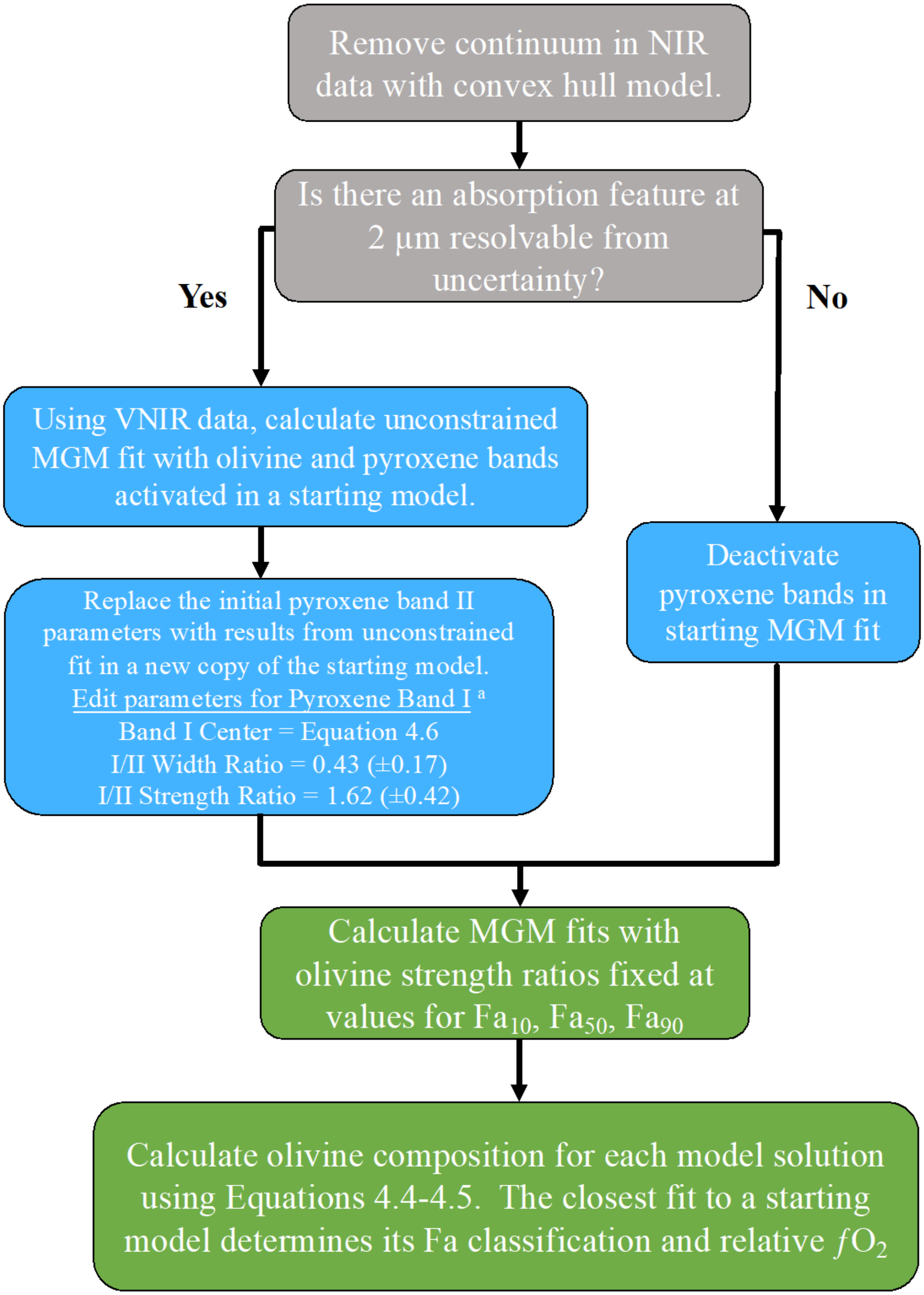

**Fig. 4.1.** Methodology flowchart for interpreting composition of olivine-dominated asteroids.

**Table 4.3. Starting model parameters used to calculate olivine composition.**

| | Fa$_{10}$ | | | |
|---|---|---|---|---|
| Contiuum: | Y-intercept [a] | | Slope [a] | |
| | 7.56E-01 | | -2.20E-05 | |
| Olivine band strength ratios | | | | |
| 300 K | I/III | 0.50 , | II/III | 0.78 |
| 175 K | I/III | 0.69 , | II/III | 1.12 |

| Absorption bands | Center (nm) | | Width (nm) | | Strength | |
|---|---|---|---|---|---|---|
| *UV-Visible* | | | | | | |
| i | 400 | ±100 | 300 | ±100 | -0.10 | ±500 |
| ii[b] | 650 | ±50 | 115 | ±20 | -0.01 | ±1 |
| *Olivine* | | | | | | |
| I | 832 | ±300 | 185 | ±50 | -0.20 | ±100 |
| II | 1020 | ±300 | 226 | ±50 | -0.31 | ±100 |
| III | 1226 | ±300 | 377 | ±50 | -0.27 | ±100 |
| *Pyroxene*[c] | | | | | | |
| I | 900 | ±100 | 228 | ±100 | -0.15 | ±10 |
| II | 1910 | ±500 | 424 | ±100 | -0.05 | ±10 |

**Table 4.3 (cont'd). Starting model parameters used to calculate olivine composition.**

| | Fa$_{50}$ | | | | | |
|---|---|---|---|---|---|---|
| Contiuum: | Y-intercept [a] | | Slope [a] | | | |
| | 7.56E-01 | | -2.20E-05 | | | |
| Olivine band strength ratios | | | | | | |
| 300 K | | | I/III =0.55 | , | II/III = 0.60 | |
| 175 K | | | I/III =0.75 | , | II/III = 0.82 | |
| Absorption bands | Center (nm) | | Width (nm) | | Strength | |
| *UV-Visible* | | | | | | |
| i | 400 | ±100 | 300 | ±100 | -0.10 | ±500 |
| ii[b] | 650 | ±50 | 115 | ±20 | -0.01 | ±1 |
| *Olivine* | | | | | | |
| I | 890 | ±300 | 247 | ±50 | -0.22 | ±100 |
| II | 1055 | ±300 | 166 | ±50 | -0.22 | ±100 |
| III | 1234 | ±300 | 377 | ±50 | -0.31 | ±100 |
| *Pyroxene*[c] | | | | | | |
| I | 900 | ±100 | 228 | ±100 | -0.15 | ±10 |
| II | 1910 | ±500 | 424 | ±100 | -0.05 | ±10 |

**Table 4.3 (cont'd). Starting model parameters used to calculate olivine composition.**

| | Fa$_{90}$ | |
|---|---|---|
| Contiuum: | Y-intercept [a] | Slope [a] |
| | 7.56E-01 | -2.20E-05 |
| Olivine band strength ratios | | |
| 300 K | | I/III =0.60 , II/III = 0.40 |
| 175 K | | I/III =0.8 , II/III = 0.48 |

| Absorption bands | Center (nm) | | Width (nm) | | Strength | |
|---|---|---|---|---|---|---|
| *UV-Visible* | | | | | | |
| i | 400 | ±100 | 300 | ±100 | -0.10 | ±500 |
| ii[b] | 650 | ±50 | 115 | ±20 | -0.01 | ±1 |
| *Olivine* | | | | | | |
| I | 890 | ±300 | 247 | ±50 | -0.22 | ±100 |
| II | 1055 | ±300 | 166 | ±50 | -0.22 | ±100 |
| III | 1234 | ±300 | 377 | ±50 | -0.31 | ±100 |
| *Pyroxene*[c] | | | | | | |
| I | 900 | ±100 | 228 | ±100 | -0.15 | ±10 |
| II | 1910 | ±500 | 424 | ±100 | -0.05 | ±10 |

[a] Starting models are initially plotted against data so that continuum parameters may be manually adjusted by visual approximation to values appropriate for the slope of an individual spectrum.

[b] The 650 nm band is removed from starting models for data that utilize SDSS filters due to the loss of resolution in the visible region. This has negligible effect on model solutions (Fig. 4.2, Table 4.4).

[c] Pyroxene band II is fit first in an unconstrained model solution and the resulting parameters for band II are used to constrain band I parameters (Fig. 4.1).

plausible solutions for each starting model at appropriate temperatures (Sunshine et al., 2007; Table 4.3). A potential compositional classification is eliminated for an asteroid or meteorite spectrum if it generates a model solution consistent with the wrong compositional category. For example, a magnesian meteorite or asteroid ($Fa_{10}$) will not yield self-consistent model results between band strength ratios and centers if it is set to initial parameters for $Fa_{90}$. This method is useful for binning olivine composition into three petrologically significant categories using Fa content as a proxy for relative oxidation state. In this work, asteroid olivine is classified as reduced if its estimated Fa content is consistent with metal-bearing primitive meteorites ($<Fa_{30}$; Chapter 2). Oxidized olivine includes compositions near the metal-sulfide core transition interpreted from brachinites ($\sim Fa_{30-40}$), and highly oxidized olivine includes compositional estimates above $\sim Fa_{40}$.

### *4.2.5 Untangling olivine and pyroxene absorptions*

Prior to modeling, spectra were visually inspected for absorption features in the 2 µm region indicative of pyroxene. This was accomplished by removing the continua of spectra with convex hull models, which generates a smallest possible polygon with no concavities that can fully enclose spectral data. A linear regression through the polygon approximates the continuum, and the data is then renormalized to a slope of zero. The data were smoothed using a boxcar average over 15 nm intervals to reduce noise and aid in visual inspection, but the complete unsmoothed datasets were used for MGM fits. This process provides a consistent method for determining if a 2 µm pyroxene band is resolvable beyond uncertainty.

When pyroxene is evident in the 2 µm region of asteroid spectra, an absorption band was added to the 2 µm region and an unconstrained MGM fit was run. Because the 2 µm is unaffected by olivine, it can be used to estimate suitable initial band center for the corresponding 1 µm pyroxene band after previous work that established correlations between the two pyroxene band parameters (Sunshine et al., 1998; Klima et al., 2007; 2011). For natural and synthetic pyroxenes, Klima et al. (2007, 2011) found compositional correlations between pyroxene band I and II centers, which can be reproduced by the following equation:

$$BIC = 0.0067e^{4.802(BIIC-1.7)} + 0.91, \qquad (\sigma = 0.02), \qquad [4.6]$$

here BIC is pyroxene's band I center (µm) and BIIC is the band II center (µm). A calculated BIIC within the range of 1.7-2.4 µm can therefore be used to estimate a reasonable starting position for BIC prior to further MGM fitting. The band I/II strength ratios (1.62 ± 0.42) and width ratios (0.43 ± 0.17) of the two pyroxene bands (Klima et al., 2007; 2011), which were derived from pyroxenes across the entire range of CaO and FeO contents, were similarly used to define starting parameters for pyroxene band I based on the results of the initial band II solution. Each of these factors were allowed to vary during final MGM fitting within the uncertainties of band parameter ratios (Table 4.3, Fig. 4.1).

If BIIC falls between 1.7-2 µm, indicating a pyroxene assemblage dominated by low-Ca endmembers, FeO content can be estimated following:

$$Fs\% = 671(BIIC)^2 - 2236(BIIC) + 1854 \qquad [4.7]$$

after Klima et al. (2007), where Fs% is the mole percent of ferrosilite ($FeSiO_3$) in low-Ca pyroxene. This can be used in tandem with calculated Fa contents to determine if olivine and pyroxene are in equilibrated based on the linear correlation between Fa and Fs content in equilibrated meteorites (e.g., Tomkins et al., 2020).

### *4.2.6 MGM fitting with sparse UV-visible data*

To ensure that MGM fits with discontinuous visible data (i.e., SDSS filters) were comparable to those with continuous spectra, SDSS data was simulated for asteroid 246 Asporina from SMASS visible data. This was accomplished by integrating SMASS data using the gaussian profiles of each SDSS spectral filter (York et al., 2000). The simulated SDSS data was then scaled to fit SpeX data using the same methods described above for discontinuous visible data. Due to the loss of resolution in the visible region, the small 0.65 µm absorptions, which are typically associated with $Fe^{2+}/Fe^{3+}$ transitions (e.g., Burns, 1970), cannot be resolved in the SDSS data. Consequently, this absorption band is excluded from initial model parameters. Additionally, the loss of resolution in this region would presumably affect parameters of olivine band I. However, the band I center is not factored into the final Fa calculation (Sunshine et al., 1993; 2007), and the effects on bands II and III are below the resolution of Fa interpretation. The minimal changes to band II and III parameters are due to constraints imposed on the continua by the steep slope between the first three SDSS points, so ultimately the loss of resolution in the UV-visible portion of the spectrum is negligible for final MGM fits (Fig. 4.2, Table 4.4).

### *4.2.7 Accounting for Surface Temperatures*

This work includes interpretation of spectra for both meteorites and asteroids. As such, the effects of temperature on olivine band strength ratios must be taken into

**Table 4.4. Comparison of model solutions between continuous and discontinuous spectra of 246 Asporina**

| | Continuous Data[a] | | | | Discontinuous (SDSS) Data[b] | | |
|---|---|---|---|---|---|---|---|
| | Y-intercept | Slope | | | Y-intercept | Slope | |
| | 7.56E-01 | -2.20E-05 | | | 7.56E-01 | -2.20E-05 | |
| Absorption bands | | | | Absorption bands | | | |
| | Center | Width | Strength | | Center | Width | Strength |
| | *434* | *300* | *-0.13* | | *400* | *300* | *-0.04* |
| | *625* | *115* | *-0.04* | | | | |
| I | 891 | 247 | -0.22 | I | 883 | 252 | -0.21 |
| II | 1057 | 166 | -0.22 | II | 1055 | 175 | -0.23 |
| III | 1233 | 377 | -0.31 | III | 1235 | 375 | -0.31 |
| | | RMS Error = | 0.0066 | | | RMS Error = | 0.0075 |
| Calculated Olivine Composition | | | | Calculated Olivine Composition | | | |
| | Strength Ratios | | Calculated Fa | | Strength Ratios | | Calculated Fa |
| I/III | 0.71 | Band I | 73% | I/III | 0.70 | Band I | 63% |
| II/III | 0.71 | Band II | 54% | II/III | 0.74 | Band II | 48% |
| | | Band III | 35% | | | Band III | 37% |
| | | Average Fa (II,III) | 44% | | | Average Fa (II,III) | 43% |
| | | **Classification:** | **Oxidized** | | | **Classification:** | **Oxidized** |

[a] Continuous data is combination of SpeX (0.45-0.9 µm) and IRTF (0.8-2.45 µm). Data normalization is described in text.

[b] Discontinuous data uses analog SDSS data integrated from SpeX.

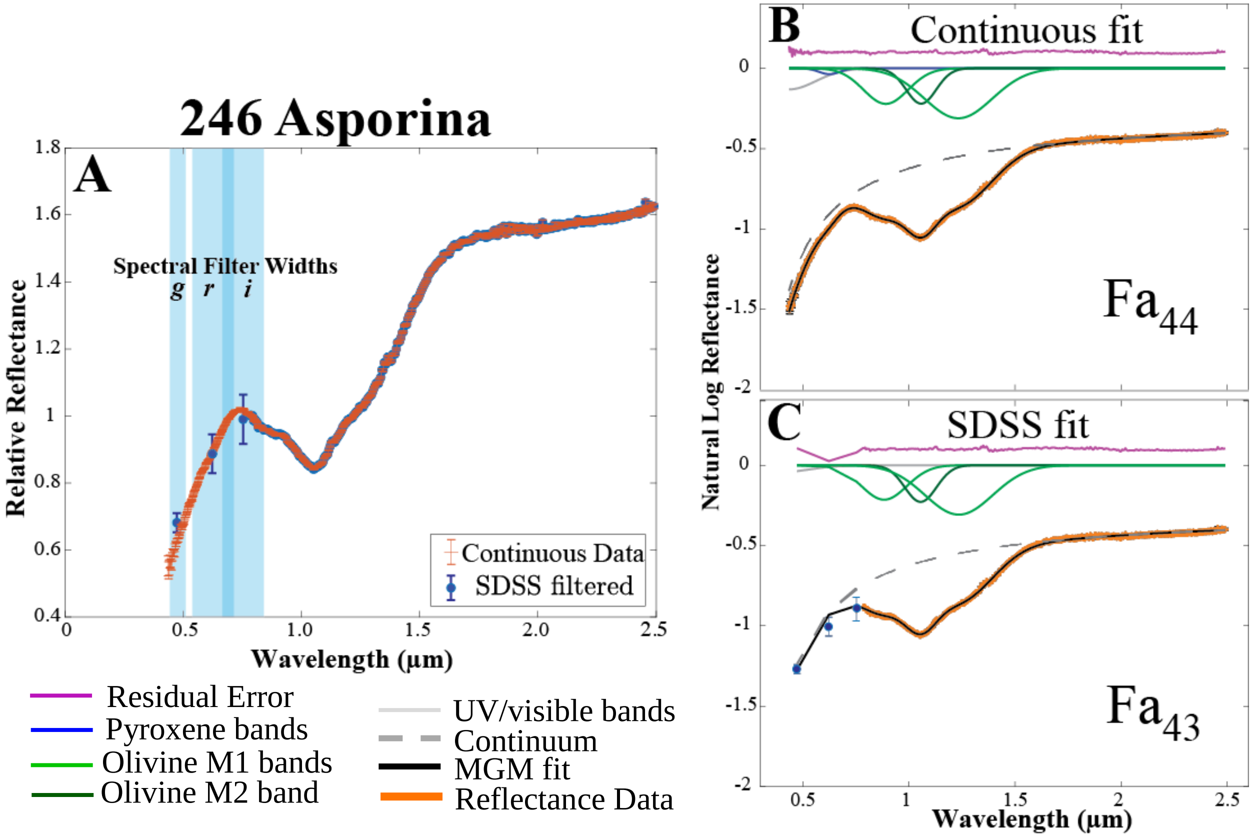

**Fig. 4.2. SDSS filter simulation and the suitability of discontinuous data for MGM fits of 246 Asporina.**
(a) Illustrates what components of the visible spectrum are sampled by the *g'*, *r'*, and *i'* SDSS filters (blue) compared to continuous visible data from SMASS (orange). The best fit for (b) continuous VNIR data is best fit by Fa$_{44}$, calculated from olivine band centers, while the discontinuous dataset using SDSS filters (c) is best fit by parameters consistent with Fa$_{43}$. The same starting models were used for both fits, apart from removal of the 650 nm absorption in (c), which is unresolvable with SDSS filters. MGM parameters for the two solutions are provided in Table 4.4. The results are well within the ~10 mol% resolution of olivine compositions calculated from MGM parameters, indicating that discontinuous visible data has a negligible effect on compositional interpretations.

account before interpreting olivine composition (Sunshine et al., 2007). The band strength ratios used for modeling meteorite spectra collected at RELAB are based on a priori parameterization for laboratory spectra at 300 K (Sunshine et al., 1993). Surface temperatures of asteroids in this work were calculated using the Standard Thermal Model, which derives temperature for a simplified, spherical asteroid model based on solar flux at a given distance from the Sun (Lebofsky and Spencer, 1989). Heliocentric distance for each asteroid on the date(s) of observation, as well as their calculated temperatures, are provided in Table 4.2. All of the asteroids analyzed in this work are main belt asteroids and have surface temperatures between ~160-195 K. MGM fits for these asteroids utilize suitable band strength ratios (Table 4.3) established for main belt asteroids within this range of surface temperatures (Sunshine et al., 2007).

### *4.2.8. Assessing the Reliability of Model Solutions*

The approach to interpreting composition and mineralogy of olivine-dominated asteroids in this work provides multiple opportunities to assess the self-consistency of model solutions using absorption band centers, band widths, and band strength ratios for both olivine and pyroxenes. First, the MGM algorithm allows for the relative strengths of the olivine bands to be constrained to ratios observed from laboratory analyses of olivine with starting model compositions of $Fa_{10}$, $Fa_{50}$, and $Fa_{90}$. To be deemed self-consistent, a model solution must first yield band centers that correspond to Fa values consistent with the predetermined strength ratios. Band centers are considered self-consistent if the calculated Fa contents for bands II and II are within 15 mol% of their averaged value. For example, if band strength ratios are constrained to values for $Fa_{90}$ (Table 4.3), but the model solution yields band centers reflective of $Fa_{50}$, the solution is not considered viable. In the event that two compositional models yield equally viable results (e.g., $Fa_{10}$ and $Fa_{50}$ models both result in band centers corresponding to $Fa_{30}$), the model solution with the lowest residual error is selected. This can occur if the Fa content olivine is equally displaced from initial model values (e.g., a $Fa_{30}$ spectrum may be fit equally well by $Fa_{10}$ and $Fa_{50}$ because it deviates from both models by 20 mol%).

Interpreted pyroxene compositions provide another opportunity to test for the self-consistency of model solutions. Due to the linear relationship between Fs content of low-Ca pyroxene and Fa content of olivine among equilibrated meteorites (e.g., Tomkins et al., 2020), agreement between the MGM-calculated compositions of pyroxene and olivine can be used to indicate that pyroxene and olivine are consistent with equilibrated meteorite mineralogies. Discordant results for olivine and pyroxene compositions would indicate that an asteroid mineral assemblage is unequilibrated (i.e., chondritic). However, discordant results between olivine and pyroxene may indicate that a model solution is invalid. This work considers such a solution to be valid if absorption band parameters for olivine and pyroxene are internally self-consistent.

## *4.3 Results*

### *4.3.1 Spectral Estimates of Fa Content for Olivine-Dominated Meteorites*

Brachinite family meteorite spectra are dominated by olivine absorption complexes centered at ~1.05 µm, consistent with their olivine-dominated mineralogies (81-95 wt%) derived from XRD analyses (Table 4.1). The spectra of oxidized ($Fa_{35}$) and reduced brachinites ($<Fa_{30}$) can be distinguished by the presence of minor pyroxene absorption features from 1.9-2.3 µm in reduced endmembers. The corresponding 0.9-1 µm band of pyroxene distorts the shape of the olivine complex from ~0.8-1.1 µm depending on the composition and proportion of pyroxene, resulting in erroneous Fa estimates if unaccounted for. By placing reasonable constraints on pyroxene band I parameters (Equation 4.6; Klima et al., 2007, 2011), olivine-dominated spectra with minor pyroxene absorptions can be fit simultaneously. Olivine and pyroxene compositions interpreted from MGM fits for meteorite are provided in Table 4.1. Band parameters for MGM fits are provided in Supplementary Materials for Ch. 4 in the Appendix.

Spectra of oxidized brachinites (NWA 4882, RaS 309, and Reid 013) are dominated by an olivine absorption complex centered at 1.05 µm with negligible pyroxene features (Fig. 4.3), consistent with high olivine/pyroxene ratios (15-39) calculated from XRD measurements. MGM-calculated Fa content for oxidized brachinites range from $Fa_{27-42}$ and are within 10 mol% of electron microprobe measurements (Table 4.1, Fig.4. 4). Small pyroxene bands can be added to account for the ~1 wt% of low-Ca pyroxene, but they do not improve Fa estimates and would otherwise be unresolvable in telescopic measurements.

The minor 2 µm low-Ca pyroxene bands seen in the spectra of reduced brachinites are resolvable for abundances of 3 wt% in NWA 7297 and 10 wt% in NWA 11756. In laboratory measurements, the 2 µm bands of high-Ca pyroxene are resolvable even at very low abundances in both NWA 7297 (~1 wt%) and

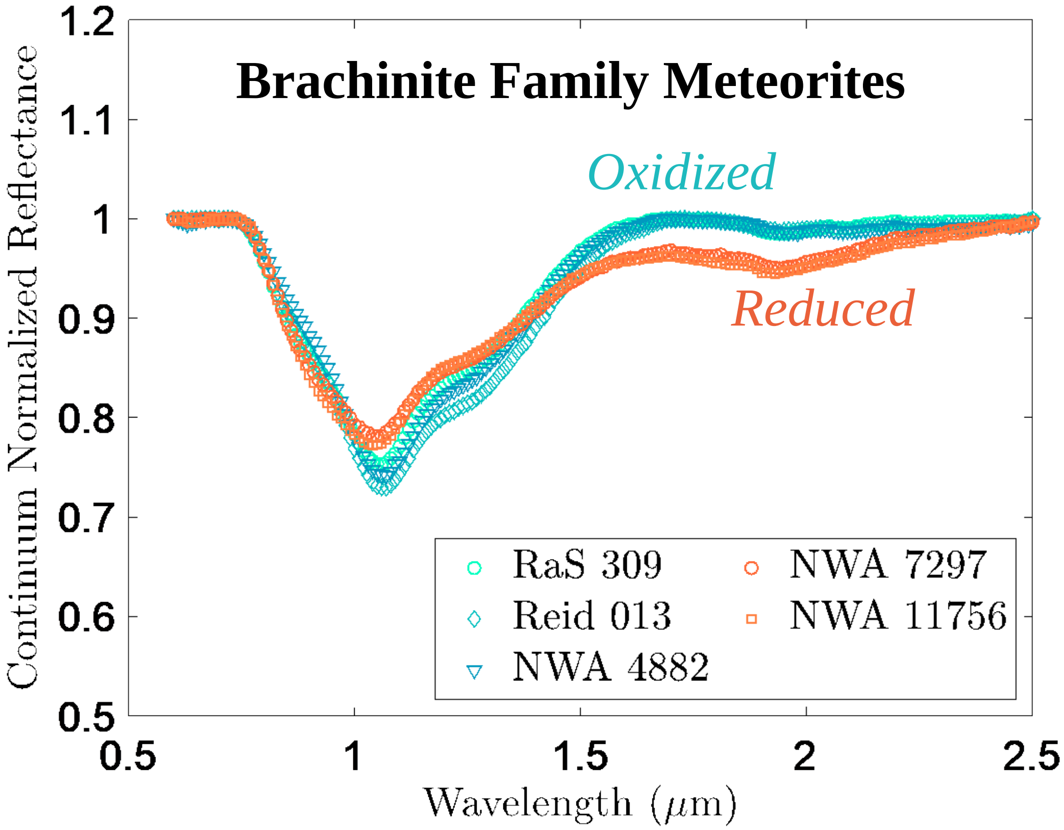

**Fig. 4.3. Continuum-removed spectra of brachinite family redox endmembers.** Redox endmembers are distinguishable due to the 2 µm absorption feature caused by pyroxene in more reduced assemblages. The 0.9-1 µm portion of the olivine complex is also distorted due to the corresponding 1 µm band of pyroxene, which complicates Fa content interpretations if unaccounted for.

NWA 11756 (~6 wt%), although these features would be unresolvable with the lower precision of telescopic observations. When the two pyroxenes are resolved in the spectrum of NWA 11756, band II of low-Ca pyroxene is best fit with a center at 1.89 µm, corresponding to $Fs_{25}$ and an initial band I center at 0.92 ± 0.02. After fitting of pyroxene, NWA 11756 olivine is best fit by $Fa_{36}$ (Table 4.1; Fig. 4.4). These estimates are within 10 mol% of EMPA measurements. If high-Ca pyroxene is not distinctly resolved, then pyroxene band II is fit by an average of the two endmember

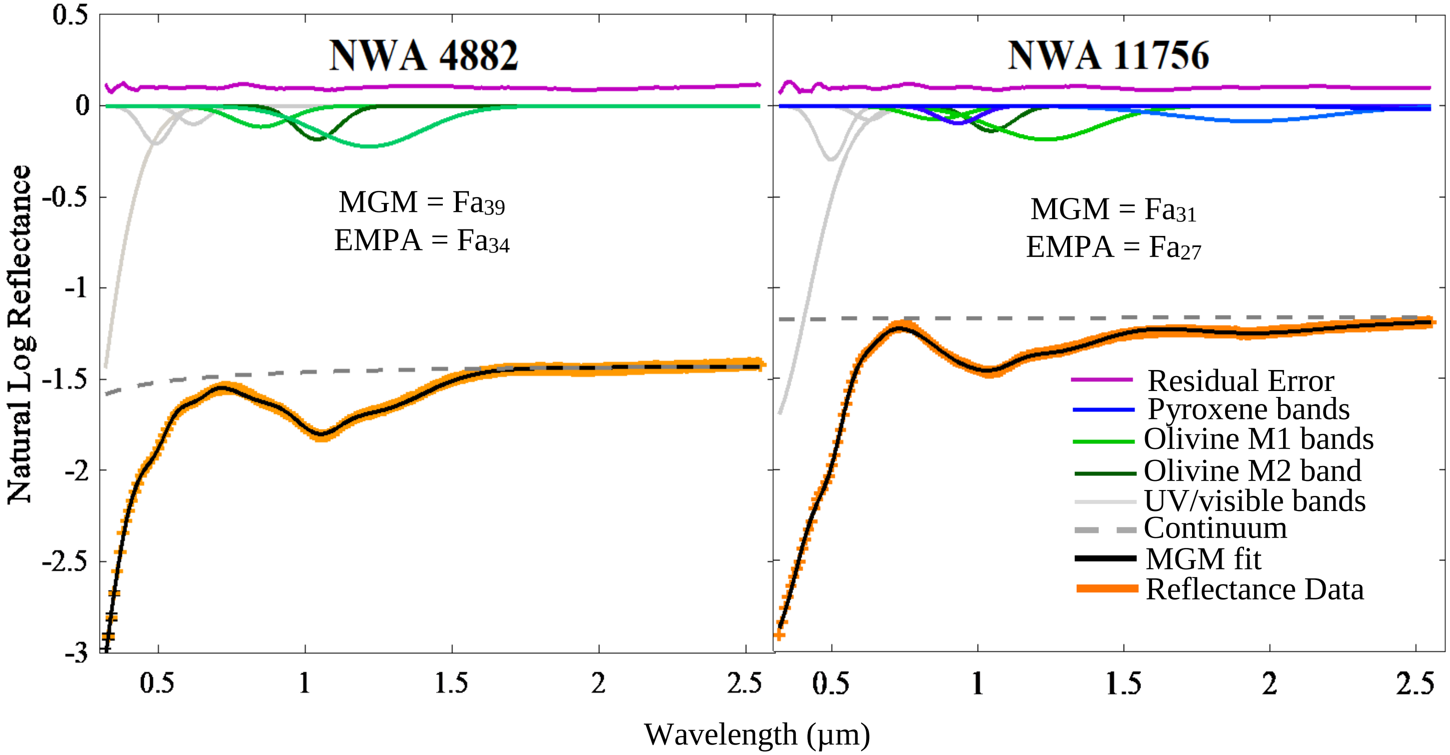

**Fig. 4.4. Example MGM fits for brachinite family meteorite endmembers**.
NWA 4882 (oxidized, $fO_2$ ~IW-1) and NWA 11756 (reduced, $fO_2$ ~IW-2) illustrate the ability of this method to fit olivine-dominated spectra with minor pyroxene (up to ~15 wt%) to the same level of precision as olivine-only fits. This method is therefore suitable for simultaneously fitting the olivine complexes with overlapping pyroxene in olivine-dominate asteroid spectra to interpret Fa content and oxidation state

bands with a center at 1.93 µm, corresponding to $Fs_{38}$ and BIC = 0.93 ±0.02 µm. Consequently, the apparent pyroxene band centers are shifted to longer wavelengths than what is predicted for their ferrosilite content. This can result in high Fs estimates for low-Ca pyroxene when high-Ca pyroxene is present but not spectrally resolvable. However, reasonable constraints can still be placed on pyroxene band I centers, because mixtures of two pyroxenes do not affect the correlation between pyroxene band I and II centers described by Equation 4.6. Similarly, the width and strength of band II allow one to extrapolate reasonable parameters for band I (Sunshine and Pieters, 1998; Klima et al., 2007, 2011). NWA 7297 has significantly less total pyroxene (~4 wt%), but nonetheless has a resolvable band II center at 1.94 µm, corresponding to BIC = 0.929 ±0.015 µm. Subsequent MGM fitting of olivine provides an estimate of $Fa_{32}$. The residual error between olivine compositions estimated from MGM fitting and the actual EMPA measurements are well within the typical 10% uncertainty of MGM fits.

### *4.3.2 Interpreted Compositions of Olivine-dominated Asteroids*

MGM results for new A-type asteroids identified by DeMeo et al. (2019) are provided below, as well as MGM results for all main belt olivine-dominated asteroids in Sunshine et al. (2007), including those with pyroxene spectral features. The asteroids are presented here according to their mineralogies (i.e., monomineralic olivine and olivine-pyroxene mixtures). Continuum-removed near-infrared spectra for asteroids (Fig. 4.5) highlight the different spectral shapes of the two groups, particularly in the 2 µm region of pyroxene band II. Estimated Fa content from MGM fits for asteroid spectra are reported in Table 4.5 and examples of fits of endmembers

**Table 4.5. Best fits for MGM-derived olivine and pyroxene compositions for A-type asteroids and petrologic interpretations.**

| Asteroid Name | $Fa_{10}$ | $Fa_{50}$ | $Fa_{90}$ | Pyroxene Composition | Petrologic Interpretation(s) |
|---|---|---|---|---|---|
| 246 Asporina | *54* | **46** | *53* | n/a | highly oxidized restite |
| 289 Nenetta | *51* | **50** | *46* | n/a | highly oxidized restite |
| 354 Eleonora | *44* | **33** | *15* | LCP (~$Fs_{20}$) | oxidized restite |
| 446 Aeternitas | *41* | **34** | *16* | LCP (~$Fs_{25}$) + HCP | *likely oxidized chondrite* |
| 863 Benkoela | *33* | **31** | *17* | LCP/Pigeonite | oxidized restite |
| 984 Gretia | *56* | **46** | *28* | LCP/Pigeonite | highly oxidized restite/chondrite |
| 2501 Lohja | *30* | *21* | *40* | LCP + HCP | *likely oxidized chondrite* |
| 3819 Robinson | *68* | **60** | *49* | LCP (~$Fs_{40}$) + HCP | highly oxidized restite/chondrite |
| (8838) 1989 UW2 | *31* | **32** | *36* | LCP/Pigeonite | oxidized restite |
| (16520) 1990 WO3 | **15** | *4* | *-3* | LCP + HCP | reduced restite |
| (17818) 1996 FE118 | *59* | **49** | *51* | n/a | highly oxidized restite |
| (21809) 1999 TG19 | 73 | **32** | *18* | Ambiguous | oxidized restite/chondrite |
| (31393) 1998 YG8 | *40* | **20** | *6* | Ambiguous | *invalid results* |
| (35925) 1999 JP104 | *52* | **35** | *29* | LCP/Pigeonite | oxidized restite |
| (36256) 1999 XT17 | *51* | **43** | 44 | n/a | highly oxidized restite/chondrite |
| (92516) 2000 ND25 | *23* | **30** | *31* | n/a | oxidized restite |

All compositions calculated with model olivine parameters at 175-190K.
Best fits indicated by bold, unitalicized font.
Green font indicates self-consistent results.

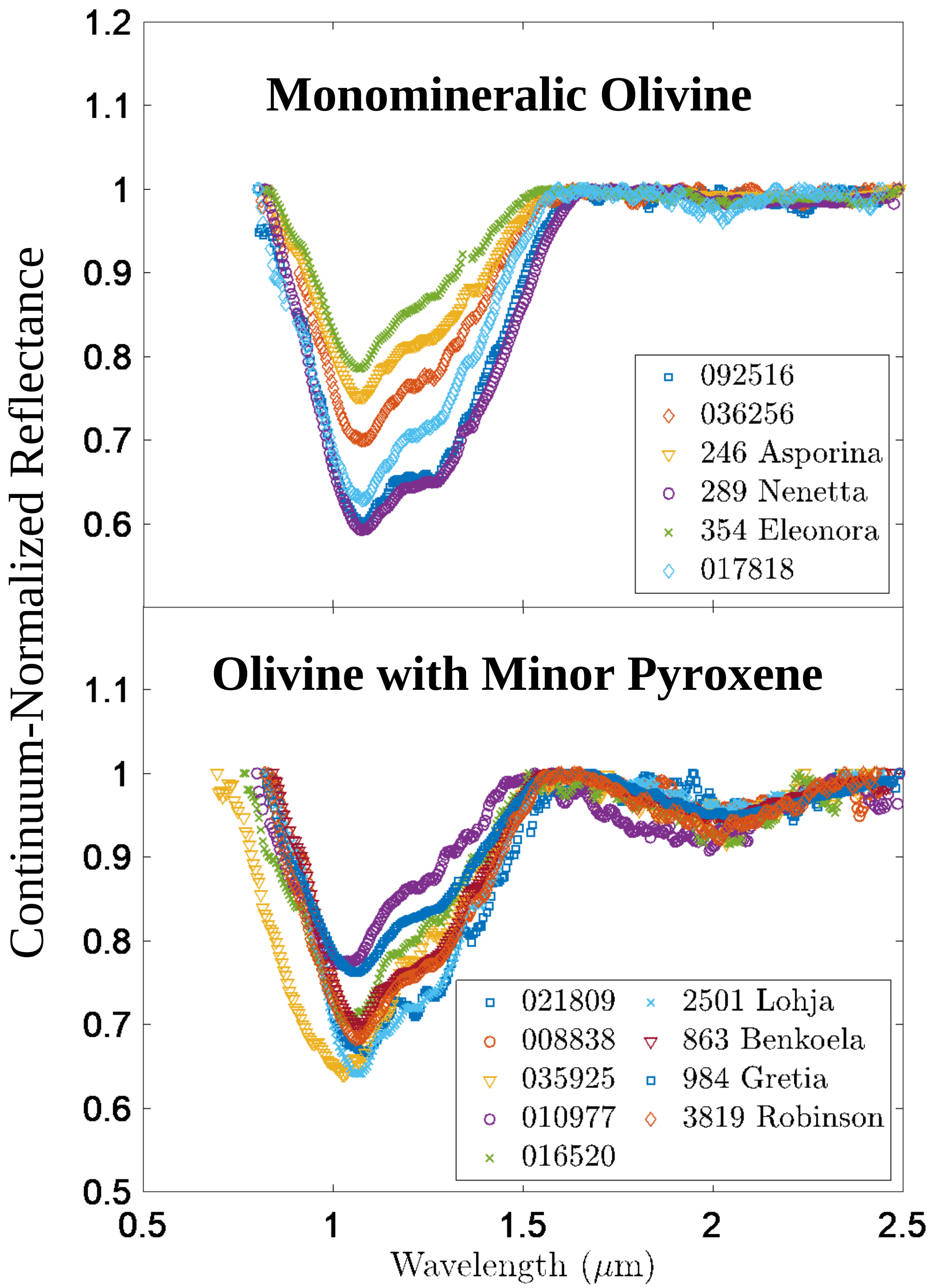

**Fig. 4.5. Continuum-removed A-type asteroid NIR reflectance spectra.** Monomineralic olivine asteroids lack the 2 μm feature, and pyroxene-bearing asteroids possess 2 μm features that are consistent with < 15 wt% pyroxene in meteorites. The two sets of asteroid spectra can be interpreted using the two approaches described in Fig. 4.1.

are shown in Fig. 4.6. These parameters are used to group asteroids into reduced, oxidized, and highly oxidized categories. Petrologic interpretations are discussed in Section 4.4.

Five of the sixteen olivine-dominated asteroids show no resolvable 2 µm pyroxene features and are considered monomineralic olivine asteroids. MGM-calculated Fa estimates for Asteroid (92516) 2000 ND25 fall within oxidized olivine parameters. Highly oxidized monomineralic olivine asteroids include 246 Asporina, 289 Nenetta, (17818) 1996 FE118, and (36256) 1999 XT17.

The remaining eleven asteroids possess resolvable absorption features in their spectra near 2 µm due to the presence of minor pyroxene. They contain an estimated 5-15 wt% total pyroxene based on comparison with pyroxene-bearing brachinite meteorites, consistent with previous estimates for A-type asteroids (Sanchez et al., 2014). Two of the olivine-pyroxene asteroids yield self-consistent compositional estimates for both olivine and low-Ca pyroxene. 354 Eleonora is best fit by oxidized olivine and low-Ca pyroxene (~$Fs_{20}$), while 3819 Robinson is fit by highly oxidized olivine, low-Ca pyroxene (~$Fs_{40}$) and high-Ca pyroxene. Pyroxene band II centers for four asteroids are between 2.0-2.2 µm, indicating that the dominant pyroxene in these assemblages is either pigeonite or mixtures of low and high-Ca endmembers that cannot be individually resolved (Klima et al., 2007; 2011). As demonstrated by the reduced brachinite meteorites in this work, the Fs content of pyroxene in these asteroids cannot be reliably interpreted from their averaged pyroxene band center. After constraining pyroxene band I parameters from band II, three of these asteroids are consistent with oxidized olivine: 863 Benkoela, (8838) 1989 UW2, and (35925)

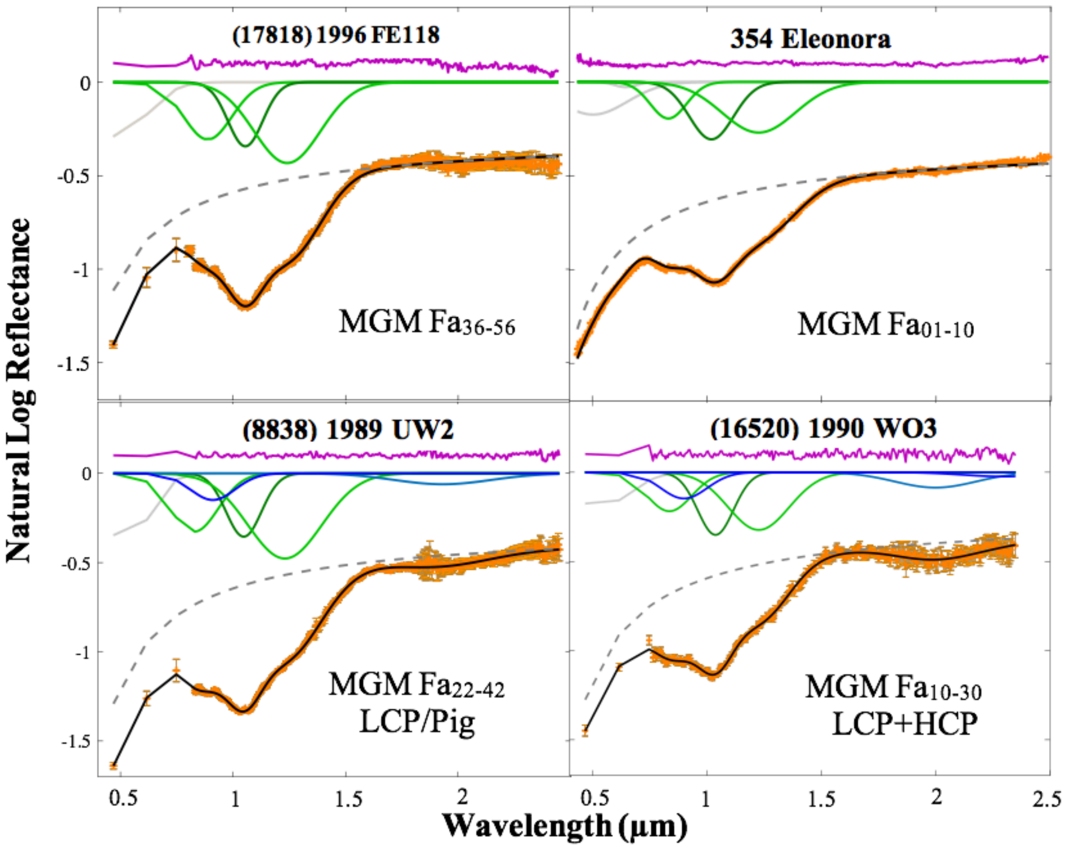

**Fig. 4.6. Example MGM fits for olivine-dominated asteroids.**
A-type asteroids include both monomineralic olivine (e.g., Asteroid 17818 and 354 Eleonora) and olivine-pyroxene (Asteroids 8838 and 16520) mineralogies that range from Fa$_{01-60}$. Symbols are the same as in Fig. 4.4. Additional fits are provided in supplementary materials.

1999 JP104. Asteroid 984 Gretia is best fit by more highly oxidized olivine parameters. Asteroid (16520) 1990 WO3 is the only asteroid in this work best fit by low Fa models and is classified as reduced olivine (Fig. 4.6). The 2 µm region is best fit by both low and small high-Ca pyroxene bands, but the uncertainty in the 2 µm region is too large to reliably interpret Fs content.

Three asteroids did not provide self-consistent results for the three starting compositional models. Pyroxene of 446 Aeternitas appears to be dominated by a high-Ca endmember with lesser contribution from low-Ca pyroxene ($Fs_{25}$). However, olivine band centers could not converge to Fa values corresponding to band strength ratios. Similarly, the 2 µm region of 2501 Lohja is fit by two pyroxene bands and is dominated by the high-Ca endmember. Olivine band centers fail to converge to within acceptable deviations for corresponding band strength ratios. Asteroid (31393) 1998 YG8 also fails to converge to self-consistent Fa values calculated from band centers. It appears to have minor pyroxene centered at ~2 µm, but the large uncertainty in this region precludes further investigation into its pyroxene composition.

## *4.4 Discussion*

### *4.4.1 Petrologic Interpretations of Inferred Asteroid Compositions*

Petrologic interpretations can be made about the formation of A-type asteroids using the calculated olivine Fa contents and approximate pyroxene abundances (i.e., < 5% pyroxene for monomineralic olivine and up to 15% in olivine-pyroxene asteroids, based on spectral detection limits for brachinites). These interpretations are limited by the assumption that olivine and pyroxene have equilibrated during metamorphism and/or partial melting. However, given that asteroid spectra are hemispheric averages, Fa content and pyroxene abundances may still be used to place some constraints on redox state and petrogenetic history even if olivine and pyroxene are unequilibrated.

The potential petrogenesis of an asteroid can be interpreted through MGM olivine compositions and pyroxene abundances when compared with the temperature-composition pseudosection (Fig. 4.7) modified from Tomkins et al. (2020) to include

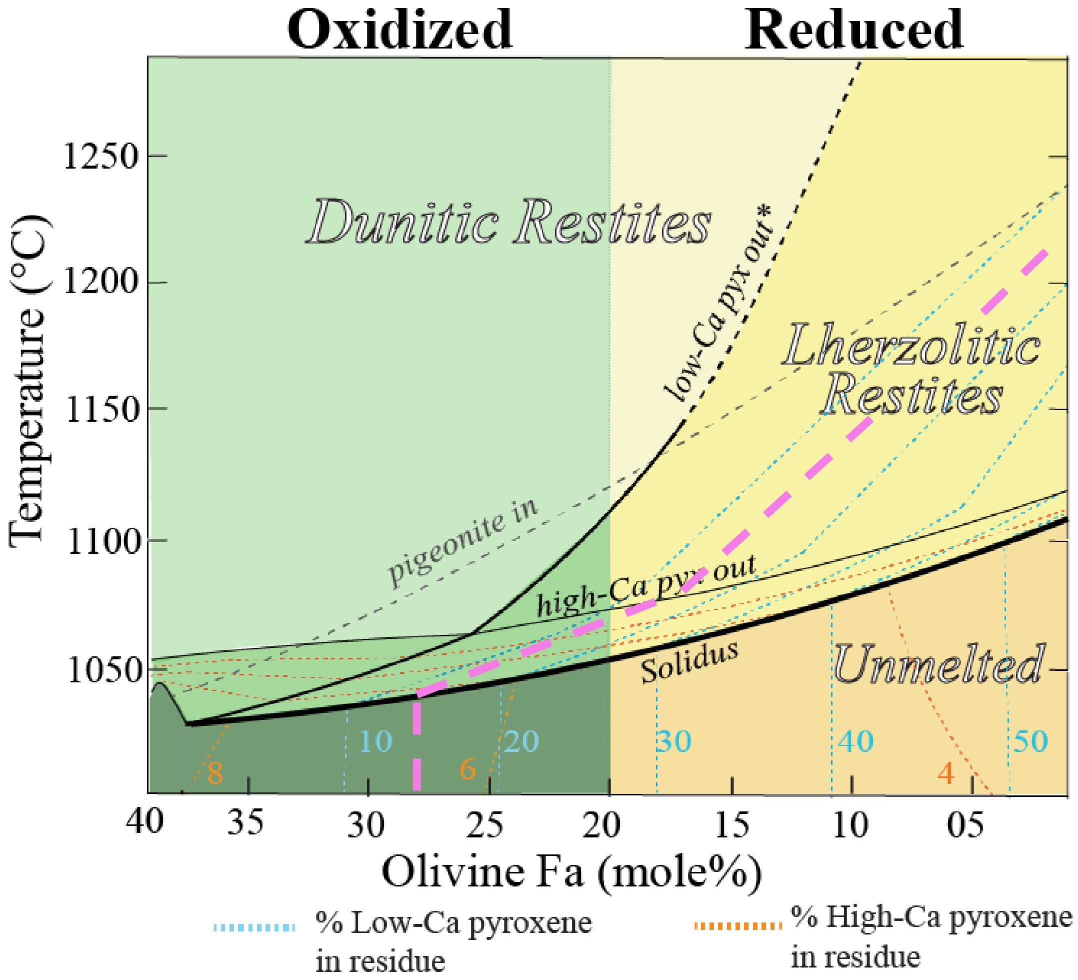

**Fig. 4.7. Composition-Temperature Pseudosection for Restitic and Metamorphosed Meteorites.**

Modified from Tomkins et al. (2020). The Fa content of olivine and proportions of pyroxene can be used to place constraints on potential petrologic interpretations for olivine asteroid spectra (Fig. 4.8). Given that olivine-dominated asteroids are consistent with less than ~20 vol% pyroxene (left of the magenta line), only the most Fa-rich (>Fa$_{30}$) pyroxene-bearing asteroids could represent chondritic mineralogies. Otherwise, olivine-dominated asteroids with or without pyroxene represent restites from a range of oxidation environments and melting histories. Compositions more Fa-rich than Fa$_{40}$ are not accounted for in thermodynamic models, as these mineralogies are only present in equilibrium among mafic enclaves of a few anomalous achondrites whose petrogenesis in unclear (Tomkins et al., 2020).

higher temperatures modeled in Sunshine et al. (2007). Interpreted relative oxidation states and petrologies are summarized in Fig. 4.8.

### *4.4.2 Reduced Restites*

The A-type asteroids, by definition, possess spectral characteristics consistent with >80% olivine (e.g., DeMeo et al., 2019). This immediately rules out a chondritic classification for olivine-dominated asteroids less ferroan than ~$Fa_{25}$, as an equilibrated, chondritic assemblage should contain >20% pyroxene under such conditions and would not be identified as an A-type asteroid. As such, A-type asteroids with reduced olivine compositions below ~$Fa_{25}$ can be considered restitic by default. The only asteroid in this work that is definitively reduced is (16520) 1990 WO3. It is best fit by a low Fa model, and its 2 µm region is dominated by low-Ca pyroxene. The large uncertainties in this region are problematic for interpreting Fs content. The best fit to its spectrum provides a band II center at 1.99 µm, which could be interpreted as FeO-rich, low-Ca pyroxene ($Fs_{60}$); pigeonite; or an unresolvable mixture of high and low-Ca endmembers. Fs-rich pyroxene is considered the least likely explanation because such compositions are not significant components of any reported meteorites and are inconsistent with Fa-Fs trends in equilibrated mineralogies. If better resolution could be acquired for the 2 µm region, it may be possibly to distinguish two-pyroxene mixtures from pigeonite, as demonstrated with laboratory spectra of brachinites in this work. This would provide further insight into the petrogeneis of (16520) 1990 WO3, as a pigeonite would imply temperatures in excess of ~1,150°C, while the presence of a high-Ca pyroxene absorption band would constrain peak temperatures to ~1,075°C.

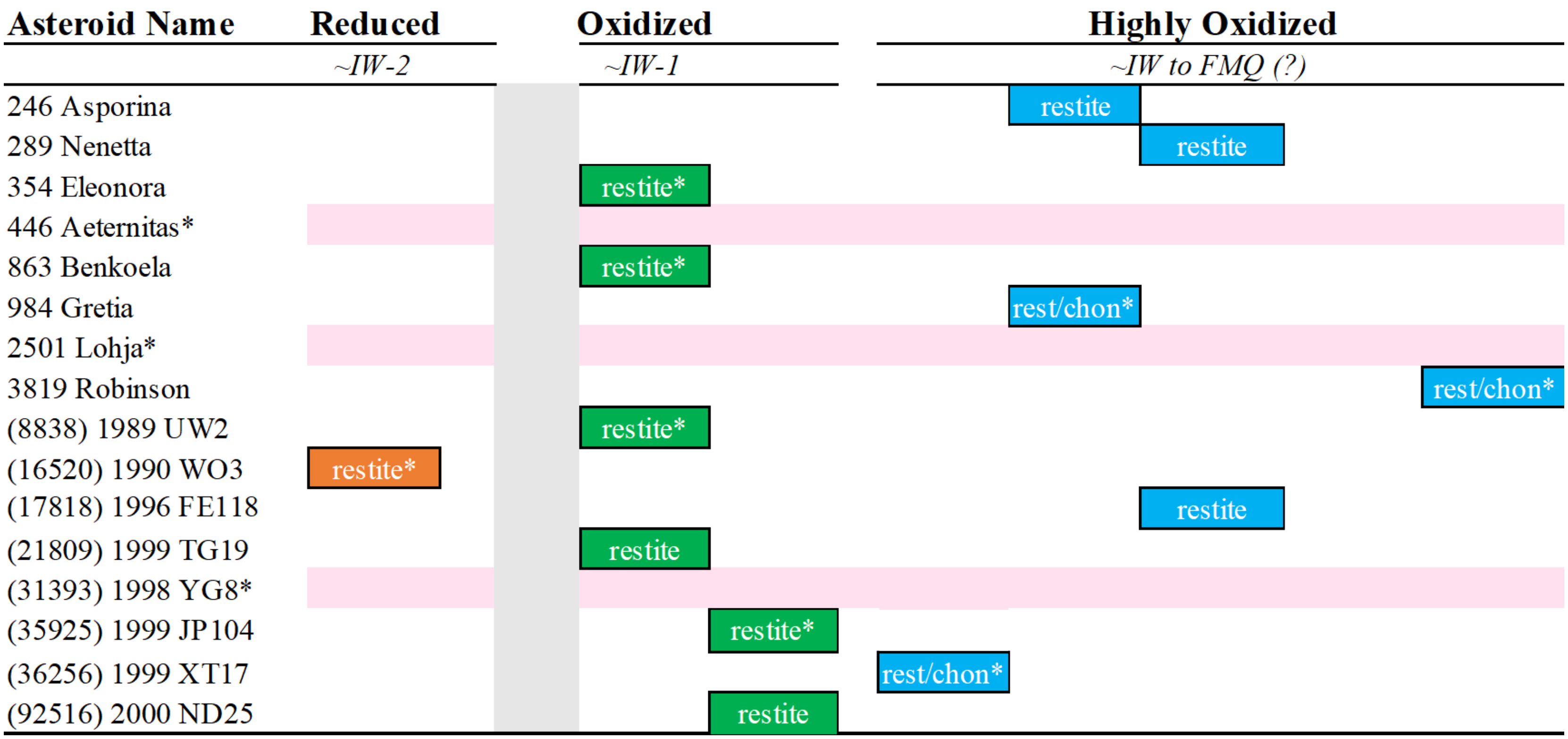

**Fig. 4.8. Comparative analysis of olivine-dominated asteroids.**
Asteroids are positioned according to their Fa content interpretted from spectral models. Oxygen fugacity estimates are based on comparison with equilibrated meteorites with similar mineral chemistries. The grey bar represents the metal-sulfide core transition proposed in previous chapters. * denotes pyroxene-bearing spectra, and pink bars are unresolved asteroids. Among olivine-dominated asteroids examined in this work, only one can be definitively considered reduced with Fa content below the metal-sulfide core transition. The remaining asteroids are consistent with $fO_2$ conditions similar to or more oxidizing than the brachinite family meteorites. Individual petrologic interpretations are detailed in the text.

When both the interpreted olivine Fa content and presence of minor pyroxene are taken into account, Asteroid (16520) 1990 WO3 most closely resembles the silicate components of pallasite meteorites (e.g., Sunshine et al., 2007). If (16520) 1990 WO3 were a pallasite, the high abundance of metal would diminish its silicate absorption features, increase its albedo, and yield a reddened slope (e.g., Cloutis et al., 1990). However, no such features are evident in the spectrum of (16520) 1990 WO3 (DeMeo et al., 2019). Instead, (16520) 1990 WO3 probably represents a fragment of restitic material akin to the silicate components in pallasites. Such residual mineralogies can be produced after ~40% partial melting of an H chondrite-like precursor (Sunshine et al., 2007).

### *4.4.3. Oxidized Chondrites and Restites*

Asteroids with oxidized olivine compositions (~$Fa_{25-40}$) can be classified as either chondritic or restitic based on the presence of pyroxene endmembers and their relative proportions inferred from pyroxene band II strengths. Asteroid spectra with resolvable high-Ca pyroxene bands imply a modal abundance greater than ~5%, according to laboratory analyses of brachinites. In equilibrium with oxidized olivine, potential interpretations of such asteroids are limited to chondritic assemblages, as high-Ca pyroxene begins melting between ~1,030-1,040°C, falling below the ~5% threshold for spectral resolvability at 1,050°C (Tomkins et al., 2020), and is completely melted by 1,100°C (Sunshine et al., 2007). No asteroids yield parameters entirely self-consistent with oxidized chondritic mineralogies, but two of the unresolved asteroids in this work possess resolvable two-pyroxene mixtures dominated by a high-Ca endmember. Similar olivine-dominated assemblages have only been reported in R chondrites (e.g., Bischoff et al., 2011; Chapter 3 of this work). Despite their olivine band centers failing to converge within acceptable limits, both low and intermediate Fa models for 446 Aeternitas and 2501 Lohja yield band centers with average Fa contents reflective of oxidized olivine (Table 4.5). Additionally, 446 Aeternitas is fit by low-Ca pyroxene ($Fs_{25}$) that is consistent oxidized, equilibrated R chondrites (Chapter 3). Thus, it is likely that 446 Aeternitas and 2501 Lohja represent oxidized chondritic asteroids similar to R chondrites, but additional work is needed to reconcile olivine band centers with band strength ratios.

Oxidized olivine asteroid spectra with only low-Ca pyroxene resolvable in the 2 µm region are most consistent with equilibrium assemblages near ~1,050°C, similar to brachinite family primitive achondrites. This includes the largest A-type asteroid, 354 Eleonora, which provides a self-consistent fit with ~$Fs_{25}$ low-Ca pyroxene. 354 Eleonora demonstrates the importance of including minor pyroxene when interpreting olivine Fa content from band centers. Previous work (Table 4.6) identified Eleonora as having band centers consistent with reduced restites (~$Fa_{10}$, Sunshine et al., 2007). However, a small pyroxene absorption is evidenced by the MGM continuum crossing through the spectrum in the 2 µm region. The addition of low-Ca pyroxene bands remedies the poor fit in this portion of the spectrum but prevents low-Fa models from converging to self-consistent results. Instead, intermediate Fa models provide the only self-consistent results between olivine and pyroxene bands centers, and 354 Eleonora is best described as an oxidized restite.

**Table 4.6. Comparison of Inferred Asteroid Oxidation States with Previous Work.**

| | Estimated Olivine Fa Content (mole %) | | | | | | |
|---|---|---|---|---|---|---|---|
| Asteroid Name | This work [a] | 1 [a] | 2 | 3 | 4 | 5 | 6 |
| 246 Asporina | >IW | IW | IW-1 | <5-15 | <IW-2 | >IW | IW to >IW |
| 289 Nenetta | >IW | IW | IW | <5-15 | IW | | >IW |
| 354 Eleonora | IW-1 | <IW-2 | | | | | IW-1 to IW |
| 446 Aeternitas | IW-1 | | | <IW-2 | | IW-2 to >IW | |
| 863 Benkoela | IW-1 | | | <IW-2 | IW-2 | | |
| 984 Gretia | >IW | | | | | | |
| 2501 Lohja | IW-1? | | | | | | |
| 3819 Robinson | >IW | | | | | | |
| (8838) 8189 UW2 | IW-1 | | | | | | |
| (16520) 1990 WO3 | <IW-2 | | | | | | |
| (17818) 1996 FE118 | >IW | | | | | | |
| (21809) 1999 TG19 | IW-1 | | | | | | |
| (31393) 1998 YG8 | ? | | | | | | |
| (35925) 1999 JP104 | IW-1 | | | | | | |
| (36256) 1999 XT17 | >IW | | | | | | |
| (92516) 2000 ND25 | IW-1 | | | | | | |

[a] Oxygen fugacities estimates based on correlation with Fa content observed in this work.
Data sources:1 Sunshine et al. (2007); 2 Cruikshank and Hartmann (1984); 3 Lucey et al. (1998); 4 Sunshine et al. (1998);
5 Reddy et al. (2005); 6 Sanchez et al. (2014). Ranges for (6) were calculated with reported precision.

Pyroxene band II centers consistent with pigeonite or unresolvable two-pyroxene mixtures with average centers at ~2 µm are also interpreted to be restites. The interpreted Fa content and proportions of pyroxene imply that these asteroids reached temperatures approaching the pigeonite facies (1,050-1,100°C; Tomkins et al, 2020). However, the long centers of band II pyroxene prevent interpretation of Fs content. Oxidized restitic asteroids with pigeonite or unresolvable pyroxene mixtures include 863 Benkoela, (8838) 1989 UW2, and (35925) 1999 XT17.

Oxidized olivine asteroids with no resolvable pyroxene are consistent with spectra of oxidized brachinite meteorites that lack resolvable low-Ca pyroxene. These materials have reached temperatures at which pyroxene was exhausted after at least 10% partial melting (1,060-1,100°C; Sunshine et al., 2007; Tomkins et al., 2020). Beyond this observation, the extent of melting is difficult to constrain for olivine-only asteroids. As demonstrated by MELTS thermodynamic models, Fa content of chondritic olivine decreases during melting (Sunshine et al., 2007). However, the Fa content of olivine initially appears to be buffered by melting of pyroxene and plagioclase, and only begins to decrease significantly after ~20% melting in H and R chondrites, after plagioclase and most of pyroxene has been exhausted. Consequently, these asteroids could represent restites after limited partial melting (~20%) of an oxidized chondritic precursor or more extensive melting (at least 30%) of a more Fa-rich, highly oxidized precursor. Additional MELTS modeling with highly oxidized, Fa-rich materials, such as the compositions inferred in the next section, would provide additional constraints on the extent of melting in oxidized olivine-only asteroids. Asteroid (92516) 2000 ND25 is the only unambiguous candidate for the oxidized, olivine-only restite category. Asteroid (21809) 1999 TG19 may also qualify as an oxidized restitic assemblage, but the large uncertainties in the 2 µm region of its spectrum preclude pyroxene fitting. The self-consistent results for olivine band centers and strength ratios, as well as the relatively flat geometry of its 2 µm region suggest that pyroxene likely is not present above a few volume percent. Thus, (21809) 1999 TG19 is considered to be a “probable” oxidized restite.

### *4.4.4 Highly Oxidized Chondrites and/or Restites*

Highly oxidized olivine asteroids include those with olivine band centers and strength ratios consistent with compositions $>Fa_{40}$. Some of the least Fa-rich assemblages may represent materials similar to the most oxidized R chondrites (e.g., Rumuruti, $Fa_{39}$; Bischoff et al., 2011), but the most Fa-rich endmembers of these asteroids are otherwise unrepresented among equilibrated meteorite groups. This complicates petrologic interpretation, as there is no sample that serves as a suitable basis for comparison. As a first order investigation into the possible petrogeneses of Fa-rich, presumably highly oxidized olivine asteroids, possible origins of Fa-rich olivine must first be considered.

While the lower end of this compositional range overlaps some of the most oxidized R chondrites, there are no reports of equilibrated, olivine-dominated meteorites above $\sim Fa_{40}$ in the Meteoritical Bulletin Database (Gattacceca et al., 2020). However, matrix olivine in unequilibrated chondrites can exceed $Fa_{50}$ (e.g., Bischoff et al., 2011; Chapter 3); it could be reasoned that the spectra of these asteroids are consistent with primitive, chondrite-like mineralogies possessing a high ratio of olivine/pyroxene and low chondrule/matrix ratio. However, even the most oxidized equilibrated R chondrites only reach ~$Fa_{39}$ near the fayalite-magnetite-quartz (FMQ) oxidation buffer. The only chondrites with higher $fO_2$ are the CK chondrites, which form magnetite at the expense of fayalite as FeO oxidizes to $Fe_2O_3$ during metamorphism (e.g., Righter and Neff, 2007). Alternatively, Fa-rich olivine may also be produced through nebular processes independent of $fO_2$. One explanation for Fa-rich matrix olivine in chondrites is the partial evaporation of chondrule precursors in the nebula. Experimental work has demonstrated that partial evaporation of olivine in low-pressure regions of the solar nebula can fractionate a Fa-rich gas component from Fa-poor residual olivine during chondrule formation (Nagahara et al., 1994). In this scenario, a recondensed Fa-rich olivine fraction could be produced without the need for high $fO_2$. However, evidence for a corresponding FeO-poor residue is lacking from the spectra of Fa-rich asteroids. Even if the residue were entirely Fa-poor olivine with no pyroxene, the hemispheric average provided by the spectra of these asteroids indicate that they are more Fa-rich than any known meteorite groups. Consequently, this mechanism could only be viable if some nebular process fractionated olivine evaporates from their residues during chondrule formation.

Fa-rich olivine can also form through low temperature aqueous alteration (e.g., Zolotov et al., 2010). No spectral evidence for hydrated phyllosilicates typical of aqueously altered meteorites is present among any of the olivine-dominated asteroid spectra investigated in this study. However, fayalite-rich olivine can form within a narrow range of water/rock ratios below ~350°C without formation of phyllosilicates, or through dehydration of Fe-rich phyllosilicates, with fayalitic olivine becoming progressively more magnesian as temperatures increase into metamorphic facies at ~400°C (Huss et al., 2006; Zolotov et al., 2010). Thus, Fa-rich, olivine-dominated asteroids may be primitive, highly oxidized assemblages that represent a transitional state from aqueously altered to dehydrated metamorphic materials. Subsequent metamorphism of such materials may produce mineralogies similar to CK chondrites or the most highly oxidized R chondrites, which are believed to have been aqueous altered and subsequently dehydrated (e.g., Righter and Neff, 2007).

Regardless of the initial source of Fa-rich olivine, the closest match to the composition of 3819 Robinson ($Fa_{60}$, $Fs_{40}$, and >5 vol% high-Ca pyroxene) is limited to mafic enclaves in some ungrouped, oligoclase-dominated achondrites, although olivine and pyroxene occur in roughly equal proportions in those meteorites (e.g., Day et al., 2009, 2012; Gardner-Vandy et al., 2013). The provenance for these mafic enclaves is unclear, but they may represent fragments of corresponding restitic assemblages from which the oligoclase-dominated melts originated (Gardner-Vandy et al., 2013). Potentially, 3819 Robinson represents a restitic or chondritic assemblage akin to the mafic enclaves in oligoclase-rich achondrites GRA 06128/9. However, additional thermodynamic models are needed to further constrain the petrogenesis of highly oxidized, olivine-dominated asteroids and their potential meteorite analogues.

The remaining four asteroids are similarly Fa-rich but lack resolvable pyroxene absorptions in their spectra. In lieu of suitable meteoritic analogues, it is not unreasonable to assume the trend of increasing abundance of high-Ca pyroxene and olivine Fa content in chondritic meteorites (Fig. 4.7) extends toward such high-Fa compositions. If this is the case, Fa-rich asteroids with no pyroxene absorptions are most likely restites after ~10-20% partial melting of high-Ca pyroxene and plagioclase. It is unlikely that these materials melted extensively, as their Fa contents would rapidly decrease if they follow melting pathways similar to R chondrites (Sunshine et al., 2007). Given these assumptions, 246 Asporina, 289 Nenetta, (17818) 1996 FE118, and (36256) 1999 XT17 are considered "probable" highly oxidized restites after limited partial melting.

Due to the lack of thermodynamic data for meteorites in this compositional space, high-Fa asteroids cannot be definitively categorized as restites or chondrites. However, the positive correlation between $f O_2$ and FeO content of silicates in equilibrated meteorites suggests that under most scenarios, high-Fa asteroids are likely highly oxidized materials, regardless of melting history.

### *4.4.5. The Population of Oxidation Environments Among Asteroidal Restites*

The apparent lack of mantle olivine in the Solar System is a longstanding problem in asteroid studies (e.g., Burbine et al., 2002), and the findings from this work do not resolve the questions surrounding the Solar System's "missing olivine". The population of olivine-dominated asteroids in this study is strongly biased toward relatively oxidized mineralogies (>IW-1). Among these, at least five are likely oxidized restites. Only one of the asteroids in this work, (16520) 1990 WO3, can be unambiguously identified as a reduced restite. This section explores the implications for the population of redox states among differentiated olivine-dominated asteroids and provides comparisons with the meteoritic record.

### *Reduced Differentiation—Where are All the Reduced Mantle Restites?*

As discussed in previous sections, the most probable petrogenesis for a low-Fa, olivine-dominated mineralogy on an asteroidal scale is as a restite after partial melting. Asteroid (16520) 1990 WO3 is the only low-Fa, reduced olivine asteroid in this study. The lack of reduced olivine among restitic asteroids appears to be at odds with differentiated meteorites, which are dominated by comparatively reduced mineralogies (~IW-2 to IW-5; Wadhwa, 2008). However, the apparent dearth of mantle restites from reduced bodies may be underrepresented among A-type and other potentially "olivine-dominated" asteroid spectral classes due in part to and petrologic and taxonomic biases. Relatively reduced precursors (~IW-2) akin to H chondrites typically contain 25-30% pyroxene (Dunn et al., 2010; Tomkins et al., 2020), which is only exhausted after ~50% partial melting at temperatures in excess of ~1,350°C (Sunshine et al., 2007). A parent body with this composition would need to accrete early enough and be sufficiently large to achieve and retain these temperatures for long enough to melt and segregate basaltic phases from residual olivine (e.g., Ghosh et al., 2002). The requirement of larger parent bodies yields several implications for the lack of magnesian olivine among asteroid spectra. Large parent bodies capable of extensive melting likely accreted early (~1-2 My after CAI; Ghosh et al., 2002) and thus were more likely to be incorporated into growing protoplanets. Consequently, most of the "missing" mantle olivine may have been consumed by planet formation. Excavation of olivine-rich mantle fragments could occur during impact and likely accounts for (16520) 1990 WO3, which is otherwise too small (3 km diameter) to have differentiated (Ghosh et al., 2002). The minor pyroxene bands in this asteroid are consistent with ~30% partial melting of an H chondrite-like precursor (e.g., Sunshine et al., 2007). For similar materials that melted less extensively, stronger pyroxene absorption bands would distort the shape of the asteroid's spectrum, which would exclude it from an A-type classification. Consequently, reduced mantle materials may be accounted for among other asteroid spectral classes such as $S_A$-type asteroids, which include broad, distorted absorption features centered around 1 µm (e.g., DeMeo et al., 2009).

Another potential explanation for the bias of A-type asteroids toward more oxidized compositions is the abundance of metal in reduced assemblages. Reduced chondritic assemblages (e.g., H chondrites) contain greater proportions of Fe metal, which cannot efficiently segregate from silicate residues until significant silicate melting has occurred (~50%, McCoy et al., 2006). As discussed earlier, despite its similar olivine composition, (16520) 1990 WO3 is not directly comparable with whole-rock spectra of pallasites because the absorption features of silicates are obscured by the presence of Fe metals (Cloutis et al., 1990). Similarly, much of the asteroidal reduced mantle materials may be obscured by metal entrapped by incomplete differentiation. This could alter the geometry of restite spectra toward characteristics more diagnostic of M or X-type asteroids, which are generally not regarded as mantle restites alongside the A-type asteroids (e.g., DeMeo et al., 2019).

When taken into account with their greater abundances of both pyroxene and Fe metal, the apparent lack of reduced mantle restites among A-type asteroids may be attributed to selection bias, first through petrologic processing and then through taxonomic classification: only extensively melted reduced bodies can efficiently segregate enough pyroxene and metal through differentiation in order to produce materials spectrally consistent with A-type classification.

*Oxidized Differentiation*

The oxidized restite asteroids ($Fa_{25-40}$) represent a critical transition in the evolutionary pathways taken by planetary bodies during differentiation. In previous chapters, it was demonstrated that oxidized, sulfur-rich R chondrites and analogous restites (oxidized brachinites) preserve evidence for the melting and removal of sulfide-dominated liquids, which may have segregated to form planetary cores. Critically, the mantle restites of oxidized bodies are resolvable from reduced restites, and some insight into the divergent differentiation pathways proposed in Chapters 2-3 can be gained at an asteroidal scale. While the transition from metal-dominated to sulfide-dominated core formation in the range of $Fa_{25-35}$ is not directly resolvable in asteroids, the inferred Fa content and pyroxene abundance of asteroids can be used to categorize olivine-dominated asteroids according to redox state and potential petrogenetic histories (i.e., differentiated or chondritic). This provides a method for distinguishing differentiated redox endmembers that may reflect the divergent pathways of core formation proposed in Chapters 2-3.

All but one of the olivine-dominated asteroids in this study occupy or exceed the range of Fa contents among brachinite family achondrites and R chondrites. This not only provides asteroidal evidence for products of oxidized differentiation, but also demonstrates that oxidized differentiation was not a unique event and was perhaps even a common occurrence. This may help to reconcile the diversity of ungrouped “brachinite-like” achondrites that do not easily fit into brachinite family classifications. If the high-Fa, olivine-only are also restites, an as of yet unexplored compositional space can be investigated and contribute to a broader understanding of planetary materials that is not limited to what is represented in the meteoritic record.

The most promising candidate for an oxidized, differentiated asteroid is 354 Eleonora. Its composition overlaps the brachinite family and it is large enough (155 km) to have exceeded the melting point of pentlandite according to thermal modeling for bodies at 2.91 AU (Ghosh et al., 2002). 354 Eleonora accounts for ~80% of the mass of A-type asteroids and provides compelling evidence that oxidized differentiation occurred on protoplanetary scales. The mean density of 354 Eleonora ($3.73 \pm 1.39$ g/cm$^3$; Carry, 2012) is approximately at the median point between olivine and sulfide densities, suggesting that 354 Eleonora could contain a large, sulfide-dominated core. Future remote investigations into oxidized differentiation and characteristics of mantles in general should include 354 Eleonora as a principal target of interest.

### *Distribution of Oxidized, Olivine-dominated Asteroids*

Olivine-dominated asteroids in general are scattered uniformly across the main belt with no association to any particular asteroid family (DeMeo et al., 2019), and this appears to be true for oxidized endmembers, as well (Fig. 4.9). However, the six most oxidized asteroids with $>Fa_{40}$ are all found within 2.77-2.93 AU. Three of these are located in relatively close proximity between 2.76-2.80 AU with proper inclinations between ~6 and 11° and eccentricities from 0.05-0.2, which overlap orbital characteristics for the Gefion family asteroids (e.g., Nesvorny et al., 2015). If there is any dynamical association between these asteroids, they may provide some

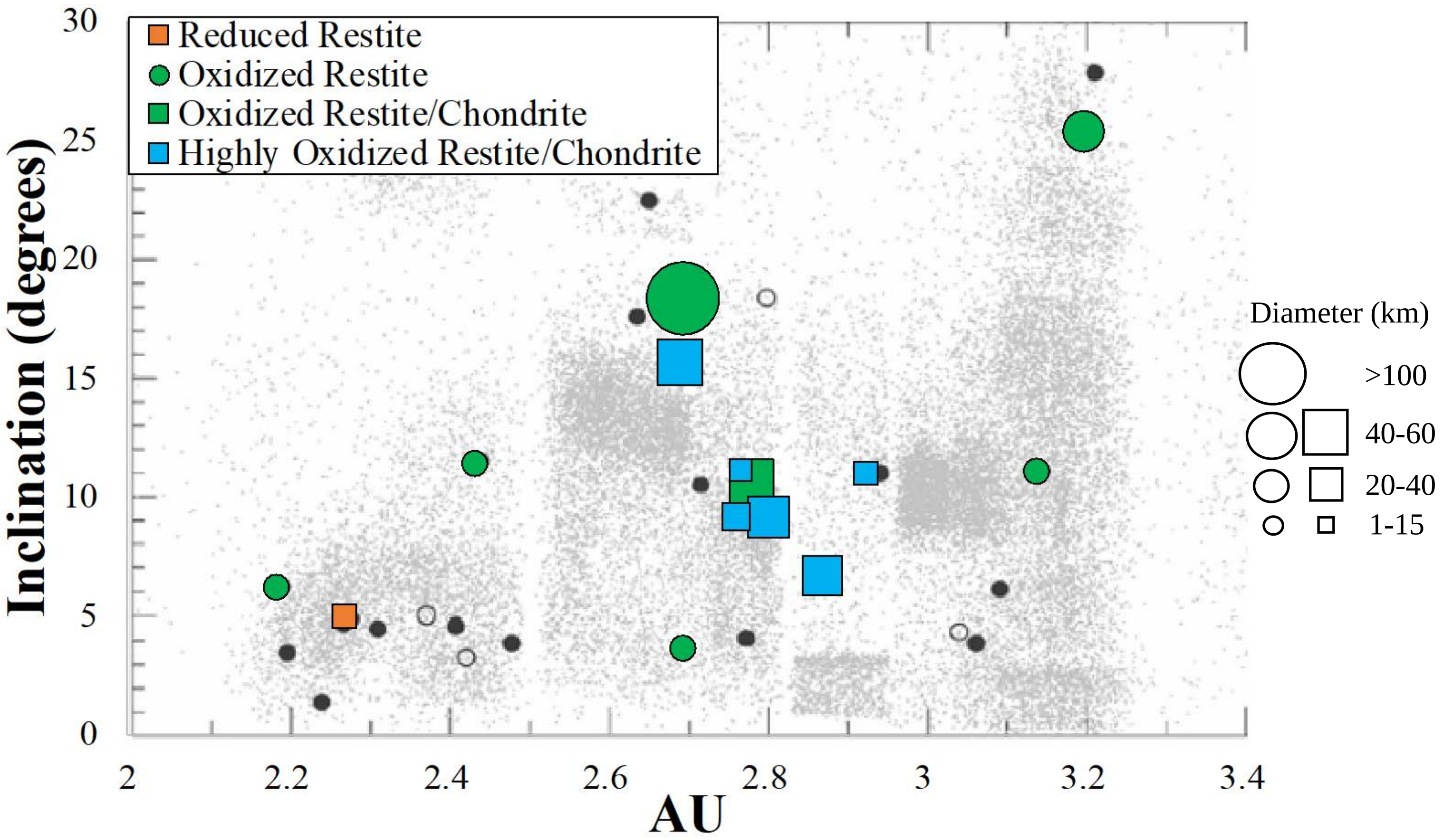

**Fig. 4.9. Olivine-dominated asteroids and ƒO2 environments in the asteroid belt.**
Grayscale circles are A-type asteroids that lack suitable data for compositional interpretation: black filled circles are confirmed A-type asteroids, hollow circles are 'probable' A-type asteroids, and small gray dots are asteroids of other spectral classes (after DeMeO et al., 2019). Only one asteroid in this work is consistent with reduced assemblages near ƒO2 ~IW-2 and is most likely a restitic fragment. Oxidized varieties, consistent with mineralogies formed near $ƒO_2$ ~IW-1, are scattered throughout the main belt with no apparent compositional structure. High Fa asteroids likely formed in highly oxidizing environments (IW to ~FMQ).

insight into the formation of Fa-rich A-type asteroids, but such calculations are beyond this scope of this work. Future work with collaborator S. Bus, who provided IRTF data, will explore potential dynamical links.

## *4.5. Conclusions*

The petrogenetic histories and relative oxidation states of olivine-dominated asteroids can be remotely interpreted from diagnostic spectral bands of olivine and pyroxene. An olivine asteroid spectrum devoid of pyroxene usually represents a restitic asteroidal fragment that formed after partial melting of a precursor parent body. Olivine-dominated asteroids with minor pyroxene absorption features at 2 µm can either represent restites after limited partial melting or unequilibrated mineralogies assembled after impact. Taken into account with Fa content, olivine-dominated asteroids can be categorized according to their inferred redox states and potential petrogenetic histories.

In contrast to previous investigations, this study has identified mineral assemblages that range from reduced mantle restites to highly oxidized, olivine-dominated materials with no suitable meteoritic analogues. This is, in part, because this is the first study to interpret mineral compositions in olivine-dominated asteroids with minor pyroxene content, but also because it is the first to successfully model absorption band parameters with discontinuous data. These two factors more than doubled the number of interpretable olivine-dominated asteroid spectra. Key interpretations for olivine-dominated asteroid spectra include:

- Oxidized restite asteroids (~IW-1) are resolvable from chondritic and reduced restite asteroids via comparison of inferred Fa content, pyroxene composition, and silicate mineral proportions with thermodynamic models generated from meteorites.
- The addition of minor pyroxene absorption bands to an olivine-dominated asteroid spectrum can substantially affect the interpreted Fa content and cannot be overlooked when fitting models to data.
- The majority of olivine-dominated asteroids have Fa content and pyroxene abundances consistent with relatively oxidizing conditions (>IW-1). Only one asteroid in this study, (16520) 1990 WO3, is unambiguously a reduced mantle restite.
- The prevalence of oxidized restitic asteroids over reduced counterparts is likely related to greater initial abundances of pyroxene and metal in reduced precursors, which could obscure diagnostic olivine spectra and bias taxonomy toward oxidized endmembers.
- Multiple oxidized restitic asteroids are identified with diameters large enough to reach internal maximum temperatures that exceed the melting point of pentlandite. The most significant of these is 354 Eleonora, which accounts for ~80% of the mass of A-type asteroids. This asteroid is an ideal candidate to further investigate a planetary body that has likely differentiated to form an oxidized, sulfide-dominated core.

# Chapter 5: Summary, Synthesis, and Future Directions

This Chapter provides a summary and synthesis of key findings from Chapters 2-4 with an emphasis on implications for oxidized differentiation and the population of olivine-dominated asteroids. Future directions for investigations into the systematics of oxidized, sulfur-rich core formation and applicability to broader questions in planetary science are discussed.

## *5.1. Oxidized, sulfur-rich differentiation*

Key findings from Chapters 2 and 3 indicate that the process of differentiation in highly oxidized, sulfur-rich bodies deviates from typical differentiation models in ways that are traceable through petrologic and geochemical investigations. Across the redox range of ~IW-1 to IW-2 and at $f\mathrm{S}_2$ > IT, a significant mineralogic change occurs in Fe-Ni-S systematics wherein the earliest melts of oxidized endmembers are dominated by liquid pentlandite (FeNiS) rather than liquid Fe-FeS. Pentlandite begins melting at ~865°C, prior to the Fe-FeS eutectic (988°C) in metal-bearing systems and before reaching the silicate eutectic (~1050°C). The composition of pentlandite could facilitate melt migration along grain boundaries via capillary action, meaning that sulfide-dominated core formation on oxidized bodies could occur early (prior to silicate melting) and via physical mechanisms that deviate from reduced, metallic core formation. Additionally, the mechanisms that govern the trace element partitioning behaviors among pentlandite-pyrrhotite assemblages in oxidized systems are also distinct from those of reduced, metal-dominated systems. Specifically, the formation of discrete and HSE-rich metals, arsenides and sulfarsenides through selective complexing and the differing affinities among siderophile elements between multiple sulfides distinguishes the trace element systematics of the two evolutionary pathways. The sulfide cores of oxidized, sulfur-rich parent bodies would likely also reflect Mo and W depletions of their precursor sulfides as these redox-sensitive elements partition increasingly into silicate phases at high $fO_2$, which could alter the ages of core formation interpreted from those isotopic systems. Ultimately, these findings provide strong evidence that initial oxidation state directs the subsequent igneous evolution of planetary bodies: reduced materials differentiate to produce an Fe,Ni metal-dominated core, a magnesian peridotitic mantle, and a mafic basaltic crust, whereas oxidized materials may produce a Fe,Ni sulfide-dominated core, a ferroan peridotitic mantle, and a more felsic crust.

### *5.1.1. New questions for oxidized, sulfide-dominated core formation*

In the pursuit of understanding how oxidation state directs core formation pathways, several new questions have arisen. This section highlights outstanding questions raised by the findings of this dissertation, and outlines for future investigations are presented in the following section.

#### *How do pentlandite melts migrate?*

One of the first questions to address for investigating oxidized, sulfur-rich core formation is the physical viability of sulfide segregation from a solid silicate residue. Melting and crystallization experiments in the Fe-Ni-S system provide evidence that pentlandite melts at lower temperatures that pyrrhotite or troilite (Kitakaze et al., 2016), but experiments have not specifically investigated the propagation of liquid pentlandite. The anion/cation ratios of pentlandite in R chondrites (Chapter 3) approach the values of sulfide melts than can propagate along grain boundaries by surface wetting (Gaetani and Grove, 1999), but the incongruent melting of pentlandite apparent in phases diagrams (Kitakaze et al., 2016) may alter those ratios. The contribution of low-Ni pyrrhotite at higher temperatures would increase the anion/cation ratio, facilitating melt propagation, and oxidation of liquid pentlandite through reactions with the residual mineralogy could also lower its surface tension and facilitate migration (Gaetani and Grove, 1999; Brenan and Rose, 2001). As temperatures approach the silicate solidus (Tomkins et al., 2020), the potential for sequestering sulfide melts to form a core decreases, because the densities sulfide melt droplets are not sufficient to overcome the high viscosity of the silicate melts in which they become suspended (e.g., McCoy et al., 2006). Consequently, much of the remaining sulfide liquid will be lost to the basaltic melt fraction that buoyantly ascends to form the crust. This is consistent with trace pentlandite-pyrrhotite assemblages found in oligoclase-rich achondrite GRA 06128/9, which may represent a basaltic melt fraction from an oxidized precursor (e.g., Day et al., 2012; Gardner-Vandy et al., 2013). The similarities between HSE patterns of GRA 06128/9 and brachinites and their overall low HSE concentrations (Day et al., 2012) imply that an HSE-rich fraction must have been segregated from these two components, possibly corresponding to a pentlandite melt (Chapter 2), but evidence for the physical viability of this process must be explored.

### *How can products of oxidized, sulfur-rich core formation be identified?*

Anomalous Ni-rich iron meteorites like Oktibbeha County may represent products of oxidized, sulfide-rich core formation according to equilibrium phase diagrams (Chapter 3; Kitakaze et al., 2016), but the trace element systematics in pentlandite-pyrrhotite-awaruite assemblages during melting and fractional crystallization remain poorly constrained. To identify products of oxidized, sulfide-dominated core formation among iron meteorites, appropriate experimental distribution coefficients for relevant mineral assemblages are needed.

### *5.1.2 Future experimental investigation*

Three key aspects of oxidized, sulfur-rich core formation can be investigated with melting and fractional crystallization experiments: 1) the physical viability of sulfide melt segregation, 2) the petrology and geochemistry of pentlandite-pyrrhotite assemblages during melting, and 3) the petrology and geochemistry of sulfide liquids during fractional crystallization and core formation (Fig. 5.1).

The most direct way of investigating the physical viability of sulfide melt migration is through melting experiments with mineral assemblages consistent with oxidized, sulfur-rich precursors like the R chondrites. Utilizing recent advances in high resolution X-ray computed tomography (μ-CT) techniques the physical process of sulfide melting can be mapped in detail, providing insight into the development of sulfide melt networks and an opportunity to model the migration of sulfide liquids using digital rock physics models (e.g., Bader et al., 2020; Fig. 5.1). This approach provides a robust method for investigating the onset of Fe-Ni-S melt migration within highly oxidized parent bodies and into how sulfide melt migration contributed to the cores of terrestrial planets.

Trace element systematics for oxidized, sulfur-rich core formation can be investigated using an approach similar to geochemical modeling of metallic core

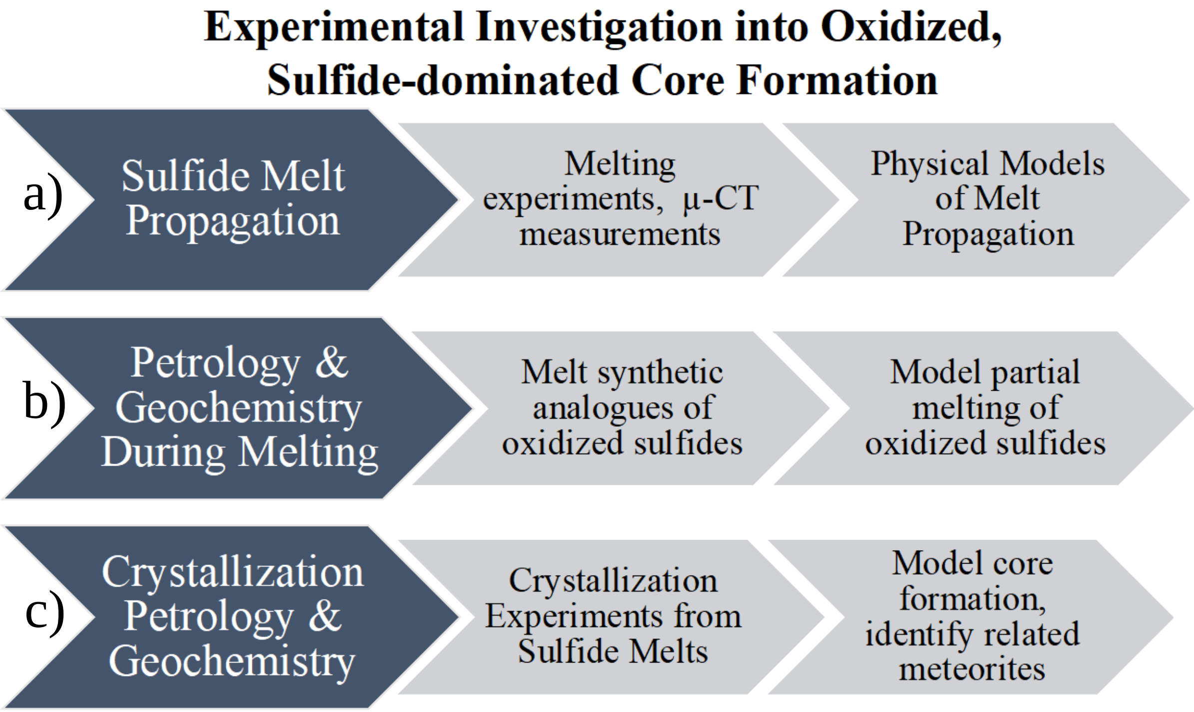

**Fig. 5.1 Outline of future experimental investigations.**
A coordinated series of melting and crystallization experiments can provide an approach to evaluating the potential physical (a), petrologic and geochemical (b-c) systematics of oxidized, sulfide-dominated core formation.

formation. The partitioning of siderophile and chalcophile trace elements among pentlandite, pyrrhotite, and liquid sulfide during partial melting can be quantified by doping synthetic analogs with trace elements concentrations established from equilibrated sulfide assemblages in R chondrites (Section 3.3.4, Fig. 3.6). These assemblages can be melted incrementally at temperatures relevant to the partial melting of Fe-Ni-S phases in oxidized chondrites, and the partitioning coefficients of trace elements between those phases can be used to model partial melting of chondritic sulfides. Results of experiments can be compared to brachinite meteorites to determine the extent of partial melting in the Fe-Ni-S system and the fraction of pentlandite that may have been sequestered to form a core.

Products of oxidized, sulfide-dominated core formation can be identified by modeling their trace element systematics using distribution coefficients from fractional crystallization experiments starting with sulfide liquids. Results from the partial melting experiments described above would provide necessary *a priori* compositional data for sulfide parent melts. Synthetic mixtures of sulfide assemblages, doped with suitable concentrations of trace elements, can be raised to superliquidus temperatures and cooled to isolate crystallization of specific mineral phases. Trace element partition coefficients from these experiments to can be used to model the formation of analogous Ni-rich iron meteorites and identify products of oxidized, sulfide-dominated core formation among the meteoritic record.

Processes of partial melting and fractional crystallization can be further explored for terrestrial planets and moons by incorporating high pressure experiments that replicate the petrologic of sulfur-rich liquids and partitioning behaviors of trace elements in core-forming environments.

## *5.2 Remote detection of oxidized, differentiated asteroids*

Chapter 5 demonstrated that the relative redox state and petrogenetic histories of asteroids can be constrained through interpretation of olivine Fa content and pyroxene abundance in VNIR spectra. It was found that the majority of olivine-dominated asteroids in the main belt are ferroan and consistent with formation in $fO_2$ environments >IW-2. Reduced assemblages are only accounted for by one small asteroid. Several of the oxidized olivine-dominated asteroids are probably mantle restites and could represent bodies that experienced sulfide-dominated core formation.

### *5.2.1 New questions for asteroid populations*

It is widely recognized that the meteoritic record is incomplete and likely offers a biased sampling of Solar System materials. The interpreted compositions of olivine-dominated asteroids in this dissertation engender additional questions about the nature of differentiated materials in the asteroid belt and how they are represented among meteorites. This section explores outstanding questions for olivine-dominated asteroid populations and the characteristics of corresponding differentiated materials.

*Where are the magnesian olivine mantles?*

As discussed in Chapter 4, the dearth of olivine-dominated asteroids in the main belt is at odds with the number of differentiated parent bodies inferred from meteorite studies (e.g., Burbine et al., 2002). Given the observed correlation between olivine/pyroxene ratios in meteorites with their calculated $fO_2$, extensive melting is required to isolate magnesian olivine from spectrally resolvable proportions of pyroxene. The larger parent body sizes required for extensive melting would require catastrophic impacts to excavate km-scale mantle olivine fragments and doing so without contamination from crustal or impactor materials is a difficult task. From this perspective, it is not surprising that there are relatively few magnesian olivine-dominated asteroid spectra. It is possible that some of the "missing" magnesian olivine is accounted for in asteroid spectra that bear >20 vol% pyroxene. Consequently, much of the olivine from reduced bodies in the asteroid belt may be overlooked because its spectral signature is overprinted by pyroxene, which could result in such asteroids being grouped among spectral classes other than A-type. An approach that is capable of remotely determining olivine/pyroxene ratios could provide some insight into the greater population olivine-dominated materials, reduced vs. oxidized environments, and the extent to which differentiation may have occurred among early Solar System objects.

*What are the high-Fa asteroids?*

There are few petrologic conditions under which Fa-rich (~$Fa_{50}$) olivine-dominated asteroids can form, and these materials are not a good mineralogic match with any known meteorite group. They may represent relatively primitive materials that formed under transitional temperature and water/rock ratio conditions between aqueous alteration and metamorphism, products of fractional evaporation and recondensation during chondrule formation, or highly oxidized R chondrite-like assemblages with very low chondrule/matrix ratios (Section 4.4). Given the narrow range of orbital properties for three of the Fa-rich asteroids, they may be sourced from a common parent body. The potential for a common origin will be explored in ongoing collaboration with Dr. S.J. Bus, who supplied the near-infrared spectra for this study.

### *Where are the Basaltic Products of Oxidized Differentiation?*

The focus of Chapter 4 was on olivine-dominated products of oxidized differentiation, but other igneous products of oxidized differentiation may also be resolvable among asteroids. In particular, the felsic crust segregated from oxidized restites should be resolvable from more reduced basaltic crusts. Experimental partial melt products from oxidized precursors are mineralogically consistent with oligoclase-rich achondrites GRA 06128/9 (Gardner-Vandy et al., 2013). Measurements of terrestrial oligoclase in the RELAB spectral database show a broad, shallow absorption at ~1 µm, but the GRA 06128/9 meteorites contain too much terrestrial alteration to interpret their spectra. If terrestrial alteration can be safely removed, its spectrum can be fit and used to search for similar asteroids, which have yet to be identified. Additionally, mafic enclaves within GRA 06128/9 are the closest match to mineral compositions inferred for high Fa asteroids (~$Fa_{60}$, $Fs_{40}$). Potentially, these could represent fragments of corresponding FeO-rich restites, although such compositions would contradict the observed $fO_2$ trend from R chondrites to CK chondrites in which magnetite forms at the expense of fayalite with increasing oxidation. Whatever the origin of the mafic enclaves, if the spectra of GRA 06128/9 contain spectral features consistent with FeO-rich olivine and pyroxene, they would provide the only suitable match to interpreted Fa-rich asteroids among the meteoritic record.

## *5.3. Future observational directions*

### *Accounting for reduced mantle olivine*

Many $S_A$-type asteroids likely contain ~50% olivine, given their spectral similarities to ordinary chondrites and acapulcoite-lodranite clan achondrites (e.g., McCoy et al., 2001; Lucas et al., 2017). Developing an MGM approach that is capable of estimating the olivine/pyroxene ratios of $S_A$-type asteroids could lend greater insight into the population of olivine-rich materials in the asteroid belt and may resolve the missing olivine debate. This could be achieved by assembling terrestrial analogs of olivine-pyroxene mixtures with known proportions and fitting MGM solutions to their laboratory-measured spectra following methods outlined in Ch. 4 for olivine-pyroxene assemblages. The change in the relative band parameters between olivine and pyroxene can be calibrated with the modal mineralogies of analog mixtures and used to estimate reasonable olivine/pyroxene ratios in asteroids. This approach provides a more robust method of interpreting mineralogy than commonly used band area ratios (e.g., Gaffey et al., 1993) because the properties of individual absorption bands are still bound by principles of Crystal Field Theory. Parameterization can also be tuned according to surface temperatures used to estimate FeO content of both olivine and pyroxene. Additionally, the more pyroxene-rich $S_A$-type asteroid spectra would be comparatively simpler to fit than the olivine-dominated spectra in this work because pyroxene features are generally stronger and more well-defined in more pyroxene-rich assemblages. However, given the large population of $S_A$-type asteroids, an automated approach to MGM fitting would be necessary for investigating the population of olivine-rich materials among S-type asteroids.

### *Identifying oxidized crust*

Oligoclase-rich achondrites GRA 06128/9 could offer an opportunity to characterize the spectral characteristics of oxidized, felsic crust, but Fe-rich terrestrial weathering products must first be removed from spectral powders. Typical treatments to remove weathering in meteorite powders involve hydrochloric acid, but this could potentially damage oligoclase and alter its reflectance spectrum. Recent work (Lucas et al., 2017) has found success in treating weathered meteorites with the organic acid ethanolamine thioglycolate, resulting in negligible alteration to silicate phases. Given the low mass of GRA 06128/9, this method could first be tested on weathered terrestrial analogs, i.e., basaltic trachyandesites (Day et al., 2009), then used to treat GRA 06128/9 to remove terrestrial alteration and characterize the reflectance spectra of oxidized crustal material. Doing so would provide valuable parameters need to search for oxidized crustal materials among asteroids.

## 5.4. Application to priority targets in planetary science

### *Asteroid 16 Psyche*

Calculated densities for asteroid 16 Psyche are much closer to the densities of sulfides than to densities of Fe,Ni metals. This has led to a wide variety of alternative hypotheses that involve exotic mineralogies and physical mechanisms to reconcile calculated density and remote interpretations of a metallic surface. Chapter 3 (Section 3.4.4) provides an alternative hypothesis for the formation of 16 Psyche that is easily testable using the Pysche mission's scientific payload. The gamma ray and neutron spectrometer will be able to measure a suite of elements that includes Fe, Ni, and S. Fe/Ni ratios ≤ 1 would provide strong evidence that Psyche is an oxidized, sulfide-dominated core, and would not only provide evidence that sulfide-dominated core formation occurred, but that is relevant on the scale of planetary embryos and possibly much larger bodies.

*Mars*

The latest results from the Mars Insight mission suggest that the Martian core is large (radius = 1830 ±30 km) with a relatively low density between 5.8-6.2 g/cm$^3$ (Stähler et al., 2021). This is consistent with a mostly liquid core dominated by Fe-sulfides and possibly a small inner core composed of metal. This structure is very similar to the predictions for oxidized, sulfide-dominated core formation within asteroidal bodies (Chapter 3, Section 3.4.3) and provides strong evidence that sulfide-dominated core formation occurred on a planetary scale. Additionally, the estimated $fO_2$ for Martian core formation is ~IW-1 (e.g., Righter et al., 2016), which overlaps conditions under which pentlandite melt segregation occurred for brachinites (Chapter 2). Thus, it is feasible that the Martian core has a bulk composition similar to pentlandite and that it formed through processes analogous to those described in Chapters 2-3. If Mars formed an oxidized, sulfide-dominated core, then some differentiated bodies in the outer Solar System bodies (i.e., Jovian and Saturnian satellites) presumably also have cores dominated by sulfides, given that moons like Io and Europa are clearly rich in sulfur and/or oxygen (e.g., Sagan, 1979).

# Appendices

The following sections contain all supplementary materials for Chapters 2-4 as referenced in the text. Chapter 2 supplementary materials are published in *Meteoritics and Planetary Science* (Crossley et al., 2020) and Chapter 3 supplementary materials were submitted along with the Chapter 3 manuscript for peer review in *Geochimica et Cosmochimica Acta*. Supplementary materials for Chapter 4 were assembled with the intention that they would be submitted for publication along with a manuscript draft of Chapter 4.

Supplementary tables, figures, and notes are listed in order according to their first reference in the main text.

# Chapter 2 Supplementary Materials

**Table S2.1.** Meteorites in this study and their sources.

| **Meteorite Name** | **Current Classification[a]** | **Recommended Classification** | **Source** | **Collection ID#** | **Possible Pairing(s)[a]** |
|---|---|---|---|---|---|
| Al Huwaysah 010 | Ungrouped Achondrite | | NHM Bern | 1001-10 | NWA 1500<br>NWA 4042 |
| Eagles Nest | Brachinite | | U of AZ, LPL | UA 140,1 | |
| NWA 4882 | Brachinite | Oxidized Brachinite | Monnig | M1432.1 | NWA 3151, NWA 4969 |
| NWA 5363 | Ungrouped Achondrite | Reduced Brachinite | R.D. Ash | personal collection | NWA 5363 |
| NWA 7297 | Brachinite | Reduced Brachinite | Kiel University | BC 2429.2 | |
| NWA 7299 | Brachinite | Reduced Brachinite | U of Alberta | MET11643/1 | |
| NWA 11304 | R Chondrite (R4) | R3-5 | R.D. Ash | personal collection | |
| NWA 11756 | Brachinite | Reduced Brachinite | R.D. Ash | personal collection | |
| RaS 309 | Brachinite | Oxidized Brachinite | NHM Bern | 0902-118 | |
| Reid 013 | Brachinite | Oxidized Brachinite | Monnig | M1305.1 | Nova 003 |

[a] As of Meteoritical Bulletin 106 (Gattacceca *et al.*, 2019)

**Table S2.2.** External precision (2σ relative % deviation) of standard measurements used for LA-ICP-MS data processing

| | NIST 610 | Coahuila | Filomena | Hoba |
|---|---|---|---|---|
| Co | 4.9 | 2.6 | 3.5 | 1.9 |
| Ni | 3.0 | 2.6 | 2.5 | 4.4 |
| Cu | | 2.6 | 5.1 | |
| Zn | 0.7 | | | |
| Ga | 1.7 | 1.1 | 0.4 | |
| Ge | 1.4 | 1.8 | 1.6 | |
| As | 0.6 | 4.2 | | |
| Mo | 1.5 | 4.6 | 3.3 | 4.2 |
| Ru | | 2.2 | 2.0 | 0.3 |
| Rh | 3.4 | 1.2 | 2.8 | 3.3 |
| Pd | 3.8 | 8.0 | 5.5 | 3.3 |
| Sb | 1.1 | | | |
| W | 0.8 | 1.1 | 2.4 | 7.4 |
| Re | 1.2 | 5.8 | | 6.7 |
| Os | | 5.5 | 4.7 | 4.5 |
| Ir | | 1.9 | 2.2 | 8.1 |
| Pt | 1.3 | 2.2 | 2.6 | 1.2 |
| Au | 3.5 | 1.6 | 4.5 | |

**Table S2.3.** Average major element compositions of olivine in brachinites (wt%)

| | Eagles Nest | σ | RaS 309 | σ | Reid 013 | σ | NWA 4882 | σ | NWA 7297 | σ | NWA 7299 | σ | NWA 11756 | σ |
|---|---|---|---|---|---|---|---|---|---|---|---|---|---|---|
| n= | 12 | | 37 | | 16 | | 24 | | 44 | | 72 | | 10 | |
| $SiO_2$ | 37.1 | *0.2* | 36.6 | *0.4* | 36.4 | *0.4* | 37.1 | *0.3* | 37.2 | *0.2* | 37.7 | *0.2* | 38.0 | *0.4* |
| $TiO_2$ | n.d. | | n.d. | | 0.05 | *0.07* | 0.02 | *0.04* | 0.01 | *0.01* | n.d. | | n.d. | |
| $Al_2O_3$ | n.d. | | n.d. | | n.d. | | 0.01 | *0.01* | n.d. | | 0.01 | *0.02* | n.d. | |
| $Cr_2O_3$ | 0.03 | *0.01* | 0.02 | *0.01* | 0.08 | *0.11* | 0.09 | *0.09* | 0.03 | *0.01* | 0.08 | *0.12* | 0.04 | *0.01* |
| FeO | 28.1 | *0.1* | 30.7 | *0.2* | 30.2 | *0.4* | 29.8 | *0.6* | 27.9 | *0.7* | 27.6 | *0.5* | 24.5 | *0.2* |
| MnO | 0.44 | *0.01* | 0.41 | *0.01* | 0.43 | *0.04* | 0.40 | *0.04* | 0.44 | *0.01* | 0.46 | *0.01* | 0.47 | *0.01* |
| MgO | 34.4 | *0.2* | 31.7 | *0.7* | 31.8 | *0.6* | 32.0 | *0.3* | 35.0 | *0.8* | 35.3 | *0.4* | 37.7 | *0.3* |
| CaO | 0.09 | *0.01* | 0.11 | *0.03* | 0.11 | *0.02* | 0.12 | *0.04* | 0.08 | *0.01* | 0.08 | *0.02* | 0.07 | *0.01* |
| NiO | 0.01 | *0.01* | 0.01 | *<0.01* | 0.02 | *0.01* | 0.01 | *<0.01* | 0.03 | *0.06* | 0.01 | *0.01* | 0.01 | *0.01* |
| $Na_2O$ | n.d. | | n.d. | | 0.01 | *0.01* | n.d. | | n.d. | | n.d. | | n.d. | |
| Sum | 100.2 | | 99.5 | | 99.0 | | 99.5 | | 100.7 | | 101.2 | | 100.8 | |
| Fe/Mg | 0.46 | *<0.01* | 0.54 | *0.01* | 0.53 | *0.01* | 0.52 | *0.01* | 0.45 | *0.02* | 0.44 | *0.01* | 0.37 | *<0.01* |
| Fe/Mn | 63.4 | *1.2* | 74.8 | *2.2* | 69.8 | *8.0* | 73.0 | *7.7* | 62.7 | *3.3* | 59.4 | *1.0* | 51.6 | *1.1* |
| Mg# | 68.5 | *0.2* | 64.7 | *0.6* | 65.3 | *0.5* | 65.7 | *0.6* | 69.1 | *1.0* | 69.5 | *0.6* | 73.3 | *0.2* |

n.d. = not detected

**Table S2.4.** Average major element compositions of high-Ca pyroxene in brachinites (wt%).

|  | Eagles Nest | σ | RaS 309 | σ | Reid 013 | σ | NWA 4882 | σ | NWA 7297 | σ | NWA 7299 | σ | NWA 11756 | σ |
|---|---|---|---|---|---|---|---|---|---|---|---|---|---|---|
| n= | 3 |  | 12 |  | 10 |  | 11 |  | 20 |  | 31 |  | 8 |  |
| $SiO_2$ | 53.0 | *0.2* | 53.2 | *0.6* | 54.3 | *0.3* | 54.3 | *0.6* | 53.4 | *0.2* | 53.7 | *0.2* | 53.3 | *0.5* |
| $TiO_2$ | 0.17 | *0.01* | 0.12 | *0.01* | 0.29 | *0.01* | 0.21 | *0.12* | 0.29 | *0.03* | 0.17 | *0.01* | 0.21 | *0.01* |
| $Al_2O_3$ | 0.79 | *0.02* | 1.03 | *0.08* | 0.95 | *0.01* | 0.98 | *0.03* | 0.70 | *0.08* | 0.74 | *0.08* | 0.90 | *0.03* |
| $Cr_2O_3$ | 0.89 | *0.01* | 0.71 | *0.06* | 0.66 | *<0.01* | 0.78 | *0.06* | 0.78 | *0.05* | 0.83 | *0.07* | 0.73 | *0.02* |
| FeO | 6.51 | *0.09* | 6.28 | *0.41* | 6.08 | *0.11* | 6.06 | *0.34* | 6.20 | *0.18* | 6.33 | *0.24* | 5.71 | *0.12* |
| MnO | 0.23 | *0.01* | 0.14 | *0.01* | 0.14 | *0.02* | 0.15 | *0.04* | 0.22 | *0.01* | 0.23 | *0.02* | 0.24 | *<0.01* |
| MgO | 15.7 | *<0.1* | 15.1 | *0.1* | 15.0 | *0.3* | 14.9 | *0.1* | 16.2 | *0.1* | 16.5 | *0.3* | 16.1 | *0.1* |
| CaO | 20.8 | *0.2* | 22.6 | *0.2* | 22.7 | *0.1* | 22.6 | *0.3* | 21.3 | *0.3* | 21.1 | *0.5* | 21.3 | *0.1* |
| NiO | n.d. |  | n.d. |  | 0.02 | *0.01* | n.d. |  | 0.02 | *0.05* | n.d. |  | 0.01 | *<0.01* |
| $Na_2O$ | 0.56 | *0.01* | 0.42 | *0.02* | 0.68 | *0.01* | 0.77 | *0.06* | 0.80 | *0.05* | 0.46 | *0.03* | 0.42 | *0.02* |
| Sum | 98.7 |  | 99.5 |  | 100.8 |  | 100.7 |  | 99.9 |  | 100.1 |  | 98.9 |  |
| Fe/Mg | 0.23 | *<0.01* | 0.23 | *<0.01* | 0.23 | *0.01* | 0.23 | *0.01* | 0.22 | *0.01* | 0.22 | *0.01* | 0.20 | *<0.01* |
| Fe/Mn | 27.6 | *1.4* | 44.0 | *2.4* | 51.3 | *2.0* | 40.4 | *12.1* | 27.4 | *0.8* | 26.7 | *2.7* | 23.4 | *0.7* |
| Mg# | 81.2 | *0.2* | 81.1 | *1.0* | 81.5 | *0.6* | 81.5 | *0.8* | 82.3 | *0.4* | 82.3 | *0.5* | 83.4 | *0.3* |
| Wo % | 43.5 | *0.3* | 46.5 | *0.5* | 46.9 | *0.4* | 46.9 | *0.5* | 43.8 | *0.5* | 43.1 | *1.0* | 44.2 | *0.3* |
| En % | 45.8 | *0.1* | 43.4 | *0.3* | 43.3 | *0.8* | 43.2 | *0.2* | 46.3 | *0.2* | 46.8 | *0.8* | 46.5 | *0.3* |
| Fs % | 10.7 | *0.2* | 10.1 | *0.6* | 9.82 | *0.58* | 9.84 | *0.52* | 9.97 | *0.31* | 10.1 | *0.4* | 9.25 | *0.20* |

**Table S2.5.** Average major element compositions of low-Ca pyroxene and plagioclase in brachinites (wt%).

| | NWA 4882 | σ | NWA 7297 | σ | NWA 7299 | σ | NWA 11756 | σ | Reid 013 | σ | | NWA 4882 | σ | NWA 7299 | σ | NWA 11756 | σ |
|---|---|---|---|---|---|---|---|---|---|---|---|---|---|---|---|---|---|
| n= | 5 | | 10 | | 30 | | 10 | | 5 | | n= | 5 | | 15 | | 5 | |
| $SiO_2$ | 54.6 | 0.3 | 54.2 | 0.2 | 55.12 | 0.1 | 54.8 | 0.5 | 54.4 | 0.3 | $SiO_2$ | 58.0 | 0.77 | 61.9 | 0.3 | 59.4 | 0.3 |
| $TiO_2$ | 0.02 | 0.01 | 0.13 | 0.02 | 0.08 | 0.01 | 0.10 | 0.01 | n.d. | 0.01 | $Al_2O_3$ | 25.6 | 0.21 | 23.9 | 0.2 | 26.3 | 0.3 |
| $Al_2O_3$ | 0.06 | 0.03 | 0.27 | 0.02 | 0.30 | 0.02 | 0.42 | 0.02 | 0.03 | 0.01 | FeO | 1.06 | 0.66 | 0.18 | 0.10 | 0.18 | 0.06 |
| $Cr_2O_3$ | n.d. | | 0.20 | 0.02 | 0.22 | 0.01 | 0.24 | 0.02 | n.d. | | MgO | 0.22 | 0.05 | 0.01 | 0.01 | 0.01 | 0.01 |
| FeO | 17.6 | 0.1 | 16.5 | 0.4 | 16.4 | 0.1 | 14.8 | 0.1 | 18.2 | 0.4 | CaO | 6.98 | 0.28 | 5.09 | 0.19 | 7.31 | 0.08 |
| MnO | 0.40 | 0.02 | 0.43 | <0.01 | 0.45 | 0.01 | 0.46 | 0.01 | 0.41 | 0.02 | $Na_2O$ | 7.45 | 0.38 | 8.47 | 0.21 | 7.44 | 0.07 |
| MgO | 26.1 | 0.3 | 26.8 | 0.3 | 27.6 | 0.1 | 27.9 | 0.2 | 26.2 | 0.3 | $K_2O$ | 0.06 | <0.01 | 0.20 | 0.02 | 0.11 | 0.01 |
| CaO | 1.21 | 0.13 | 1.07 | 0.02 | 1.12 | 0.03 | 1.06 | 0.01 | 0.95 | 0.21 | Sum | 99.4 | | 99.7 | | 100.7 | |
| NiO | n.d. | | 0.02 | 0.01 | 0.01 | 0.01 | 0.01 | <0.01 | n.d. | | An % | 34.0 | 1.9 | 24.6 | 1.1 | 35.0 | 0.4 |
| $Na_2O$ | 0.02 | 0.01 | 0.04 | 0.01 | 0.02 | 0.01 | 0.03 | 0.01 | 0.01 | 0.01 | Ab % | 65.7 | 1.9 | 74.2 | 1.1 | 64.4 | 0.4 |
| Sum | 99.94 | | 99.7 | | 101.4 | | 99.8 | | 100.2 | | Or % | 0.37 | 0.01 | 1.13 | 0.11 | 0.64 | 0.06 |
| Fe/Mg | 0.38 | 0.01 | 0.35 | 0.01 | 0.33 | <0.01 | 0.30 | <0.01 | 0.39 | 0.01 | | | | | | | |
| Fe/Mn | 43.3 | 2.00 | 38.3 | 0.8 | 36.3 | 0.4 | 32.0 | 0.5 | 43.9 | 2.0 | | | | | | | |
| Mg# | 72.6 | 0.4 | 74.3 | 0.6 | 75.0 | 0.2 | 77.2 | 0.1 | 71.9 | 0.6 | | | | | | | |
| Wo % | 2.36 | 0.26 | 2.09 | 0.04 | 2.15 | 0.05 | 2.06 | 0.04 | 1.84 | 0.41 | | | | | | | |
| En % | 70.9 | 0.5 | 72.8 | 0.6 | 73.3 | 0.2 | 75.6 | 0.1 | 70.6 | 0.8 | | | | | | | |
| Fs % | 26.8 | 0.3 | 25.1 | 0.6 | 24.5 | 0.2 | 22.4 | 0.1 | 26.8 | 0.6 | | | | | | | |

**Table S2.6.** Average major element compositions of chromite in brachinites (wt%).

| | Eagles Nest | σ | RaS 309 | σ | Reid 013 | σ | NWA 4882 | σ | NWA 7297 | σ | NWA 7299 | σ | NWA 11756 | σ |
|---|---|---|---|---|---|---|---|---|---|---|---|---|---|---|
| n= | 2 | | 20 | | 27 | | 30 | | 8 | | 32 | | 13 | |
| $TiO_2$ | 1.31 | *0.02* | 0.90 | *0.02* | 0.99 | *0.01* | 0.76 | *0.01* | 1.46 | *0.01* | 1.25 | *0.01* | 1.28 | *0.02* |
| $SiO_2$ | n.d. | | 0.02 | *0.01* | 0.10 | *0.01* | 0.11 | *0.01* | 0.10 | *0.01* | 0.10 | *0.01* | 0.01 | *0.01* |
| $Cr_2O_3$ | 56.2 | *0.1* | 51.2 | *0.2* | 51.4 | *0.2* | 52.0 | *0.2* | 55.6 | *0.3* | 56.3 | *0.2* | 54.9 | *0.3* |
| $Al_2O_3$ | 8.17 | *0.01* | 13.5 | *0.1* | 13.6 | *0.2* | 13.5 | *0.2* | 8.49 | *0.11* | 8.55 | *0.08* | 11.1 | *0.3* |
| $V_2O_3$ | 0.72 | *0.01* | 0.68 | *0.01* | 0.73 | *0.01* | 0.75 | *0.01* | 0.74 | *0.01* | 0.76 | *0.01* | 0.62 | *0.01* |
| FeO | 28.0 | *<0.1* | 28.3 | *0.3* | 28.1 | *0.2* | 27.8 | *0.2* | 27.8 | *0.4* | 27.3 | *0.4* | 26.4 | *0.4* |
| MnO | 0.48 | *0.01* | 0.40 | *0.01* | 0.36 | *0.01* | 0.36 | *0.01* | 0.46 | *0.01* | 0.43 | *0.01* | 0.57 | *0.01* |
| MgO | 4.39 | *0.04* | 4.81 | *0.10* | 4.81 | *0.14* | 4.88 | *0.10* | 4.35 | *0.13* | 4.68 | *0.22* | 5.62 | *0.24* |
| ZnO | 0.38 | *0.01* | 0.27 | *0.11* | 0.34 | *0.06* | 0.35 | *0.07* | 0.11 | *0.04* | 0.17 | *0.11* | 0.02 | *0.05* |
| CaO | n.d. | | n.d. | | 0.01 | *0.01* | n.d. | | n.d. | | n.d. | | 0.01 | *0.01* |
| Sum | 99.7 | | 100.0 | | 100.5 | | 100.4 | | 99.2 | | 99.6 | | 100.6 | |
| Fe/Mg | 3.60 | *0.02* | 3.31 | *0.10* | 3.28 | *0.12* | 3.19 | *0.08* | 3.59 | *0.14* | 3.27 | *0.22* | 2.64 | *0.17* |
| Fe/Mn | 57.3 | *1.4* | 70.3 | *1.8* | 77.3 | *1.7* | 77.1 | *1.6* | 60.0 | *1.1* | 62.2 | *1.1* | 46.0 | *0.8* |
| Mg# | 21.8 | *0.1* | 23.2 | *0.5* | 23.4 | *0.6* | 23.9 | *0.4* | 21.8 | *0.7* | 23.4 | *1.1* | 27.5 | *1.2* |
| Cr# | 82.2 | *<0.1* | 71.8 | *0.2* | 71.7 | *0.3* | 72.2 | *0.3* | 81.5 | *0.3* | 81.6 | *0.1* | 76.8 | *0.5* |
| Cm% | 60.8 | *0.2* | 53.1 | *0.4* | 52.7 | *0.6* | 53.2 | *0.4* | 59.9 | *0.5* | 59.2 | *1.0* | 52.5 | *0.9* |
| Pc% | 18.5 | *0.1* | 17.0 | *0.4* | 17.2 | *0.5* | 17.5 | *0.3* | 18.4 | *0.6* | 19.7 | *0.9* | 21.8 | *1.0* |
| Hc% | 13.2 | *<0.1* | 20.9 | *0.2* | 20.8 | *0.2* | 20.5 | *0.2* | 13.6 | *0.3* | 13.4 | *0.2* | 15.8 | *0.5* |
| Sp% | 4.01 | *0.03* | 6.69 | *0.15* | 6.78 | *0.23* | 6.77 | *0.15* | 4.19 | *0.10* | 4.45 | *0.23* | 6.57 | *0.28* |
| Uv% | 3.51 | *0.04* | 2.34 | *0.04* | 2.56 | *0.02* | 1.96 | *0.02* | 3.91 | *0.02* | 3.32 | *0.04* | 3.31 | *0.06* |

**Table S2.7.** Major element compositions of olivine and high-Ca pyroxene in ungrouped achondrites.

| | *Olivine* | | | | | *High-Ca Pyroxene* | | | |
|---|---|---|---|---|---|---|---|---|---|
| | NWA 5363 | σ | Al Huw. 010 | σ | | NWA 5363 | σ | Al Huw. 010 | σ |
| n= | 10 | | 8 | | n= | 5 | | 10 | |
| $SiO_2$ | 37.6 | *0.5* | 39.5 | *0.2* | $SiO_2$ | 53.7 | *0.3* | 54.0 | *0.4* |
| $TiO_2$ | n.d. | | n.d. | | $TiO_2$ | 0.19 | *0.01* | 0.12 | *0.01* |
| $Al_2O_3$ | n.d. | | n.d. | | $Al_2O_3$ | 0.69 | *0.06* | 0.73 | *0.04* |
| $Cr_2O_3$ | 0.08 | *0.12* | 0.02 | *0.01* | $Cr_2O_3$ | 0.77 | *0.05* | 0.70 | *0.03* |
| FeO | 27.1 | *0.4* | 16.7 | *0.1* | FeO | 6.11 | *0.09* | 7.14 | *0.11* |
| MnO | 0.45 | *0.01* | 0.51 | *0.01* | MnO | 0.22 | *0.01* | 0.21 | *0.01* |
| MgO | 35.4 | *0.2* | 43.6 | *0.1* | MgO | 15.7 | *<0.1* | 15.6 | *0.1* |
| CaO | 0.08 | *0.01* | 0.03 | *0.01* | CaO | 21.2 | *0.2* | 20.9 | *0.2* |
| NiO | 0.02 | *0.03* | n.d. | | NiO | 0.01 | *<0.01* | n.d. | |
| $Na_2O$ | n.d. | | n.d. | | $Na_2O$ | 0.47 | *0.03* | 0.40 | *0.02* |
| Sum | 100.8 | | 100.3 | | Sum | 99.2 | | 98.8 | |
| Fe/Mg | 0.43 | *0.01* | 0.21 | *<0.01* | Fe/Mg | 0.22 | *<0.01* | 0.26 | *0.01* |
| Fe/Mn | 59.4 | *1.8* | 32.0 | *0.5* | Fe/Mn | 27.0 | *0.7* | 33.1 | *0.8* |
| Mg# | 70.0 | *0.4* | 82.4 | *<0.1* | Mg# | 82.2 | *0.2* | 79.6 | *0.3* |
| | | | | | Wo % | 44.3 | *0.3* | 43.3 | *0.3* |
| | | | | | En % | 45.8 | *0.2* | 45.1 | *0.2* |
| | | | | | Fs % | 9.94 | *0.14* | 11.6 | *0.2* |

**Table S2.8.** Major element compositions of chromite in ungrouped achondrites

|  | NWA 5363 | σ | Al Huwaysah 010 | σ |
|---|---|---|---|---|
| n= | 14 |  | 20 |  |
| $TiO_2$ | 1.40 | *0.03* | 1.03 | *0.01* |
| $SiO_2$ | 0.01 | *0.01* | 0.02 | *0.01* |
| $Cr_2O_3$ | 56.7 | *0.5* | 56.4 | *0.3* |
| $Al_2O_3$ | 8.36 | *0.15* | 10.2 | *0.1* |
| $V_2O_3$ | 0.67 | *0.02* | 0.71 | *0.01* |
| FeO | 27.8 | *0.6* | 23.4 | *0.3* |
| MnO | 0.56 | *0.01* | 0.75 | *0.02* |
| MgO | 4.47 | *0.40* | 7.42 | *0.21* |
| ZnO | 0.14 | *0.07* | 0.03 | *0.03* |
| CaO | n.d. |  | n.d. |  |
| Sum | 100.1 |  | 99.9 |  |
| Fe/Mg | 3.48 | *0.38* | 1.77 | *0.08* |
| Fe/Mn | 49.2 | *0.8* | 31.0 | *0.58* |
| Mg# | 22.3 | *1.9* | 36.1 | *1.0* |
| Cr# | 82.0 | *0.3* | 78.9 | *0.2* |
| Cm% | 60.0 | *1.6* | 47.6 | *0.8* |
| Pc% | 19.0 | *1.6* | 29.2 | *0.8* |
| Hc% | 13.2 | *0.4* | 12.8 | *0.2* |
| Sp% | 4.16 | *0.37* | 7.83 | *0.22* |
| Uv% | 3.72 | *0.05* | 2.66 | *0.03* |

**Table S2.9.** Average major element compositions for silicates in R chondrite NWA 11304 (wt%)

| | *Olivine* | σ | *High-Ca Pyroxene* | σ | *Low-Ca Pyroxene* | σ |
|---|---|---|---|---|---|---|
| n= | 17 | | 3 | | 14 | |
| $SiO_2$ | 36.8 | *0.4* | 54.7 | *2.1* | 55.7 | *3.5* |
| $TiO_2$ | 0.03 | *0.04* | 0.11 | *0.09* | 0.12 | *0.14* |
| $Al_2O_3$ | 0.08 | *0.15* | 0.62 | *1.10* | 0.40 | *3.45* |
| $Cr_2O_3$ | 0.15 | *0.16* | 0.37 | *0.24* | 0.60 | *0.54* |
| FeO | 33.3 | *0.5* | 5.81 | *3.80* | 13.9 | *7.6* |
| MnO | 0.42 | *0.01* | 0.12 | *0.12* | 0.40 | *0.08* |
| MgO | 30.3 | *0.37* | 15.5 | *1.6* | 25.8 | *9.1* |
| CaO | 0.09 | *0.04* | 23.0 | *1.5* | 3.90 | *1.64* |
| NiO | 0.22 | *0.07* | n.d. | | n.d. | |
| $Na_2O$ | 0.01 | *0.01* | 0.40 | *0.12* | 0.20 | *0.78* |
| Sum | 101.3 | | 100.5 | | 101.0 | |
| Fe/Mg | 0.62 | *0.01* | 0.21 | *0.20* | 0.31 | *0.72* |
| Fe/Mn | 79.1 | *1.4* | 44.6 | *5.5* | 34.1 | *20.4* |
| Mg# | 61.8 | *0.5* | 82.7 | *10.4* | 76.9 | *19.5* |

n.d. = not detected

**Table S2.10.** Re-Os isotopic ratios and analytical parameters for bulk samples of NWA 4882 and NWA 11756.

| | NWA 4882 | NWA 11756 |
|---:|:---:|:---:|
| Re (ppb) | 31.3 | 28.5 |
| Os (ppb) | 127 | 2900 |
| $^{187}$Re/$^{188}$Os | 1.18 | 0.047 |
| ±2SE | 0.0071 | 0.0003 |
| $^{187}$Os/$^{188}$Os | 0.128 | 0.123 |
| ±2SE | 0.00008 | 0.00009 |
| $^{187}$Os/$^{188}$Os(i) | 0.035 | 0.120 |
| $^{187}$Os/$^{188}$Os(i) CH | 0.095 | 0.095 |
| Sample wt., g | 0.04801 | 0.00814 |
| Total Re, ng | 1.50 | 0.23 |
| % Re blank | 0.09 | 0.59 |
| Total Os, ng | 6.11 | 23.60 |
| % Os blank | 0.005 | 0.001 |
| Smpl wt., g | 0.048 | 0.008 |
| Total Ir, ng | 2.58 | 20.5 |
| % Ir blank | 0.18 | 0.02 |
| Total Ru, ng | 9.16 | 19.5 |
| % Ru blank | 0.03 | 0.01 |
| Total Pt, ng | 2.98 | 29.3 |
| % Pt blank | 4.10 | 0.42 |
| Total Pd, ng | 1.27 | 7.85 |
| % Pd blank | 0.71 | 0.12 |

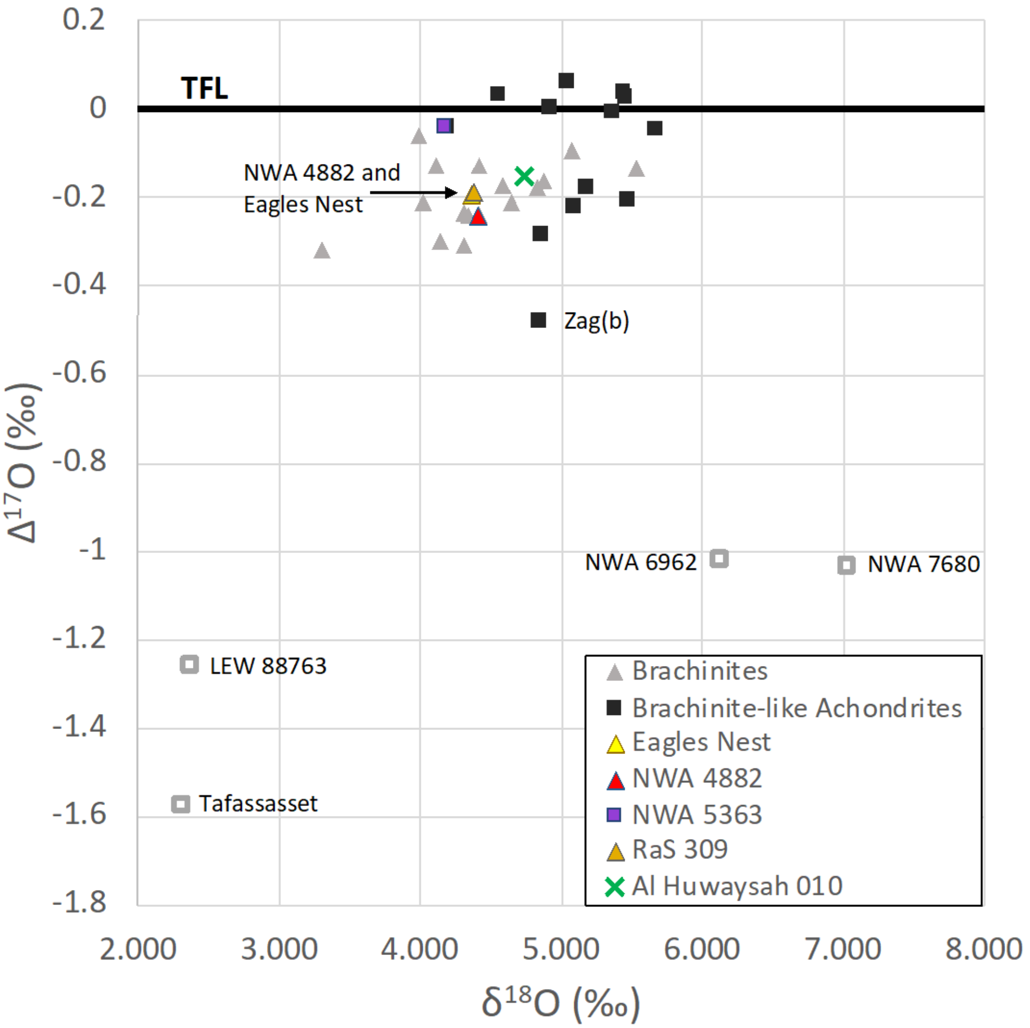

**Figure S2.1. Oxygen isotopes for the brachinite family and ferrous oxidized asteroidal achondrites.** Most brachinite family members fall within ~0.06 to -0.3 ‰ $\Delta^{17}O$. Unique symbols are meteorites that were analyzed in this study. All oxygen isotopic data are from Goodrich *et al.* (2012), Keil (2014), and Greenwood *et al.* (2012, 2017). No O-isotope data have been published for NWA 7297, 7299, and 11756; their classification as brachinites is based on modal mineralogy and mineral chemistry.

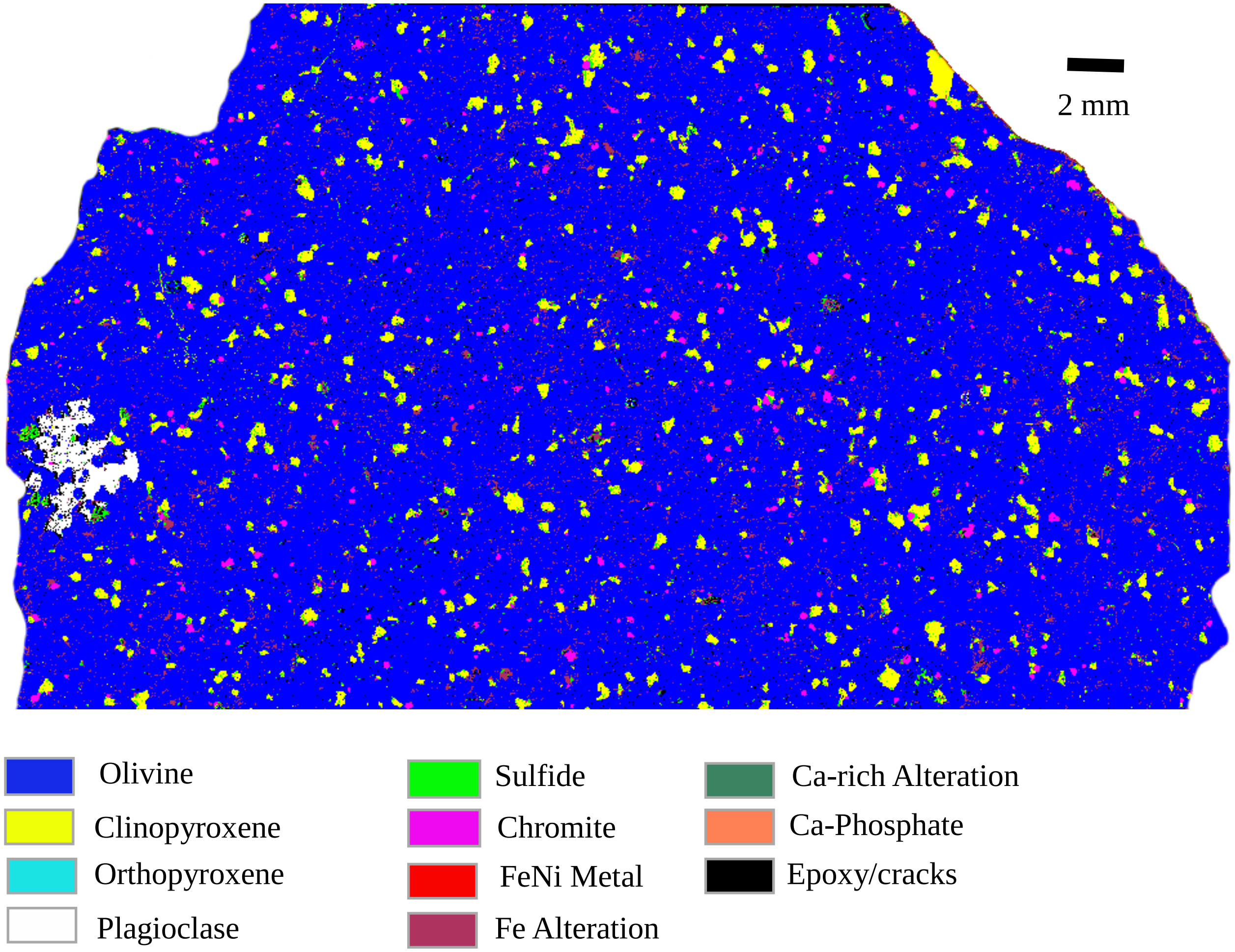

**Figure S2.2.** Modal mineral map of Al Huwaysah 010.

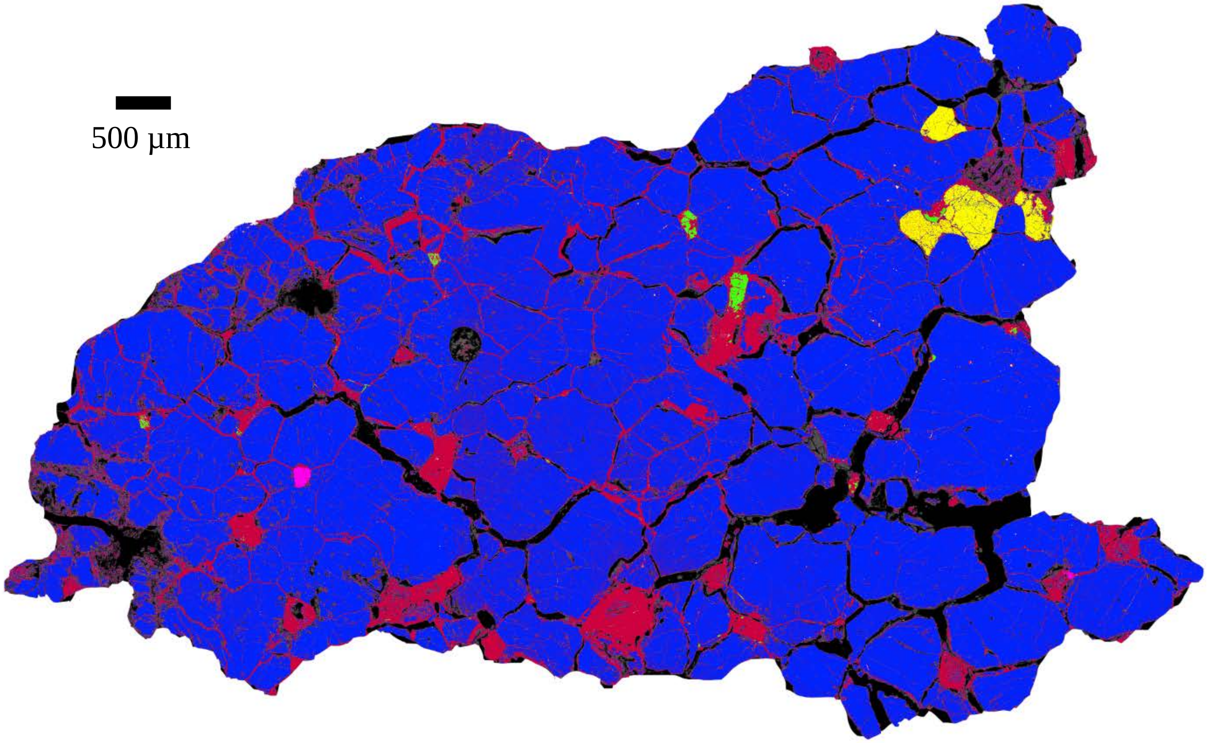

**Figure S2.3.** Modal mineral map of Eagles Nest. Colors indicate the same mineral phases as in Figure S2.2. Due to an EDS detector malfunction, a typical modal mineral map could not be produced using our methods, so EDS maps of Eagles Nest were combined with reflected light microscopy and BSE imagery to identify mineral phases. Grains were indexed manually in Adobe Photoshop and modal abundance was calculated using the same pixel counting methods as in other specimens.

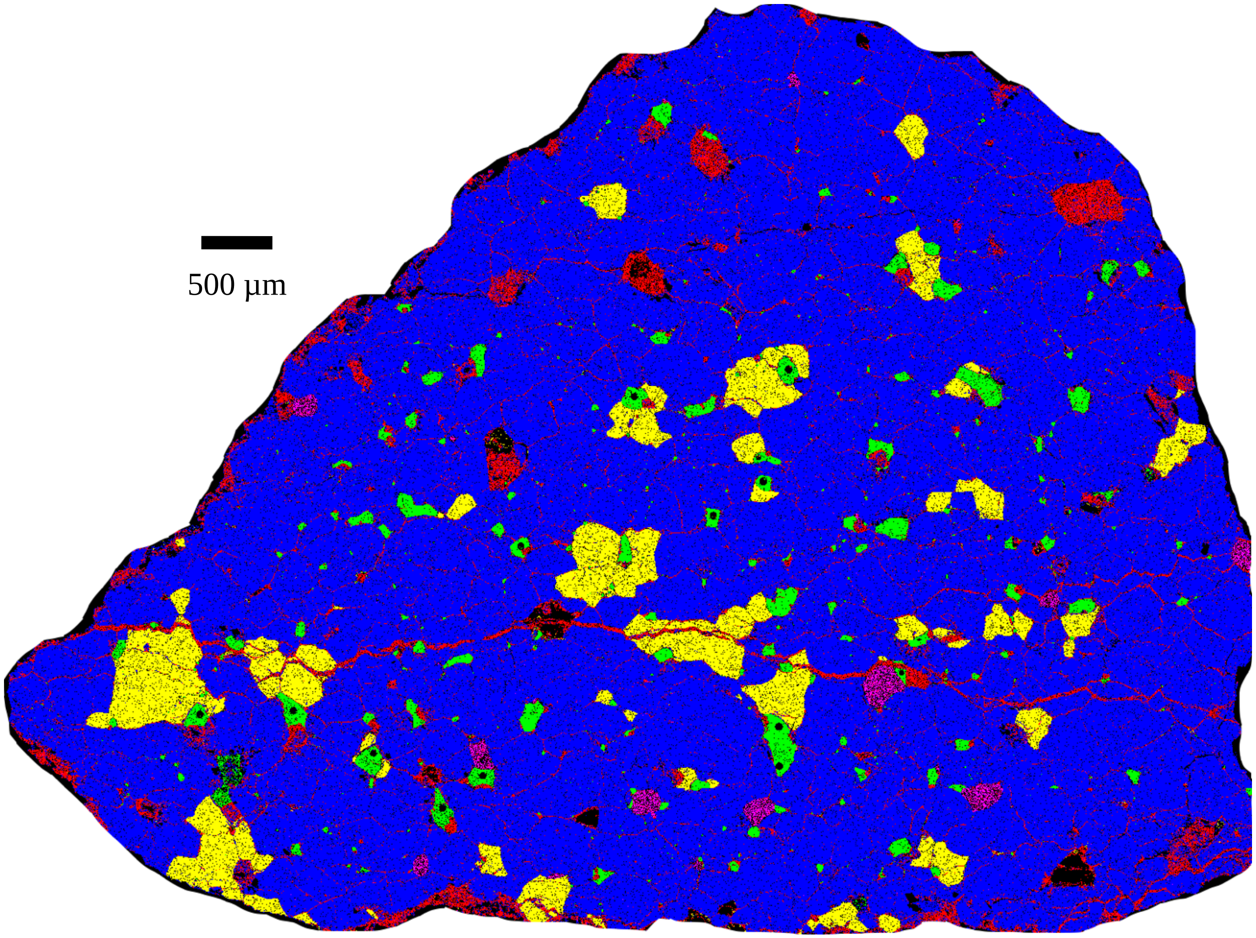

**Figure S2.4.** Modal mineral map of NWA 5363. Colors indicate the same mineral phases as Figure S2.2. Small black circles in sulfides are laser ablation pits.

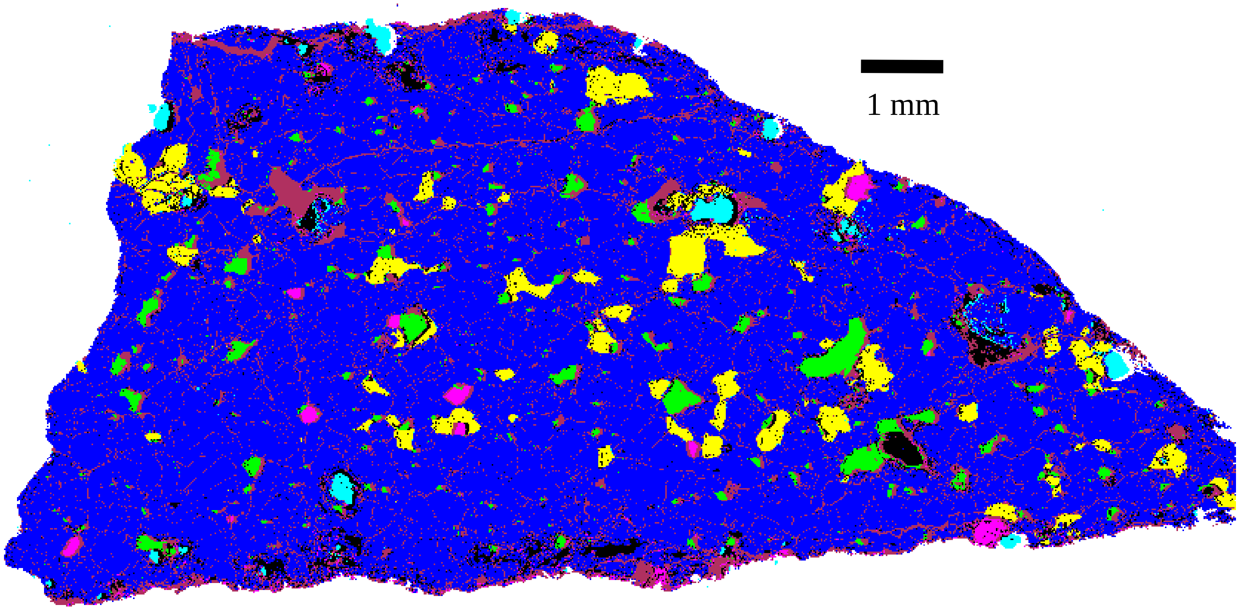

**Figure S2.5.** Modal mineral map of NWA 7297. Colors indicate the same mineral phases as Figure S2.2.

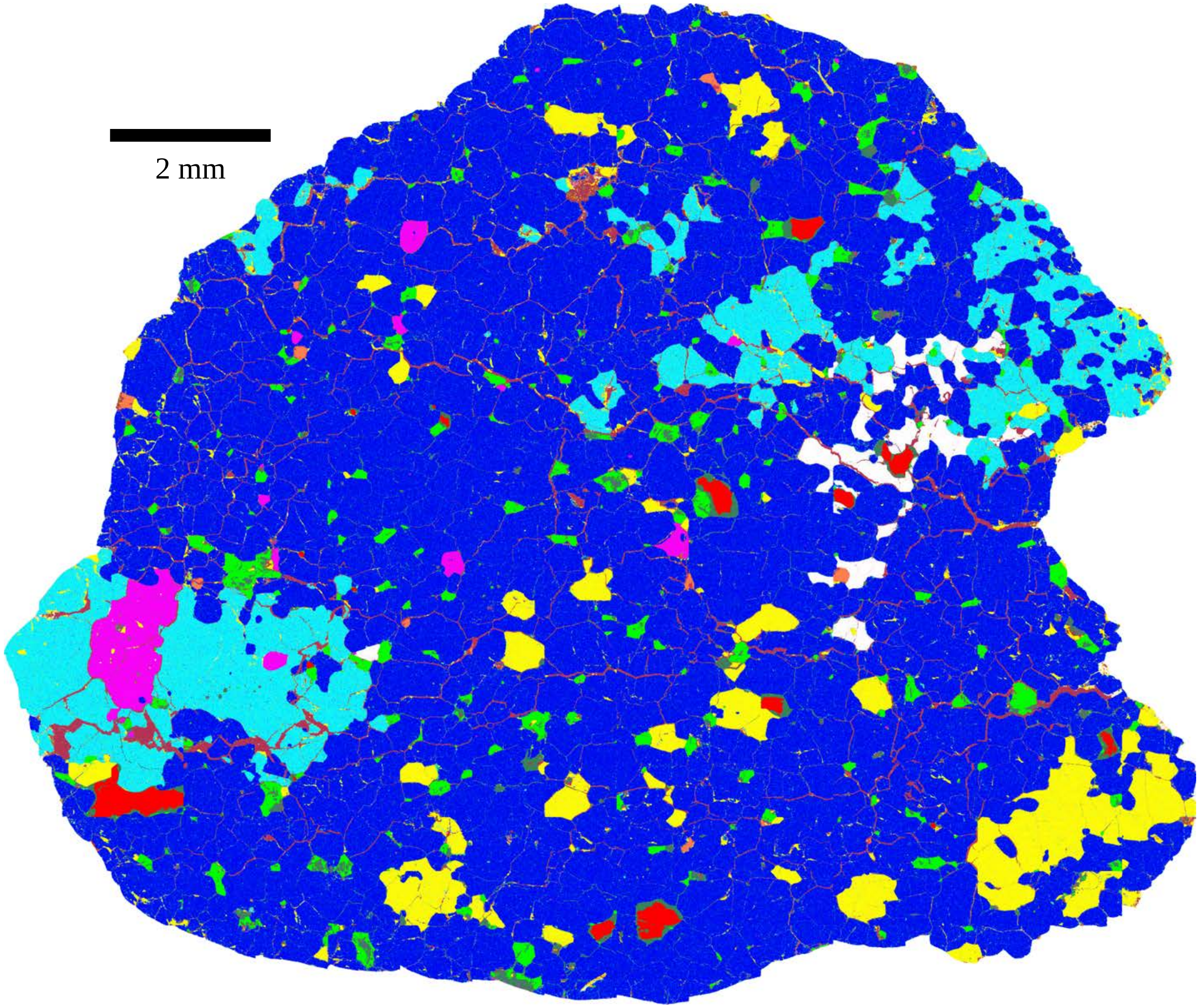

**Figure S2.6.** Modal mineral map of NWA 7299. Colors indicate the same mineral phases as Figure S2.2.

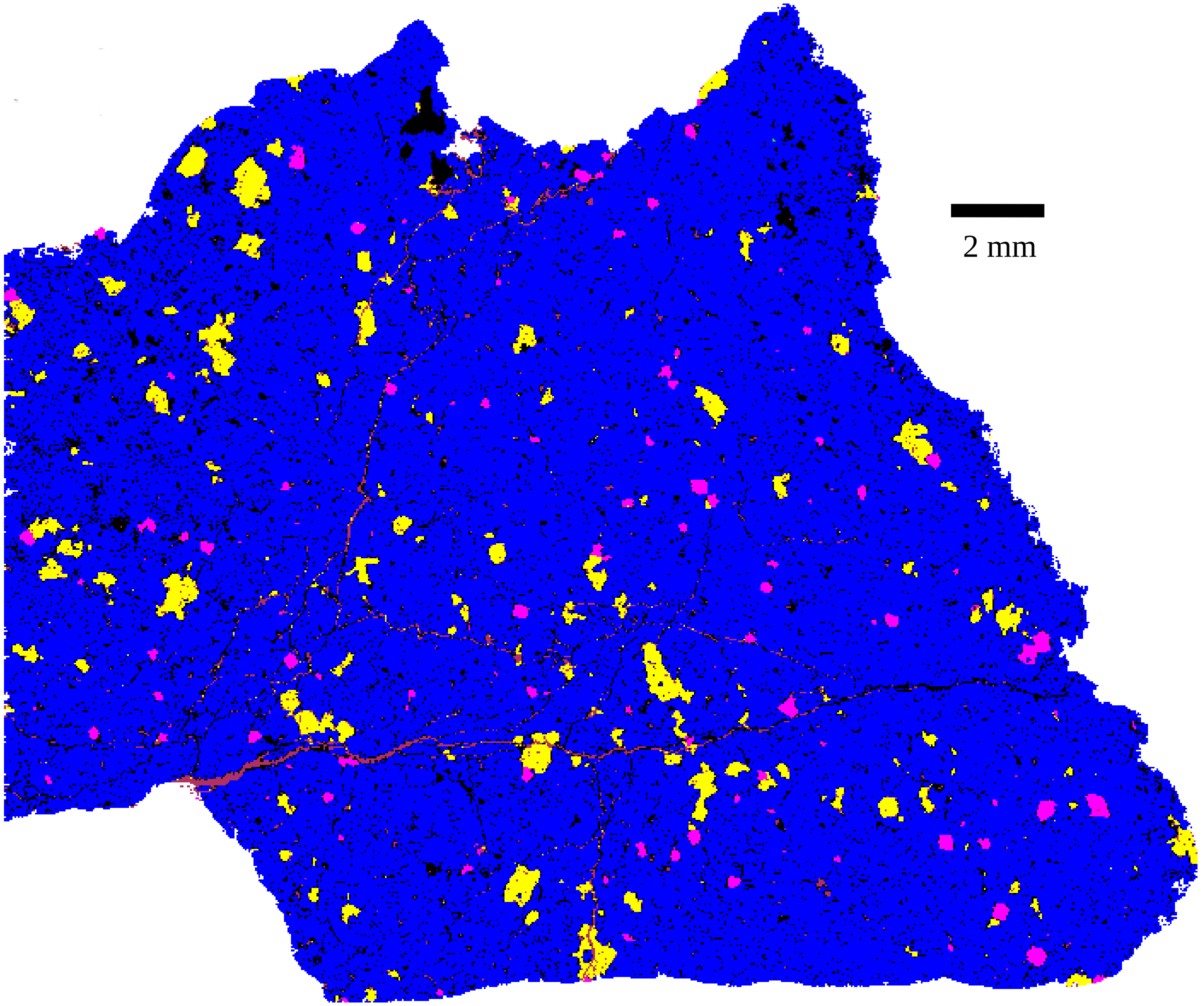

**Figure S2.7.** Modal mineral map of RaS 309. Colors indicate the same mineral phases as Figure S2.2.

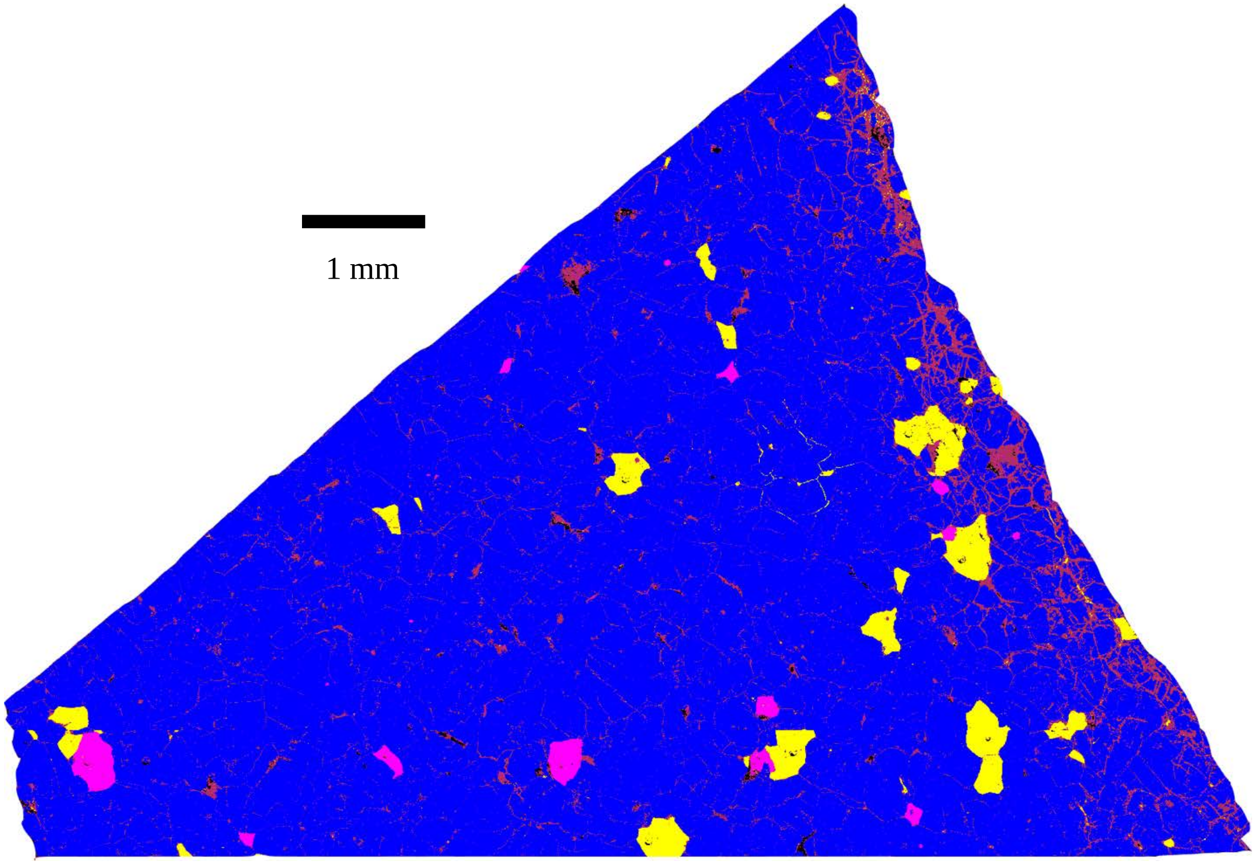

**Figure S2.8.** Modal mineral map of Reid 013. Colors indicate the same mineral phases as Figure S2.2.

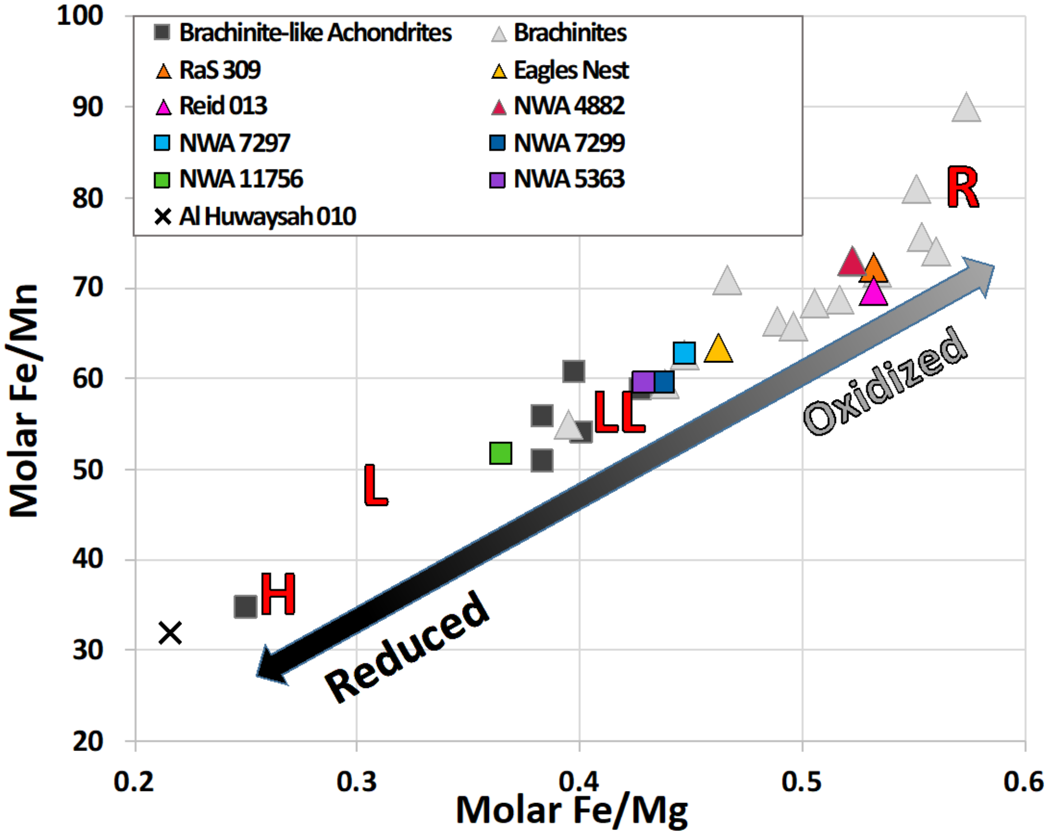

**Figure S2.9**. Fe-Mg-Mn redox trend after Goodrich and Delaney (2000) for brachinites and brachinite-like achondrite olivine. Black squares and grey triangles are brachinite-like achondrites and brachinites from literature, respectively. Colored symbols are data from this study, and shape corresponds to our suggested classification. Average H, L, LL, and R chondrite olivine, which form a similar redox trend, are shown for comparison. R chondrites are represented by our measurements of NWA 11304. Literature data are from Dunn *et al.* (2010), Day *et al.* (2012 and 2019), Keil (2014), Goodrich *et al.* (2017), and references therein. Al Huwaysah 010 is anomalous from all other samples in this study.

# Chapter 3 Supplementary Materials

**Table S3.1.** Major element oxides for nonopaque mineral endmembers listed in Table 1.

*Olivine*

|  | Type 3 | σ | Type 4 | σ | Type 5 | σ | Impact | σ |
|---|---|---|---|---|---|---|---|---|
| n= | 19 |  | 16 |  | 17 |  | 19 |  |
| $SiO_2$ | 35.5 | 2.08 | 36.1 | 1.1 | 36.7 | 0.4 | 36.2 | 1.7 |
| $TiO_2$ | 0.05 | 0.05 | b.d.l. |  | 0.03 | 0.04 | 0.04 | 0.05 |
| $Al_2O_3$ | 0.16 | 0.18 | 0.09 | 0.13 | 0.08 | 0.15 | 0.06 | 0.08 |
| $Cr_2O_3$ | 0.27 | 0.41 | 0.18 | 0.19 | 0.15 | 0.16 | 0.10 | 0.10 |
| FeO | 36.5 | 8.3 | 33.3 | 5.3 | 33.3 | 0.5 | 30.6 | 7.7 |
| MnO | 0.39 | 0.05 | 0.37 | 0.07 | 0.42 | 0.01 | 0.37 | 0.09 |
| MgO | 26.7 | 7.6 | 29.7 | 4.6 | 30.3 | 0.4 | 31.7 | 6.6 |
| CaO | 0.20 | 0.15 | 0.14 | 0.19 | 0.09 | 0.04 | 0.15 | 0.32 |
| NiO | 0.19 | 0.15 | 0.22 | 0.06 | 0.22 | 0.07 | 0.18 | 0.09 |
| $Na_2O$ | 0.18 | 0.23 | b.d.l. |  | 0.01 | 0.01 | 0.02 | 0.04 |
| Total | 100.1 |  | 100.1 |  | 101.4 |  | 99.5 |  |

*Low-Ca Pyroxene*

|  | Type 3 | σ | Type 4 | σ | Type 5 | σ | Impact | σ |
|---|---|---|---|---|---|---|---|---|
| n= | 4 |  | 6 |  | 3 |  | 4 |  |
| $SiO_2$ | 56.4 | 2.0 | 54.1 | 2.0 | 53.9 | 0.928 | 49.9 | 3.3 |
| $TiO_2$ | 0.03 | 0.02 | 0.02 | 0.02 | 0.18 | 0.07 | 0.27 | 0.14 |
| $Al_2O_3$ | 0.35 | 0.18 | 0.48 | 0.48 | 0.24 | 0.11 | 7.2 | 1.7 |
| $Cr_2O_3$ | 0.42 | 0.19 | 0.37 | 0.21 | 0.83 | 1.26 | 0.96 | 0.89 |
| FeO | 13.6 | 7.3 | 16.3 | 3.6 | 20.3 | 0.675 | 24.2 | 10.7 |
| MnO | 0.30 | 0.10 | 0.30 | 0.07 | 0.38 | 0.005 | 0.32 | 0.14 |
| MgO | 29.2 | 5.4 | 23.5 | 4.0 | 25.1 | 0.406 | 11.7 | 6.3 |
| CaO | 0.66 | 0.58 | 4.6 | 6.9 | 0.55 | 0.13 | 3.9 | 1.2 |
| NiO | b.d.l. |  | b.d.l. |  | b.d.l. |  | b.d.l. |  |
| $Na_2O$ | 0.03 | 0.05 | 0.17 | 0.23 | 0.04 | 0.02 | 1.4 | 0.7 |
| Total | 100.9 |  | 99.9 |  | 101.5 |  | 99.8 |  |

**Table S3.2.** Modal mineralogy calculations.

| *NWA 11304* | Type 3 | | Type 4 | | Type 5 | | Impact Melted Clasts | |
|---|---|---|---|---|---|---|---|---|
| ENVI Classes | Pixel Count | Percent | Pixel Count | Percent | Pixel Count | Percent | Pixel Count | Percent |
| Olivine (Mg# = 81+) | 63,838 | 4.0 | 175,339 | 3.4 | 79,457 | 3.0 | 37,767 | 4.0 |
| Olivine (Mg# = 56-80) | 593,628 | 37.3 | 2,630,067 | 51.0 | 1,383,892 | 52.7 | 485,042 | 51.9 |
| Olivine (Mg# = 40-55) | 117,570 | 7.4 | 289,426 | 5.6 | 96,468 | 3.7 | 49,234 | 5.3 |
| High-Ca Pyroxene | 34,343 | 2.2 | 290,505 | 5.6 | 113,796 | 4.3 | 41,554 | 4.5 |
| Low-Ca Pyroxene(LowFs) | 60,491 | 3.8 | 50,343 | 1.0 | 6,316 | 0.2 | 15,422 | 1.7 |
| Low-Ca Pyroxene(HighFs) | 108,127 | 6.8 | 395,375 | 7.7 | 193,907 | 7.4 | 80,462 | 8.6 |
| Plagioclase (Na-rich) | 59,522 | 3.7 | 358,995 | 7.0 | 216,172 | 8.2 | 24,960 | 2.7 |
| Plagioclase (K-rich) | 135,420 | 8.5 | 480,003 | 9.3 | 230,243 | 8.8 | 108,563 | 11.6 |
| Pentlandite | 34,317 | 2.2 | 139,868 | 2.7 | 98,493 | 3.8 | 36,510 | 3.9 |
| Pyrrhotite | 41,760 | 2.6 | 146,844 | 2.8 | 110,634 | 4.2 | 31,742 | 3.4 |
| Oxides | 38,782 | 2.4 | 109,603 | 2.1 | 47,850 | 1.8 | 18,896 | 2.0 |
| Phosphate | 8,514 | 0.5 | 36,938 | 0.7 | 21,477 | 0.8 | 691 | 0.1 |
| Epoxy/Cracks | 297,288 | 18.7 | 53,247 | 1.0 | 25,500 | 1.0 | 2,911 | 0.3 |
| Total | 1,593,600 | | 5,156,553 | | 2,624,205 | | 933,754 | |
| Mineral Phase | Vol% | | Vol% | | Vol% | | | Vol% |
| Olivine | 59.8 | | 60.6 | | 60.0 | | | 61.5 |
| Feldspar | 15.0 | | 16.4 | | 17.2 | | | 14.3 |
| High-Ca Pyx | 2.6 | | 5.7 | | 4.4 | | | 4.5 |
| Low-Ca Pyx | 13.0 | | 8.7 | | 7.7 | | | 10.3 |
| Pentlandite | 2.6 | | 2.7 | | 3.8 | | | 3.9 |
| Pyrrhotite | 3.2 | | 2.9 | | 4.3 | | | 3.4 |
| Oxides | 3.0 | | 2.1 | | 1.8 | | | 2.0 |
| Phosphates | 0.7 | | 0.7 | | 0.8 | | | 0.1 |

**Table S3.2 (con't).** Modal mineralogy calculations.

| *LAP 04840* | Pixel Count | Volume % |
|---|---|---|
| *Opaque Abundance* | | |
| Total Sample Area | 15,026,776 | |
| Total Opaque Area | 1,044,449 | 7.0 |
| *Opaque Assemblages* | | |
| Pentlandite | 4,517,980 | 13.4 |
| MSS | 25,185,486 | 74.5 |
| Magnetite | 4,092,574 | 12.1 |
| Total | 33,796,040 | |

**Table S3.3.** EMPA Corrective factors.

| Troilite Standard | LAP 04840 Measured Avg | NMNH Standard Correct Avg | % correction | Chromite Standard | LAP 04840 Measured Avg | NMNH Standard Correct Avg | % correction |
|---|---|---|---|---|---|---|---|
| Fe | 57.185 | 63.875 | 10.5 | FeO | 12.253 | 13.04 | 6.04 |
| 2σ | 0.654 | 0.071 | | 2σ | 0.106 | -- | |
| S | 31.878 | 36.218 | 12.0 | $Cr_2O_3$ | 55.896 | 60.5 | 7.61 |
| 2σ | 0.266 | 0.148 | | 2σ | 0.318 | -- | |

Uncertainty for chromite FeO and $Cr_2O_3$ not reported in Jarosewich (2002).

**Table S3.4.** Detection limits for EMPA measurements.

| NWA 11304 | | | | LAP 04840 | |
|---|---|---|---|---|---|
| Sulfides | | Silicates | | Sulfide & Oxides | |
| | wt% | | wt% | | wt% |
| Fe | 0.035 | Fe | 0.03 | Fe | 0.034 |
| Ni | 0.032 | Ca | 0.009 | Ti | 0.05 |
| Cr | 0.022 | Ti | 0.064 | Ni | 0.031 |
| Si | 0.008 | Ni | 0.029 | Mn | 0.034 |
| Mg | 0.009 | Mn | 0.029 | Cr | 0.022 |
| S | 0.017 | Cr | 0.018 | Si | 0.009 |
| P | 0.012 | Si | 0.007 | Al | 0.01 |
| Co | 0.035 | Al | 0.01 | Mg | 0.009 |
| Zn | 0.159 | Na | 0.024 | S | 0.02 |
| Cu | 0.050 | Mg | 0.007 | P | 0.015 |
| | | | | Co | 0.036 |
| | | | | Zn | 0.114 |
| | | | | Cu | 0.05 |

**Table S3.5.** External precision (2σ, relative % deviation) of standard measurements and detection limits used for LA-ICP-MS data processing.

| | NIST 610 | Coahuila | Filomena | Detection Limit (ppm) |
|---|---|---|---|---|
| Co | | 0.4 | 3.5 | 1.7 |
| Ni | | 3.2 | 1.4 | 3.1 |
| Cu | 0.6 | 2.9 | 5.1 | 25 |
| Zn | 2.2 | | | 1.6 |
| Ga | 0.9 | 3.2 | 0.4 | 0.09 |
| Ge | 1.9 | 3.0 | 1.6 | 0.32 |
| As | 1.3 | 1.3 | 11.6 | 0.17 |
| Mo | 3.6 | 10.3 | 3.3 | 0.01 |
| Ru | | 3.1 | 2.0 | 0.01 |
| Rh | 5.1 | 5.3 | 2.8 | 0.01 |
| Pd | 4.4 | 15 | 5.5 | 0.07 |
| Sn | 3.1 | | | 0.18 |
| Sb | 2.4 | | | 0.08 |
| Te | 1.9 | | | 0.26 |
| W | 0.6 | 9.5 | 2.4 | 0.01 |
| Re | 0.5 | 3.6 | 20.4 | 0.03 |
| Os | | 3.4 | 4.7 | 0.01 |
| Ir | | 2.1 | 3.3 | 0.01 |
| Pt | 3.4 | 6.3 | 2.6 | 0.01 |
| Au | 0.1 | 11.1 | 4.5 | 0.01 |

**Table S3.6.** Average siderophile and chalcophile trace element concentrations (in ppm) in non-opaque mineral phases.

| | Olivine | | | | High-Ca Pyroxene | | |
|---|---|---|---|---|---|---|---|
| | Type 3 Matrix | Type 3 Chondrule | Type 4 | Type 5 | Type 3 | Type 4 | Type 5 |
| n= | 4 | 5 | 8 | 9 | 3 | 2 | 4 |
| Ni | 13050 | 1487 | 1197 | 1679 | 676 | 1221 | 2396 |
| Cu | 107 | 2.0 | 7.1 | 2.9 | 7.7 | 5.8 | 40 |
| Ga | 11.1 | 0.49 | 1.8 | 0.76 | 8.2 | 11 | 12 |
| Ge | 11.7 | 3.6 | 5.8 | 13.5 | 1.3 | 2.3 | 2.8 |
| W | 0.21 | 0.02 | 0.10 | 0.05 | 0.15 | b.d.l. | 0.10 |

| | Low-Ca Pyroxene | | Plagioclase | Ca-Phosphate |
|---|---|---|---|---|
| | Type 3 | Type 4 | Type 5 | Type 5 |
| n= | 11 | 1 | 3 | 6 |
| Ni | 827 | 665 | 2044 | - |
| Cu | 6.8 | 3.1 | 22 | - |
| Ga | 0.85 | 4.5 | 29 | - |
| Ge | 0.74 | b.d.l. | b.d.l. | - |
| W | 0.02 | b.d.l. | 0.35 | 0.11 |

Pyroxene averages are biased toward chondrules and chondrule fragments in petrologic types 3 and 4 due to the small grain sizes of pyroxene (< 20 µm) outside of chondrules. Ni, Cu, Ga, and Ge were not measured in phosphate analyses, which are limited to type 5 because phosphate grains only reach suitable diameters in these clasts.

**Table S7.** Calculations for size estimate of Psyche's precursor parent body.

| | | |
|---|---|---|
| Psyche diameter[a] | 253 | km |
| Psyche volume | 8,475,005 | $km^3$ |
| Total volume of Psyche sulfides (if Psyche is 10 vol% silicate[b]) | 7,627,504 | $km^3$ |
| Volume of Precursor (assuming 8 vol% precursor sulfides) | 95,343,806 | $km^3$ |
| Precursor diameter | 567 | km |

Calculations assume a spherical geometry for Psyche.

[a] From Shepard et al., 2017

[b] Based on metal, nonmetal, and void space mixtures to account for bulk density in Elkins-Tanton et al. (2020). This calculation assumes that nonmetals are dominated by sulfides with an average density of approximately 4.5 $g/cm^3$.

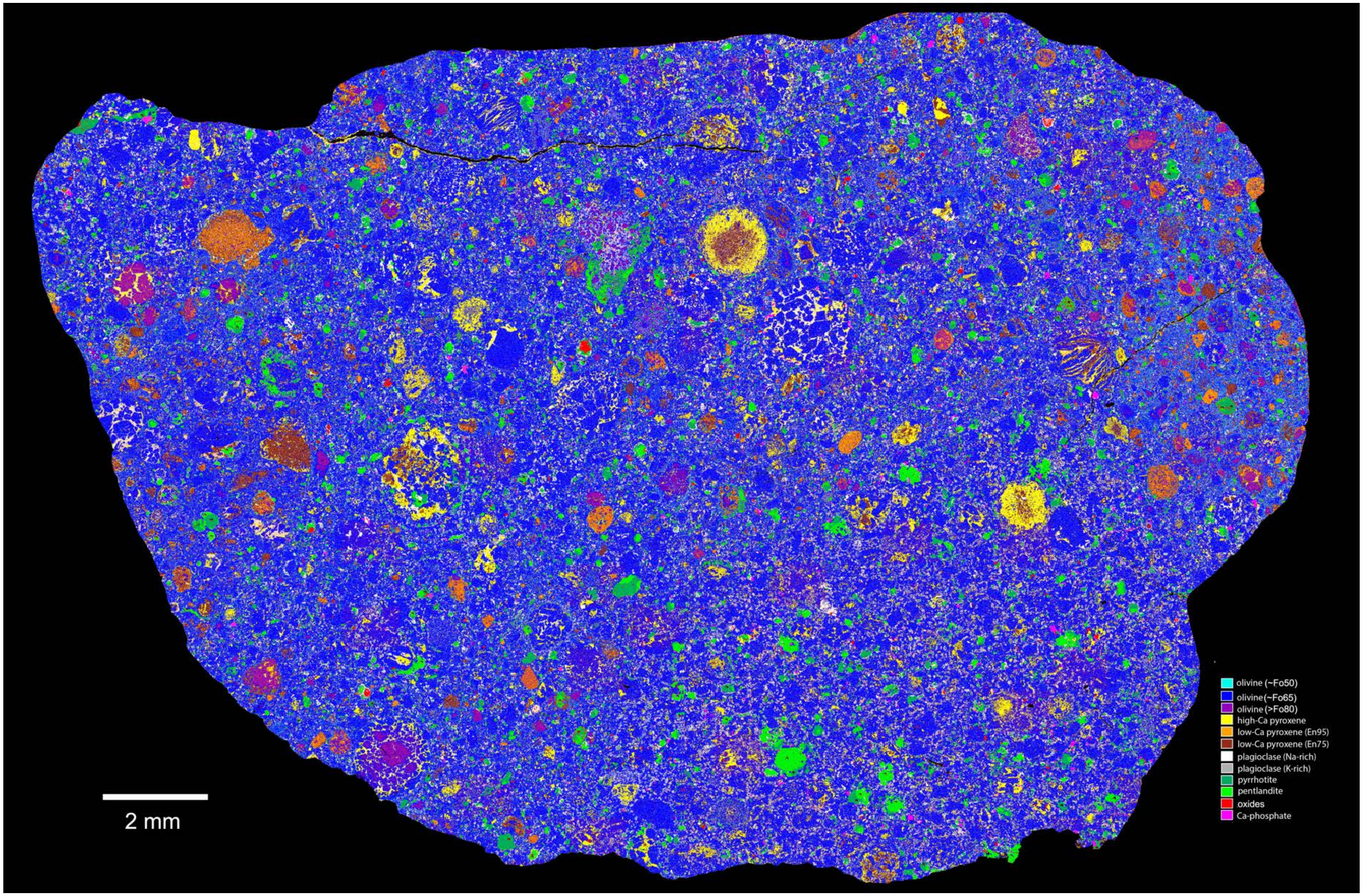

**Fig. S3.1**. Mineral Classification Map of NWA 11304. Mineral modes were calculated by counting pixels for each of the classes.

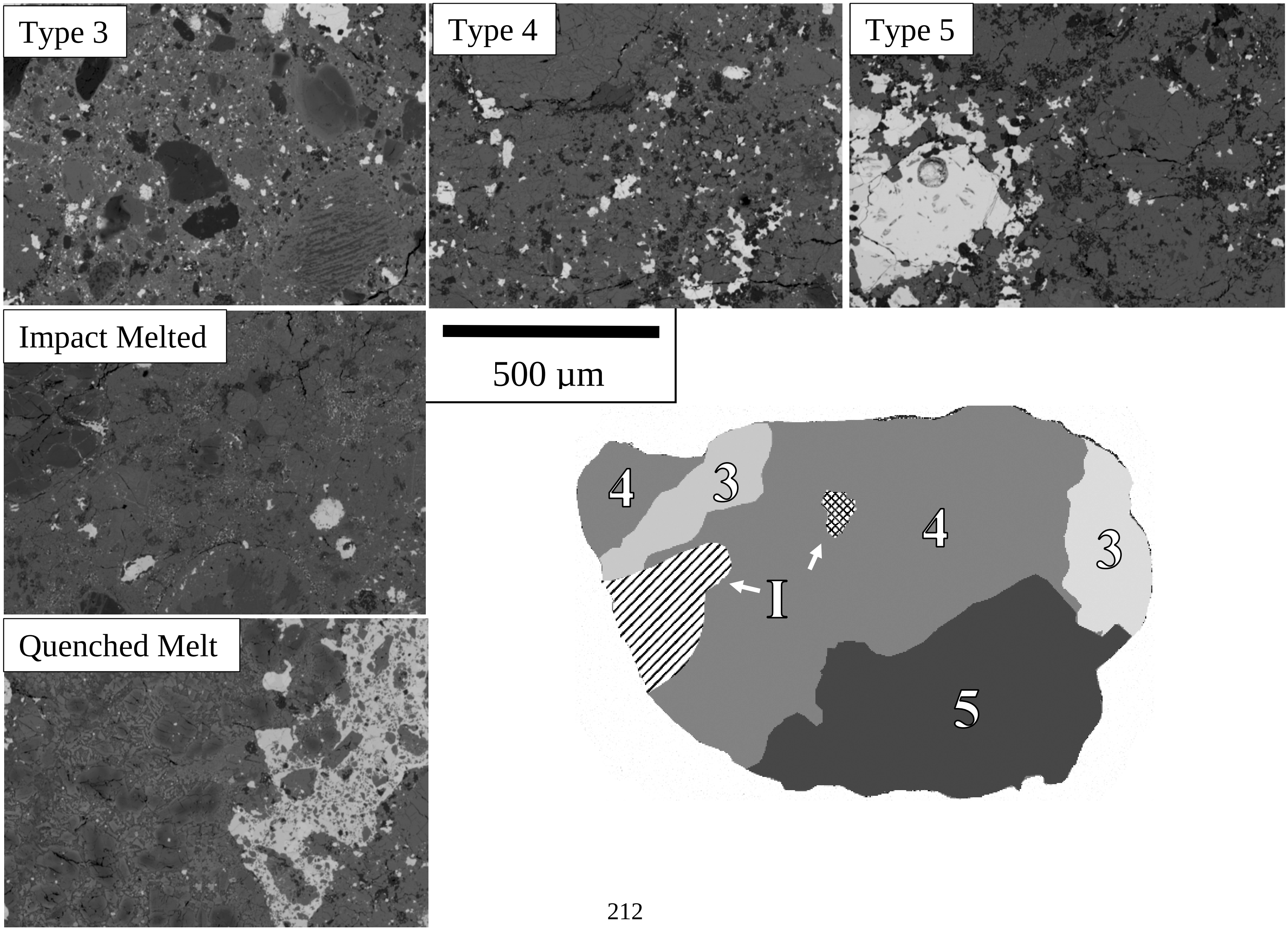
Type 3
Type 4
Type 5
Impact Melted
500 µm
Quenched Melt
4
3
4
3
I
5

**Fig. S3.2 (previous page)**. Diagram of clasts in NWA 11304 and their assigned petrologic types. BSE images show representative textures for each petrologic type (3-5) and for impact-melted clasts (IM) as described in Section 3.1.1. In the diagram, the quenched melt is the smallest clast with the hashed line fill. The other impact melt (diagonal stripes) is less extensively melted with some relict chondrules and chondrule fragments. The scale bar applies to the BSE images. Mineral modes for each clast were calculated by applying clast boundaries to the mineral classification maps and counting pixels subtotals for each.

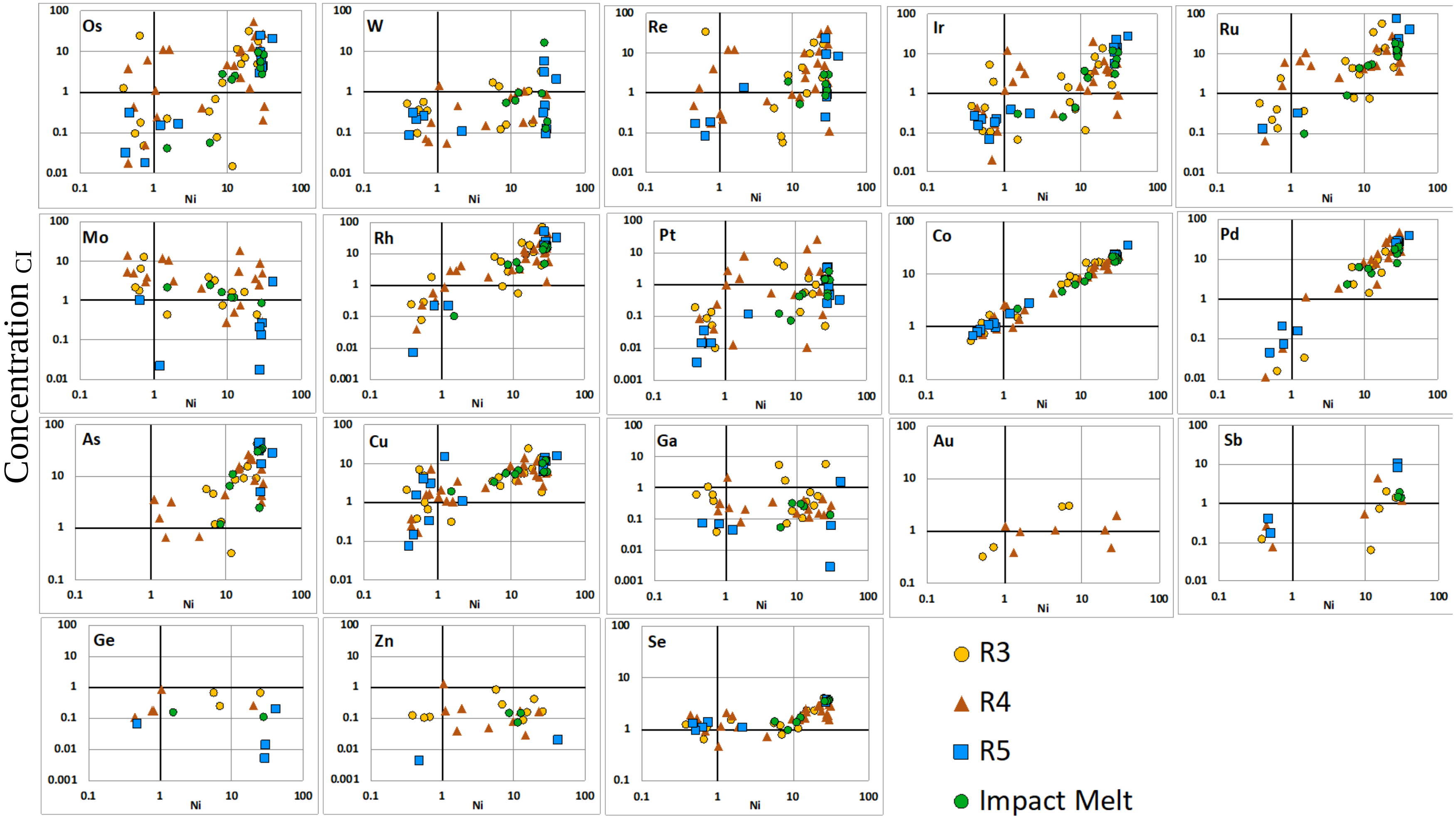

**Fig S3.3**. Individual CI-normalized measurements for siderophile and chalcophile trace elements vs. Ni in NWA 11304 sulfides.

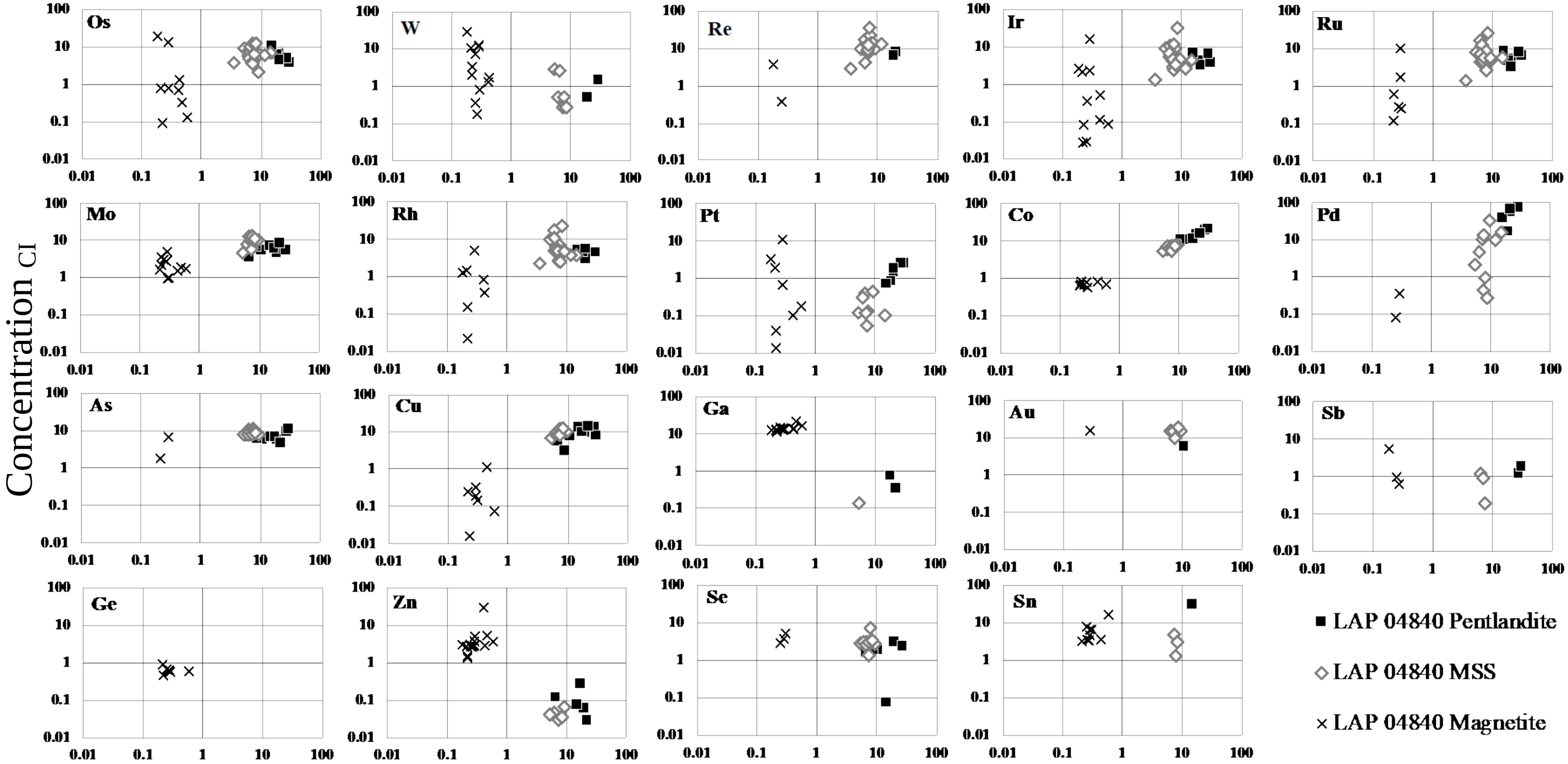

**Fig. S3.4**. Individual CI-normalized measurements for siderophile and chalcophile trace elements vs. Ni in LAP 04840 sulfides and oxides.

**Table S4.1. MGM Results for RaS 309**

| Olivine | Strengths | | Centers |
|---|---|---|---|
| Band I | -1.42E-01 | | 8.60E+02 |
| Band II | -1.75E-01 | | 1.05E+03 |
| Band III | -2.17E-01 | | 1.22E+03 |
| Strength Ratios | | | Fa (mole frac) |
| I/III | 0.65 | I | .346 |
| II/III | 0.81 | II | .322 |
| | | III | .225 |
| | | (II+III)/2 | **.274** |

Continuum:

| Y-int | slope |
|---|---|
| 3.14E-01 | -1.23E-06 |

Absorption Bands

| | Center | Width | Strength |
|---|---|---|---|
| 1 | 2.13E+02 | 3.84E+02 | -2.18E+00 |
| 2 | 5.03E+02 | 1.15E+02 | -2.58E-01 |
| 3 | 6.36E+02 | 1.15E+02 | -7.57E-02 |
| 4 | 8.60E+02 | 2.28E+02 | -1.42E-01 |
| 5 | 1.05E+03 | 1.76E+02 | -1.75E-01 |
| 6 | 1.22E+03 | 4.23E+02 | -2.17E-01 |
| 7 | 9.53E+02 | 1.15E+02 | -3.50E-02 |
| 8 | 1.99E+03 | 4.24E+02 | -2.10E-02 |

RMS 5.03E-03

**Table S4.2. MGM results for Reid 013**

| Olivine | Strengths | | Centers |
|---|---|---|---|
| Band I | -1.22E-01 | | 8.78E+02 |
| Band II | -1.84E-01 | | 1.05E+03 |
| Band III | -2.41E-01 | | 1.24E+03 |
| Strength Ratios | | | Fa (mole frac) |
| I/III | 0.51 | I | .573 |
| II/III | 0.76 | II | .449 |
| | | III | .389 |
| | | (II+III)/2 | **.419** |

Continuum:

| Y-int | slope |
|---|---|
| 3.01E-01 | -3.22E-06 |

Absorption Bands

| | Center | Width | Strength |
|---|---|---|---|
| 1 | 1.44E+02 | 3.82E+02 | -2.50E+00 |
| 2 | 4.83E+02 | 1.16E+02 | -2.81E-01 |
| 3 | 5.75E+02 | 1.15E+02 | -1.29E-01 |
| 4 | 8.78E+02 | 2.28E+02 | -1.22E-01 |
| 5 | 1.05E+03 | 1.76E+02 | -1.84E-01 |
| 6 | 1.24E+03 | 4.26E+02 | -2.41E-01 |

RMS 1.22E-02

**Table S4.3 MGM results for NWA 4882.**

| Olivine | Strengths | | Centers |
|---|---|---|---|
| Band I | -1.03E-01 | | 8.64E+02 |
| Band II | -1.77E-01 | | 1.05E+03 |
| Band III | -2.15E-01 | | 1.23E+03 |
| Strength Ratios | | | Fa (mole frac) |
| I/III | 0.48 | I | .402 |
| II/III | 0.82 | II | .443 |
| | | III | .333 |
| | | (II+III)/2 | **.388** |

Continuum:

| Y-int | slope |
|---|---|
| 2.52E-01 | -1.22E-06 |

Absorption Bands

| | Center | Width | Strength |
|---|---|---|---|
| 1 | 2.13E+02 | 3.84E+02 | -2.18E+00 |
| 2 | 5.03E+02 | 1.15E+02 | -2.58E-01 |
| 3 | 6.36E+02 | 1.15E+02 | -7.57E-02 |
| **4** | **8.60E+02** | **2.28E+02** | **-1.42E-01** |
| **5** | **1.05E+03** | **1.76E+02** | **-1.75E-01** |
| **6** | **1.22E+03** | **4.23E+02** | **-2.17E-01** |
| 7 | 9.53E+02 | 1.15E+02 | -3.50E-02 |
| 8 | 1.99E+03 | 4.24E+02 | -2.10E-02 |

RMS 6.25E-03

**Table S4.4. MGM results for NWA 7297.**

| Olivine | Strengths | | Centers |
|---|---|---|---|
| Band I | -1.09E-01 | | 8.58E+02 |
| Band II | -1.59E-01 | | 1.05E+03 |
| Band III | -1.98E-01 | | 1.23E+03 |
| Strength Ratios | | | Fa (mole frac |
| I/III | 0.55 | I | .326 |
| II/III | 0.80 | II | .324 |
| | | III | .351 |
| | | (II+III)/2 | **.337** |

Continuum:

| Y-int | slope |
|---|---|
| 2.14E-01 | -2.44E-06 |

Absorption Bands

| | Center | Width | Strength |
|---|---|---|---|
| 1 | 2.25E+02 | 3.56E+02 | -1.99E+00 |
| 2 | 5.00E+02 | 1.16E+02 | -2.52E-01 |
| 3 | 6.28E+02 | 1.15E+02 | -8.87E-02 |
| **4** | **8.58E+02** | **2.26E+02** | **-1.09E-01** |
| **5** | **1.05E+03** | **1.76E+02** | **-1.59E-01** |
| **6** | **1.23E+03** | **4.32E+02** | **-1.98E-01** |
| 7 | 9.24E+02 | 1.43E+02 | -6.86E-02 |
| 8 | 1.94E+03 | 7.40E+02 | -9.22E-02 |
| 9 | 2.50E+03 | 2.57E+02 | -1.90E-02 |

RMS 5.45E-03

**Table 4.5. MGM results for NWA 11756**

| Olivine | Strengths | | Centers |
|---|---|---|---|
| Band I | -1.16E-01 | | 8.57E+02 |
| Band II | -1.69E-01 | | 1.05E+03 |
| Band III | -2.11E-01 | | 1.23E+03 |
| Strength Ratios | | | Fa (mole frac) |
| I/III | 0.55 | I | .313 |
| II/III | 0.80 | II | .301 |
| | | III | .339 |
| | | (II+III)/2 | **.320** |

Continuum:

| Y-int | slope |
|---|---|
| 3.02E-01 | -1.20E-06 |

Absorption Bands

| | Center | Width | Strength |
|---|---|---|---|
| 1 | 2.66E+02 | 3.57E+02 | -1.85E+00 |
| 2 | 5.00E+02 | 1.16E+02 | -2.78E-01 |
| 3 | 6.37E+02 | 1.15E+02 | -9.04E-02 |
| **4** | **8.57E+02** | **2.27E+02** | **-1.16E-01** |
| **5** | **1.05E+03** | **1.75E+02** | **-1.69E-01** |
| **6** | **1.23E+03** | **4.31E+02** | **-2.11E-01** |
| 7 | 9.26E+02 | 1.47E+02 | -8.87E-02 |
| 8 | 1.94E+03 | 7.86E+02 | -1.26E-01 |
| 9 | 2.50E+03 | 3.03E+02 | -3.90E-02 |

RMS 7.09E-03

**Table S4.6 MGM results for 246 Asporina**

| $Fa_{10}$ | | $Fa_{50}$ | | $Fa_{90}$ | |
|---|---|---|---|---|---|
| Y-intercept | Slope | Y-intercept | Slope | Y-intercept | Slope |
| 7.55E-01 | -2.20E-05 | 7.55E-01 | -2.20E-05 | 7.55E-01 | -2.20E-05 |

Absorption bands

| | Center | Width | Strength | Center | Width | Strength | Center | Width | Strength |
|---|---|---|---|---|---|---|---|---|---|
| *1* | *4.36E+02* | *3.07E+02* | *-1.26E-01* | *4.49E+02* | *2.99E+02* | *-1.22E-01* | *4.36E+02* | *2.86E+02* | *-1.33E-01* |
| *2* | *6.29E+02* | *1.15E+02* | *-3.57E-02* | *6.28E+02* | *1.15E+02* | *-3.00E-02* | *6.21E+02* | *1.14E+02* | *-3.68E-02* |
| **3** | **8.69E+02** | **2.15E+02** | **-2.03E-01** | **8.92E+02** | **2.46E+02** | **-2.22E-01** | **9.17E+02** | **2.83E+02** | **-2.42E-01** |
| **4** | **1.05E+03** | **2.03E+02** | **-3.25E-01** | **1.06E+03** | **1.66E+02** | **-2.23E-01** | **1.07E+03** | **1.49E+02** | **-1.54E-01** |
| **5** | **1.26E+03** | **3.30E+02** | **-2.90E-01** | **1.23E+03** | **3.75E+02** | **-3.09E-01** | **1.23E+03** | **3.82E+02** | **-3.11E-01** |
| | | RMS Error = | 6.44E-03 | | RMS Error = | 6.44E-03 | | RMS Error = | 6.44E-03 |

Calculated Olivine Composition

| | Strength Ratios | | Fa (Mole Frac) | Strength Ratios | | Fa (Mole Frac) | Strength Ratios | | Fa (Mole Frac) |
|---|---|---|---|---|---|---|---|---|---|
| I/III | 0.70 | Band I | .46 | .72 | Band I | .74 | .78 | Band I | 1.05 |
| II/III | 1.12 | Band II | .40 | .72 | Band II | .55 | .50 | Band II | .73 |
| | | Band III | .68 | | Band III | .36 | | Band III | .33 |
| | | **Avg Fa (II,III)** | **.54** | | **Avg Fa (II,III)** | **.46** | | **Avg Fa (II,III)** | **.53** |

**Table S4.7 MGM results for 289 Nenetta**

| Fa$_{10}$ | | Fa$_{50}$ | | Fa$_{90}$ | |
|---|---|---|---|---|---|
| Y-intercept | Slope | Y-intercept | Slope | Y-intercept | Slope |
| 7.34E-01 | -2.20E-05 | 7.15E-01 | -2.00E-05 | 7.34E-01 | -2.20E-05 |

Absorption bands

| | Center | Width | Strength | Center | Width | Strength | Center | Width | Strength |
|---|---|---|---|---|---|---|---|---|---|
| *1* | *5.22E+02* | *1.40E+02* | *-1.53E-01* | *5.23E+02* | *3.11E+02* | *-2.04E-01* | *5.71E+02* | *3.96E+02* | *-1.61E-01* |
| *2* | *6.36E+02* | *1.12E+02* | *-1.43E-01* | *6.35E+02* | *1.12E+02* | *-5.47E-02* | *6.16E+02* | *1.15E+02* | *-4.55E-02* |
| **3** | **8.23E+02** | **2.10E+02** | **-3.73E-01** | **8.50E+02** | **2.30E+02** | **-4.30E-01** | **8.72E+02** | **2.32E+02** | **-4.07E-01** |
| **4** | **1.04E+03** | **2.50E+02** | **-6.16E-01** | **1.05E+03** | **2.09E+02** | **-4.94E-01** | **1.06E+03** | **1.79E+02** | **-3.71E-01** |
| **5** | **1.28E+03** | **3.87E+02** | **-5.90E-01** | **1.26E+03** | **4.13E+02** | **-6.37E-01** | **1.24E+03** | **4.38E+02** | **-6.72E-01** |
| 6 | 9.29E+02 | 2.22E+02 | -4.58E-02 | 9.27E+02 | 2.24E+02 | -4.62E-02 | 9.25E+02 | 2.24E+02 | -4.73E-02 |
| 7 | 1.92E+03 | 5.20E+02 | -1.66E-03 | 1.92E+03 | 5.20E+02 | -1.00E-03 | 1.92E+03 | 5.20E+02 | -7.01E-03 |
| | | RMS Error = | 9.03E-03 | | RMS Error = | 9.62E-03 | | RMS Error = | 1.24E-02 |

Calculated Olivine Composition

| | Strength Ratios | | Fa (Mole Frac) | Strength Ratios | | Fa (Mole Frac) | Strength Ratios | | Fa (Mole Frac) |
|---|---|---|---|---|---|---|---|---|---|
| I/III | 0.63 | Band I | -.10 | .68 | Band I | .23 | .61 | Band I | .50 |
| II/III | 1.04 | Band II | .14 | .78 | Band II | .35 | .55 | Band II | .50 |
| | | Band III | .88 | | Band III | .64 | | Band III | .42 |
| | | **Avg Fa (II,III)** | **.51** | | **Avg Fa (II,III)** | **.50** | | **Avg Fa (II,III)** | **.46** |

**Table S4.8 MGM results for 354 Eleonora.**

| $Fa_{10}$ | | $Fa_{50}$ | | $Fa_{90}$ | |
|---|---|---|---|---|---|
| Y-intercept | Slope | Y-intercept | Slope | Y-intercept | Slope |
| 7.27E-01 | -2.00E-05 | 7.38E-01 | -2.00E-05 | 7.34E-01 | -2.20E-05 |

Absorption bands

| | Center | Width | Strength | Center | Width | Strength | Center | Width | Strength |
|---|---|---|---|---|---|---|---|---|---|
| *1* | *5.10E+02* | *3.94E+02* | *-2.01E-01* | *5.08E+02* | *3.91E+02* | *-2.02E-01* | *4.97E+02* | *3.87E+02* | *-2.04E-01* |
| *2* | *6.30E+02* | *1.15E+02* | *-2.26E-02* | *6.30E+02* | *1.15E+02* | *-2.49E-02* | *6.28E+02* | *1.15E+02* | *-3.16E-02* |
| **3** | **8.45E+02** | **2.20E+02** | **-1.89E-01** | **8.48E+02** | **2.23E+02** | **-2.05E-01** | **8.51E+02** | **2.31E+02** | **-2.09E-01** |
| **4** | **1.05E+03** | **1.93E+02** | **-2.82E-01** | **1.05E+03** | **1.88E+02** | **-2.62E-01** | **1.05E+03** | **1.78E+02** | **-1.96E-01** |
| **5** | **1.24E+03** | **3.69E+02** | **-2.80E-01** | **1.23E+03** | **3.86E+02** | **-2.89E-01** | **1.20E+03** | **4.23E+02** | **-3.12E-01** |
| 6 | 9.24E+02 | 2.24E+02 | -9.45E-02 | 9.25E+02 | 2.24E+02 | -6.83E-02 | 9.26E+02 | 2.24E+02 | -4.74E-02 |
| 7 | 1.87E+03 | 5.20E+02 | -2.87E-02 | 1.87E+03 | 5.20E+02 | -2.93E-02 | 1.87E+03 | 5.20E+02 | -3.07E-02 |
| | | RMS Error = | 7.38E-03 | | RMS Error = | 6.67E-03 | | RMS Error = | 6.73E-03 |

Calculated Olivine Composition

| | Strength Ratios | | Fa (Mole Frac) | Strength Ratios | | Fa (Mole Frac) | Strength Ratios | | Fa (Mole Frac) |
|---|---|---|---|---|---|---|---|---|---|
| I/III | 0.67 | Band I | .16 | .71 | Band I | .21 | .67 | Band I | .24 |
| II/III | 1.01 | Band II | .42 | .91 | Band II | .35 | .63 | Band II | .31 |
| | | Band III | .46 | | Band III | .32 | | Band III | .00 |
| | | **Avg Fa (II,III)** | **.44** | | **Avg Fa (II,III)** | **.33** | | **Avg Fa (II,III)** | **.15** |

Calculated Low-Ca Pyroxene Composition

| | Fs (Mole Frac) |
|---|---|
| BIIC | 0.20 |

**Table S4.9 MGM results for 446 Aeternitas.**

| Fa$_{10}$ | | Fa$_{50}$ | | Fa$_{90}$ | |
|---|---|---|---|---|---|
| Y-intercept | Slope | Y-intercept | Slope | Y-intercept | Slope |
| 8.44E-01 | -2.40E-05 | 8.47E-01 | -2.40E-05 | 8.64E-01 | -2.40E-05 |

Absorption bands

| | Center | Width | Strength | Center | Width | Strength | Center | Width | Strength |
|---|---|---|---|---|---|---|---|---|---|
| *1* | *4.63E+02* | *4.00E+02* | *-3.06E-01* | *4.73E+02* | *3.34E+02* | *-3.15E-01* | *4.67E+02* | *3.30E+02* | *-3.65E-01* |
| *2* | *6.30E+02* | *1.15E+02* | *-1.25E-02* | *6.48E+02* | *1.14E+02* | *-5.11E-02* | *6.43E+02* | *1.14E+02* | *-6.18E-02* |
| **3** | **8.49E+02** | **2.25E+02** | **-2.50E-01** | **8.28E+02** | **1.87E+02** | **-2.75E-01** | **8.29E+02** | **2.04E+02** | **-2.99E-01** |
| **4** | **1.06E+03** | **1.75E+02** | **-3.11E-01** | **1.04E+03** | **1.82E+02** | **-3.04E-01** | **1.04E+03** | **1.58E+02** | **-2.25E-01** |
| **5** | **1.27E+03** | **3.44E+02** | **-4.27E-01** | **1.26E+03** | **3.64E+02** | **-4.32E-01** | **1.24E+03** | **4.08E+02** | **-4.78E-01** |
| 6 | 9.25E+02 | 2.20E+02 | -9.10E-02 | 9.25E+02 | 2.10E+02 | -8.99E-02 | 9.29E+02 | 2.18E+02 | -9.00E-02 |
| 7 | 1.04E+03 | 2.89E+02 | -1.82E-01 | 1.05E+03 | 3.04E+02 | -1.81E-01 | 1.05E+03 | 2.82E+02 | -1.82E-01 |
| 8 | 1.89E+03 | 5.12E+02 | -5.75E-02 | 1.89E+03 | 5.14E+02 | -5.90E-02 | 1.89E+03 | 5.13E+02 | -7.68E-02 |
| 9 | 2.34E+03 | 6.67E+02 | -1.08E-01 | 2.34E+03 | 6.69E+02 | -1.09E-01 | 2.34E+03 | 6.69E+02 | -1.29E-01 |
| | | RMS Error = | **1.04E-02** | | RMS Error = | 7.12E-03 | | RMS Error = | 6.71E-03 |

Calculated Olivine Composition

| | Strength Ratios | | Fa (Mole Frac) | Strength Ratios | | Fa (Mole Frac) | Strength Ratios | | Fa (Mole Frac) |
|---|---|---|---|---|---|---|---|---|---|
| I/III | 0.59 | Band I | .22 | .64 | Band I | -.04 | .63 | Band I | -.03 |
| II/III | 0.73 | Band II | .53 | .70 | Band II | .10 | .47 | Band II | .08 |
| | | Band III | .68 | | Band III | .59 | | Band III | .37 |
| | | **Avg Fa (II,III)** | **.60** | | **Avg Fa (II,III)** | **.34** | | **Avg Fa (II,III)** | **.23** |

Calculated Low-Ca Pyroxene Composition

| | Fs (Mole Frac) |
|---|---|
| BIIC | 0.25 |

**Table S4.10 MGM results for 863 Benkoela.**

| $Fa_{10}$ | | $Fa_{50}$ | | $Fa_{90}$ | |
|---|---|---|---|---|---|
| Y-intercept | Slope | Y-intercept | Slope | Y-intercept | Slope |
| 7.67E-01 | -2.20E-05 | 7.79E-01 | -2.20E-05 | 7.75E-01 | -2.20E-05 |

Absorption bands

| | Center | Width | Strength | Center | Width | Strength | Center | Width | Strength |
|---|---|---|---|---|---|---|---|---|---|
| *1* | *4.84E+02* | *2.89E+02* | *-2.73E-01* | *4.77E+02* | *2.89E+02* | *-3.12E-01* | *4.80E+02* | *2.91E+02* | *-2.99E-01* |
| *2* | *6.41E+02* | *1.14E+02* | *-6.86E-02* | *6.37E+02* | *1.15E+02* | *-7.19E-02* | *6.39E+02* | *1.15E+02* | *-7.16E-02* |
| **3** | **8.38E+02** | **2.18E+02** | **-2.81E-01** | **8.42E+02** | **2.46E+02** | **-2.97E-01** | **8.50E+02** | **2.36E+02** | **-3.39E-01** |
| **4** | **1.04E+03** | **2.05E+02** | **-4.44E-01** | **1.05E+03** | **1.74E+02** | **-3.23E-01** | **1.04E+03** | **1.81E+02** | **-3.42E-01** |
| **5** | **1.25E+03** | **3.24E+02** | **-4.07E-01** | **1.23E+03** | **3.64E+02** | **-4.48E-01** | **1.22E+03** | **3.69E+02** | **-4.47E-01** |
| 6 | 2.02E+03 | 4.22E+02 | -5.92E-02 | 2.03E+03 | 5.45E+02 | -7.52E-02 | 2.03E+03 | 5.00E+02 | -7.00E-02 |
| 7 | 9.11E+02 | 2.26E+02 | -8.58E-02 | 9.33E+02 | 2.25E+02 | -1.40E-01 | 9.37E+02 | 2.28E+02 | -4.35E-02 |
| | | RMS Error = | 6.92E-03 | | RMS Error = | 7.06E-03 | | RMS Error = | 6.77E-03 |

Calculated Olivine Composition

| | Strength Ratios | | Fa (Mole Frac) | Strength Ratios | | Fa (Mole Frac) | Strength Ratios | | Fa (Mole Frac) |
|---|---|---|---|---|---|---|---|---|---|
| I/III | 0.69 | Band I | .09 | .66 | Band I | .13 | .76 | Band I | .23 |
| II/III | 1.09 | Band II | .15 | .72 | Band II | .34 | .76 | Band II | .12 |
| | | Band III | .51 | | Band III | .29 | | Band III | .22 |
| | | **Avg Fa (II,III)** | **.33** | | **Avg Fa (II,III)** | **.31** | | **Avg Fa (II,III)** | **.17** |

**Table S4.11 MGM results for 984 Gretia.**

| $Fa_{10}$ | | $Fa_{50}$ | | $Fa_{90}$ | |
|---|---|---|---|---|---|
| Y-intercept | Slope | Y-intercept | Slope | Y-intercept | Slope |
| 7.35E-01 | -1.50E-05 | 7.15E-01 | -1.16E-05 | 7.32E-01 | -1.09E-05 |

Absorption bands

| | $Fa_{10}$ | | | $Fa_{50}$ | | | $Fa_{90}$ | | |
|---|---|---|---|---|---|---|---|---|---|
| | Center | Width | Strength | Center | Width | Strength | Center | Width | Strength |
| *1* | *4.06E+02* | *2.90E+02* | *-2.92E-01* | *4.04E+02* | *3.02E+02* | *-4.30E-01* | *4.10E+02* | *3.00E+02* | *-4.94E-01* |
| *2* | *6.15E+02* | *1.14E+02* | *-4.13E-02* | *6.22E+02* | *1.15E+02* | *-6.43E-02* | *6.21E+02* | *1.15E+02* | *-7.91E-02* |
| **3** | **8.72E+02** | **2.07E+02** | **-2.02E-01** | **8.74E+02** | **2.45E+02** | **-2.29E-01** | **8.81E+02** | **2.72E+02** | **-2.98E-01** |
| **4** | **1.05E+03** | **2.01E+02** | **-3.19E-01** | **1.06E+03** | **1.71E+02** | **-2.32E-01** | **1.06E+03** | **1.55E+02** | **-1.48E-01** |
| **5** | **1.26E+03** | **3.31E+02** | **-2.93E-01** | **1.24E+03** | **3.77E+02** | **-3.23E-01** | **1.20E+03** | **4.56E+02** | **-3.71E-01** |
| 6 | 2.01E+03 | 4.91E+02 | -6.08E-02 | 2.01E+03 | 4.52E+02 | -6.07E-02 | 1.95E+03 | 4.59E+02 | -8.21E-02 |
| 7 | 2.30E+03 | 4.62E+02 | -1.39E-02 | 2.30E+03 | 4.17E+02 | -1.00E-02 | 2.30E+03 | 4.64E+02 | -4.49E-02 |
| 8 | 9.11E+02 | 2.18E+02 | -1.06E-01 | 9.18E+02 | 2.23E+02 | -1.24E-01 | 9.47E+02 | 2.28E+02 | -2.99E-02 |
| | | RMS Error = | 8.57E-03 | | RMS Error = | 8.39E-03 | | RMS Error = | 8.37E-03 |

Calculated Olivine Composition

| | Strength Ratios | | Fa (Mole Frac) | Strength Ratios | | Fa (Mole Frac) | Strength Ratios | | Fa (Mole Frac) |
|---|---|---|---|---|---|---|---|---|---|
| I/III | 0.69 | Band I | .49 | .71 | Band I | .53 | .80 | Band I | .60 |
| II/III | 1.09 | Band II | .45 | .72 | Band II | .55 | .40 | Band II | .51 |
| | | Band III | .68 | | Band III | .37 | | Band III | .06 |
| | | **Avg Fa (II,III)** | **.56** | | **Avg Fa (II,III)** | **.46** | | **Avg Fa (II,III)** | **.28** |

**Table S4.12 MGM results for 2501 Lohja.**

| $Fa_{10}$ |  | $Fa_{50}$ |  | $Fa_{90}$ |  |
|---|---|---|---|---|---|
| Y-intercept | Slope | Y-intercept | Slope | Y-intercept | Slope |
| 8.51E-01 | -2.40E-05 | 8.51E-01 | -2.40E-05 | 8.68E-01 | -2.40E-05 |

Absorption bands

|  | Center | Width | Strength | Center | Width | Strength | Center | Width | Strength |
|---|---|---|---|---|---|---|---|---|---|
| *1* | *4.58E+02* | *3.65E+02* | *-3.42E-01* | *4.54E+02* | *3.68E+02* | *-3.58E-01* | *4.36E+02* | *4.00E+02* | *-3.51E-01* |
| *2* | *6.37E+02* | *1.14E+02* | *-7.08E-02* | *6.34E+02* | *1.14E+02* | *-7.16E-02* | *6.19E+02* | *1.15E+02* | *-5.80E-02* |
| **3** | **8.24E+02** | **1.85E+02** | **-3.04E-01** | **8.33E+02** | **1.98E+02** | **-3.48E-01** | **8.45E+02** | **2.26E+02** | **-2.73E-01** |
| **4** | **1.04E+03** | **2.07E+02** | **-4.85E-01** | **1.04E+03** | **1.92E+02** | **-3.78E-01** | **1.05E+03** | **1.77E+02** | **-3.82E-01** |
| **5** | **1.24E+03** | **3.39E+02** | **-4.65E-01** | **1.23E+03** | **3.58E+02** | **-4.89E-01** | **1.25E+03** | **3.43E+02** | **-4.55E-01** |
| 6 | 9.39E+02 | 2.24E+02 | -1.20E-01 | 9.95E+02 | 2.27E+02 | -1.40E-01 | 9.70E+02 | 3.29E+02 | -1.80E-01 |
| 7 | 1.97E+03 | 3.92E+02 | -6.72E-02 | 1.96E+03 | 4.08E+02 | -7.28E-02 | 1.96E+03 | 3.85E+02 | -7.24E-02 |
| 8 | 2.37E+03 | 5.88E+02 | -1.03E-01 | 2.37E+03 | 5.85E+02 | -1.09E-01 | 2.35E+03 | 5.45E+02 | -1.06E-01 |
|  |  | RMS Error = | 1.25E-02 |  | RMS Error = | 1.24E-02 |  | RMS Error = | 1.37E-02 |

Calculated Olivine Composition

|  | Strength Ratios |  | Fa (Mole Frac) | Strength Ratios |  | Fa (Mole Frac) | Strength Ratios |  | Fa (Mole Frac |
|---|---|---|---|---|---|---|---|---|---|
| I/III | 0.65 | Band I | -.09 | .71 | Band I | .02 | .60 | Band I | .16 |
| II/III | 1.04 | Band II | .12 | .77 | Band II | .08 | .84 | Band II | .32 |
|  |  | Band III | .47 |  | Band III | .34 |  | Band III | .48 |
|  |  | **Avg Fa (II,III)** | **.30** |  | **Avg Fa (II,III)** | **.21** |  | **Avg Fa (II,III)** | **.40** |

Calculated Low-Ca Pyroxene Composition

|  | Fs (Mole Frac) |
|---|---|
| BIIC | 0.49 |

**Table S4.13 MGM results for 3819 Robinson.**

| $Fa_{10}$ | | $Fa_{50}$ | | $Fa_{90}$ | |
|---|---|---|---|---|---|
| Y-intercept | Slope | Y-intercept | Slope | Y-intercept | Slope |
| 7.86E-01 | -1.50E-05 | 8.51E-01 | -2.40E-05 | 8.09E-01 | -1.50E-05 |

Absorption bands

| | Center | Width | Strength | Center | Width | Strength | Center | Width | Strength |
|---|---|---|---|---|---|---|---|---|---|
| *1* | *3.32E+02* | *3.94E+02* | *-3.96E-01* | *3.35E+02* | *3.98E+02* | *-4.07E-01* | *3.43E+02* | *3.95E+02* | *-4.15E-01* |
| *2* | *6.35E+02* | *1.14E+02* | *-5.06E-02* | *6.36E+02* | *1.15E+02* | *-5.33E-02* | *6.36E+02* | *1.15E+02* | *-5.74E-02* |
| **3** | **8.69E+02** | **2.17E+02** | **-2.46E-01** | **8.76E+02** | **2.26E+02** | **-2.70E-01** | **8.76E+02** | **2.31E+02** | **-2.79E-01** |
| **4** | **1.06E+03** | **2.01E+02** | **-3.93E-01** | **1.06E+03** | **1.82E+02** | **-3.16E-01** | **1.06E+03** | **1.74E+02** | **-2.40E-01** |
| **5** | **1.27E+03** | **3.37E+02** | **-3.88E-01** | **1.25E+03** | **3.67E+02** | **-4.14E-01** | **1.23E+03** | **4.03E+02** | **-4.40E-01** |
| 6 | 9.35E+02 | 2.23E+02 | -1.54E-01 | 9.43E+02 | 2.27E+02 | -1.55E-01 | 9.53E+02 | 2.30E+02 | -1.44E-01 |
| 7 | 1.94E+03 | 4.14E+02 | -9.83E-02 | 1.94E+03 | 4.14E+02 | -1.06E-01 | 1.94E+03 | 4.14E+02 | -1.17E-01 |
| 8 | 2.30E+03 | 4.89E+02 | -7.93E-02 | 2.30E+03 | 4.89E+02 | -8.76E-02 | 2.31E+03 | 4.89E+02 | -9.73E-02 |
| | | RMS Error = | 1.31E-02 | | RMS Error = | 1.30E-02 | | RMS Error = | 1.30E-02 |

Calculated Olivine Composition

| | Strength Ratios | | Fa (Mole Frac) | Strength Ratios | | Fa (Mole Frac) | Strength Ratios | | Fa (Mole Frac) |
|---|---|---|---|---|---|---|---|---|---|
| I/III | 0.64 | Band I | .47 | .65 | Band I | .55 | .63 | Band I | .54 |
| II/III | 1.01 | Band II | .64 | .76 | Band II | .67 | .54 | Band II | .65 |
| | | Band III | .71 | | Band III | .53 | | Band III | .32 |
| | | **Avg Fa (II,III)** | **.68** | | **Avg Fa (II,III)** | **.60** | | **Avg Fa (II,III)** | **.49** |

Calculated Low-Ca Pyroxene Composition

| | Fs (Mole Frac) |
|---|---|
| BIIC | 0.41 |

**Table S4.14 MGM results for (8838) 1989 UW2**

| $Fa_{10}$ | | $Fa_{50}$ | | $Fa_{90}$ | |
|---|---|---|---|---|---|
| Y-intercept | Slope | Y-intercept | Slope | Y-intercept | Slope |
| 7.38E-01 | -2.20E-05 | 7.44E-01 | -2.20E-05 | 7.63E-01 | -2.20E-05 |

Absorption bands

| | Center | Width | Strength | Center | Width | Strength | Center | Width | Strength |
|---|---|---|---|---|---|---|---|---|---|
| *1* | *5.32E+02* | *1.97E+02* | *-4.33E-01* | *5.22E+02* | *2.41E+02* | *-3.99E-01* | *5.23E+02* | *2.54E+02* | *-4.67E-01* |
| **2** | **8.08E+02** | **2.17E+02** | **-2.98E-01** | **8.27E+02** | **2.52E+02** | **-3.27E-01** | **9.10E+02** | **2.86E+02** | **-1.71E-01** |
| **3** | **1.04E+03** | **2.15E+02** | **-4.72E-01** | **1.05E+03** | **1.85E+02** | **-3.55E-01** | **1.06E+03** | **1.54E+02** | **-2.32E-01** |
| **4** | **1.25E+03** | **3.60E+02** | **-4.42E-01** | **1.23E+03** | **3.87E+02** | **-4.77E-01** | **1.21E+03** | **4.36E+02** | **-5.21E-01** |
| 5 | 1.92E+03 | 4.42E+02 | -5.26E-02 | 1.93E+03 | 5.08E+02 | -6.12E-02 | 1.96E+03 | 5.52E+02 | -9.32E-02 |
| 6 | 8.85E+02 | 2.14E+02 | -1.52E-01 | 9.10E+02 | 2.33E+02 | -1.49E-01 | 8.61E+02 | 2.59E+02 | -2.99E-01 |
| | | RMS Error = | 1.15E-02 | | RMS Error = | 1.10E-02 | | RMS Error = | 1.25E-02 |

Calculated Olivine Composition

| | Strength Ratios | | Fa (Mole Frac) | Strength Ratios | | Fa (Mole Frac) | Strength Ratios | | Fa (Mole Frac) |
|---|---|---|---|---|---|---|---|---|---|
| I/III | 0.67 | Band I | -.28 | .68 | Band I | -.05 | .33 | Band I | .96 |
| II/III | 1.07 | Band II | .09 | .74 | Band II | .32 | .45 | Band II | .59 |
| | | Band III | .53 | | Band III | .32 | | Band III | .13 |
| | | **Avg Fa (II,III)** | **.31** | | **Avg Fa (II,III)** | **.32** | | **Avg Fa (II,III)** | **.36** |

Calculated Low-Ca Pyroxene Composition

| | Fs (Mole Frac) |
|---|---|
| BIIC | 0.39 |

**Table S4.15 MGM results for (16520) 1990 WO3**

| | $Fa_{10}$ | | $Fa_{50}$ | | $Fa_{90}$ | |
|---|---|---|---|---|---|---|
| | Y-intercept | Slope | Y-intercept | Slope | Y-intercept | Slope |
| | 7.92E-01 | -2.40E-05 | 7.89E-01 | -2.20E-05 | 7.63E-01 | -2.20E-05 |

Absorption bands

| | $Fa_{10}$ | | | $Fa_{50}$ | | | $Fa_{90}$ | | |
|---|---|---|---|---|---|---|---|---|---|
| | Center | Width | Strength | Center | Width | Strength | Center | Width | Strength |
| *1* | *5.04E+02* | *3.24E+02* | *-2.79E-01* | *4.93E+02* | *3.42E+02* | *-3.15E-01* | *4.90E+02* | *3.05E+02* | *-3.84E-01* |
| **2** | **8.25E+02** | **2.24E+02** | **-1.80E-01** | **8.41E+02** | **2.54E+02** | **-2.35E-01** | **8.45E+02** | **2.92E+02** | **-2.44E-01** |
| **3** | **1.04E+03** | **1.83E+02** | **-3.60E-01** | **1.04E+03** | **1.63E+02** | **-2.65E-01** | **1.04E+03** | **1.54E+02** | **-2.04E-01** |
| **4** | **1.22E+03** | **3.22E+02** | **-3.28E-01** | **1.20E+03** | **3.76E+02** | **-3.67E-01** | **1.18E+03** | **4.36E+02** | **-4.10E-01** |
| 5 | 1.99E+03 | 3.50E+02 | -7.99E-02 | 1.97E+03 | 4.24E+02 | -9.58E-02 | 1.94E+03 | 4.40E+02 | -1.24E-01 |
| 6 | 2.30E+03 | 4.47E+02 | -3.03E-02 | 2.30E+03 | 4.24E+02 | -3.71E-02 | 2.30E+03 | 4.28E+02 | -7.23E-02 |
| 7 | 8.85E+02 | 2.28E+02 | -1.97E-01 | 8.95E+02 | 2.36E+02 | -1.47E-01 | 8.67E+02 | 2.61E+02 | -1.29E-01 |
| | | RMS Error = | 1.67E-02 | | RMS Error = | 1.64E-02 | | RMS Error = | 1.69E-02 |

Calculated Olivine Composition

| | Strength Ratios | | Fa (Mole Frac) | Strength Ratios | | Fa (Mole Frac) | Strength Ratios | | Fa (Mole Frac) |
|---|---|---|---|---|---|---|---|---|---|
| I/III | 0.55 | Band I | -.08 | .64 | Band I | .12 | .59 | Band I | .17 |
| II/III | 1.10 | Band II | .05 | .72 | Band II | .11 | .50 | Band II | .15 |
| | | Band III | .24 | | Band III | -.02 | | Band III | -.21 |
| | | **Avg Fa (II,III)** | **.15** | | **Avg Fa (II,III)** | **.04** | | **Avg Fa (II,III)** | **-.03** |

Calculated Low-Ca Pyroxene Composition

| | Fs (Mole Frac) |
|---|---|
| BIIC | 0.60 |

**Table S4.16 MGM results for (17818) 1996 FE118**

| Fa$_{10}$ |  | Fa$_{50}$ |  | Fa$_{90}$ |  |
|---|---|---|---|---|---|
| Y-intercept | Slope | Y-intercept | Slope | Y-intercept | Slope |
| 7.63E-01 | -2.20E-05 | 7.65E-01 | -2.20E-05 | 7.66E-01 | -2.20E-05 |

Absorption bands

|  | Center | Width | Strength | Center | Width | Strength | Center | Width | Strength |
|---|---|---|---|---|---|---|---|---|---|
| *1* | *5.17E+02* | *3.01E+02* | *-1.91E-01* | *4.85E+02* | *3.07E+02* | *-1.92E-01* | *5.12E+02* | *2.97E+02* | *-1.98E-01* |
| **2** | **8.90E+02** | **2.27E+02** | **-2.81E-01** | **8.98E+02** | **2.49E+02** | **-2.96E-01** | **9.30E+02** | **2.87E+02** | **-3.26E-01** |
| **3** | **1.06E+03** | **1.90E+02** | **-4.26E-01** | **1.06E+03** | **1.78E+02** | **-3.28E-01** | **1.06E+03** | **1.53E+02** | **-2.10E-01** |
| **4** | **1.26E+03** | **3.09E+02** | **-4.08E-01** | **1.24E+03** | **3.43E+02** | **-4.24E-01** | **1.23E+03** | **3.55E+02** | **-4.30E-01** |
|  |  | RMS Error = | 1.93E-02 |  | RMS Error = | 1.99E-02 |  | RMS Error = | 2.01E-02 |

Calculated Olivine Composition

|  | Strength Ratios |  | Fa (Mole Frac) | Strength Ratios |  | Fa (Mole Frac) | Strength Ratios |  | Fa (Mole Frac) |
|---|---|---|---|---|---|---|---|---|---|
| I/III | 0.69 | Band I | .72 | .70 | Band I | .82 | .76 | Band I | 1.21 |
| II/III | 1.04 | Band II | .54 | .77 | Band II | .54 | .49 | Band II | .66 |
|  |  | Band III | .63 |  | Band III | .44 |  | Band III | .36 |
|  |  | **Avg Fa (II,III)** | **.59** |  | **Avg Fa (II,III)** | **.49** |  | **Avg Fa (II,III)** | **.51** |

**Table S4.17 MGM results for (21809) 1999 TG19**

| Fa$_{10}$ | | Fa$_{50}$ | | Fa$_{90}$ | |
|---|---|---|---|---|---|
| Y-intercept | Slope | Y-intercept | Slope | Y-intercept | Slope |
| 7.03E-01 | -2.20E-05 | 7.65E-01 | -2.20E-05 | 7.66E-01 | -2.20E-05 |

Absorption bands

| | Center | Width | Strength | Center | Width | Strength | Center | Width | Strength |
|---|---|---|---|---|---|---|---|---|---|
| *1* | *3.46E+02* | *3.00E+02* | *-1.55E-01* | *4.01E+02* | *3.00E+02* | *-1.55E-01* | *5.01E+02* | *3.00E+02* | *-1.47E-01* |
| **2** | **9.03E+02** | **2.29E+02** | **-3.81E-01** | **8.83E+02** | **2.54E+02** | **-3.41E-01** | **8.87E+02** | **2.82E+02** | **-2.87E-01** |
| **3** | **1.07E+03** | **1.78E+02** | **-4.29E-01** | **1.05E+03** | **1.62E+02** | **-3.06E-01** | **1.05E+03** | **1.52E+02** | **-1.87E-01** |
| **4** | **1.27E+03** | **3.04E+02** | **-4.35E-01** | **1.23E+03** | **3.81E+02** | **-4.75E-01** | **1.20E+03** | **4.47E+02** | **-4.96E-01** |
| | | RMS Error = | 2.83E-02 | | RMS Error = | 1.99E-02 | | RMS Error = | 2.01E-02 |

Calculated Olivine Composition

| | Strength Ratios | | Fa (Mole Frac) | Strength Ratios | | Fa (Mole Frac) | Strength Ratios | | Fa (Mole Frac) |
|---|---|---|---|---|---|---|---|---|---|
| I/III | 0.88 | Band I | .88 | .72 | Band I | .63 | .58 | Band I | .68 |
| II/III | 0.99 | Band II | .77 | .64 | Band II | .35 | .38 | Band II | .39 |
| | | Band III | .69 | | Band III | .30 | | Band III | -.03 |
| | | **Avg Fa (II,III)** | **.73** | | **Avg Fa (II,III)** | **.32** | | **Avg Fa (II,III)** | **.18** |

**Table S4.18 MGM results for (31393) 1998 YG8.**

| $Fa_{10}$ | | $Fa_{50}$ | | $Fa_{90}$ | |
|---|---|---|---|---|---|
| Y-intercept | Slope | Y-intercept | Slope | Y-intercept | Slope |
| 6.99E-01 | -2.20E-05 | 7.44E-01 | -2.20E-05 | 7.08E-01 | -2.20E-05 |

Absorption bands

| | Center | Width | Strength | Center | Width | Strength | Center | Width | Strength |
|---|---|---|---|---|---|---|---|---|---|
| *1* | *5.22E+02* | *2.89E+02* | *-1.99E-01* | *5.22E+02* | *2.23E+02* | *-2.33E-01* | *5.05E+02* | *2.94E+02* | *-2.29E-01* |
| **2** | **8.05E+02** | **2.35E+02** | **-2.93E-01** | **8.09E+02** | **2.59E+02** | **-3.27E-01** | **8.37E+02** | **2.91E+02** | **-3.41E-01** |
| **3** | **1.05E+03** | **2.25E+02** | **-4.58E-01** | **1.04E+03** | **1.97E+02** | **-3.40E-01** | **1.04E+03** | **1.64E+02** | **-2.43E-01** |
| **4** | **1.25E+03** | **3.55E+02** | **-4.47E-01** | **1.22E+03** | **3.91E+02** | **-4.86E-01** | **1.21E+03** | **4.29E+02** | **-5.03E-01** |
| 5 | 2.04E+03 | 4.00E+02 | -5.41E-02 | 2.04E+03 | 4.06E+02 | -6.53E-02 | 2.04E+03 | 4.22E+02 | -7.54E-02 |
| 6 | 9.70E+02 | 2.45E+02 | -1.49E-01 | 1.00E+03 | 2.69E+02 | -1.49E-01 | 1.07E+03 | 2.62E+02 | -1.31E-01 |
| | | RMS Error = | 3.82E-02 | | RMS Error = | 3.80E-02 | | RMS Error = | 3.79E-02 |

Calculated Olivine Composition

| | Strength Ratios | | Fa (Mole Frac) | Strength Ratios | | Fa (Mole Frac) | Strength Ratios | | Fa (Mole Frac) |
|---|---|---|---|---|---|---|---|---|---|
| I/III | 0.65 | Band I | -.32 | .67 | Band I | -.27 | .68 | Band I | .08 |
| II/III | 1.02 | Band II | .27 | .70 | Band II | .13 | .48 | Band II | .06 |
| | | Band III | .53 | | Band III | .27 | | Band III | .06 |
| | | **Avg Fa (II,III)** | **.40** | | **Avg Fa (II,III)** | **.20** | | **Avg Fa (II,III)** | **.06** |

**Table S4.19 MGM results for (35925) JP104.**

| | Fa$_{10}$ | | Fa$_{50}$ | | Fa$_{90}$ |
|---|---|---|---|---|---|
| Y-intercept | Slope | Y-intercept | Slope | Y-intercept | Slope |
| 7.20E-01 | -2.00E-05 | 7.25E-01 | -2.00E-05 | 7.32E-01 | -2.00E-05 |

Absorption bands

| | Center | Width | Strength | Center | Width | Strength | Center | Width | Strength |
|---|---|---|---|---|---|---|---|---|---|
| *1* | *5.17E+02* | *4.05E+02* | *-5.67E-02* | *5.16E+02* | *3.22E+02* | *-7.71E-02* | *4.33E+02* | *3.30E+02* | *-1.06E-01* |
| **2** | **8.89E+02** | **2.34E+02** | **-2.09E-01** | **8.96E+02** | **2.55E+02** | **-2.29E-01** | **8.90E+02** | **2.85E+02** | **-2.24E-01** |
| **3** | **1.05E+03** | **2.04E+02** | **-3.31E-01** | **1.06E+03** | **1.76E+02** | **-2.33E-01** | **1.06E+03** | **1.60E+02** | **-1.35E-01** |
| **4** | **1.25E+03** | **3.24E+02** | **-2.84E-01** | **1.22E+03** | **3.79E+02** | **-3.17E-01** | **1.19E+03** | **4.43E+02** | **-3.40E-01** |
| 5 | 1.96E+03 | 4.16E+02 | -5.68E-02 | 1.97E+03 | 4.25E+02 | -6.72E-02 | 1.97E+03 | 4.33E+02 | -8.18E-02 |
| 6 | 9.17E+02 | 2.31E+02 | -1.50E-01 | 9.17E+02 | 2.24E+02 | -1.50E-01 | 9.46E+02 | 2.33E+02 | -1.45E-01 |
| | | RMS Error = | 3.82E-02 | | RMS Error = | 3.80E-02 | | RMS Error = | 1.86E-02 |

Calculated Olivine Composition

| | Strength Ratios | | Fa (Mole Frac) | Strength Ratios | | Fa (Mole Frac) | Strength Ratios | | Fa (Mole Frac) |
|---|---|---|---|---|---|---|---|---|---|
| I/III | 0.74 | Band I | .70 | .72 | Band I | .79 | .66 | Band I | .72 |
| II/III | 1.16 | Band II | .47 | .74 | Band II | .49 | .40 | Band II | .66 |
| | | Band III | .56 | | Band III | .21 | | Band III | -.08 |
| | | **Avg Fa (II,III)** | **.52** | | **Avg Fa (II,III)** | **.35** | | **Avg Fa (II,III)** | **.29** |

Calculated Low-Ca Pyroxene Composition

| | Fs (Mole Frac) |
|---|---|
| BIIC | 0.52 |

**Table S4.20 MGM results for (36256) 1999 XT17.**

| $Fa_{10}$ | | $Fa_{50}$ | | $Fa_{90}$ | |
|---|---|---|---|---|---|
| Y-intercept | Slope | Y-intercept | Slope | Y-intercept | Slope |
| 7.29E-01 | -1.50E-05 | 7.47E-01 | -1.80E-05 | 7.47E-01 | -1.80E-05 |

Absorption bands

| | Center | Width | Strength | Center | Width | Strength | Center | Width | Strength |
|---|---|---|---|---|---|---|---|---|---|
| *1* | *3.28E+02* | *3.00E+02* | *-5.60E-01* | *3.66E+02* | *2.90E+02* | *-2.60E-01* | *1.70E+02* | *2.96E+02* | *-3.13E+00* |
| **2** | **8.62E+02** | **2.30E+02** | **-2.32E-01** | **8.90E+02** | **2.52E+02** | **-2.18E-01** | **9.20E+02** | **2.90E+02** | **-2.30E-01** |
| **3** | **1.05E+03** | **1.97E+02** | **-3.66E-01** | **1.06E+03** | **1.69E+02** | **-2.51E-01** | **1.06E+03** | **1.45E+02** | **-1.69E-01** |
| **4** | **1.26E+03** | **3.25E+02** | **-3.38E-01** | **1.23E+03** | **3.62E+02** | **-3.47E-01** | **1.22E+03** | **3.77E+02** | **-3.52E-01** |
| | | RMS Error = | 1.19E-02 | | RMS Error = | 1.40E-02 | | RMS Error = | 1.41E-02 |

Calculated Olivine Composition

| | Strength Ratios | | Fa (Mole Frac) | Strength Ratios | | Fa (Mole Frac) | Strength Ratios | | Fa (Mole Frac |
|---|---|---|---|---|---|---|---|---|---|
| I/III | 0.68 | Band I | .37 | .63 | Band I | .71 | .65 | Band I | 1.08 |
| II/III | 1.08 | Band II | .41 | .72 | Band II | .51 | .48 | Band II | .63 |
| | | Band III | .61 | | Band III | .34 | | Band III | .24 |
| | | **Avg Fa (II,III)** | **.51** | | **Avg Fa (II,III)** | **.43** | | **Avg Fa (II,III)** | **.44** |

**Table S4.21 MGM results for (92516) 2000 ND25.**

| $Fa_{10}$ | | $Fa_{50}$ | | $Fa_{90}$ | |
|---|---|---|---|---|---|
| Y-intercept | Slope | Y-intercept | Slope | Y-intercept | Slope |
| 7.34E-01 | -2.00E-05 | 7.55E-01 | -2.00E-05 | 7.37E-01 | -2.00E-05 |

Absorption bands

| | $Fa_{10}$ | | | $Fa_{50}$ | | | $Fa_{90}$ | | |
|---|---|---|---|---|---|---|---|---|---|
| | Center | Width | Strength | Center | Width | Strength | Center | Width | Strength |
| *1* | *3.04E+02* | *4.00E+02* | *-7.15E-02* | *3.03E+02* | *4.00E+02* | *-5.90E-02* | *3.02E+02* | *4.00E+02* | *-4.97E-02* |
| *2* | *6.66E+02* | *1.15E+02* | *-3.82E-01* | *6.68E+02* | *1.15E+02* | *-3.97E-01* | *6.57E+02* | *1.15E+02* | *-3.27E-01* |
| **3** | **8.39E+02** | **2.29E+02** | **-4.24E-01** | **8.43E+02** | **2.29E+02** | **-4.36E-01** | **8.43E+02** | **2.28E+02** | **-4.45E-01** |
| **4** | **1.04E+03** | **1.79E+02** | **-3.85E-01** | **1.04E+03** | **1.80E+02** | **-4.11E-01** | **1.04E+03** | **1.78E+02** | **-4.28E-01** |
| **5** | **1.23E+03** | **4.25E+02** | **-6.40E-01** | **1.23E+03** | **4.14E+02** | **-6.28E-01** | **1.24E+03** | **4.09E+02** | **-6.24E-01** |
| 6 | 9.04E+02 | 2.28E+02 | -4.38E-02 | 9.09E+02 | 2.28E+02 | -4.35E-02 | 9.10E+02 | 2.28E+02 | -4.13E-02 |
| | | RMS Error = | 1.38E-02 | | RMS Error = | 1.43E-02 | | RMS Error = | 1.51E-02 |

Calculated Olivine Composition

| | $Fa_{10}$ | | | $Fa_{50}$ | | | $Fa_{90}$ | | |
|---|---|---|---|---|---|---|---|---|---|
| | Strength Ratios | | Fa (Mole Frac) | Strength Ratios | | Fa (Mole Frac) | Strength Ratios | | Fa (Mole Frac) |
| I/III | 0.66 | Band I | .10 | .69 | Band I | .14 | .71 | Band I | .14 |
| II/III | 0.60 | Band II | .17 | .65 | Band II | .24 | .69 | Band II | .24 |
| | | Band III | .28 | | Band III | .35 | | Band III | .39 |
| | | **Avg Fa (II,III)** | **.23** | | **Avg Fa (II,III)** | **.30** | | **Avg Fa (II,III)** | **.31** |

Calculated Low-Ca Pyroxene Composition

| | Fs (Mole Frac) |
|---|---|
| BIIC | n/a |

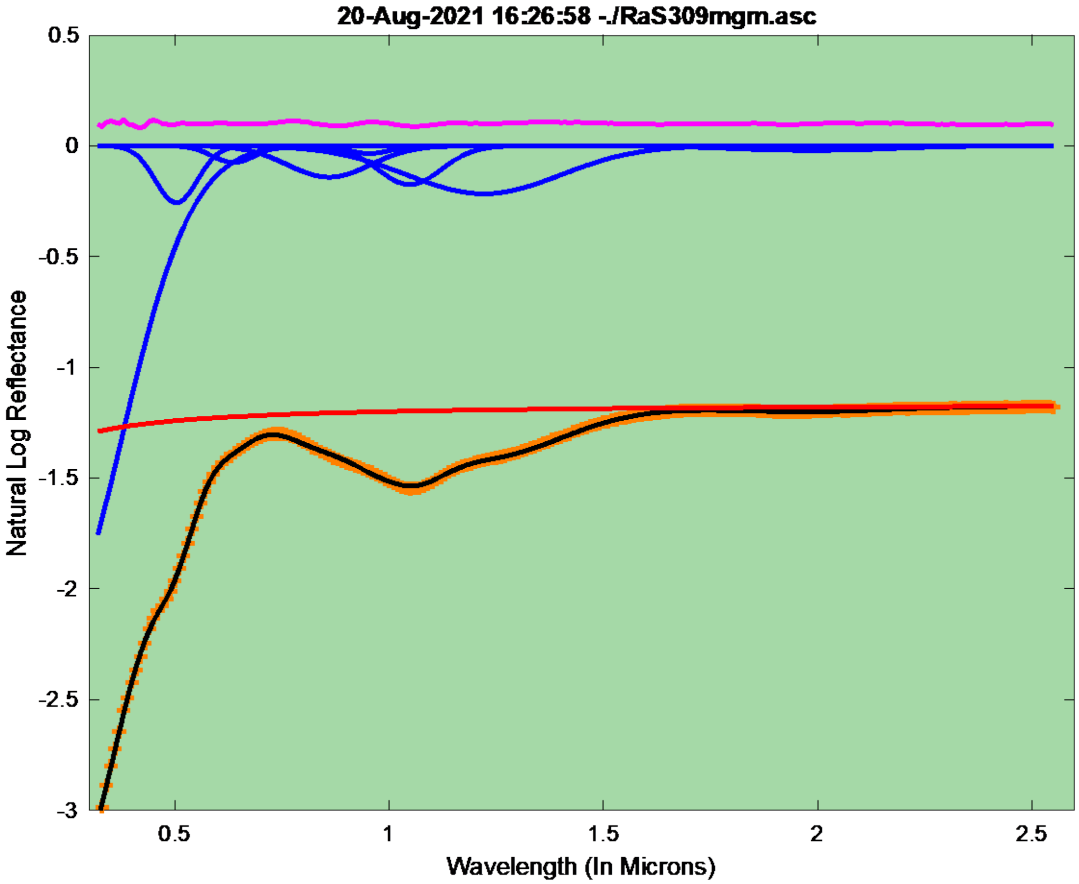

**Fig. S4.1.** MGM fit for oxidized brachinite RaS 309.

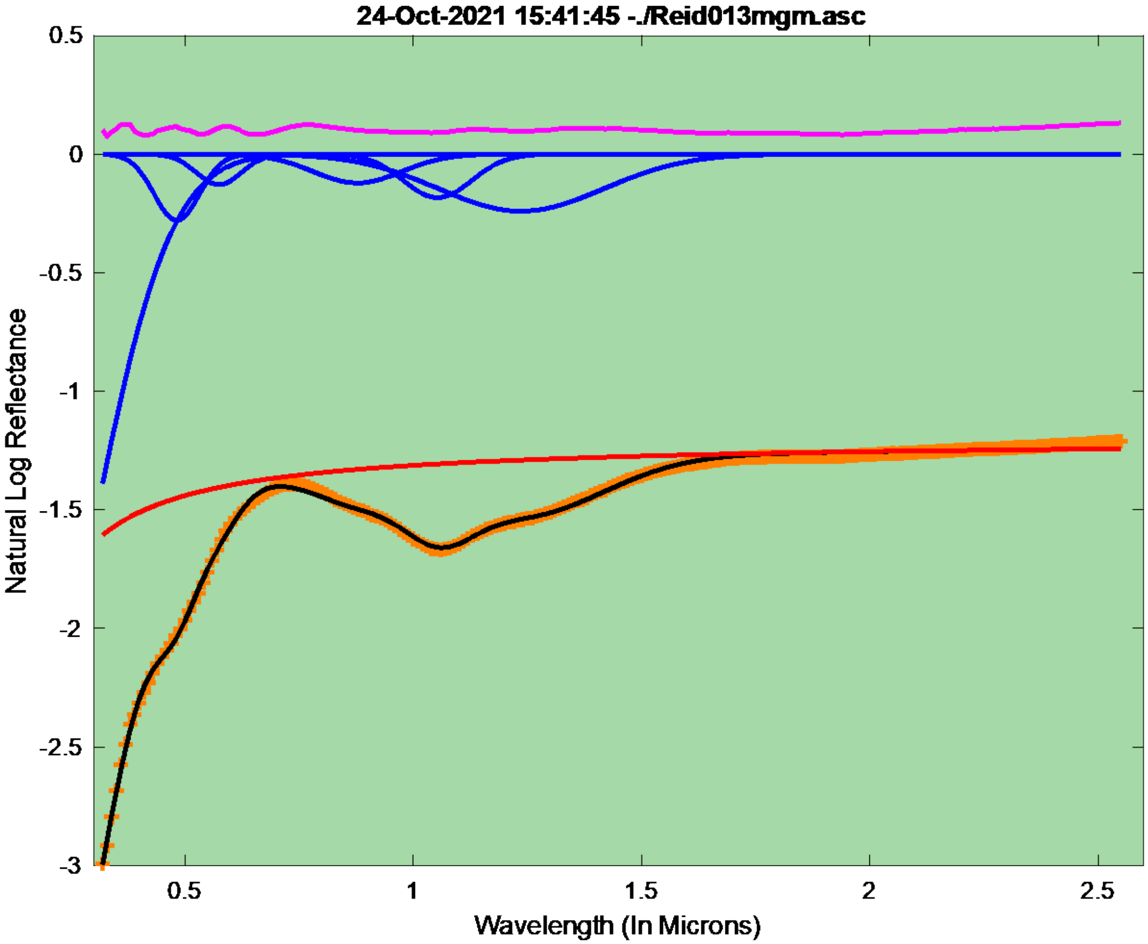

**Fig. S4.2.** MGM fit for oxidized brachinite Reid 013.

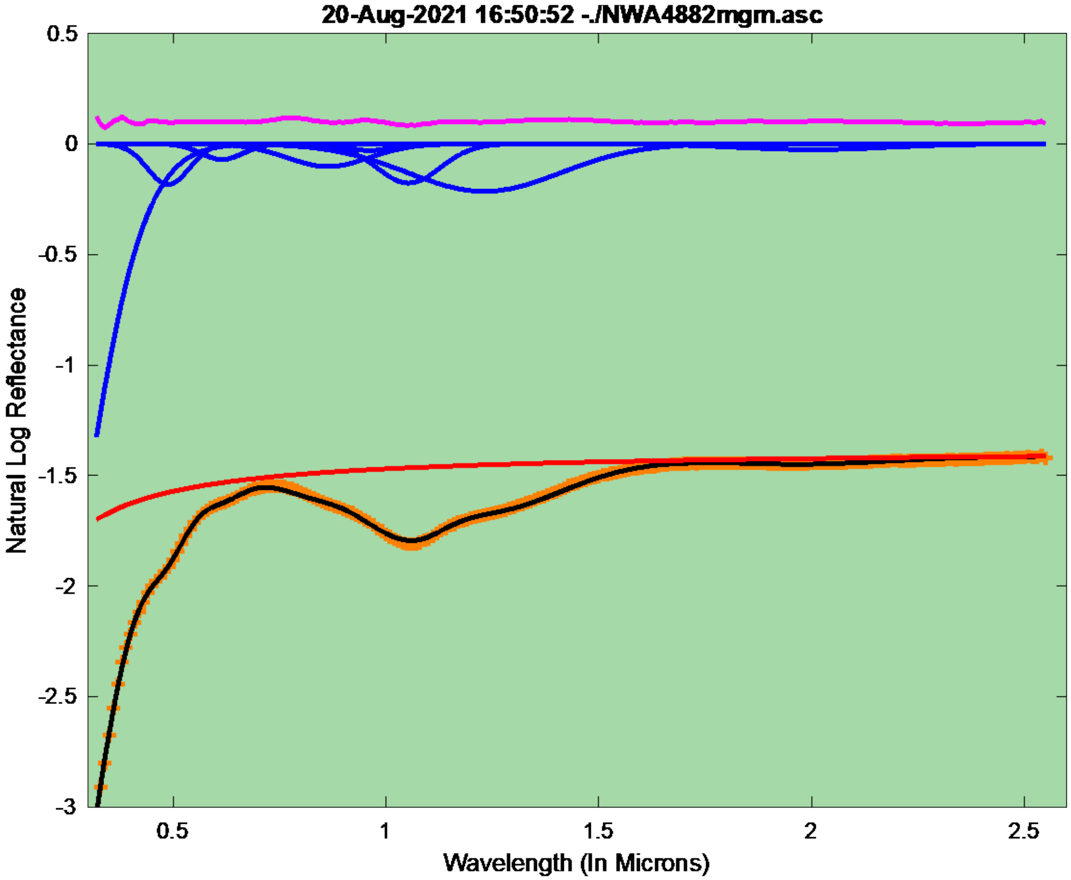

**Fig. S4.3.** MGM fit for oxidized brachinite NWA 4882.

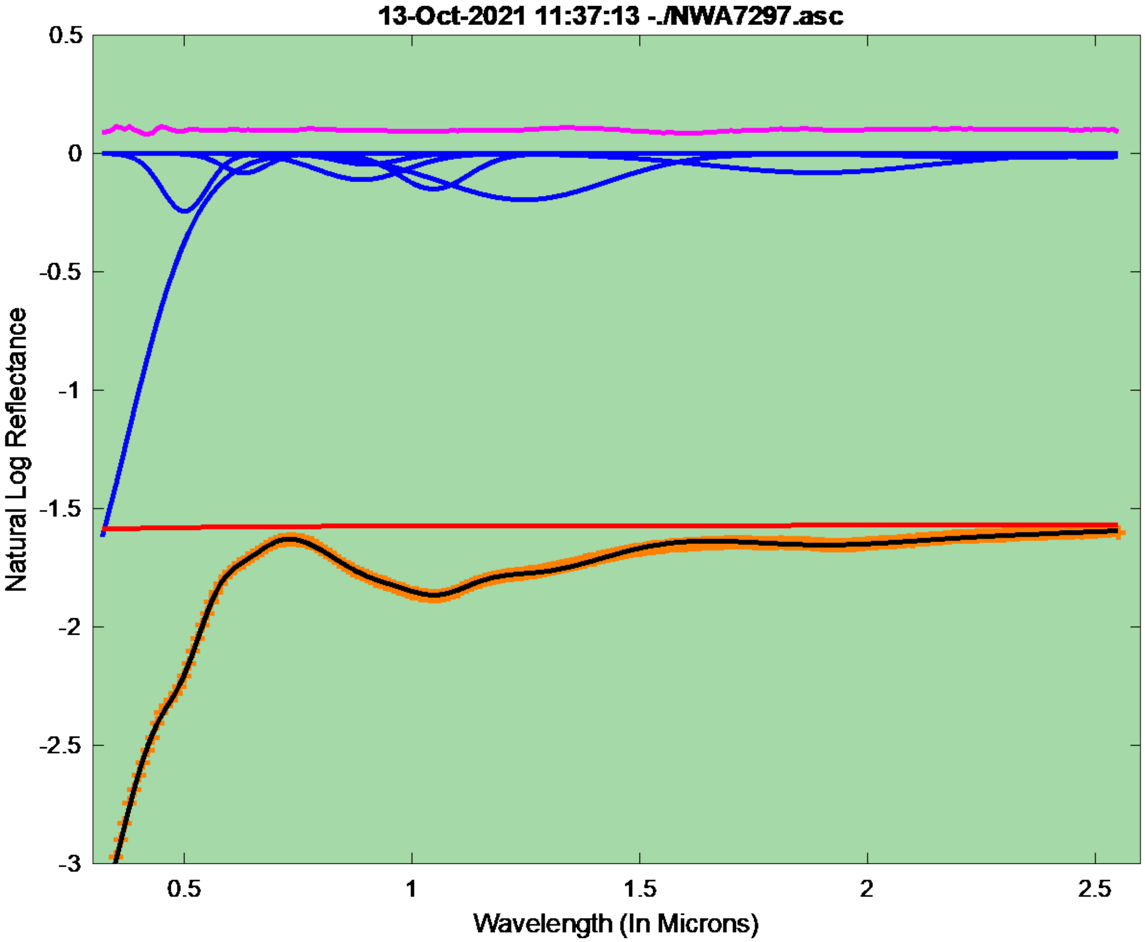

**Fig. S4.4.** MGM fit for reduced brachinite NWA 7297.

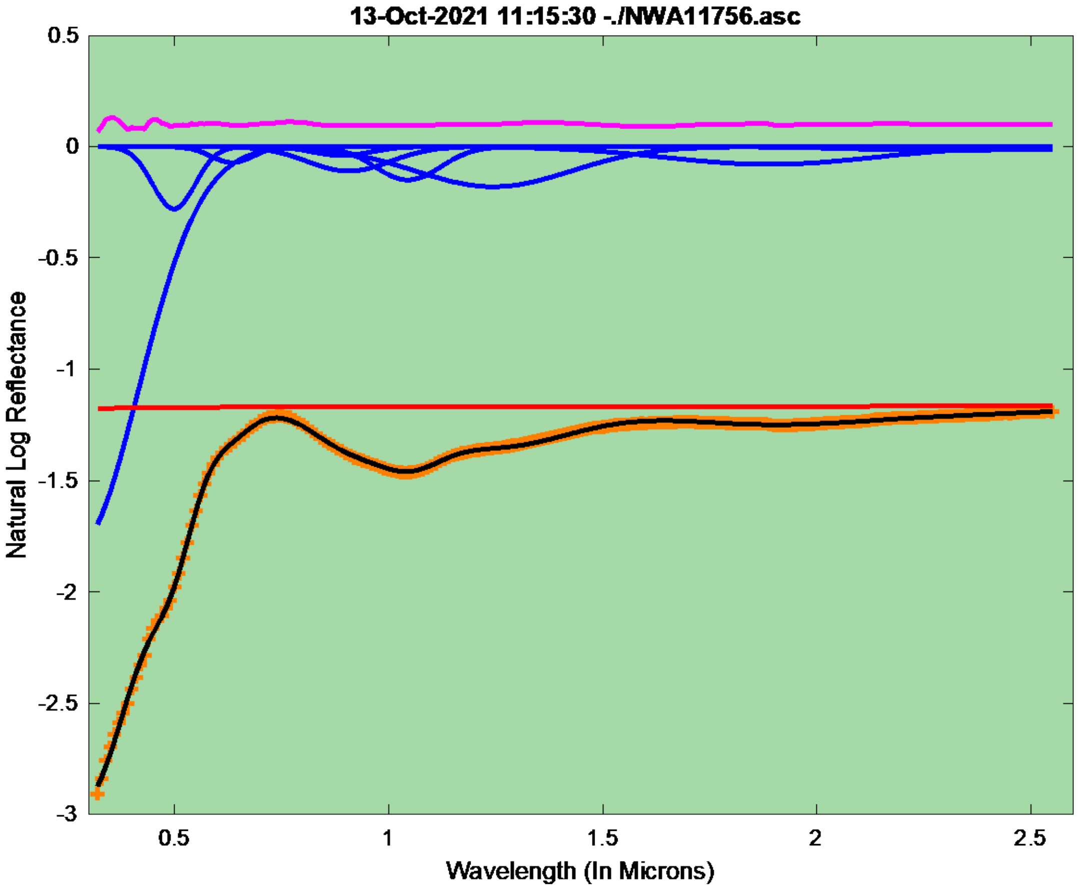

**Fig. S4.5.** MGM fit for reduced brachinite NWA 11756.

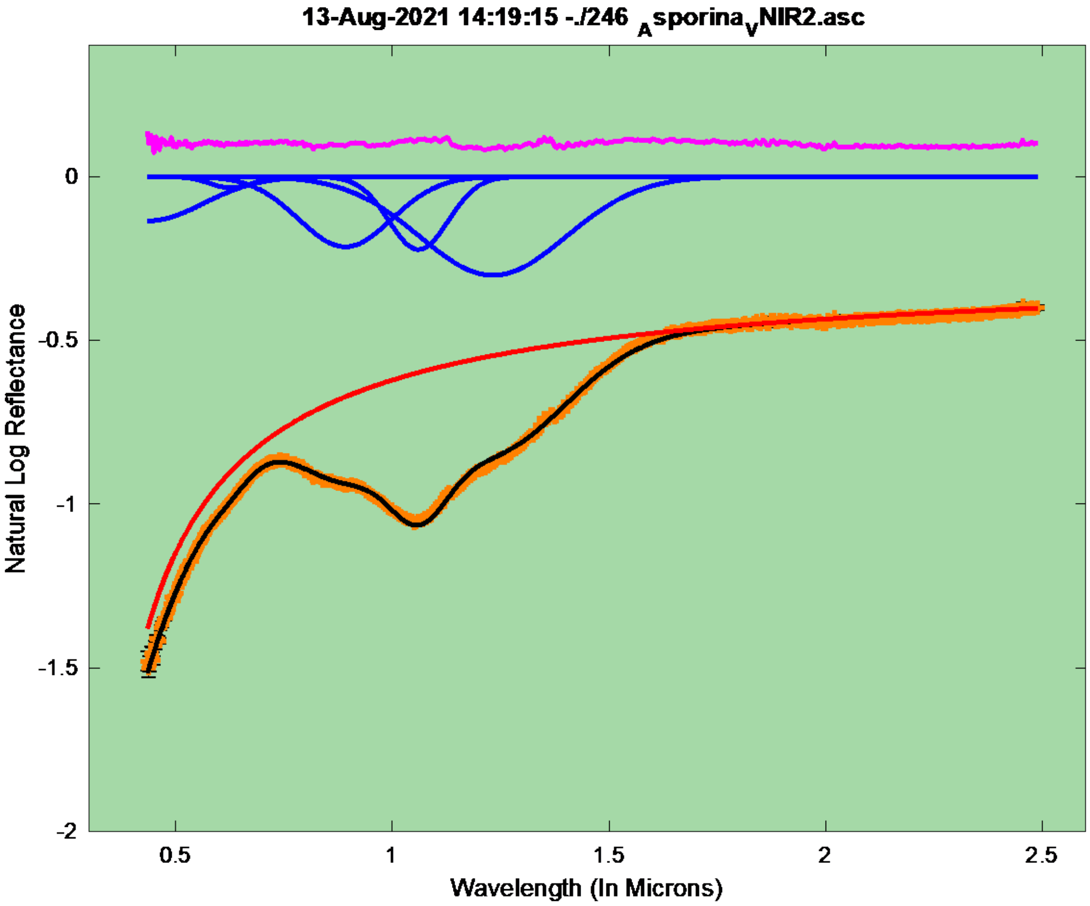

**Fig. S4.6.** MGM fit for asteroid 246 Asporina.

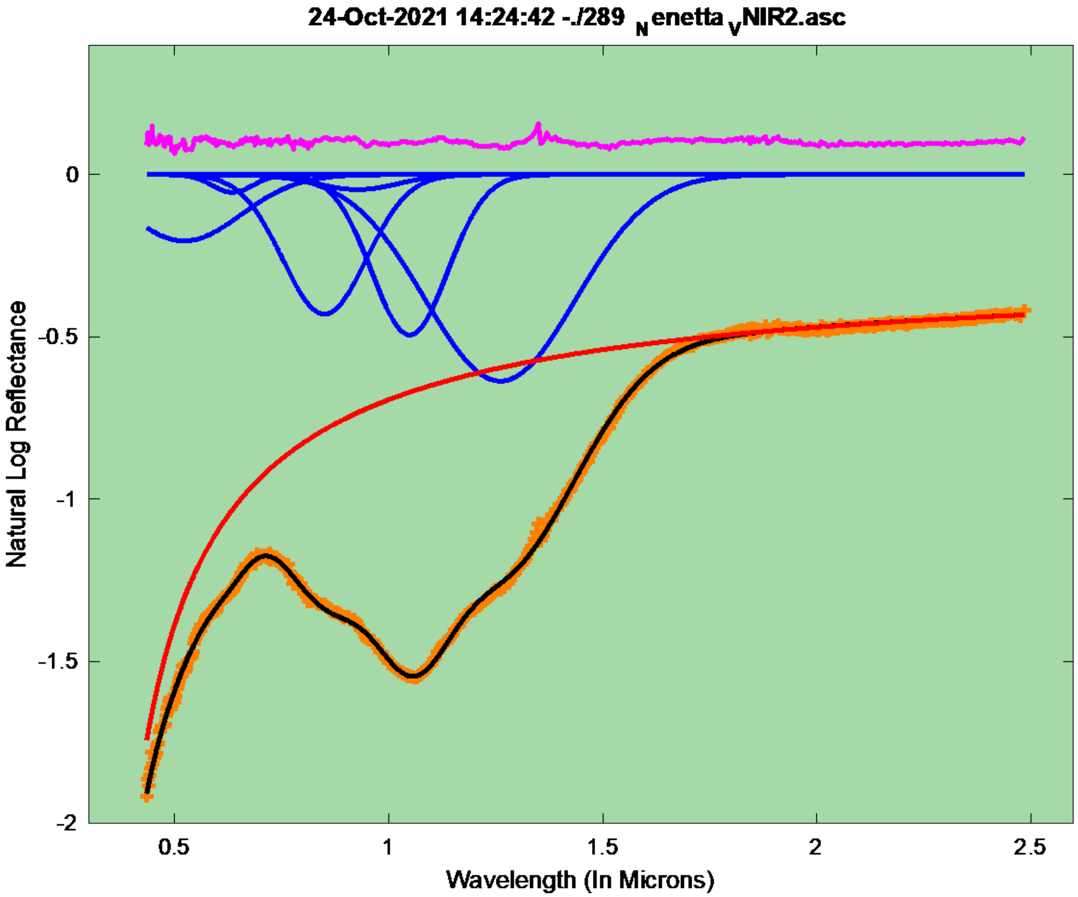

**Fig. S4.7.** MGM fit for asteroid 289 Nenetta.

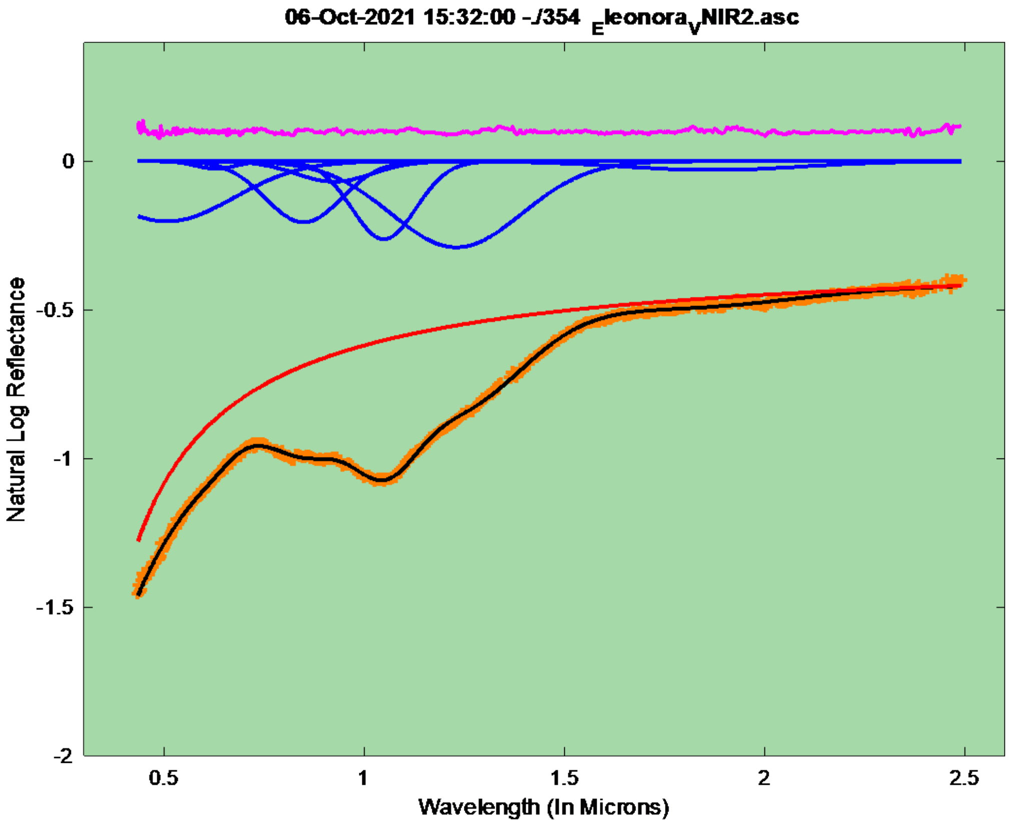

**Fig. S4.8.** MGM fit for asteroid 354 Eleonora.

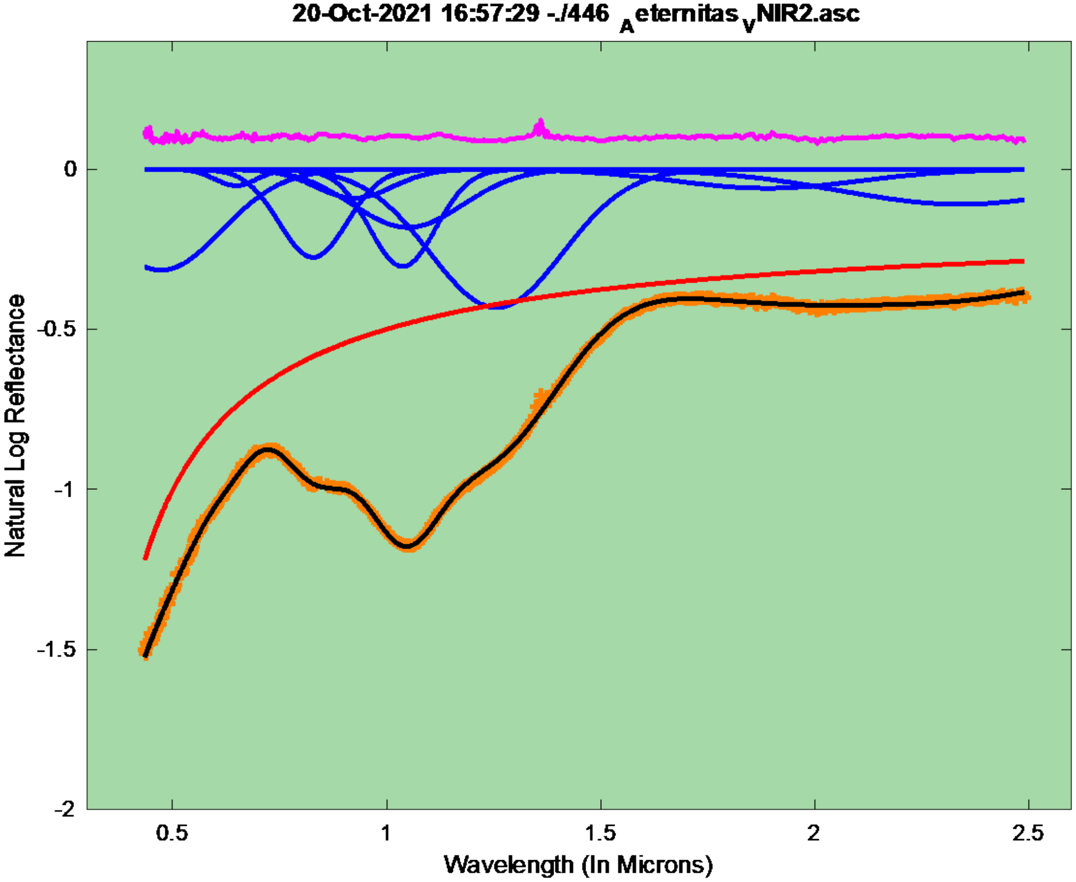

**Fig. S4.9.** MGM fit for asteroid 446 Aeternitas. Band centers for olivine yield inconsistent results (Table S4.9).

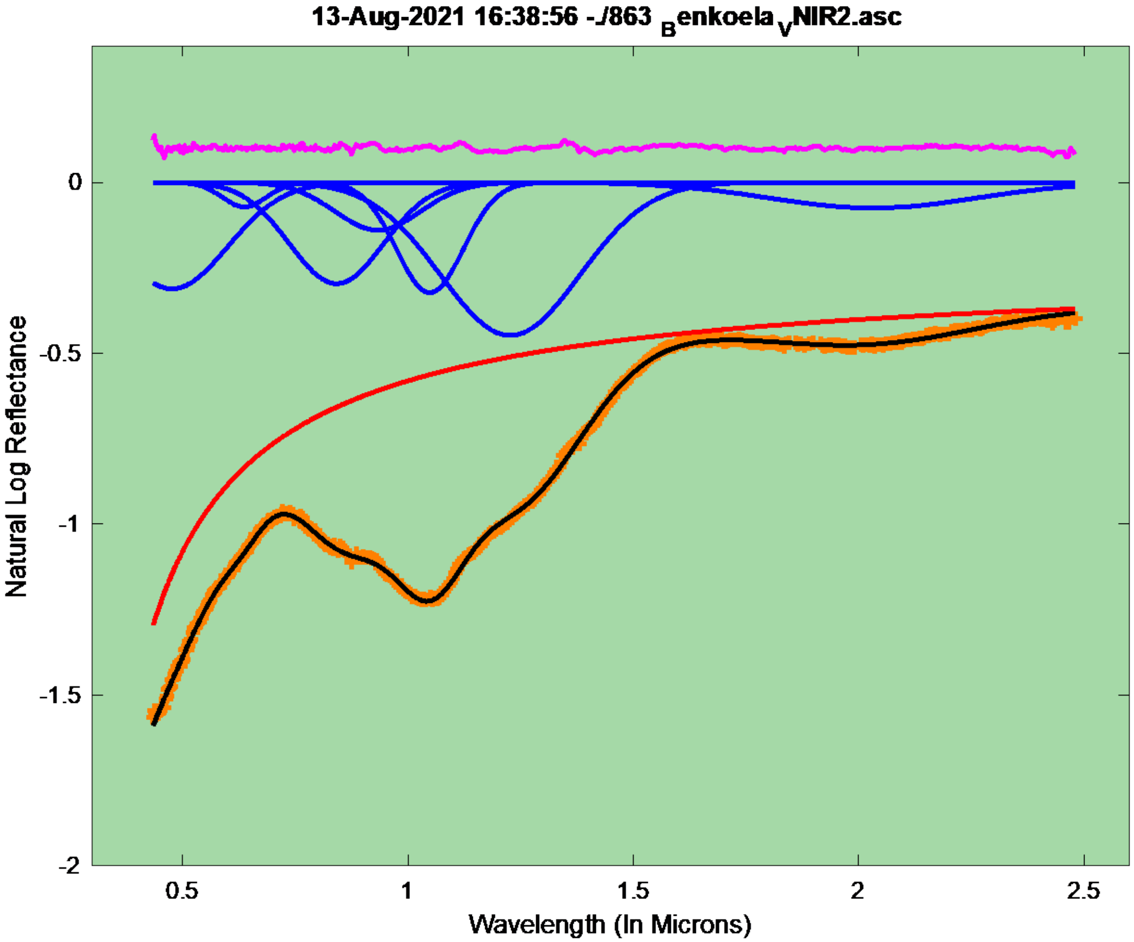

**Fig. S4.10.** MGM fit for asteroid 863 Benkoela.

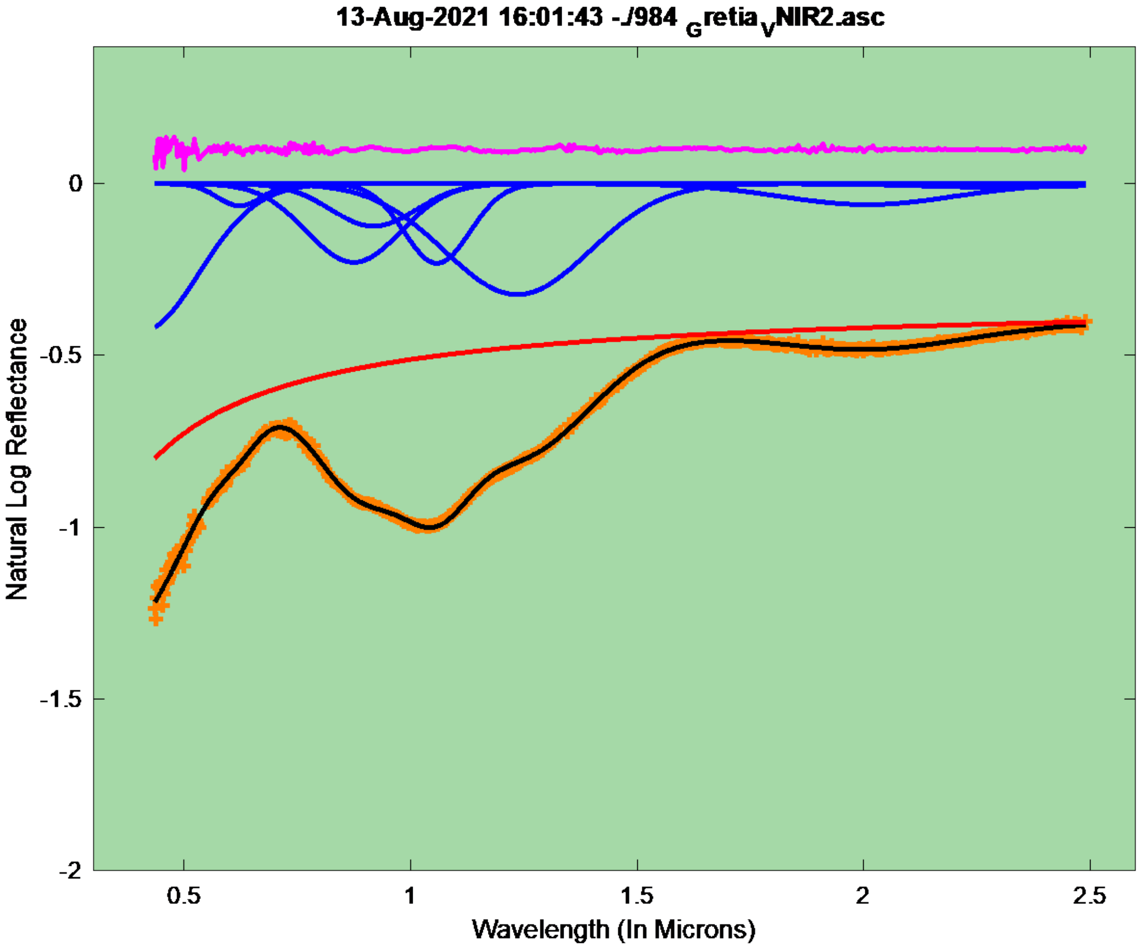

**Fig. S4.11.** MGM fit for asteroid 984 Gretia.

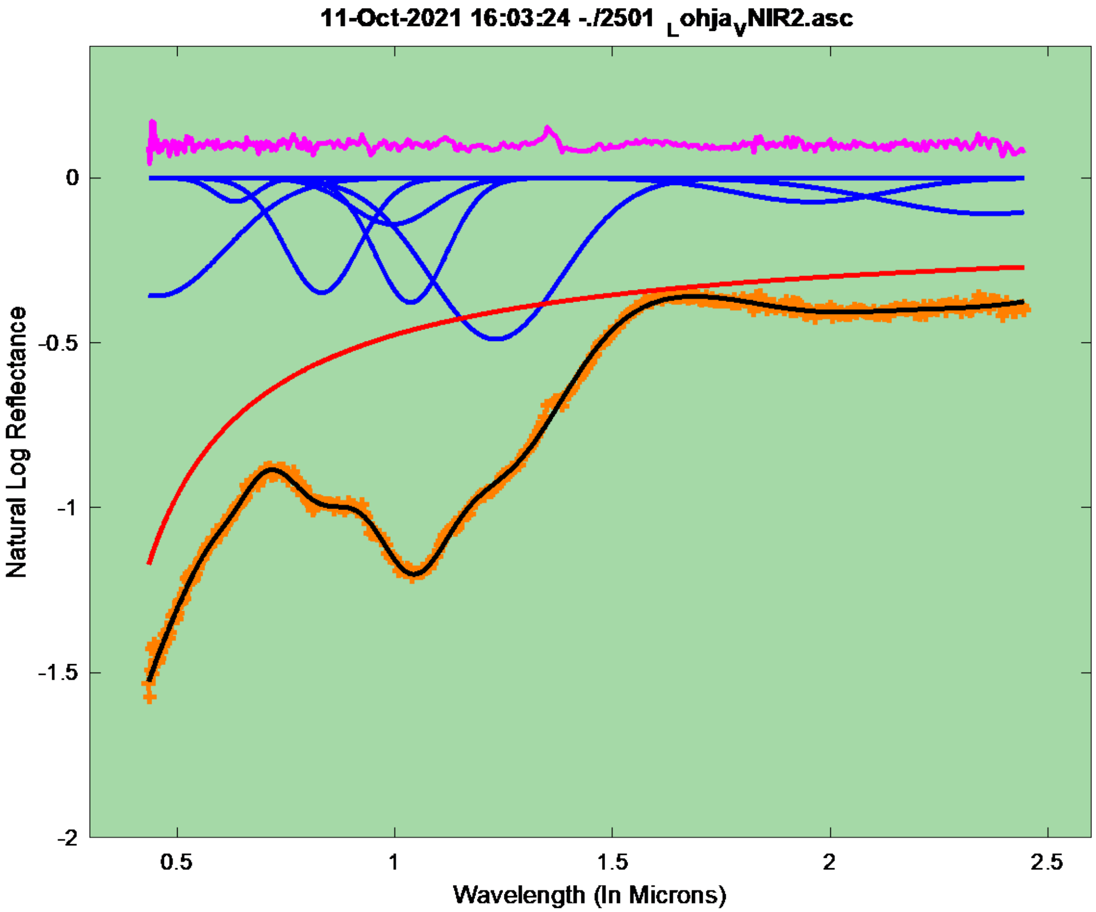

**Fig. S4.12.** MGM fit for asteroid 2501 Lohja. Band centers for olivine yield inconsistent results (Table S4.12).

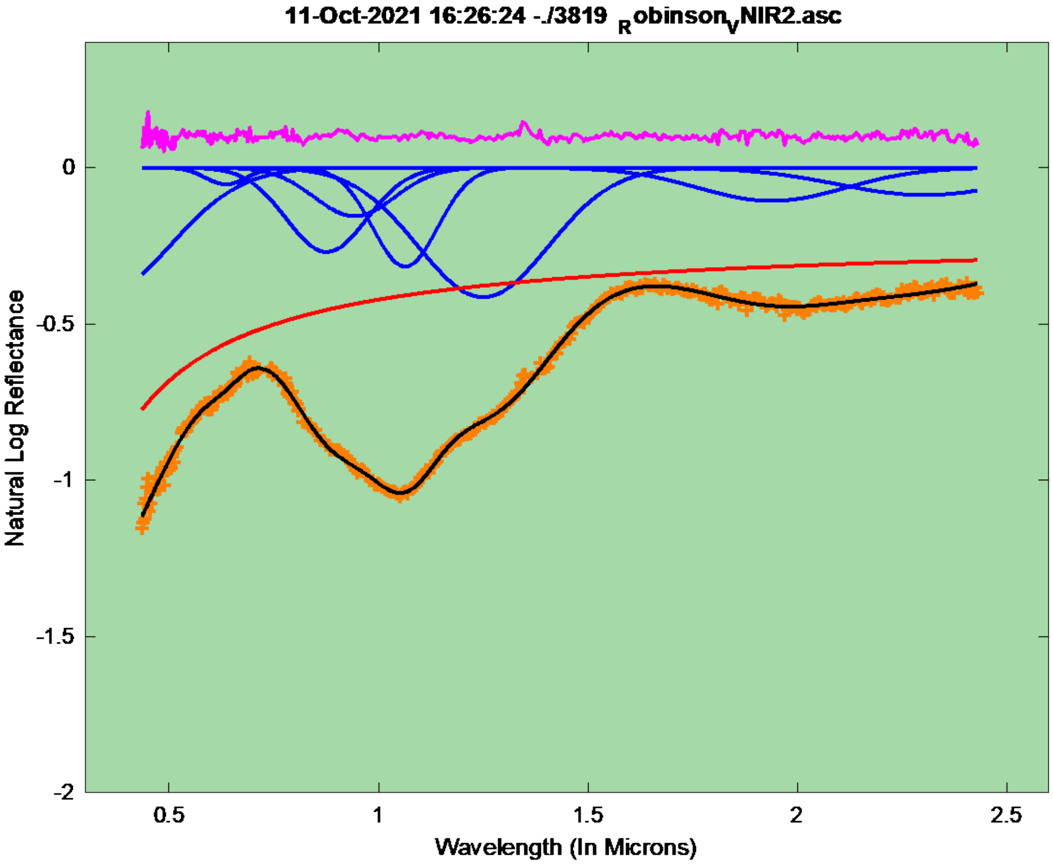

**Fig. S4.13.** MGM fit for asteroid 3819 Robinson.

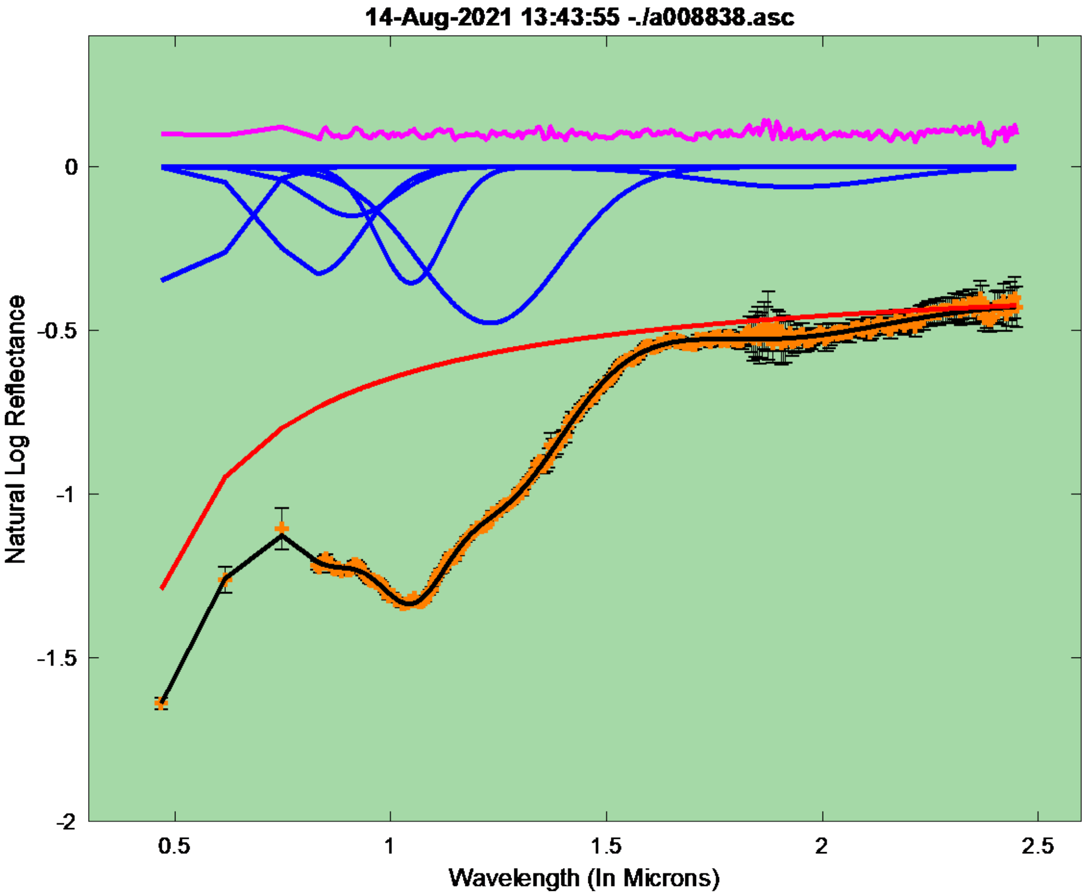

**Fig. S4.14.** MGM fit for asteroid (8838) 1989 UW2.

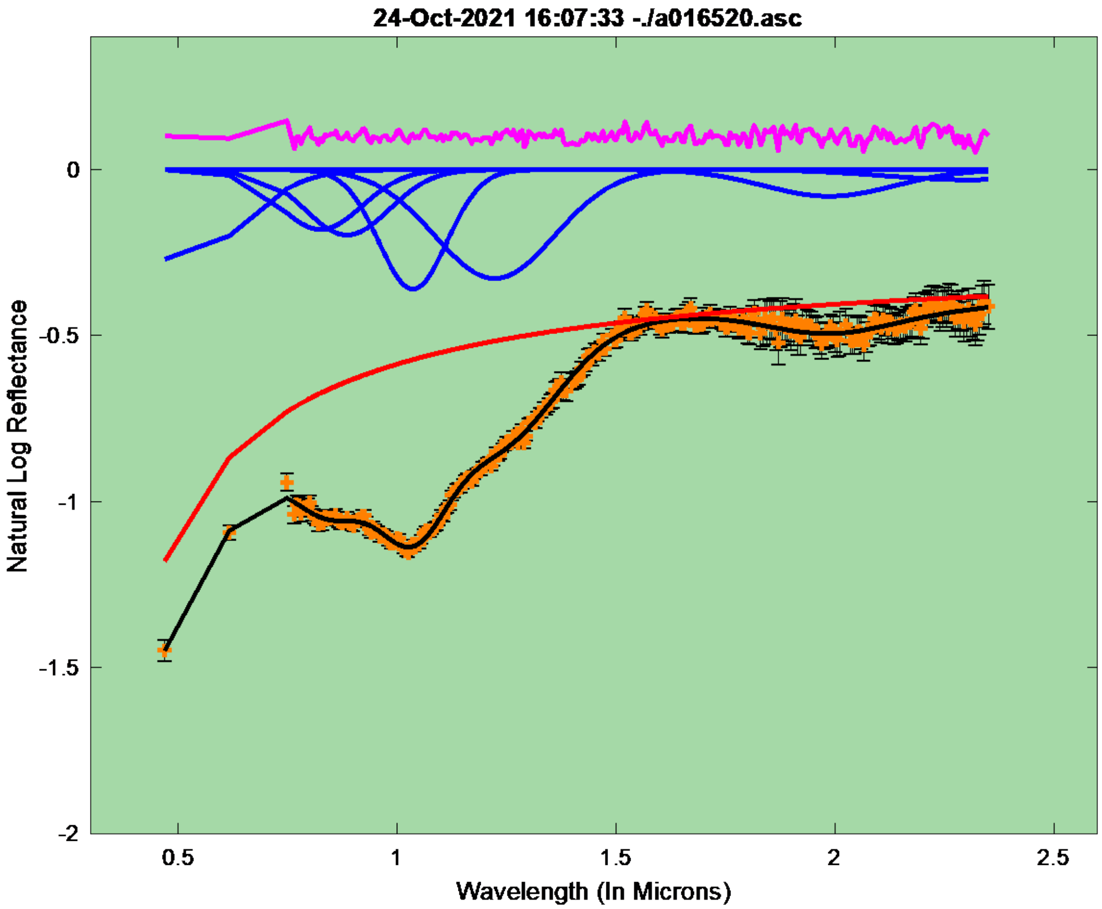

**Fig. S4.15.** MGM fit for asteroid (16520) 1990 WO3.

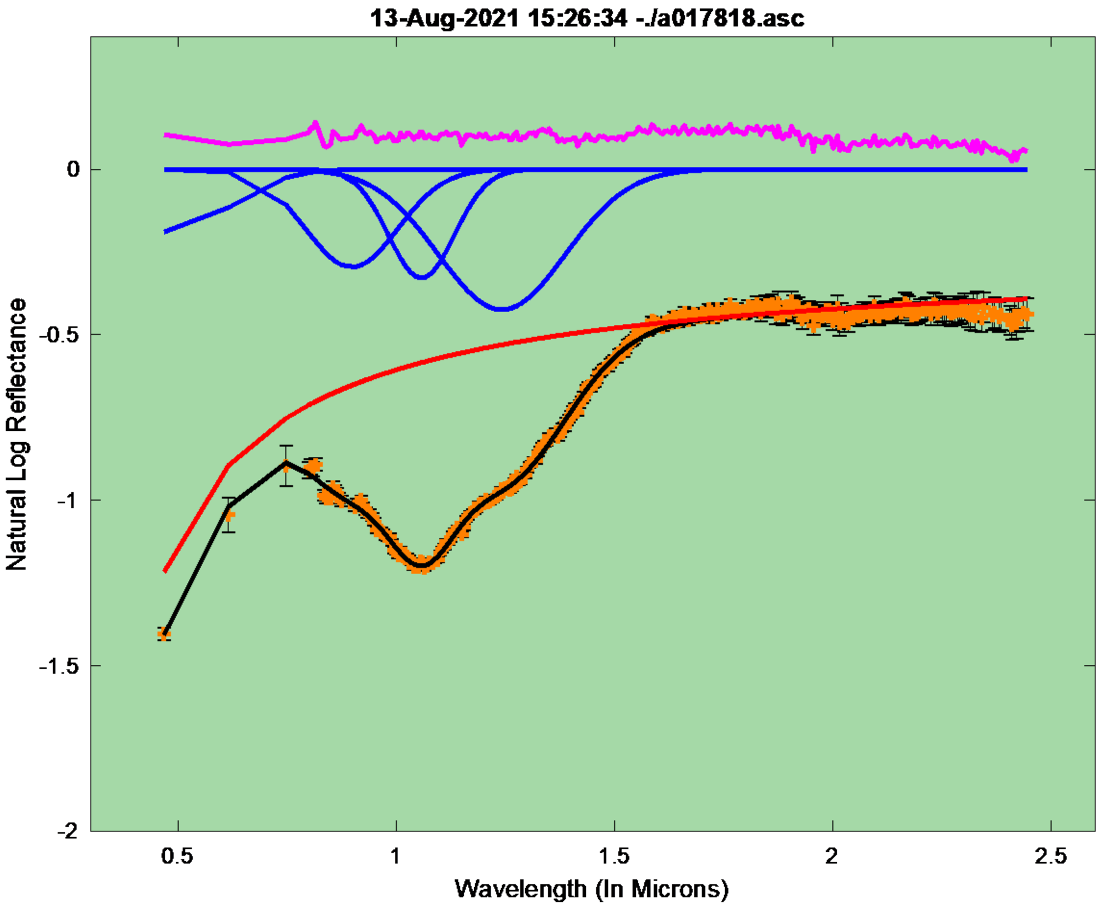

**Fig. S4.16.** MGM fit for asteroid (17818) 1996 FE118.

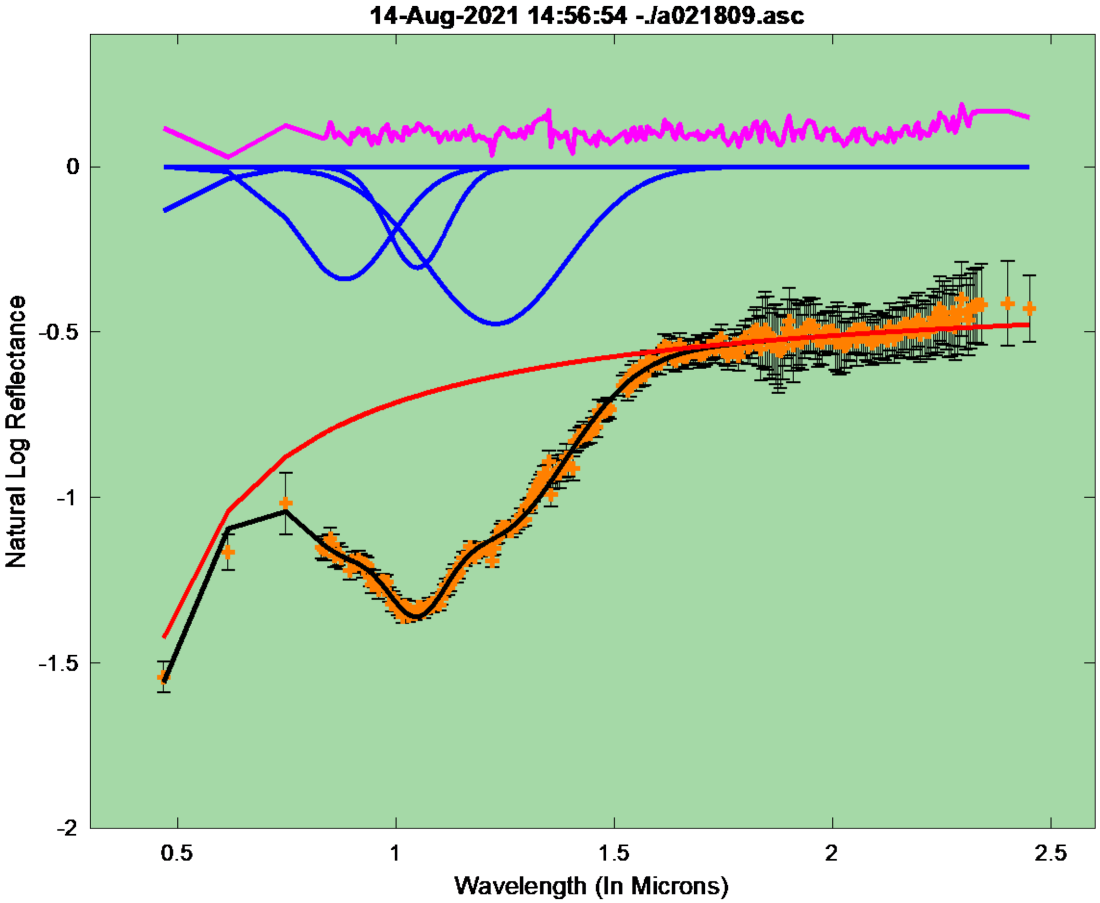

**Fig. S4.17.** MGM fit for asteroid (21809) 1999 TG19.

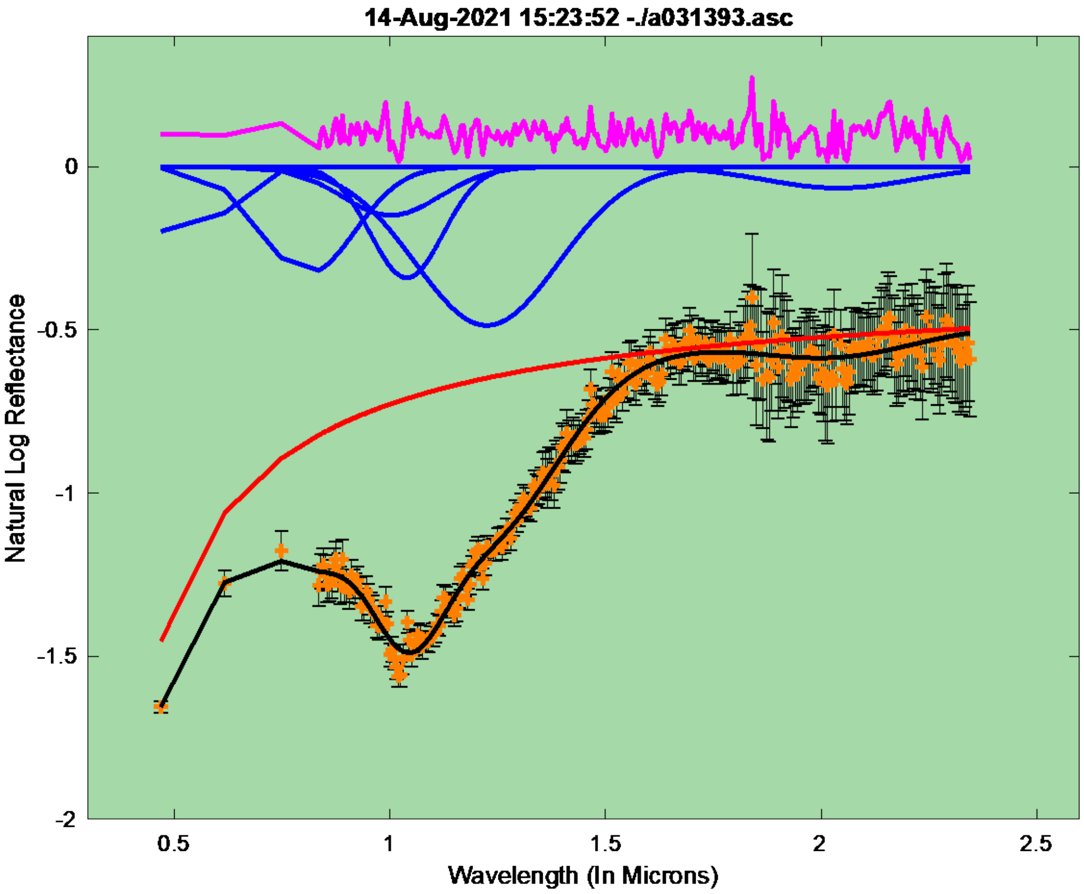

**Fig. S4.18.** MGM fit for asteroid (31393) 1998 YG8.

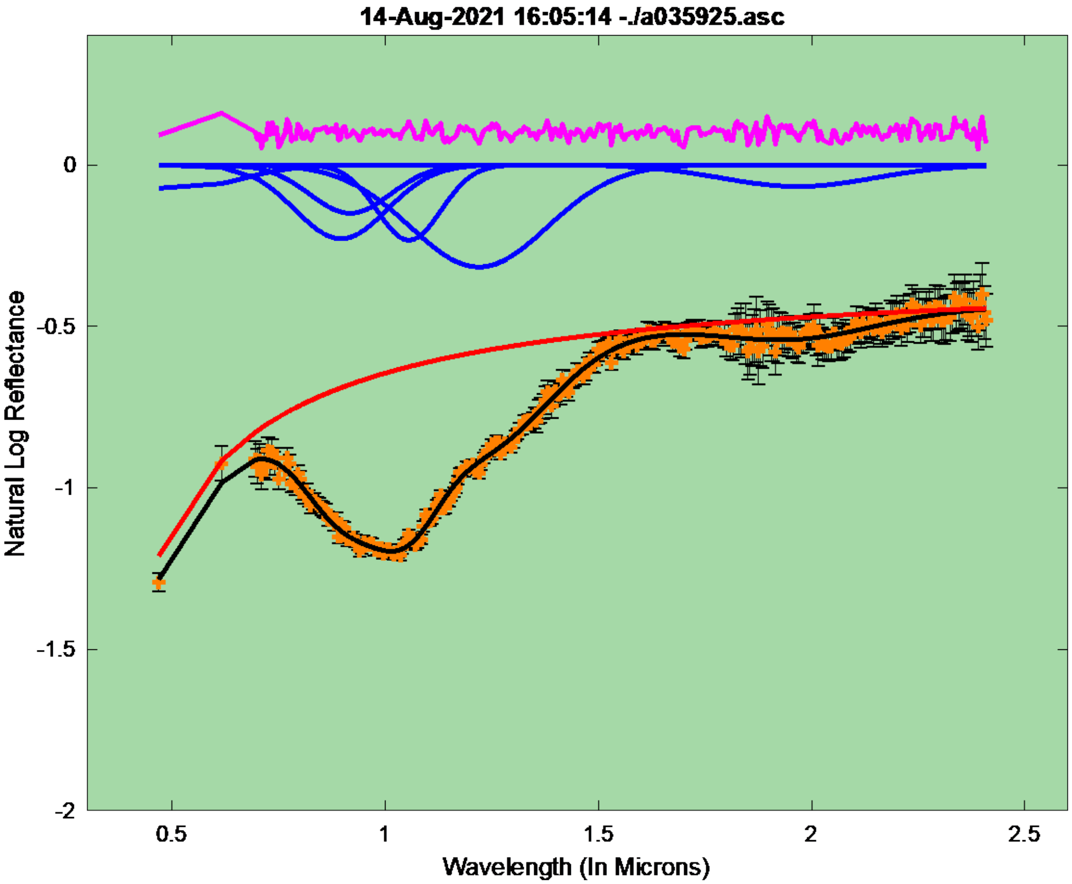

**Fig. S4.19.** MGM fit for asteroid (35925) 1999 JP104.

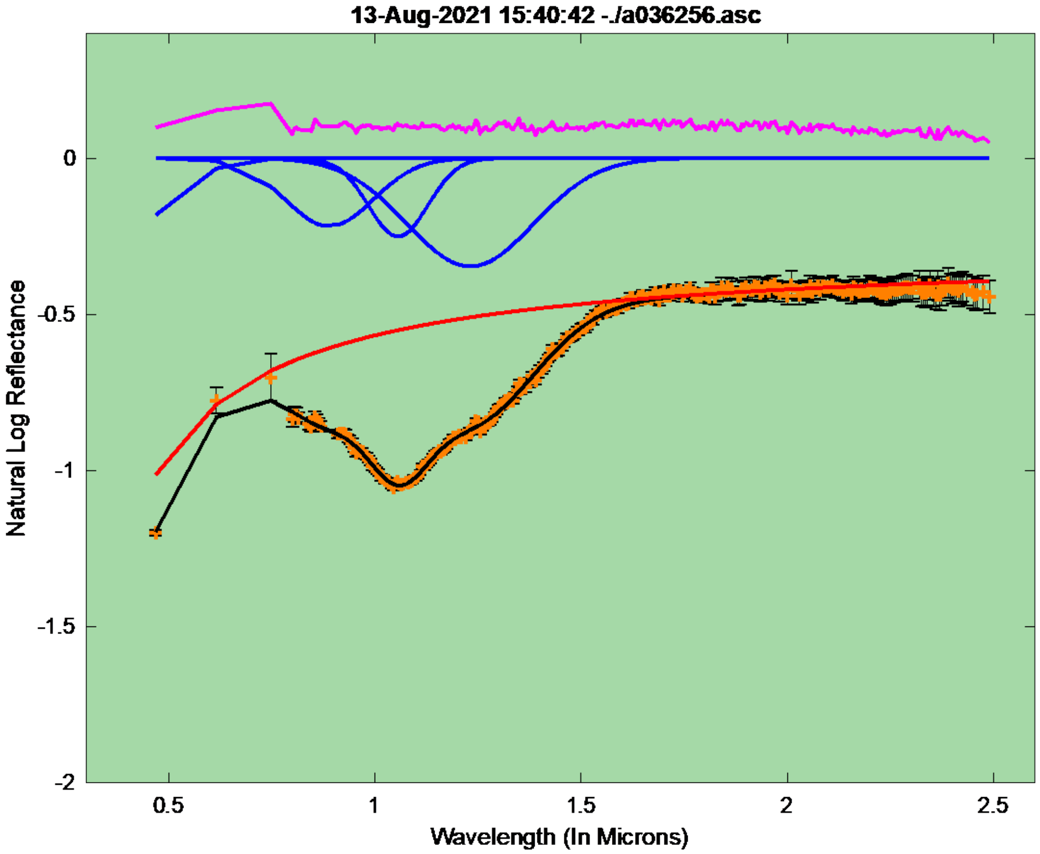

**Fig. S4.20.** MGM fit for asteroid (36256) 1999 XT17.

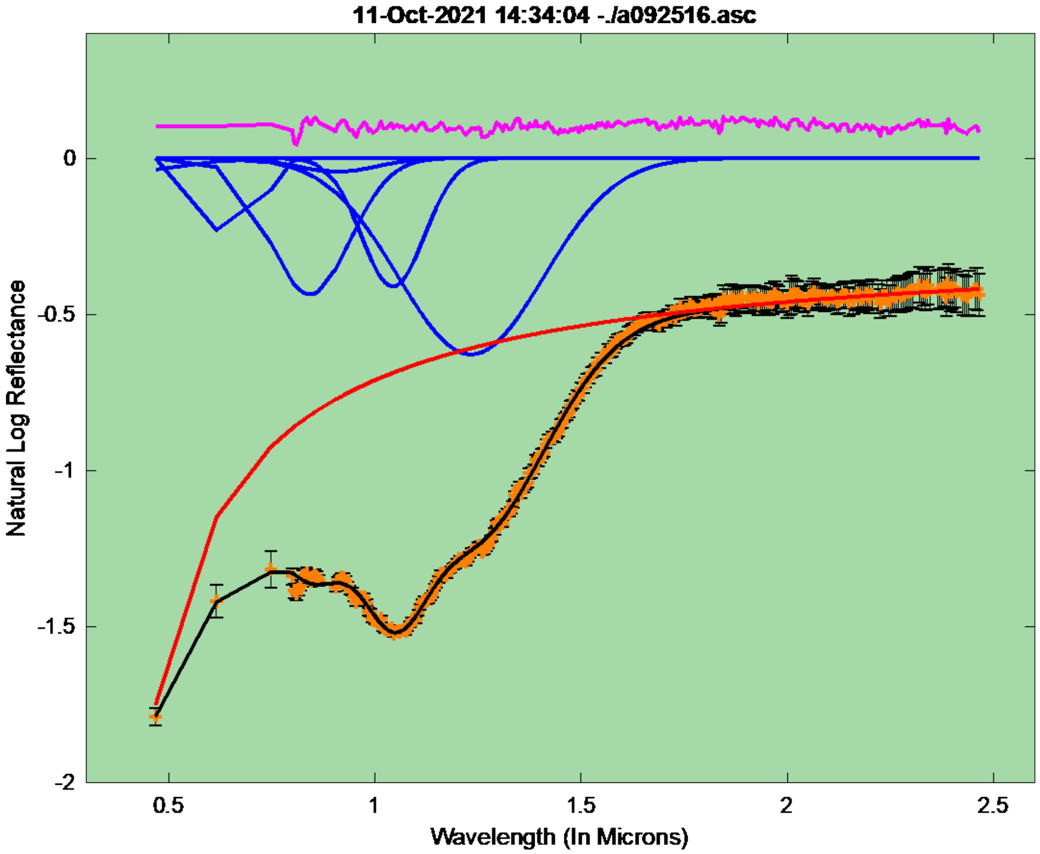

**Fig. S4.21.** MGM fit for asteroid (92516) 2000 ND25.

# Bibliography

Achterbergh E. V., Ryan C. G., Jackson S. E. and Griffin W. L. Appendix 3: Data reduction software for LA-ICP-MS. In *Laser Ablation-ICP-MS in the Earth Sciences (ed. P. Sylvester)* Short Course Series. Mineralogical Association of Canada.

Adams J. B. (1974) Visible and near-infrared diffuse reflectance spectra of pyroxenes as applied to remote sensing of solid objects in the solar system. *Journal of Geophysical Research (1896-1977)* **79**, 4829–4836.

Archer G. J., Walker R. J., Tino J., Blackburn T., Kruijer T. S. and Hellmann J. L. (2019) Siderophile element constraints on the thermal history of the H chondrite parent body. *Geochimica et Cosmochimica Acta* **245**, 556–576.

Bader J. A., Zhu W., Montesi L., Cordonnier B., Qi C. and Kohlstedt D. L. (2020) Strongly focused flow along shear-induced melt bands in experimental olivine-basalt aggregate. In *AGU Fall Meeting Abstracts*, DI007-0005.

Barnes S.-J., Cox R. A. and Zientek M. L. (2006) Platinum-group element, Gold, Silver and Base Metal distribution in compositionally zoned sulfide droplets from the Medvezky Creek Mine, Noril'sk, Russia. *Contrib Mineral Petrol* **152**, 187–200.

Beck A. W., Welten K. C., McSween H. Y., Viviano C. E. and Caffee M. W. (2012) Petrologic and textural diversity among the PCA 02 howardite group, one of the largest pieces of the Vestan surface. *Meteoritics & Planetary Science* **47**, 947-969.

Benedix G. K., Lauretta D. S. and McCoy T. J. (2005) Thermodynamic constraints on the formation conditions of winonaites and silicate-bearing IAB irons. *Geochimica et Cosmochimica Acta* **69**, 5123-5131.

Birck J. L., Barman M. R. and Capmas F. (1997) Re-Os Isotopic Measurements at the Femtomole Level in Natural Samples. *Geostandard and Geoanalytical Research* **21**,19-27.

Bischoff A., Scott E. R. D., Metzler K. and Goodrich C. A. (2006) Nature and Origins of Meteoritic Breccias. *Meteorites and the Early Solar System II*, 679–712.

Bischoff A., Vogel N. and Roszjar J. (2011) The Rumuruti chondrite group. *Geochemistry* **71**, 101–133.

Brearley A. J. (2006) *Meteorites and the Early Solar System II*. (Eds. Lauretta D. S. and McSween H. Y.), The action of water, University of Arizona Press, 555-566.

Burbine T. H., McCoy T. J., Meibom A., Gladman B. and Keil K. (2002) *Asteroids III.*, Meteoritic parent bodies: their number and identification. University of Arizona Press. 653-667.

Burbine T. H., Buchanan P. C., Dolkar T. and Binzel R. P. (2009) Pyroxene mineralogies of near-Earth vestoids. *Meteoritics & Planetary Science* **44**, 1331–1341.

Bums R. G. (1970) *Mineralogical Applications to Crystal Field Theory*, Cambridge University Press, New York.

Bus S. J. and Binzel R. P. (2002) Phase II of the Small Main-Belt Asteroid Spectroscopic Survey: A Feature-Based Taxonomy. *Icarus* **158**, 146–177.

Campbell A. J. and Humayun M. (2003) Formation of metal in Grosvenor Mountains 95551 and comparison to ordinary chondrites. *Geochimica et Cosmochimica Acta* **67**, 2481–2495.

Carry B. (2012) Density of asteroids. *Planetary and Space Science* **73**, 98–118.

Chabot N. L. and Jones J. H. (2003) The parameterization of solid metal-liquid metal partitioning of siderophile elements. *Meteoritics & Planetary Science* **38**, 1425–1436.

Clark R. N. (1987) Reflectance Spectra. In *AGU Reference Shelf* (ed. T. J. Ahrens). American Geophysical Union, Washington, D. C., 178–188.

Cohen A. S. and Waters F. G. (1996) Separation of osmium from geological materials by solvent extraction for analysis by thermal ionization mass spectrometry. *Analytica Chimica Acta*, **332**,269-275.

Chabot N. L. and Jones J. H. (2003) The parameterization of solid metal–liquid metal partitioning of siderophile elements. *Meteoritics & Planetary Science* **38**, 1425-1436.

Cloutis E. A., Gaffey M. J., Smith D. G. W. and Lambert R. St. J. (1990) Reflectance spectra of “featureless” materials and the surface mineralogies of M- and E-class asteroids. *J. Geophys. Res.* **95**, 281.

Collinet, M. and Grove, T. L. (2020) Formation of primitive achondrites by partial melting of alkali-undepleted planetesimals in the inner solar system. *Geochimica et Cosmochimica Acta* **277**, 358-376.

Creaser R. A., Papanastassiou D. A. and Wasserburg G. J. (1991) Negative thermal ion mass spectrometry of osmium, rhenium and iridium. *Geochimica et Cosmochimica Acta* **55**, 397-401.

Crossley S. D., Ash R. D., Sunshine J. M., Corrigan C. M., McCoy T. J., Mittlefehldt D. W. and Puchtel I. S. (2020) Sulfide-dominated partial melting pathways in brachinites. *Meteorit Planet Sci* **55**, 2021–2043.

Cruikshank D. P. and Hartmann W. K. (1984) The meteorite-asteroid connection: Two olivine-rich asteroids. Science **223**, 281–283.

Day, J. M. D., Ash, R. D., Liu, Y., Bellucci, J. J., Rumble, D. III., McDonough, W. F., Walker, R. J. and Taylor, L. A. (2009) Early formation of evolved asteroidal crust. *Nature* **457**, 179-182.

Day J. M. D., Corder C. A., Assayag N., Cartigny P. (2019) Ferrous oxide-rich asteroid achondrites. *Geochimica et Cosmochimica Acta* **266**, 544-567.

Day J. M. D., Corder C. A., Rumble D., Assayag N., Cartigny P. and Taylor L. A. (2015) Differentiation processes in FeO-rich asteroids revealed by the achondrite Lewis Cliff 88763. *Meteoritics & Planetary Science* **50**, 1750-1766.

Day J. M. D., Walker R. J., Ash R. D, Liu Y., Rumble D., Irving A. J., Goodrich C. A., Tait K., McDonough W. F. and Taylor L. A. (2012) Origin of felsic achondrites Graves Nunataks 06128 and 06129 and ultramafic brachinites and brachinite-like achondrites by partial melting of volatile-rich primitive parent bodies. *Geochimica et Cosmochimica Acta* **81**, 94-128

DeMeo F. E., Binzel R. P., Slivan S. M. and Bus S. J. (2009) An extension of the Bus asteroid taxonomy into the near-infrared. *Icarus* **202**, 160–180.

DeMeo F. E., Polishook D., Carry B., Burt B. J., Hsieh H. H., Binzel R. P., Moskovitz N. A. and Burbine T. H. (2019) Olivine-dominated A-type asteroids in the main belt: Distribution, abundance and relation to families. *Icarus* **322**, 13–30.

Dunn T. L., McSween H. Y., McCoy T. J. and Cressey G. (2010) Analysis of ordinary chondrites using powder X-ray diffraction: 2. Applications to ordinary chondrite parent-body processes. *Meteoritics and Planetary Science* **45**, 135-156.

Elkins-Tanton L. T., Asphaug E., Bell J. F., Bercovici H., Bills B., Binzel R., Bottke W. F., Dibb S., Lawrence D. J., Marchi S., McCoy T. J., Oran R., Park R. S., Peplowski P. N., Polanskey C. A., Prettyman T. H., Russell C. T., Schaefer L., Weiss B. P., Wieczorek M. A., Williams D. A. and Zuber M. T. (2020) Observations, meteorites, and models: a preflight assessment of the composition and formation of (16) Psyche. *J. Geophys. Res. Planets* **125**.

ENVI 4.4. *ITT Visual Information Solutions*. (2006) Boulder, Colorado.

Frost B. R. (1991) Introduction to oxygen fugacity and its petrologic importance. *Oxide Minerals* (ed. Lindsley D.H.) Berlin, Boston: De Gruyter, 1-10.

Gaetani G. A. and Grove T. L. (1999) Wetting of mantle olivine by sulfide melt: implications for Re/Os ratios in mantle peridotite and late-stage core formation. *Earth and Planetary Science Letters* **169**, 147–163.

Gaffey M. J., Bell J. F., Brown R. H., Burbine T. H., Piatek J. L., Reed K. L. and Chaky D. A. (1993) Mineralogical Variations within the S-Type Asteroid Class. *Icarus* **106**, 573–602.

Gardner-Vandy, K. G., Lauretta D. S., Greenwood R. C., McCoy T. J., Killgore M. and Franchi I. A. (2012) The Tafassasset primitive achondrite: insights into initial stages of planetary differentiation. *Geochimica Cosmochimica Acta* **85**, 142-159.

Gardner-Vandy K. G., Lauretta D. S. and McCoy T. J. (2013) A petrologic, thermodynamic and experimental study of brachinites: Partial melt residues of an R chondrite-like precursor. *Geochimica et Cosmochimica Acta* **122**, 36–57.

Gattacceca J., Bouvier A., Grossman J., Metzler K. and Uehara M. (2019) The Meteoritical Bulletin No. 107. *Meteoritics & Planetary Science* **54**, 469-471.

Gattacceca J., McCubbin F. M., Bouvier A. and Grossman J. N. (2020) The Meteoritical Bulletin, no. 108. *Meteoritics and Planetary Science* **55**, 1146–1150.

Goodrich C. A. and Delaney J. S. (2000) Fe/Mg-Fe/Mn relations of meteorites and primary heterogeneity of achondrite parent bodies. *Geochimica et Cosmochimica Acta* **64**, 149-160.

Gattacceca J., Mccubbin F. M., Bouvier A. and Grossman J. (2020) The Meteoritical Bulletin, No. 107. *Meteoritics & Planetary Science* **55**, 460–462.

Ghosh A., Weidenschilling S. J., McSween H. Y., and Rubin A. (2002) *Meteorites and the Early Solar System II.* (Eds. Lauretta D. S. and McSween H. Y.) Asteroidal heating and thermal stratification of the asteroid belt, University of Arizona Press, 587-624.

Gilmour C. M. and Herd C. D. K. (2020) In situ analysis of platinum group elements in equilibrated ordinary chondrite kamacite and taenite. *Meteorit Planet Sci* **55**, 679–702.

Goldschmidt V. M. (1937) The principles of distribution of chemical elements in minerals and rocks. *Journal of Chemical Society*, 655–673.

Goldstein J. I., Scott E. R. D. and Chabot N. L. (2009) Iron meteorites: Crystallization, thermal history, parent bodies, and origin. *Geochemistry* **69**, 293–325.

Goodrich C. A., Kita N. T., Spicuzza M. J., Valley J. W., Zipfel J., Mikouchi T. and Miyamoto M. (2011) The Northwest Africa 1500 meteorite: not a ureilite, maybe a brachinite. *Meteoritics & Planetary Science* **45**, 1906–1928.

Goodrich C. A., Kita N. T., Warren P. H. and Rubin A. E. (2012) MIL 090340 and MIL 090206: Two more brachinite-like achondrites misidentified as ureilites. *Meteoritics & Planetary Science* **47**, 5272

Goodrich C. A., Wlotzka F., Ross D. K., and Bartoschewitz R. (2006) Northwest Africa 1500: Plagioclase-bearing monomict ureilite or ungrouped achondrite? *Meteoritics & Planetary Science* **41**, 925–952.

Goodrich C. A., Kita N.T., Sutton S.R., Wirick S. and Gross J. (2017) The Miller Range 090340 and 090206 meteorites: Identification of new brachinite-like achondrites with implications for the diversity and petrogenesis of the brachinite clan. *Meteoritics & Planetary Sci*ence **52**, 949-978.

Greenwood J. P., Rubin A. E. and Wasson J. T. (2000) Oxygen isotopes in R-chondrite magnetite and olivine: links between R chondrites and ordinary chondrites. *Geochimica et Cosmochimica Acta* **64**, 3897–3911.

Greenwood R.C., Franchi I.A., Gibson, J.M. and Benedix G.K. (2012) Oxygen isotope variation in primitive achondrites: the influence of primordial, asteroidal and terrestrial processes. *Geochimica Cosmochimica Acta* **94**, 146-163.

Greenwood R. C., Burbine T. H., Miller M.F. and Franchi I.A. (2017) Melting and differentiation of early-formed asteroids: The perspective from high precision oxygen isotope studies. *Chemie de Erde* **77**, 1-43.

Greenwood R. C., Franchi I. A., Jambon A. and Buchanan P. C. (2005) Widespread magma oceans on asteroidal bodies in the early solar system. *Nature* **435**, 916–918.

Grossman L., Beckett J. R., Fedkin A. V., Simon S. B. and Ciesla F. J. (2008) Redox Conditions in the Solar Nebula: Observational, Experimental, and Theoretical Constraints. *Reviews in Mineralogy and Geochemistry* **68**, 93–140.

Haack H. and McCoy T. J. (2007) 1.12 - Iron and Stony-Iron Meteorites. In *Treatise on Geochemistry* (eds. H. D. Holland and K. K. Turekian). Pergamon, Oxford. 1–22.

Hapke B. (1981) Bidirectional reflectance spectroscopy. I - Theory. *Journal of Geophysical Research* **86**, 3039–3054.

Helmy H. M., Ballhaus C., Fonseca R. and Nagle T. (2013) Fractionation of platinum, palladium, nickel, and copper in sulfide–arsenide systems at magmatic temperature. *Contributions in Mineralogy and Petrology* **166**, 1725–1737.

Helmy H. M. and Bragagni A. (2017) Platinum-group elements fractionation by selective complexing, the Os, Ir, Ru, Rh-arsenide-sulfide systems above 1020°C. *Geochimica et Cosmochimica Acta* **216**, 169-183.

Hillgren V. J. (1991) Partitioning behavior of Ni, Co, Mo, and W between basaltic liquid and Ni-rich metal: Implications for the origin of the moon and lunar core formation. *Geophys. Res. Lett.* **18**, 2077–2080.

Holwell D. A., Adeyemi Z., Ward L. A., Smith D. J., Graham S. D., McDonald I. and Smith J. W. (2017) Low temperature alteration of magmatic Ni-Cu-PGE sulfides as a source for hydrothermal Ni and PGE ores: A quantitative approach using automated mineralogy. *Ore Geology Reviews* **91**, 718–740.

Huss G. R., Rubin A. E. and Grossman J. N. (2006) Thermal Metamorphism in Chondrites. In *Meteorites and the Early Solar System II* (eds. D. S. Lauretta and H. Y. McSween). p. 567-586.

Hyde B. C., Day J. M., Tait K. T., Ash R. D., Holdsworth D. W. and Moser D. E. (2014) Characterization of weathering and heterogeneous mineral phase distribution in brachinite Northwest Africa 4872. *Meteoritics & Planetary Science* **49**, 1141-1156.

Iida T. and Guthrie R. I. L. (2015) *The thermophysical properties of metallic liquids*. First edition., Oxford University Press, United Kingdom.

Isa J., Rubin A. E. and Wasson J. T. (2014) R-chondrite bulk-chemical compositions and diverse oxides: Implications for parent-body processes. *Geochimica et Cosmochimica Acta* **124**, 131–151.

Jarosewich E. (1990) Chemical analyses of meteorites: A compilation of stony and iron meteorite analyses. *Meteoritics* **25**, 323–337.

Jarosewich E. (2002) Smithsonian Microbeam Standards. *J. Res. Natl. Inst. Stand. Technol.* **107**, 681.

Jennings E. S., Jacobson S. A., Rubie D. C., Nakajima Y., Vogel A. K., Rose-Weston L. A. and Frost D. J. (2021) Metal–silicate partitioning of W and Mo and the role of carbon in controlling their abundances in the bulk silicate earth. *Geochimica et Cosmochimica Acta* **293**, 40–69.

Keil K. (2014) Brachinite meteorites: Partial melt residues from an FeO-rich asteroid. *Chemie der Erde* **74**, 311–329.

Kerridge J. F. (1976) Formation of iron sulphide in solar nebula. *Nature* **259**, 189–190.

Kessel R., Beckett J. R., Huss G. R. and Stolper E. M. (2004) The activity of chromite in multicomponent spinels: Implications for T- $fO_2$ conditions of equilibrated H chondrites. *Meteoritics & Planetary Science* **39**, 1287–1305.

Kimura M., Grossman J. N. and Weisberg M. K. (2008) Fe-Ni metal in primitive chondrites: Indicators of classification and metamorphic conditions for ordinary and CO chondrites. *Meteoritics & Planetary Science* **43**, 1161–1177.

King A. J., Schofield P. F., Howard K. T. and Russell S. S. (2015) Modal mineralogy of CI and CI-like chondrites by X-ray diffraction. *Geochimica et Cosmochimica Acta* **165**, 148–160.

Kitakaze A., Itoh H. and Komatsu R. (2011) A revision of phase relations in the system Fe–Ni–S from 650 to 450°C. *Canadian Mineralogist* **49**, 1687–1710.

Kitakaze A., Machida T. and Komatsu R. (2016) Phase relations in the system Fe–Ni–S from 875 to 650°C. *Canadian Mineralogist* **54**, 1175-1186.

Klima R. L., Dyar M. D. and Pieters C. M. (2011) Near-infrared spectra of clinopyroxenes: Effects of calcium content and crystal structure: Near-infrared spectra of clinopyroxenes. *Meteoritics & Planetary Science* **46**, 379–395.

Klima R. L., Pieters C. M. and Dyar M. D. (2007) Spectroscopy of synthetic Mg-Fe pyroxenes I: Spin-allowed and spin-forbidden crystal field bands in the visible and near-infrared. *Meteoritics & Planetary Science* **42**, 235–253.

Kong P. and Ebihara M. (1997) The origin and nebular history of the metal phase of ordinary chondrites. *Geochimica et Cosmochimica Acta* **61**, 2317–2329.

Kracher A. and Wasson J. T. (1982) The role of S in the evolution of the parental cores of the iron meteorites. *Geochimica et Cosmochimica Acta* **46**, 2419–2426.

Kretz, R. (1982) Transfer and exchange equilibria in a portion of the pyroxene quadrilateral as deduced from natural and experimental data. *Geochimica et Cosmochimica Acta* **46**, 411–422.

Krot A. N., Keil K., Scott E. R. D., Goodrich C. A. and Weisberg M. K. (2014) Classification of Meteorites and Their Genetic Relationships. In *Meteorites and Cosmochemical Processes* (ed. A. M. Davis). pp. 1–63.

Kruijer T. S., Kleine T. and Borg L. E. (2020) The great isotopic dichotomy of the early Solar System. *Nature Astronomy* **4**, 32–40.

Kullerud G. (1963) The Fe-Ni-S system. *Carnegie Institution, Annual Report of Director of Geophysical Laboratory* **62**, 175-189.

Kushiro I. and Mysen B. O. (1979) Melting experiments on a Yamato chondrite. *Proc. 4th Symp. Antarctic Met., Mem. Natl. Inst. Polar Res.* **15**, 165-170.

Larimer J. W. (1968) Experimental studies on system Fe-MgO-$SiO_2$-$O_2$ and their bearing on petrology of chondritic meteorites. *Geochimica et Cosmochimica Acta* **32**, 1187-1207.

Lauretta D. S., Lodders K. and Fegley B. (1998) Kamacite sulfurization in the solar nebula. *Meteoritics & Planetary Science* **33**, 821–833.

Lebofsky L. A. and Spencer J. R. (1989) Radiometry and thermal modeling of asteroids. In Asteroids II (R. P. Binzel et al., eds.), 128–147. Univ. of Arizona, Tucson.

Lodders K. (2003) Solar System Abundances and Condensation Temperatures of the Elements. *The Astrophysical Journal* **591**, 1220–1247.

Lucas M. P., Emery J. P., Hiroi T. and McSween H. Y. (2019) Spectral properties and mineral compositions of acapulcoite-lodranite clan meteorites: Establishing S-type asteroid-meteorite connections. *Meteorit Planet Sci* **54**, 157–180.

Lucey P. G., Keil K., and Whitely R. (1998) The influence of temperature on the spectra of A-asteroids and implications for their silicate chemistry. *Journal of Geophysical Research*, **103**, 5865–5871

Lunning N. G., Gardner-Vandy, K. G., Sosa E. S., McCoy T. J., Bullock E. S. and Corrigan C. M. (2017) Partial melting of oxidized planetesimals: An experimental study to test the formation of oligoclase-rich achondrites Graves Nunataks 06128 and 06129. *Geochimica et Cosmochimica Acta* **214**, 73-85.

Mainzer A. K., Bauer J. M., Cutri R. M., Grav T., Kramer E. A., Masiero J. R., Nugent C. R., Sonnett S. M., Stevenson R. A. and Wright E. L. (2016) NEOWISE Diameters and Albedos V1.0. *NASA Planetary Data System*, EAR-A-COMPIL-5-NEOWISEDIAM-V1.0.

Malvin D. J., Jones J. H. and Drake M. J. (1986) Experimental investigations of trace element fractionation in iron meteorites. III: Elemental partitioning in the system Fe-Ni-S-P. *Geochimica et Cosmochimica Acta* **50**, 1221–1231.

McCanta M. C., Treiman A. H., Dyar M. D., Alexander C. M. O'D., Rumble D. and Essene E. J. (2008) The LaPaz Icefield 04840 meteorite: Mineralogy, metamorphism, and origin of an amphibole- and biotite-bearing R chondrite. *Geochimica et Cosmochimica Acta* **72**, 5757-5780.

McCoy T. J., Burbine T. H., McFadden L. A., Starr R. D., Gaffey M. J., Nittler L. R., Evans L. G., Izenberg N., Lucey P. G., Trombka J. I., Bell J. F. III, Clark B. E., Clark P. E., Squyres S. W., Chapman C. R., Boynton W. V., and Veverka J. (2001) The composition of 433 Eros: A mineralogical-chemical synthesis. *Meteoritics & Planetary Science*, **36**,1661–1672.

McCoy T. J., Mittlefehldt D. W. and Wilson L. (2006) Asteroid Differentiation. In *Meteorites and the Early Solar System II* (eds. D. S. Lauretta and H. Y. McSween). p. 733-745.

McDonough W. F. and Sun S. S. (1995) The composition of the Earth. *Chemical Geology* **120**, 223-254.

McSween H. Y., Binzel R. P., De Sanctis M. C., Ammannito E., Prettyman T. H., Beck A. W., Reddy V., Le Corre L., Gaffey M. J., McCord T. B., Raymond C. A., Russell C. T., and the Dawn Science Team (2013) Dawn; the Vesta-HED connection; and the geologic context for eucrites, diogenites, and howardites. *Meteorit Planet Sci* **48**, 2090–2104.

Miller K. E., Lauretta D. S., Connolly H. C., Berger E. L., Nagashima K. and Domanik K. (2017) Formation of unequilibrated R chondrite chondrules and opaque phases. *Geochimica et Cosmochimica Acta* **209**, 24–50.

Mittlefehldt D. W., Lindstrom M. M., Bogard D. D., Garrison D. H. and Field S. W. (1996) Acapulco- and Lodran-like achondrites: Petrology, geochemistry, chronology, and origin. *Geochimica et Cosmochimica Acta* **60**, 867–882.

Mittlefehldt D. W., Bogard D. D., Berkley J. L. and Garrison D. (2003) Brachinites: Igneous rocks from a differentiated asteroid. *Meteoritics & Planetary Science* **38**, 1601–1625.

Mittlefehldt D. W. 2007. *Achondrites*. In: Meteorites, Comets and Planets. Treatise on Geochemistry, Vol. 1, edited by Davis A.M. Amsterdam: Elsevier, pp. 1–40.

Mungall J. and Su S. (2005) Interfacial tension between magmatic sulfide and silicate liquids: Constraints on kinetics of sulfide liquation and sulfide migration through silicate rocks. *Earth and Planetary Science Letters* **234**, 135–149.

Nehru C. E., Prinz M., Delaney J. S., Dreibus G., Palme H., Spettel B. and Wänke H. (1983) Brachina: a new type of meteorite, not a chassignite. Proceedings of the 14th Lunar and Planetary Science Conference, *Journal of Geophysical Research* **88**, B237-244.

Nehru C. E., Prinz M., Weisberg M. K., Ebihara M. E., Clayton R. N. and Mayeda T. K. (1996) A new brachinite and petrogenesis of the group. *Lunar and Planetary Science Conference XXVII*, 943-944 (abst.).

Nesvorny D., Broz M. and Carruba V. (2015) Identification and Dynamical Properties of Asteroid Families. *arXiv:1502.01628 [astro-ph]*.

Palme H. 2008. Platinum-group elements in cosmochemistry. *Elements* **4**, 33-38.

Pieters C. M. and Hiroi T. (2004) Relab user's manual. http://www.planetary.brown.edu/relab.

Pontoppidan K. M., Salyk C., Bergin E. A., Brittain S., Marty B., Mousis O. and Öberg K. I. (2014) Volatiles in Protoplanetary Disks. In *Protostars and Planets VI,* University of Arizona Press, 1-24.

O'Neill H. S. C. and Pownceby M. I. (1993) Thermodynamic data from redox reactions at high temperatures. I. An experimental and theoretical assessment of the electrochemical method using stabilized zirconia electrolytes, with revised values for the Fe-"FeO", Co-CoO, Ni-NiO and Cu-$Cu_2O$ oxygen buffers, and new data for the W-$WO_2$ buffer. *Contrib. Mineral Petrol.* **144**, 296-314.

Puchtel I. S., Blichert-Toft J., Touboul M. and Walker R.J. 2018. $^{182}$W and HSE constraints from 2.7 Ga komatiites on the heterogeneous nature of the Archean mantle. *Geochimica et Cosmochimica Acta*, **228**, 1-26.

Rayner J. T., Toomey D. W., Onaka P. M., Denault A. J., Stahlberger, W. E., Vacca W. D., and Cushing M. C. (2003) SpeX: A medium resolution 0.8–5.5 micron spectrograph and imager for the NASA infrared telescope facility. *Astronomical Society of the Pacific*. 362–382.

Reddy V., Hardersen P. S., Gaffey M. J., and Abell P. A. (2005) Mineralogy and temperature-induced spectral investigations of A-type asteroids 246 Asporina and 446 Aeternitas. *Lunar and Planetary Science Conference XXXVI*, #1375 (abst.).

Reddy, V., Nathues, A., Gaffey, M.J., Schaeff, S., (2011) Mineralogical characterization of potential targets for the ASTEX mission scenario. *Planet. Space Sci*. **59**, 772–778.

Rehkämper M. and Halliday A.N. (1997) Development and application of new ion-exchange techniques for the separation of the platinum group and other siderophile elements from geological samples. *Talanta* **44**, 663-672.

Righter K. and Drake M. J. (1996) Core formation in Earth’s moon, Mars, and Vesta. *Icarus* **124**, 513–529.

Righter K. and Neff K. E. (2007) Temperature and oxygen fugacity constraints on CK and R chondrites and implications for water and oxidation in the early solar system. *Polar Science* **1**, 25–44.

Righter K., Sutton S. R., Danielson L., Pando K., and Newville M. (2016) Redox variations in the inner solar system with new constraints from vanadium XANES in spinels. *American Mineralogist* **101**, 1928–1942.

Rose L. A. and Brenan J. M. (2001) Wetting properties of Fe-Ni-Co-Cu-O-S melts against olivine: Implications for sulfide melt mobility. *Economic Geology*, **96**, 145-157.

Rubie D. C., Jacobson S. A., Morbidelli A., O’Brien D. P., Young E. D., de Vries J., Nimmo F., Palme H. and Frost D. J. (2015) Accretion and differentiation of the terrestrial planets with implications for the compositions of early-formed Solar System bodies and accretion of water. *Icarus* **248**, 89–108.

Rubin A. E. (1990) Kamacite and olivine in ordinary chondrites: intergroup and intragroup relationships. *Geochemica et Cosmochemica Acta* **54**, 1217-1232.

Sack R. O. and Ghiorso M. S. (1991a). An internally consistent model for the thermodynamic properties of Fe-Mg-titanomagnetite-aluminate spinels. *Contributions in Mineral Petrology* **106**, 474-505.

Sack R. O. and Ghiorso M. S. (1991b) Chromian spinels as petrogenetic indicators: thermodynamics and petrological applications. *American Mineralogist* **76**, 827-847.

Sanchez J. A., Reddy V., Kelley M. S., Cloutis E. A., Bottke W. F., Nesvorný D., Lucas M. P., Hardersen P. S., Gaffey M. J., Abell P. A. and Corre L. L. (2014) Olivine-dominated asteroids: Mineralogy and origin. *Icarus* **228**, 288–300.

Satterwhite C. and Righter K. (2006) Plans for the 2006-2007 Field Season. Antarctic Meteorite Newsletter. **41**, 1-41.

Scott E.R.D. (1977) Geochemical relationships between some pallasites and iron meteorites. *Mineralogical magazine.* **41**, 265-272.

Scott E. R. D., Krot A. N. and Sanders I. S. (2018) Isotopic Dichotomy among Meteorites and Its Bearing on the Protoplanetary Disk. *Astrophys J* **854**, 164.

Shearer C. K., Burger P. V., Neal C., Sharp Z., Spivak-Birndorf L., Borg L., Fernandes V., Papike J. J., Karner J., Wadhwa M., Gaffney A. M., Shafer J., Geissman J., Atudorei N. -V., Herd C., Weiss B. P., King P. L., Crowther S. A. and Gilmour J. D. (2010) Non-basaltic asteroidal magmatism during the earliest stages of Solar System evolution. A view from Antarctic achondrites Graves Nunataks 06128 and 06129. *Geochimica et Cosmochimica Acta* **74**, 1172-1199.

Shepard M. K., Richardson J., Taylor P. A., Rodriguez-Ford L. A., Conrad A., de Pater I., Adamkovics M., de Kleer K., Males J. R., Morzinski K. M., Close L. M., Kaasalainen M., Viikinkoski M., Timerson B., Reddy V., Magri C., Nolan M. C., Howell E. S., Benner L. A. M., Giorgini J. D., Warner B. D. and Harris A. W. (2017) Radar observations and shape model of asteroid 16 Psyche. *Icarus* **281**, 388–403.

Shu F. H., Shang H., and Lee T. (1996) Toward an Astrophysical Theory of Chondrites. *Science* **271**, 5255, 1545–1552.

Smyth J. R. and Mccormick T. C. (1995) Crystallographic Data for Minerals. In *Mineral Physics & Crystallography* American Geophysical Union (AGU). pp. 1–17.

Stähler S. C., Khan A., Banerdt W. B., Lognonné P., Giardini D., Ceylan S., Drilleau M., Duran A. C., Garcia R. F., Huang Q., Kim D., Lekic V., Samuel H., Schimmel M., Schmerr N., Sollberger D., Stutzmann É., Xu Z., Antonangeli D., Charalambous C., Davis P. M., Irving J. C. E., Kawamura T., Knapmeyer M., Maguire R., Marusiak A. G., Panning M. P., Perrin C., Plesa A.-C., Rivoldini A., Schmelzbach C., Zenhäusern G., Beucler É., Clinton J., Dahmen N., van Driel M., Gudkova T., Horleston A., Pike W. T., Plasman M. and Smrekar S. E. (2021) Seismic detection of the martian core. *Science* **373**, 443–448.

Stolper E. and Walker D. (1980) Melt density and the average composition of basalt. *Contr. Mineral. and Petrol.* **74**, 7–12.

Sugaki A. and Kitakaze A. (1998) High form pentlandite and its thermal stability. *American Mineralogist* **83**, 133-140.

Sunshine J. M., Pieters C. M., and Pratt S. F. (1990) Deconvolution of mineral absorption bands: an improved approach. *Journal of Geophysical Research,* **95**, 6955–6966.

Sunshine J. M., Bus S. J., McCoy T. J., Burbine T. H., Corrigan C. M. and Binzel R. P. (2004) High-calcium pyroxene as an indicator of igneous differentiation in asteroids and meteorites. *Meteoritics & Planetary Science* **39**, 1343–1357.

Sunshine J. M., Bus S. J., Corrigan C. M., McCoy T. J. and Burbine T. H. (2007) Olivine-dominated asteroids and meteorites: Distinguishing nebular and igneous histories. *Meteoritics & Planetary Science* **42**, 155–170.

Sunshine J. M. and Pieters C. M. (1993) Estimating modal abundances from the spectra of natural and laboratory pyroxene mixtures using the modified Gaussian model. *J. Geophys. Res.* **98**, 9075–9087.

Sunshine J. M. and Pieters C. M. (1998) Determining the composition of olivine from reflectance spectroscopy. *J. Geophys. Res.* **103**, 13675–13688.

Swindle, T. D., Kring, D. A., Burkland, M. K., Hill, D. H. and Boynton, W. V. (1998) Noble gases, bulk chemistry, and petrography of olivine-rich achondrites Eagles Nest and Lewis Cliff 88763: Comparison to brachinites. *Meteoritics and Planetary Science* **33**, 31-48.

Terranova U., Mitchell C., Sankar M., Morgan D. and de Leeuw N. H. (2018) Initial Oxygen Incorporation in the Prismatic Surfaces of Troilite FeS. *J. Phys. Chem. C* **122**, 12810–12818.

Tomkins A. G., Johnson T. E. and Mitchell J. T. (2020) A review of the chondrite–achondrite transition, and a metamorphic facies series for equilibrated primitive stony meteorites. *Meteorit Planet Sci* **55**, 857–885.

Walker R. (2016) Siderophile Elements in Tracing Planetary Formation and Evolution. *Geochem. Persp.* **5**, 1–145.

Walker R. J., McDonough W. F., Honesto J., Chabot N. L., McCoy T. J., Ash R. D. and Bellucci J. J. (2008) Modeling fractional crystallization of group IVB iron meteorites. *Geochimica et Cosmochimica Acta* **72**, 2198–2216.

Walter, M.J., Newsom, H.E., Ertel, W., Holzheid, A. (2000) Siderophile elements in the Earth and Moon: metal/silicate partitioning and implications for core formation. In: Canup, R.M., Righter, K. (Eds.) *Origin of the Earth and Moon*. University of Arizona Press, Tucson, 265-289

Wang, K., Day, J. M. D., Korotev, R. L., Zeigler, R. A. and Moynier, F. (2014) Iron isotope fractionation during sulfide-rich felsic partial melting in early planetesimals. *Earth and Planetary Science Letters* **392**, 124-132.

Warren, P. H. (2011) Stable-isotopic anomalies and the accretionary assemblage of the Earth and Mars: A subordinate role for carbonaceous chondrites. *Earth and Planetary Science Letters* **311**, 93-100.

Wasson J. T., Willis J., Wai C. M. and Kracher A. (1980) Origin of Iron Meteorite Groups IAB and IIICD. *Zeitschrift für Naturforschung A* **35**, 781–795.

Wlotzka (1993) A weathering scale for ordinary chondrites. *Meteoritics*,**28**, 460.

Wood B. J., Smythe D. J. and Harrison T. (2019) The condensation temperatures of the elements: A reappraisal. *American Mineralogist* **104**, 844–856.

Xu S., Binzel R. P., Burbine T. H. and Bus S. J. (1995) Small Main-belt Asteroid Spectroscopic Survey: initial results, *Icarus* **115**, 1–35.

York D. G., Adelman J., John E. Anderson Jr., Anderson S. F., Annis J., Bahcall N. A., Bakken J. A., Barkhouser R., Bastian S., Berman E., Boroski W. N., Bracker S., Briegel C., Briggs J. W., Brinkmann J., Brunner R., Burles S., Carey L., Carr M. A., Castander F. J., Chen B., Colestock P. L., Connolly A. J., Crocker J. H., Csabai I., Czarapata P. C., Davis J. E., Doi M., Dombeck T., Eisenstein D., Ellman N., Elms B. R., Evans M. L., Fan X., Federwitz G. R., Fiscelli L., Friedman S., Frieman J. A., Fukugita M., Gillespie B., Gunn J. E., Gurbani V. K., Haas E. de, Haldeman M., Harris F. H., Hayes J., Heckman T. M., Hennessy G. S., Hindsley R. B., Holm S., Holmgren D. J., Huang C., Hull C., Husby D., Ichikawa S.-I., Ichikawa T., Ivezić Ž., Kent S., Kim R. S. J., Kinney E., Klaene M., Kleinman A. N., Kleinman S., Knapp G. R., Korienek J., Kron R. G., Kunszt P. Z., Lamb D. Q., Lee B., Leger R. F., Limmongkol S., Lindenmeyer C., Long D. C., Loomis C., Loveday J., Lucinio R., Lupton R. H., MacKinnon B., Mannery E. J., Mantsch P. M., Margon B., McGehee P., McKay T. A., Meiksin A., Merelli A., Monet D. G., Munn J. A., Narayanan V. K., Nash T., Neilsen E., Neswold R., Newberg H. J., Nichol R. C., Nicinski T., Nonino M., Okada N., Okamura S., Ostriker J. P., Owen R., Pauls A. G., Peoples J., Peterson R. L., Petravick D., Pier J. R., Pope A., Pordes R., Prosapio A., Rechenmacher R., Quinn T. R., Richards G. T., Richmond M. W., Rivetta C. H., Rockosi C. M., Ruthmansdorfer K., Sandford D., Schlegel D. J., Schneider D. P., Sekiguchi M., Sergey G., Shimasaku K., Siegmund W. A., Smee S., Smith J. A., Snedden S., Stone R., Stoughton C., Strauss M. A., Stubbs C., SubbaRao M., Szalay A. S., Szapudi I., Szokoly G. P., Thakar A. R., Tremonti C., Tucker D. L., Uomoto A., Berk D. V., Vogeley M. S., Waddell P., Wang S., Watanabe M., Weinberg D. H., Yanny B. and Yasuda N. (2000) The Sloan Digital Sky Survey: Technical Summary. *The Astronomical Journal* **120**, 1579–1587.

Zolotov M. Yu., Mironenko M. V. and Shock E. L. (2006) Thermodynamic constraints on fayalite formation on parent bodies of chondrites. *Meteoritics & Planetary Science* **41**, 1775–1796.